Annual Report 2016

Physik-Department

Lehrstuhl für Funktionelle Materialien
mit dem
Fachgebiet Physik Weicher Materie

Technische Universität München

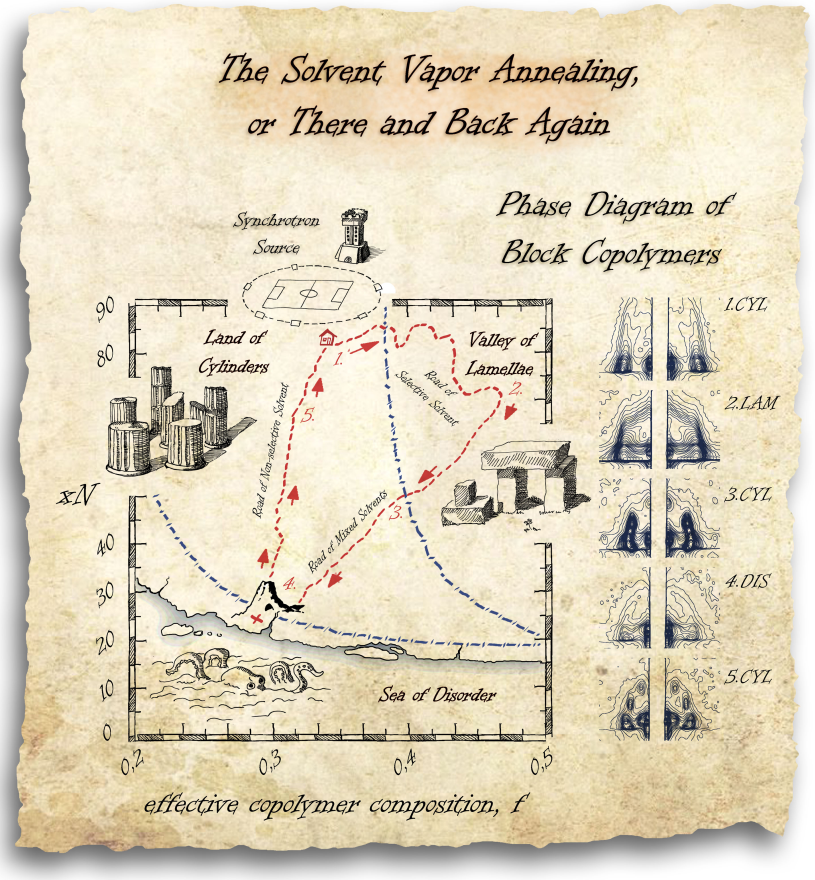

Prof. Dr. Winfried Petry
Chair of Functional Materials
Physik-Department

Deputy chairman for Prof. Dr. Winfried Petry:
Prof. Dr. Peter Müller-Buschbaum

Prof. Dr. Christine M. Papadakis
Soft Matter Physics Group

Physik-Department
Technische Universität München
James-Franck-Straße 1
85748 Garching

Secretaries: Marion Waletzki
Carola Kappauf

Tel.: +49(0)89 289 12452
Fax: +49(0)89 289 12473

Email: peter.mueller-buschbaum@ph.tum.de
papadakis@tum.de
marion.waletzki@ph.tum.de
carola.kappauf@ph.tum.de
http://www.functmat.ph.tum.de
http://www.softmatter.ph.tum.de

Editor: Dr. Anatoly V. Berezkin

Cover-page picture:

Probing of the phase diagram of the diblock copolymer with *in-situ* GISAXS upon solvent vapor annealing of the copolymer film.

Preface

It is a great pleasure to present the annual report for the year 2016 in the name of the staff of the Chair of Functional Materials and the Soft Matter Physics Group. It provides an overview of our teaching, research, and development activities. Our research activities are focused on functional materials and cover a broad range from soft matter physics to developments of methods and instrumentation. We examine the fundamental physics of material properties using mainly scattering methods (neutron, x-ray and light scattering). The general goal of our research is to explain the functional characteristics of soft condensed matter from the knowledge of the molecular dynamics and nanostructure.

In 2016, the chair activities covered the specific areas of water-based polymer systems, thin polymer films, polymer films for application in photovoltaics, polymer-hybrid systems and new materials. The activities in the fields of polymer films for application in photovoltaics and polymer-hybrid systems are successfully increasing. With *"TUM.solar"*, the keylab in the network of in the Bavarian Collaborative Research Project *"Solar Technologies go Hybrid"* (SolTec) headed by Prof. Müller-Buschbaum was running in the fifth year of funding. Research on *"Morphological degradation in low bandgap polymer solar cells - an in operando study"*, on *"Spray deposition of titania films with incorporated crystalline nanoparticles for all-solid-state dye-sensitized solar cells using P3HT"* and on *"A low temperature route towards hierarchically structured titania films for thin hybrid solar cells"* were featured on front covers of the high impact journals Advanced Energy Materials and Advanced Functional Materials, respectively. Investigations on perovskite solar cells complemented these activities. Moreover, nanostructured block copolymer thin films, polymer nanocomposites, multiresponsive polymer systems as well as polymers for medical applications were again in the focus of the research. Some of these results were featured on front covers of the journals Macromolecular Rapid Communications and Macromolecular Chemistry and Physics.

The in-house experiments available in the laboratories of the chair were supplemented by the lively activities at numerous large scale facilities, comprising synchrotron radiation and neutron scattering experiments, also at the FRM II. In particular, the in-house x-ray scattering experiments were operated with full time schedule. Glovebox environment for improved sample preparation of devices relying on air sensitive materials such as conjugated polymers was extended to perovskite materials. With the addition of instruments to measure the external quantum efficiencies and the development of a novel in-operando IV-measurement chamber for characterization of solar cells, new experimental options were added to our facilities. The sample environment for in-situ investigations of solvent vapor annealing was substantially improved, allowing higher flexibility. Moreover, together with our guest, Prof. Alfons Schulte, the high-pressure sample environments was modified to allow for automatic operation.

In 2016, the Chair of Functional Materials comprised 10 fellows, 46 PhD students, 39 master students, 18 bachelor students, 6 student assistants and 9 administrative and technical staff members. Six PhD theses were accomplished; moreover, 13 master theses as well as 15 bachelor theses were finished. As all the years before, we had the pleasure to host several guests from abroad, which stimulated a lively and inspiring scientific atmosphere.

In general, all members of the chair were very active at conferences and workshops, participating with both, talks and posters. Bart-Jan Niebuur won the price for the best talk of a young scientist at the Greek-German Workshop 2016 and Franziska Löhrer was rewarded with the price for the best talk on the "6th Colloquium of the Munich School of Engineering". Moreover, important conferences were organized by members of the chair: Prof. Winfried Petry co-organized the *"Neutrons for Energy"* conference in Bad Reichenhall, the *"50 years of neutron backscattering spectroscopy"* workshop in Graching and the *"VDI-TUM Experten Forum"* in Garchinf. Prof. Müller-Buschbaum was organizer of the *"5th International SolTech Conference"* in Munich hosting 200 participants. Moreover, he co-organized the *"Europolymer Conference 2016 (EUPOC2016): Block Copolymers for Nanotechnology Applications"* in Gargano (Italy) and the international workshop *"GISAXS 2016"* in Hamburg. Prof. Christine M. Papadakis co-organized the Greek-German Workshop 2016 *"Nanostructured soft materials: From polymer self-assembly to stimuli-responsive materials"*, held in Athens in September in the framework of the partnership with The National Technical University of Athens. Again, two Edgar-Lüscher seminars were organized, this year on the subjects *"Biophysik"* and *"Bionik"*. The 6th Colloquium of the Munich School of Engineering *"New concepts in Energy Science and Engineering"* took place in Garching. For the chair, a very important event this year was the summer school in Bergheim (Obertauern) in Austria - in the wonderful scenery of the Austrian Alps, all members of the chair gave talks on general subjects from the field of polymer physics. Everybody enjoyed the extensive discussions in combination with a fascinating landscape a lot!

Regarding teaching activities of the chair, we offered general physics lectures for the TUM elite engineers in the Munich School of Engineering (MSE) (Müller-Buschbaum), *"Advanced Physics for Teachers for Vocational Schools"* and *"Introduction to Condensed Matter Physics"* (Papadakis). Specialized lectures comprised *"Polymer physics"* and *"Nanostructured soft materials"*. Prof. Papadakis acted again as a deputy women's representative of the Physics Department. Moreover, Prof. Müller-Buschbaum is heading the activities in the *"Network Renewable Energies (NRG)"* in the MSE.

As a service to the community, Prof. Papadakis acted as one of the Editors-in-Chief of *"Colloid and Polymer Science"* and Prof. Müller-Buschbaum served as Associate Editor at *"ACS Applied Materials & Interfaces"*.

This annual report comprises a selection of the different research topics and projects carried out in the individual groups of the chair. It highlights the dedicated and successful research activities and collaborations with other groups and large scale facilities. We wish all chair members a fruitful continuation and a very successful year 2017.

Peter Müller-Buschbaum and Christine M. Papadakis March 2017

Contents

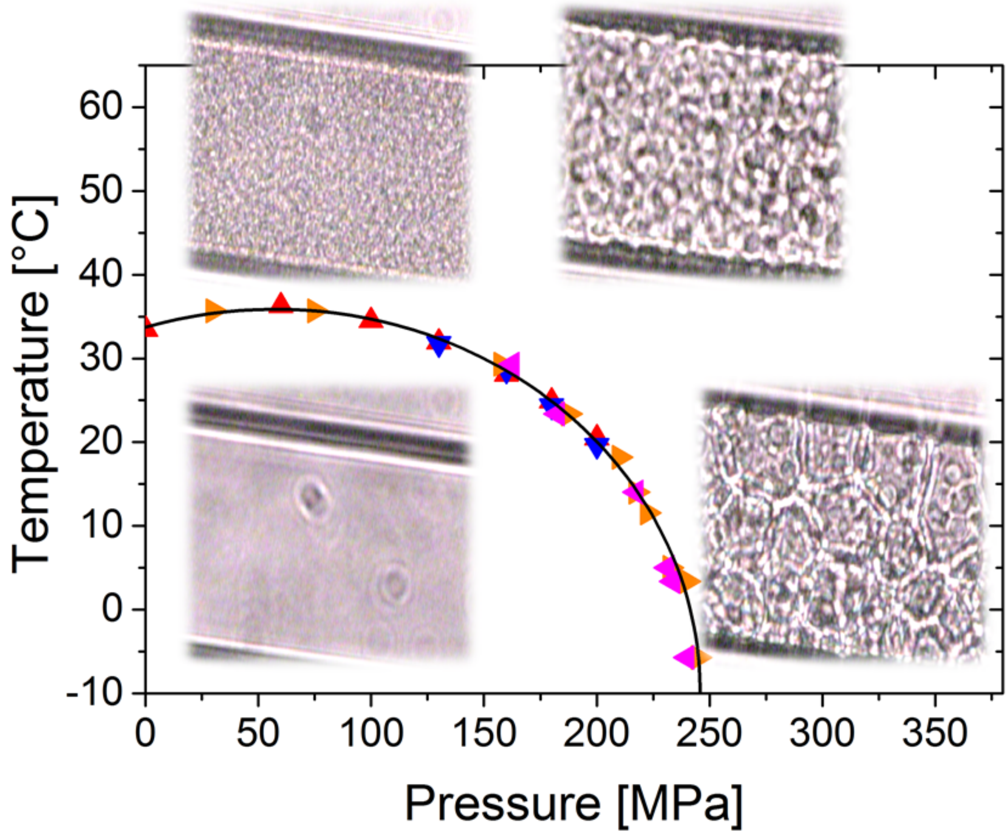
Temperature [°C]
60
50
40
30
20
10
0
-10
0
50
100
150
200
250
300
350
Pressure [MPa]

1.1 Water dynamics in a solution of PNIPAM in a water/methanol mixture - a quasi-elastic neutron scattering study

K. Kyriakos, M. Philipp, L. Silvi[1], W. Lohstroh[1], W. Petry[1], P. Müller-Buschbaum,
C. M. Papadakis

[1] MLZ, Garching, Germany

The hydration behavior of poly(N-isopropyl acrylamide) (PNIPAM) changes strongly at the cloud point, T_{cp}. Whereas the polymers are hydrated and water-soluble below, phase separation occurs above, along with a partial release of the associated water molecules. In particular, the mechanisms that govern the solvation of the PNIPAM chain in a mixed solvent of water and, e. g., methanol – termed cononsolvency – is far from being well understood. Albeit, at room temperature, both water and methanol are good solvents for the polymer, phase separation is encountered in a certain composition range of the solvent mixture. Quasi-elastic neutron scattering (QENS) revealed that, even several Kelvin above T_{cp}, PNIPAM is hydrated.

In the present work, we focus on the diffusion dynamics of water in a 25 wt% solution of PNIPAM (20-25 kg/mol) in a water/methanol mixture, aiming to elucidate the molecular interactions giving rise to cononsolvency. A 85:15 v/v mixture from H_2O and fully deuterated methanol (*d*-MeOD) was chosen. In the energy range studied, the signal is dominated by the dynamics of H_2O. Due to the high polymer concentration, the majority of the solvent molecules are expected to be associated to the polymer chain.

QENS experiments were performed at the time-of-flight direct spectrometer TOF-TOF at MLZ, Garching. Energy transfers in the range -1.4 to 10.0 meV and momentum transfers $q = 0.4 - 2.0$ $Å^{-1}$ were probed. Acquisition times were 4 h at each temperature. The samples were mounted in cylindrical aluminum cells having a slit width of 0.1 mm. The QENS spectra were modeled by a sum of an elastic component and 3 Lorentzians having amplitudes A_i and widths Γ_i.

Figure 1.1a shows a representative QENS spectrum at 21 °C. The fastest process giving rise to the broadest Lorentzian is ascribed to a superposition of local motions of the water molecules. The other two contributions account for the long-range diffusion of two different water species. The narrow and the broad contribution are attributed to strongly arrested and slightly arrested water dynamics.

The diffusion coefficients, D, of these two water species arising from the analysis of the q-dependence of the width within the isotropic jump diffusion model are given in Figure 1.1b together with the values in bulk water and in the H2O:*d*-MeOD mixture. The two types of water exhibit significantly different values of D. Comparison with the dynamics of the water molecules in bulk water and in the H_2O:*d*-MeOD mixture reveals that the strongly arrested water is related to water-polymer interactions, since it has not been observed in the absence of polymer. Interestingly, the signal of this contribution persists even 8 K above T_{cp}, i. e., water resides in the PNIPAM-rich aggregates even in the demixed phase. The diffusion coefficients of the slightly arrested water are in the same range as the ones obtained for the water molecules in H_2O:*d*-MeOD without polymer (Figure 1.1b). Thus, we assign this population to water molecules that interact with methanol molecules via the kosmotropic effect, while interactions with the polymer cannot be excluded, such as the participation in hydration layers of higher order or the formation of cages around the hydrophobic isopropyl groups. The behavior of the residence times of the two types of water (Figure 1.1c) is in accordance with this picture. The residence times of the strongly arrested water are $\sim$ 3 ps, thus much longer than the ones of the slightly arrested water are 0.2-0.8 ps, which are comparable to the ones in bulk water and in H_2O:*d*-MeOD. The relative peak amplitudes of the two Lorentzians as a function of temperature (Fig. 1.1d) show that the number of strongly arrested water molecules decreases above T_{cp} in favor of the number of the slightly arrested ones. This observation is in agreement with the

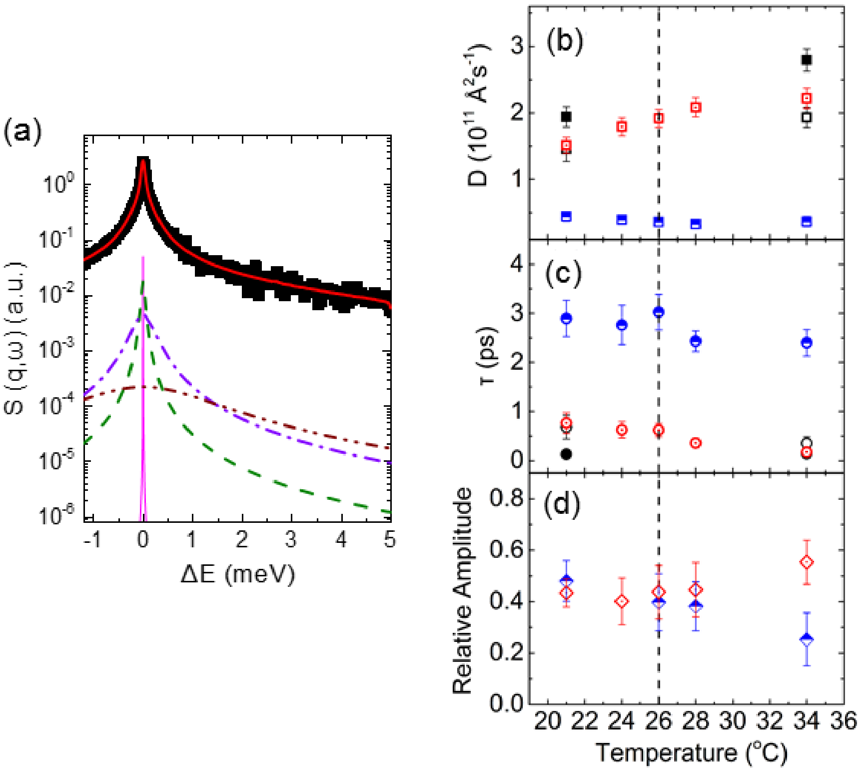

Figure 1.1:
(a) QENS spectrum $S(q, \omega)$ versus energy transfer ΔE of the 25 wt.-% solution of PNIPAM in 85:15 v/v H_2O:*d*-MeOD at $q = 1.1$ Å^{-1} and 21 °C. Black squares: experimental data, solid red line: full fit, dashed green line: long range diffusion of strongly arrested H_2O molecules, dash-dotted purple line: long range diffusion of slightly arrested H_2O molecules, dash-double-dotted red line: superposition of local motions of the H_2O molecule, magenta solid line: elastic component. (b-c) Resulting dynamic parameters: (b) the diffusion coefficients, (c) the residence times and the relative amplitudes of the water molecules with strongly arrrested dynamics (half-filled blue symbols) and with slightly arrested dynamics (dotted red symbols). Solid black and open black symbols are from H_2O and from H_2O:*d*-MeOD.

expectation that the collapse of the PNIPAM chain leads to a release of a fraction of those water molecules in direct interaction, since the contraction of the chain at T_{cp} is expected to reduce the number of the available H-bonding sites. Interestingly, this transition does not occur abruptly at T_{cp}, but spans over several Kelvin, in good agreement with our previous results [1].

We conclude that the solvent dynamics in concentrated PNIPAM solutions in water/methanol mixtures are complex. Water presumably forms hydrogen bonds with the amide group of PNIPAM, which is affected by the cloud point, in contrast to the less strongly bound population. QENS together with contrast variation is a powerful tool to detect and characterize the local diffusional processes of the water molecules.

This work was supported by the DFG priority program SPP1259 “Intelligente Hydrogele” (Pa771/4, Mu1487/8).

[1] M. Philipp, K. Kyriakos, L. Silvi, W. Lohstroh, W. Petry, J.K. Krüger, C. M. Papadakis, P. Müller-Buschbaum, *J. Phys. Chem. B* **118**, 4253-4260 (2014)

[2] K. Kyriakos, M. Philipp, L. Silvi, W. Lohstroh, W. Petry, P. Müller-Buschbaum, C. M. Papadakis, *J. Phys. Chem. B* **120**, 4679-4688 (2016)

1.2 Multi stimuli-responsive polymer thin films

C. Herold, M. Philipp, V. Hildebrand[1], A. Laschewsky[2], R. Cubitt[3], P. Müller-Buschbaum

[1] Universität Potsdam, Institut für Chemie, Potsdam-Golm, Germany
[2] Fraunhofer Institut für Angewandte Polymerforschung, Potsdam-Golm, Germany
[3] ILL, Grenoble, France

Thin films from stimuli-responsive polymers react strongly to small changes of environmental parameters such as temperature, humidity or pH value. As a response, the polymer films swell or deswell by incorporating or releasing water. [1] The high sensitivity and almost instant response make these materials very interesting for a wide spectrum of applications such as sensors, drug release, bio engineering and surface coatings. [2]
In order to design novel stimuli responsive materials, a variety of new homopolymers and block-copolymers were synthesized, all with at least one block consisting of an UCST type phase transition polymer. In the present study, we focus on the homopolymer poly(SPP)$_{79}$ which is a so called sulfobetaine. The polymer in aqueous solution has an UCST-type phase transition at 12 °C in H_2O and at 18 °C in D_2O. [3]
Big advantage of the polymer is the presence of zwitterionic side chains, leading to a very high sensitivity to the ionic concentration (e.g. pH value) of the environment. It is possible to tune the phase transition behavior of the solved polymers by changing the ionic concentration of the environment. [3] The key to the design and implementation of these so called „smart“ polymeric materials is an in depth understanding of their response to external stimuli. In this respect, both, the macroscopic swelling behavior as well as the processes on the molecular level are of great importance. With different characterization methods, we were able to follow the temperature dependent hydration of thin poly(SPP)$_{79}$ films both, on the macroscopic and on the molecular level.

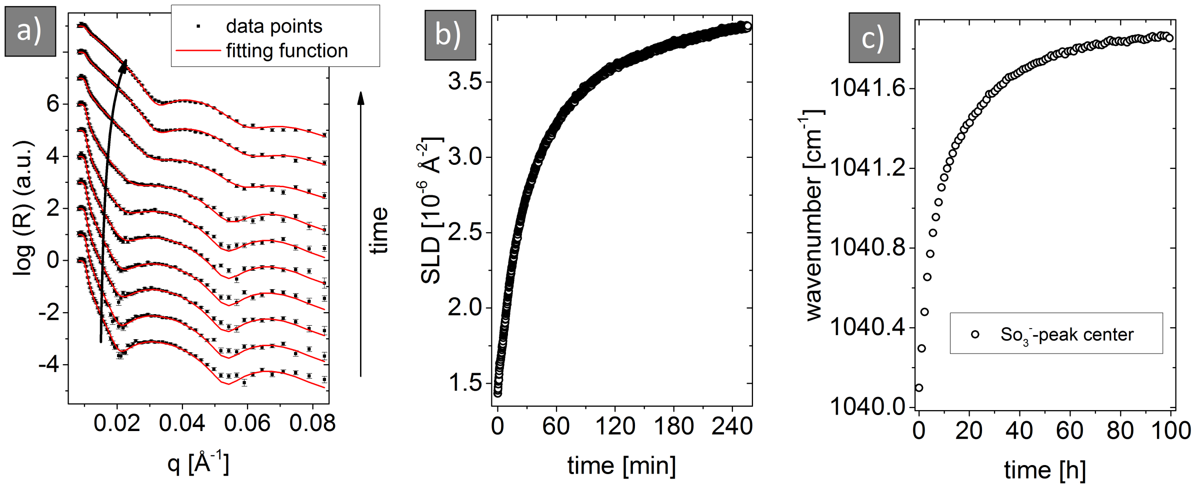

Figure 1.2:
Hydration of a thin film from different viewpoints: a) Fitted NR data sets from the hydration of the sample. b) Modeled development of the polymer layer SLD from the NR data sets. c) Evolution of the peak center from vibrational absorbance peak of the SO_3^- group, seen with FTIR spectroscopy.

For sample preparation, silicon substrates were first cleaned with an acid bath and oxygen plasma. The dry polymer was dissolved with TFE. Then the polymer was spin coated or solution casted on the substrate, depending on the characterization method used.

Neutron reflectivity (NR) measurements allow to do very precise in situ studies on thickness, roughness and water content of the film. The NR measurements were done the D17 instrument at ILL, Grenoble. In Fig. 1.2 a) NR curves are shown that were taken while the polymer film was swelling with D_2O. The data collection started immediately after the sample was exposed to D_2O vapor with one NR measurement acquired every 5 s. To fit the NR data, a multi-layer model was simulated using the MOTOFIT software. For this model, we considered a thin silicon oxide layer on top of the silicon substrate as well as a single polymer layer. To fit all 2600 NR curves measured during the hydration process, a batch processing approach was taken where the fitted parameters are used as starting values for the next fit.

In Fig. 1.2 b) the results of the NR data analysis are shown. The SLD of the polymer layer increases strongly as D_2O is incorporated in the film. This is due to D_2O having a much higher SLD ($6.38 \cdot 10^{-6}$ Å^{-2}) as compared with H_2O ($0.56 \cdot 10^{-6}$ Å^{-2}).

Fourier-Transform Infrared spectroscopy (FTIRS) allows to analyze the development of the molecular bonds in a sample, by measuring the absorbance in the infrared range. In Fig. 1.2 c) the shift of the IR-absorbance peak center assigned to the SO_3^- group of SPP is depicted. At the beginning, the sample is exposed to water vapor and it takes in a significant amount of water over time. The change of the peak position is due to the bigger number of water molecules surrounding the SO_3^- group. It is also very much possible that a water shell of oriented water molecules forms around the group due to it's net charge.

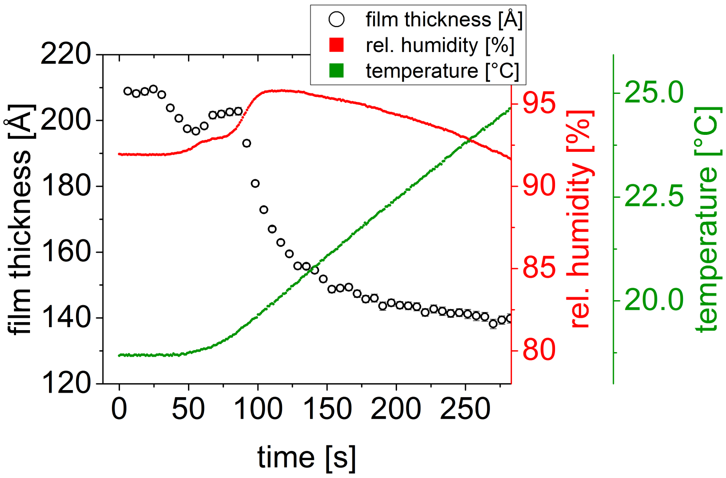

Figure 1.3:
Response of a thin swollen poly(SPP)$_{79}$ polymer film to an increase in temperature as measured by NR. The film suddenly collapses hinting towards a phase transition.

With changing temperature the interaction energies between the molecules vary and thus the macroscopic film can respond to a temperature change. In Fig. 1.3 the results from the analysis of the NR data are shown that were taken while the temperature was increased. It can be seen that the film strongly collapses while humidity is increasing. Therefore, we believe that this phase transition is triggered by a temperature change.

In conclusion we were able to follow both, the macroscopic response of the film to changes in the environment as well as the rearrangements on the molecular level that underlie this behavior. Further evaluation of the data will show if we can describe the behavior of the films with already existing models.

[1] D. Magerl, M. Philipp, X. P. Qiu, F. M. Winnik, P. Müller-Buschbaum, *Macromolecules* **48**, 3104–3111 (2015)

[2] R. Hoogenboom, *Smart polymers and their applications*, 15-44 (2014)

[3] V. Hildebrand, A. Laschewsky, D. Zehm, *J. Biomat. Sci.-Polym. E.* **25**, 1602-1618 (2014)

1.3 Aggregation behavior of doubly thermoresponsive diblock copolymers consisting of poly(sulfobetaine) and poly(*N*-isopropylacrylamide) or poly(*N*-isopropylmethacrylamide)

N. S. Vishnevetskaya, V. Hildebrand[1], Z. Di[2], A. Laschewsky[13], P. Müller-Buschbaum, C. M. Papadakis

[1] Institute of Chemistry, University of Potsdam, Germany
[2] MLZ, Garching, Germany
[3] Fraunhofer Institut für Angewandte Polymerforschung, Potsdam-Golm

Water-soluble thermoresponsive polymers are a subclass of stimuli-sensitive polymeric systems, which are promising for a number of applications. In most aqueous thermo-sensitive polymeric solutions, lower critical solution temperature (LCST) or upper critical solution temperature (UCST) behavior is found, depending on whether the miscibility gap occurs at high or low temperatures. Twofold thermoresponsive diblock copolymers PSBP-*b*-PNIPAM (Fig. 1.4a) and PSBP-*b*-PNIPMAM (Fig. 1.4b), which consist of a zwitterionic polysulfobetaine poly(*N*,*N*-dimethyl-*N*-(3-methacrylamidopropyl)-ammoniobutanesulfonate) (PSBP) block and a nonionic poly(*N*-isopropylacrylamide) (PNIPAM) or poly(*N*-isopropylmethacrylamide) (PNIPMAM) block, combine a LCST and an UCST in aqueous solution, respectively, of the constitutive homopolymers. PSBP is a permanently zwitterionic polymer, and its UCST can be decreased by adding small amounts of electrolyte [1,2]. This special feature of PSB will affect the phase transition temperatures of the block copolymers as shown in Fig. 1.4c.

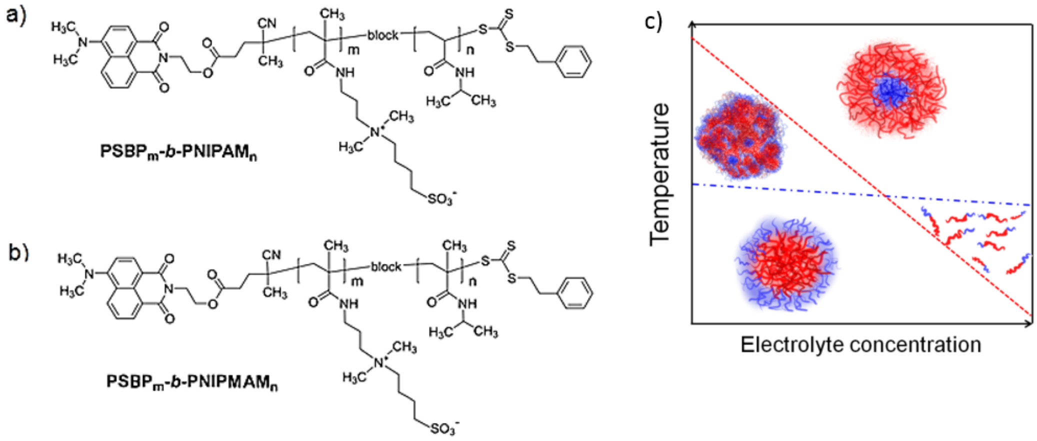

Figure 1.4:
Chemical structures of (a) PSBP-*b*-PNIPAM (m = 78, n = 100) and (b) PSBP-*b*-PNIPMAM (m = 78, n = 115). (b) Expected structures in aqueous solution: micelles with PNIPAM/PNIPMAM shell and PSB core or vice versa at low and high temperatures and large aggregates/precipitates or molecularly dissolved polymers in the intermediate temperature range, with changes in UCST and LCST transitions caused by the addition of an electrolyte.

Using turbidimetry, we investigated the phase behavior of 5 wt.-% solutions of the PSBP-*b*-PNIPAM and PSBP-*b*-PNIPMAM in D_2O and in 0.004 M NaBr in D_2O. These results show that, in salt-free D_2O, both polymer solutions are turbid at all investigated temperatures, which is presumably due to the aggregation of the PSB (UCST) and PNIPAM/PNIPMAM (LCST) and very similar values of their cloud points. Addition of small amounts of NaBr causes the appearance of an intermediate temperature range, where the light transmission is marginally increased. In the PSBP-*b*-PNIPAM solution, this range spans from 27°C to 35°C; in the PSBP-*b*-PNIPMAM solution, the range is from 27°C to 43°C. The UCST thus decreases upon addition of NaBr, which illustrates the ionic-strength sensitive properties of the PSBP block that leads to the behavior sketched in Fig. 0.1c.

A detailed structural characterization of 5 wt.-% solutions of the diblock copolymers in D_2O and in 0.004 M NaBr in D_2O was carried out using temperature-resolved small-angle neutron scattering (SANS). Measurements were carried out during heating in steps of 5°C or 10°C, respectively, with equilibration times of 15 min. SANS experiments were performed at the instrument KWS-1 at the JCNS outstation at MLZ in Garching, Germany.

The temperature-resolved SANS curves of the diblock copolymers in aqueous solution are shown in Fig. 1.5a and b. From the curve shapes, two regimes are clearly discernible, presumably below the UCST and above the LCST cloud points, which are very close to each other. The curves below the UCST (Fig. 1.5a (10-30°C), b (20-45°C)) were fitted using a model for polydisperse, homogeneous spheres correlated by a hard-sphere structure factor, plus an Ornstein-Zernike (OZ) term describing the concentration fluctuations in the noncompact shell, and Porod scattering due to very large aggregates at low and high q-values, respectively. The curves above the LCST (Fig. 1.5a (40-50°C), b (50-65°C)) were fitted using a model for flexible cylinders with a polydisperse radius together with the hard-sphere structure factor, a solvation term describing the concentration fluctuations typical for polyelectrolytes and a Porod term. The contour length of the cylinders increases during heating. The core and shell of the micelles could neither be distinguished below the UCST nor above the LCST transitions. We conclude that both diblock copolymers form spherical particles below the UCST-type transition and cylindrical ones above the LCST-type transition. The salt-induced structural changes, investigated at the example of PSBP-*b*-PNIPMAM, are evident below the LCST-type transition. The decrease of the sphere radii at 35-45°C indicates a disintegration of the micelles in the intermediate range between the UCST- and LCST-type transitions, that appear in 0.004 NaBr in D_2O (Fig. 1.5c,d). Thus, the system indeed displays the behavior sketched in Fig. 1.4c.

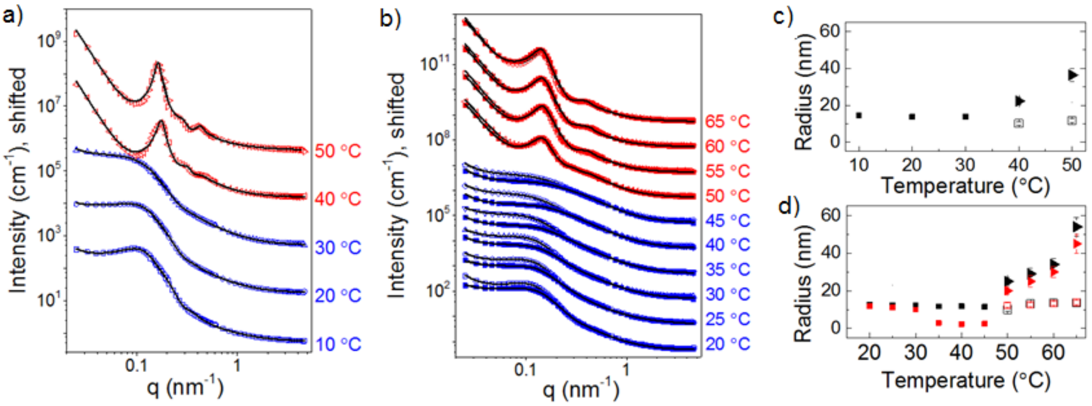

Figure 1.5:
Temperature-resolved SANS curves from 5 wt.-% solutions of PSBP-*b*-PNIPAM (a) and PSBP-*b*-NIPMAM (b) in salt-free D_2O (closed symbols) and in 0.004 M NaBr (open symbols) in D_2O, in double-logarithmic representation. Temperature dependence of the corresponding radius of spheres (closed squares) and cylinders (open squares), contour cylinder length (closed triangles) of PSBP-*b*-PNIPAM (c) and PSBP-*b*-NIPMAM (d) without salt (black symbols) and with NaBr (red symbols).

The work is funded by the DFG (Pa771/14-1).

[1] P. Köberle, A. Laschewsky, T. D. Lomax, *Makromol. Chem.* **12**, 427 (1991)

[2] V. Hildebrand, A. Laschewsky, E. Wischerhoff, *Polym. Chem.* **7**, 731 (2016)

1.4 H_2O-D_2O exchange kinetics of thermoresponsive block copolymer films followed with in situ time-of-flight neutron reflectivity

L. Kreuzer, T. Widmann, A. Laschewsky[1], V. Hildebrand[1], J.-F. Moulin[2], M. Haese[2]
P. Müller-Buschbaum

[1] Universität Potsdam and Fraunhofer Institute for Applied Polymer Research, Potsdam-Golm, Germany

[2] MLZ, Garching, Germany

The ability of block copolymers to self-assemble into micro-domains has gained high scientific interest and is exploited in a broad range of applications such as lithography, molecular biology, colloid science and many more. More flexibility can be reached by using thermoresponsive block copolymers since they can undergo strong changes in volume only by a small change of temperature. In the present work we prepared thin block copolymer films consisting of a zwitterionic poly(sulfobetaine) (PSB) block and a non-ionic poly(N-isopropylacrylamide) (PNIPAM) block (Figure 1.6a). Both homopolymers exhibit different phase behavior, namely a lower critical solution temperature (LCST in case of PNIPAM) and an upper critical solution temperature (UCST for PSB block) behavior in aqueous solutions [1]. A reproducible and reversible uptake of penetrants is crucial in case of sensors, microfluidic devices, separation membranes and drug carriers. Therefore, it is essential to understand and control the sorption/desorption and diffusion processes of low-molecular penetrants interacting with the polymer [2-4].

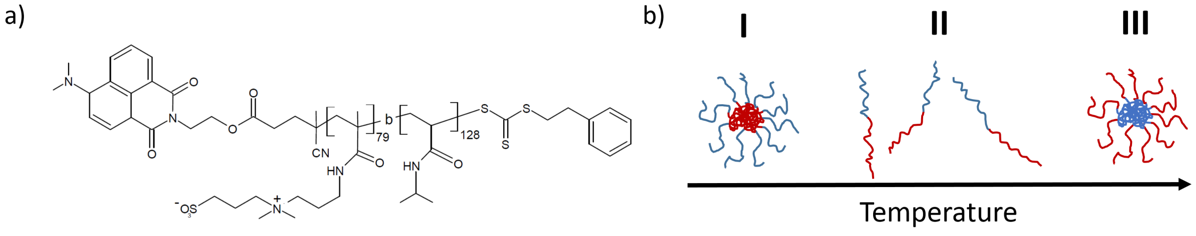

Figure 1.6:
a) Chemical structure of the studied block copolymer PSB-*b*-PNIPAM. b) possible structures of PSB-*b*-PNIPAM as temperature increases: (I) micelles with a PSB core and PNIPAM as shell at low temperatures, (II) unimers in the intermediate temperature range and (III) micelles with a PNIPAM core and a PSB shell at high temperatures.

Sorption, diffusion and the resulting swelling processes are usually followed by measuring the changes in chemical composition, mass or dimensions with techniques such as quartz crystal microbalance, ellipsometry, X-ray reflectivity and infrared spectroscopy. We focus in-situ on the H_2O – D_2O (and vice versa) exchange kinetics of PNIPAM-b-PSB films using time-of-flight (TOF) neutron reflectivity. The outstanding feature of the TOF mode lies in the possibility to tune the wavelength band of the incident neutrons within a resolution of 0.2 and 10 %. Furthermore the intensity is maximized by using an 80 millimeter broad, slit collimated neutron beam. In TOF mode a large q range is accessible at a fixed incident angle and the kinetics can be followed without any motor movement with a high time resolution to determine the underlying fundamental processes. Block copolymer films of high homogeneity and tunable thickness (30 nm to 100 nm) were prepared via spin coating on silicon substrates. For measurements, the samples were placed in our specially designed vapor chamber in which we were able to generate either a D_2O or an H_2O atmosphere respectively with an adjustable relative humidity, simply by injecting D_2O (or H_2O) into the reservoir of the chamber. Figure 1.7

shows neutron reflectivity data of the exchange kinetics of H_2O by D_2O (a) and vice versa (b) in thin (40 nm) PSB-*b*-PNIPAM films. The experiment was carried out at the REFSANS instrument at the FRM II neutron source in Garching. A strong increase in intensity is observable due to the higher scattering length density (SLD) of D_2O. Furthermore, a second fringe appears with time, indicating swelling and as a result an increased film thickness. During the reversed experiment (Figure 1.7b) the expected decrease in intensity is clearly observable and proves the exchange of D_2O molecules by H_2O. Although there is a shift of the fringes towards smaller q_z values the distance between the minima is not altered during the whole experiment, which suggests no change in film thickness.

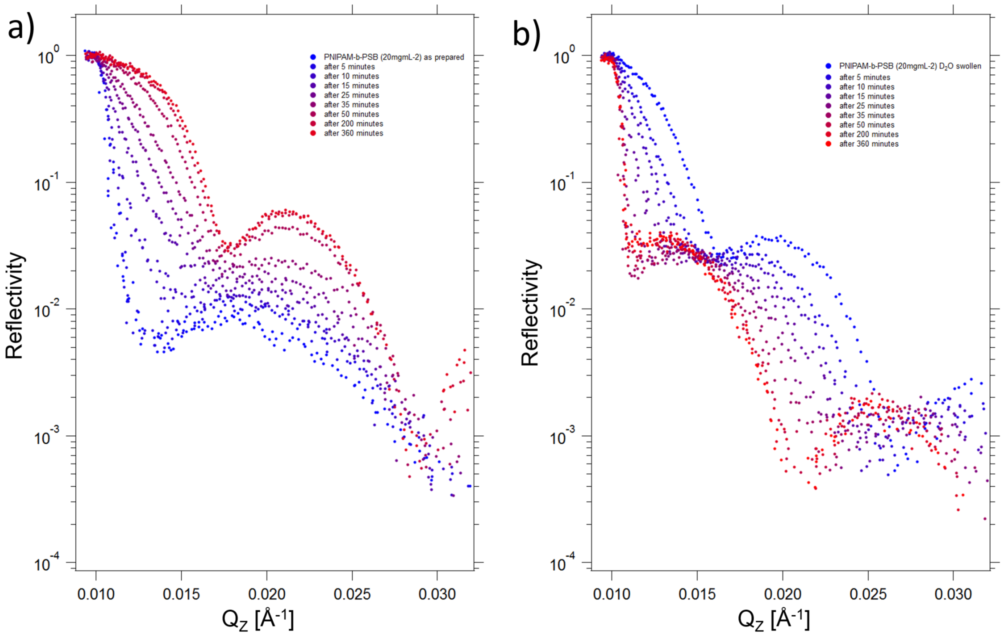

Figure 1.7:
Kinetic TOF neutron reflectivity measurements of PSB-*b*-PNIPAM films (40 nm) in a D_2O atmosphere (a) and the subsequent kinetic measurement of the same, now D_2O-swollen, film in a H_2O atmosphere (b).

In conclusion, we were able to follow in-situ the H_2O – D_2O (and vice versa) exchange kinetics of a block copolymer that shows both, an LCST and an UCST behavior. A detailed data analysis is ongoing and will give information about time constants of the kinetics as well fundamental information about the processes involved.

In further experiments, we plan to vary the film thickness to determine the effect of the thickness on the D_2O - H_2O exchange. Those experiments result in a more detailed insight into the mechanism of the interaction of low-molecular penetrants and polymer films in order to generate sophisticated materials.

[1] M. Mertoglu, S. Garnier, A. Laschewsky, K. Skrabania, J. Storsberg, *Polymer* **46**, 7726 (2005)

[2] M. Koenig, D. Magerl, M. Philipp, K. J. Eichhorn, M. Müller, P. Müller-Buschbaum, M. Stamm, P. Uhlmann, *RSC Advances* **4**, 17579-17586 (2014)

[3] M. Philipp, V. Körstgens, D. Magerl, C. Heller, Y. Yao, W. Wang, G. Santoro, S. V. Roth, P. Müller-Buschbaum, *Langmuir* **31**, 9619-9627 (2015)

[4] M. A. Cole, N. H. Voelcker, H. Thissen, H. J. Griesser, *Biomaterials* **30**, 1827-1850 (2009)

1.5 Influence of pressure on the aggregation behavior of aqueous PNIPAM solutions

B.-J. Niebuur, K.-L. Claude, S. Pinzek, C. Cariker[1], K.N. Raftopoulos, V. Pipich[2], M.-S. Appavou[2], A. Schulte [1], C.M. Papadakis

[1] University of Central Florida, Orlando, USA
[2] MLZ, Garching, Germany

Poly(N-isopropylacrylamide) (PNIPAM) is one of the most investigated thermoresponsive polymers in the last decades because of its applications as smart materials or as a model to study the behavior of more complex proteins. In aqueous solutions, PNIPAM features a lower critical solution temperature (LCST) at ~31 °C [1]. Below the LCST, the chains are hydrated, an ordered shell of water surrounds the hydrophobic methyl groups, and the polymer is soluble. When the temperature is increased above the LCST, the polymeric chains dehydrate. The system phase-separates into a solvent-rich phase and polymer-rich mesoglobules, which are stable in size at long time scales [2]. The origin of the stabilizing mechanism is still under debate.

In the present study, we use pressure as an additional thermodynamic parameter to investigate the stability of the mesoglobules formed by PNIPAM. Previous studies on the phase behavior have revealed that the phase boundary in the temperature-pressure frame is elliptical [3], as expected from theoretical calculations [4]. Using IR spectroscopy, the mechanism of phase separation induced by pressure was found to be fundamentally different from phase separation induced by temperature at atmospheric pressure [5].

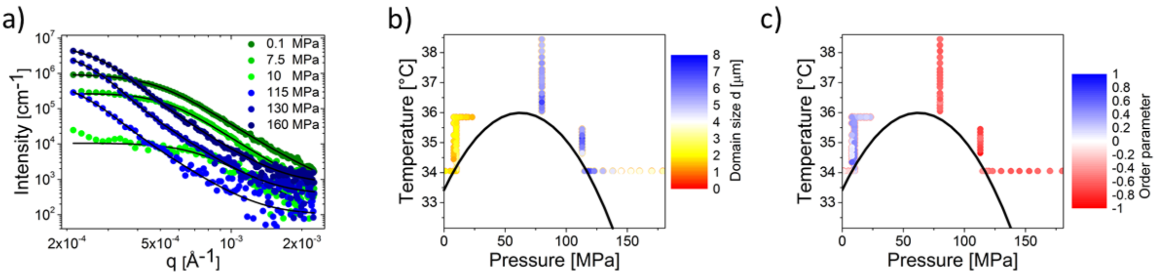

Figure 1.8:
(a) V-SANS curves from a 3 wt% PNIPAM solutions in D_2O at 33.8 °C with increasing pressure in the low-pressure regime (green), the one-phase region (red) and the high-pressure regime (blue). Resulting values of the domain size (b) and of the order parameter (c) for all measurements.

We used very small-angle neutron scattering (V-SANS) to characterize the mesoglobules in a 3 wt% PNIPAM solution in D_2O in dependence on temperature and pressure. The experiments were performed at the instrument KWS-3 at the JCNS at MLZ. A q-range of $2 \cdot 10^{-4}$ - $2 \cdot 10^{-3}$ $Å^{-1}$ was covered. Measurements of 5 min were repeated multiple times at each measured temperature and pressure. The 2D scattering patterns were corrected for background scattering and azimuthally averaged. The obtained scattering curves, shown in Fig. 1.8a for selected pressures, were fitted with the Teubner-Strey structure factor, which describes scattering from a bicontinuous system. Fig. 1.8b shows the resulting domain size from all measurements in dependence on temperature and pressure. At atmospheric pressure, the mesoglobule size is ~1 μm. In contrast, the mesoglobules are much larger at high pressures. Directly after reaching the two-phase region, the mesoglobules have sizes up to 8 μm, but they shrink to ~4 μm further away from the phase boundary. Time-resolved measurements at constant temperature and pressure show that, close to the phase boundary, the system is not in equilibrium. Only further away, a steady state is reached.

A second fitting parameter is the order parameter, shown in Fig. 1.8c. It relates the domain size and the correlation length and gives information about the structural order of the system. Also here, a clear difference between the investigated pressure regimes is found. At low pressure, the value of the order parameter is close to one, which means that the system is only poorly ordered. At high pressure, the order parameter is close to -1, suggesting that the domains are spatially correlated with each other.

Further understanding of the system is obtained by Raman spectroscopy. Fig. 1.9a and 1.9b show spectra at atmospheric pressure and at 113.8 MPa, respectively, with increasing temperature across the phase transition temperature. The changes in the vibrational frequency, shown in Fig. 1.9c for the antisymmetric CH_3 stretching band, reveal changes of the interactions of the hydrophobic groups of PNIPAM with water. In the one-phase region, the CH_3 groups form improper hydrogen bonds with water at all investigated pressures. Above the phase transition temperature, a clear decrease of the vibrational frequency is observed at atmospheric pressure, indicating that the PNIPAM chains lose water during phase separation. At increased pressure, the decrease of vibrational frequency is less pronounced, implying that the chains stay hydrated in the two-phase region.

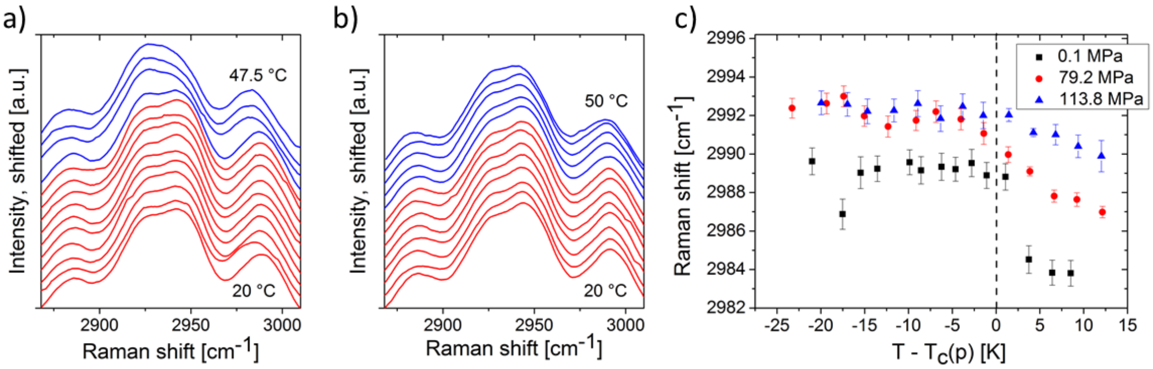

Figure 1.9:
Raman spectra at the CH-stretching region at atmospheric pressure (a) and at 113.8 MPa (b), red curves represent measurements in the one-phase region, blue curves in the two-phase region. (c) Frequency of the antisymmetric CH_3 stretching band as a function of temperature.

The molecular approach of Raman spectroscopy may explain the mesoscopic structure found using V-SANS. The polymer-rich domains at high pressure contain more water than at low pressure, indicating that the increased domain size at high pressure is due to the decreased efficiency of the phase separation with respect to atmospheric pressure.

[1] M. Heskins, J.E. Guillet, *J. Macromol. Sco., Part A* **2**, 1441-1445 (1968)

[2] V. Aseyev, S. Hietala, A. Laukkanen, M. Nuopponen, O. Confortini, F.E. Du Prez, H. Tenhu, *Polymer* **46**, 7118-7131 (2005)

[3] K. Otake, R. Karaki, T. Ebina, C. Yokoyama, S. Takahashi, *Macromolecules* **26**, 2194-2197 (1993)

[4] S.A. Hawley, *Biochemistry* **10**, 2436-2442 (1971)

[5] F. Meersman, J. Wang, Y. Wu, K. Heremans, *Macromolecules* **38**, 8923-8928 (2005)

1.6 Structure and properties of self-assembled thermoresponsive diblock copolymer films

E. Metwalli, H. Xu, P. Müller-Buschbaum

Stimuli-responsive polymers are able to change their chemical and physical properties using an external stimulus, such as temperature, pH, or light [1]. Thus, thermoresponsive polymers gives more flexibilities and possibilities in the design and construction of nanoscale hybrid materials. In this report, the thermoresponsive behavior of free-standing bulk nanostructured polystyrene-*block*-poly(N-isopropylacrylamide) PS-*b*-PNIPAM diblock copolymer (DBC) film is investigated. Swelling/deswelling behavior upon water vapor uptake was studied using the in situ small-angle X-ray scattering (SAXS) for two different PS-*b*-PNIPAM DBCs: one DBC with a major PNIPAM weight fraction and another with a major PS weight fraction. Bulk samples were prepared via solution casting method and annealed at 130°C for 48 h to create nanostructured film. A special temperature and humidity controlling cell was designed and constructed to perform the in situ SAXS study on the nanostructured PS-*b*-PNIPAM DBC free standing bulk film. The experiment was performed at two temperature jumps above (40°C) and below (20°C) the characteristic lower critical solution temperature of the PNIPAM block (LCST = 32°C), and at three different relative humidities of 5, 70, and 90% (Fig. 1.10). Relative humidity at temperatures below the LCST had a significant effect on the thermoresponsive behavior of the DBC bulk film with major PNIPAM block. At high relative humidity (90%), the DBC bulk film systematically swelled in water vapor within several hours at 20°C. Upon switching from high to low (5%) relative humidity at the same temperature, significant deswelling of the DBC film was observed, indicating the strong sensitivity of the system to the humidity environment at temperatures below the LCST. This behavior has, to the best of our knowledge, been rarely reported in previous investigations of nanostructured thermoresponsive hydrogel "dry" systems. A phase transition from a lamellar/cylindrical to a mainly cylindrical DBC bulk film morphology was observed after several hours' exposure to water vapor at 20°C. Upon the temperature jump from 20°C to 40°C, the swollen DBC film quickly shrank, going through a reversible phase transition from cylindrical to its initial lamellar structure. Between temperature jumps, the film was quite reversible in the swelling/deswelling process, exhibiting a stable and consistent behavior. In contrast, in the PS-*b*-PNIPAM DBC bulk film with major PS block, the swelling/deswelling behavior of the PNIPAM domains was dramatically limited due to the confinement effect of the rigid glassy PS matrix. In order to determine how far the swelling of the PS-*b*-PNIPAM DBCs could proceed and to achieve an equilibrium state, ex situ SAXS experiments were also performed on the films after they had been subjected to water vapor swelling for 1-2 weeks. In this second set of experiments, the PS-*b*-PNIPAM DBC with major PS block again swelled to a much lesser extent than the PS-*b*-PNIPAM DBC bulk film with major PNIPAM block. For the latter DBC, however, an equilibrated structure was not achieved even after two weeks of water vapor exposure. Possible deterioration/deformation of the free standing DBC films upon long time water vapor exposure has also to be taken into account.

This interesting behavior of the bare nanostructured DBC in swelling/deswelling upon simple water vapor exposure involves a change in the inter-domain spacing, which in turn implies the potential for optical/sensor related applications in case of metal or metal oxide incorporation in one or other polymer domain [2]. The ability to manipulate the periodic spacing between nanoscale particles within metal oxide NPs/DBC hybrid nanomaterials using thermoresponsive-type DBCs is potentially foreseen and is currently under investigation.

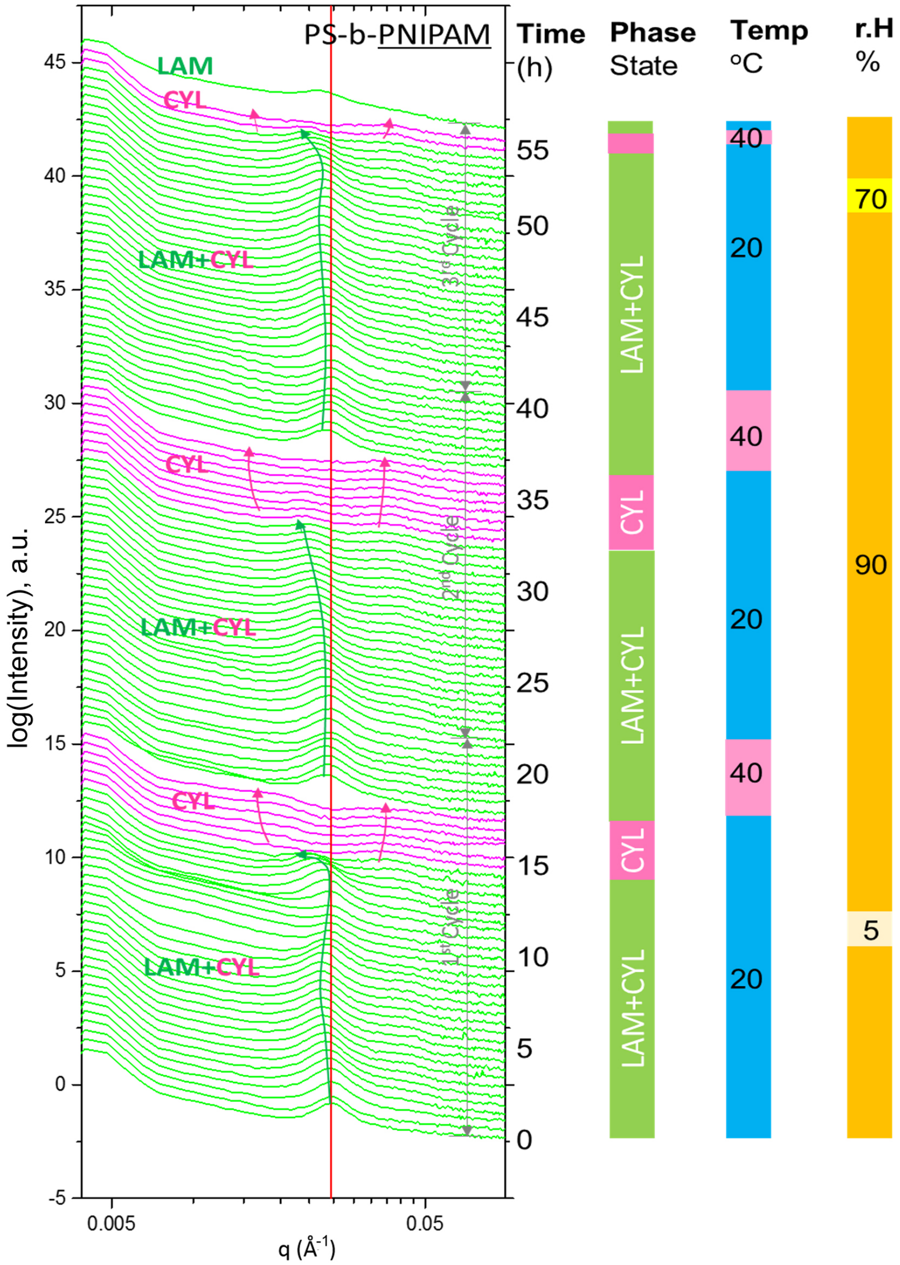

Figure 1.10:
Evolution of in situ SAXS 1D profiles of bare PS-*b*-PNIPAM DBC with major PNIPAM block during temperature jumps. The red vertical line indicates the initial peak position. For this in situ SAXS experiment, the q value decreases gradually in the beginning at 20°C, indicating the progressive swelling of the DBC free-standing film in water vapor. At the temperature jump to 40°C, the PNIPAM block dramatically shrinks and deswells most of the physically absorbed water. This is indicated by the immediate shift in the q value to its initial value. A phase transition from lamella to cylinder morphologies is observed near the end of each swelling cycle at 20°C.

[1] Q. Zhong, E. Metwalli, M. Rawolle, G. Kaune, A.M. Bivigou-Koumba, A. Laschewsky, C.M. Papadakis, R. Cubitt, P. Müller-Buschbaum, *Macromolecules* **48**, 3604-3612 (2015)

[2] Y. Yao, E. Metwalli, B. Su, V. Körstgens, D. Mosegui-Gonzalez, A. Miasnikova, A. Laschewsky, M. Opel, G. Santoro, S.V. Roth, P. Müller-Buschbaum, *ACS Appl. Mater. Interfaces* **7**, 13080-91 (2015)

1.7 Molecular dynamics of PNIPAM in concentrated water methanol mixtures, as studied by dynamic light scattering

M. Nüber, K. N. Raftopoulos, B. J. Niebuur, C. M. Papadakis

The microscopic origin of cononsolvency is not well understood yet. Cononsolvency is the phenomenon where a substance dissolves well in two solvents separately, but not in the mixture of the two. Although several hypotheses have been put forward, none of them has been yet supported strongly by the experiment, and more insight is needed.

A very characteristic occurrence of cononsolvency is in solutions of Poly(N-isopropylacrylamide) (PNIPAM) in water-alcohol mixtures: PNIPAM in aqueous solutions collapses and precipitates at a lower critical solution temperature (LCST, cloud point) of 32°C and is perfectly soluble e.g. in methanol. However, in water-methanol mixtures with water as majority component, the cloud point decreases by a few degrees. The proposed hypotheses for the description of the phenomenon include (i) formation of sequences of solvent molecules along the macromolecular contour which leave unhydrated chain segments [1], (ii) formation of water-alcohol complexes in the solvent, which withdraw solvent molecules from the polymer [2] (iii) formation of methanol-bridges between remote chain segments [3], while (iv) a thermodynamic interpretation has been also proposed, i.e. increase in configurational entropy of the globular state due to methanol preferentially binding to the chain [4].

In this work, we studied the dynamics of PNIPAM in concentrated solutions, with dynamic light scattering, at temperatures 2 and 5 K below their respective cloud points, and in water methanol mixtures of 100:0, 90:10, and 85:15 v/v% [5]. In order to understand the effect of polymer concentration we measured solutions of quite high polymer concentrations: 10 and 25 wt%. We measured at varying angles in the range 30 - 90 ° in order to follow the q-dependence of dynamics. Furthermore the solutions were prepared with deuterated solvents, so that the results are directly compared to existing and projected neutron scattering experiments, especially Neutron Spin Echo ones.

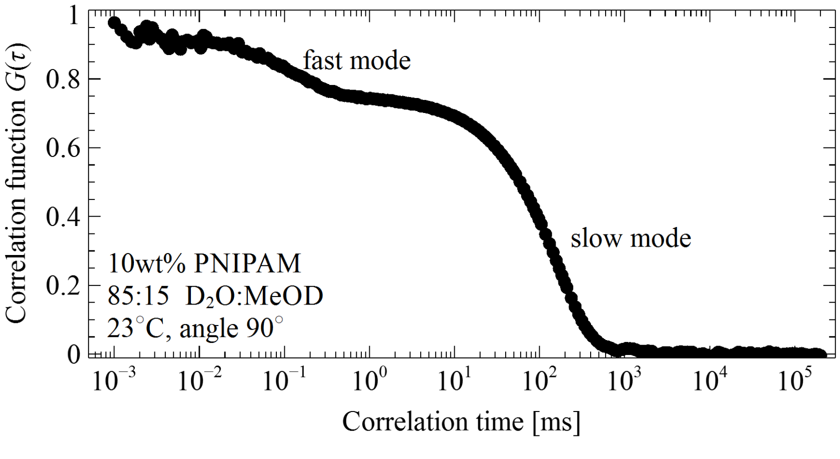

Figure 1.11:
Representative dynamic light scattering curve recorded with a selected solution, 2 K below its respective cloud point and at a direction perpendicular to the incoming light.

Figure 1.11 shows typical data recorded with the more concentrated aqueous solution at 90°. Two decays (relaxation modes) are visible. A weak fast one is visible in the region of $10^{-2}(ms)$, and a more prominent, slow one is in the region of $10^2 - 10^3$ms. The fast one, has been attributed to the cooperative motion of the transient network, while the slow one is quite broad and ascribed in the literature to the viscoelastic behavior of the system [6].

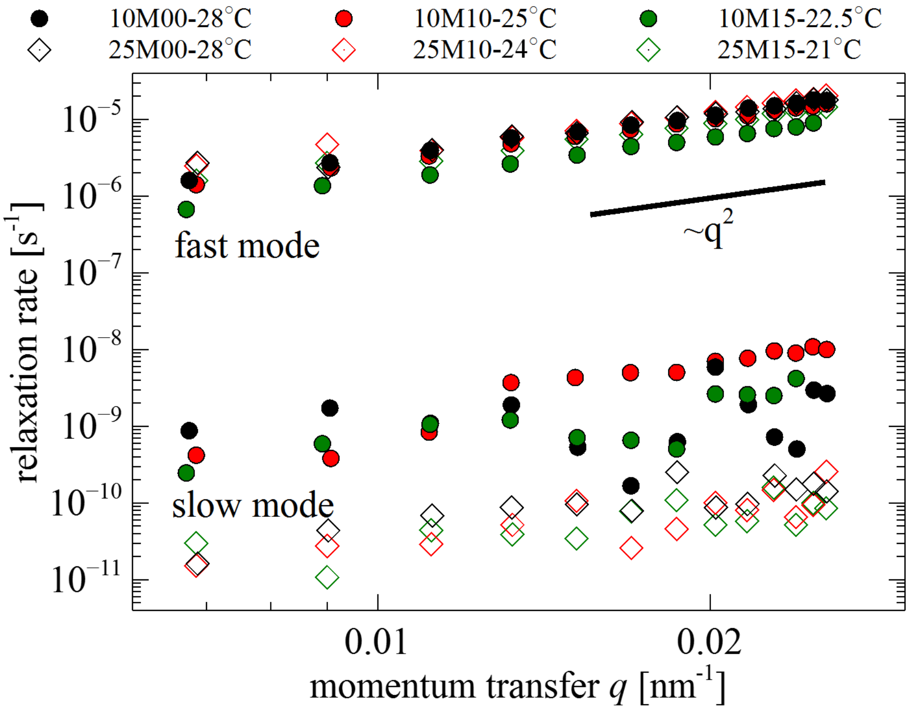

Figure 1.12:
Dependence of dynamic light scattering relaxation rates on the momentum transfer (angle) for both the fast and slow relaxation mode. The samples are designated as xxMyy, where xx is the fraction of polymer (wt%) in the solution and yy is the fraction of methanol in the solvent. Reproduced from [5].

We analyzed the resulting correlation functions with the REPES approach as implemented in the Gendist software [7]. This is a numerical approach for the approximate solution of ill-posed integral equations. This provided the mean relaxation rates Γ for the two decays as a function of the momentum transfer q, and the results are shown in Figure 1.12. The fast relaxation clearly follows a $\Gamma = D \cdot q^2$ dependence , in agreement with its attribution to a diffusive mode. The dynamics in aqueous solutions is identical for both concentrations. However with increasing methanol content the dynamics slows down, more prominently for the more dilute solutions. The results for the fast relaxation are quite scattered, and do not allow at this time for a clear interpretation, however, we can already observe that the dynamics of the dilute solutions is much faster than this of the concentrated ones. This is in agreement with the attribution of the mode to the overall mobility of the system, which is more viscous for higher polymer concentration. These observations will be co-evaluated with neutron spin echo experiment results at higher relaxation rated - larger q-values. This co-evaluation is expected to shed more light to the origin of cononsolvency in PNIPAM.

[1] G. Zhang, C. Wu, *J. Am. Chem. Soc.* **123**, 1376 - 1380 (2001)

[2] F. Tanaka, T. Koga, H. Kojima, N. Xue, F. M. Winnik, *Macromolecules* **44**, 2978 - 2989 (2011)

[3] D. Mukherji, C. M. Marques, K. Kremer, *Nat. Commun.* **5**, 4882 (2014)

[4] F. Rodríguez-Ropero, T. Hajari, N. F. A. van der Vegt, *J. Phys. Chem. B* **119**, 15780 - 15788 (2015)

[5] M. Nuber, Bachelor's Thesis, TU München, 2016

[6] T. Nicolai, W. Brown, R. M. Johnsen, P. Stepanek, *Macromolecules*, **23**, 1165-1174 (1990)

[7] J. Jakes, *Collect. Czech. Chem. Commun.* **60**, 1781 - 1797 (1995)

1.8 Phase behavior of the thermoresponsive polymer PNIPMAM in dependence on temperature and pressure

K.-L. Claude, D. Aravopoulou[1], B.-J. Niebuur, A. Schulte[2], V. Hildebrand[3], P. Müller-Buschbaum, A. Laschewsky[3], A. Kyritsis[1], C. M. Papadakis

[1] National Technical University of Athens, Athens, Greece
[2] University of Central Florida, Orlando, U.S.A.
[3] Universität Potsdam and Fraunhofer Institute for Applied Polymer Research, Potsdam-Golm, Germany

Thermoresponsive polymers constitute an important class of soft matter. One of the most studied polymers is Poly(N-isopropylacrylamide) (PNIPAM), which exhibits lower critical solution temperature (LCST) behavior: When heated above its cloud point in water ($T_{CP} \cong 32$ °C), the chains release water and collapse, leading to phase separation [1].

Poly(N-isopropyl**meth**acrylamide) (PNIP**M**AM) has an additional methyl group attached to the vinyl backbone thus, it may be expected to be more hydrophobic than PNIPAM. However, its cloud point is about 10 °C higher ($T_{CP} \cong 42$ °C), which was tentatively explained by the steric hindrance induced by the presence of the additional methyl group [2, 3].

In order to elucidate the origin of the differences in phase behavior in dependence on temperature, pressure and concentration, we investigated the transition by differential scanning calorimetry (DSC) and mapped out the pressure-dependent phase diagram using turbidimetry. The DSC measurements were performed with a Q200 (TA Instruments), calibrated with indium. The samples were mounted in low-mass hermetic aluminium pans which were placed on the disk-type measuring system inside the device. Turbidimetry measurements were carried out using a He-Ne Laser with a wavelength of $\lambda = 633$ nm and a power of $P = 10$ mW, which impinges on the sample located in a pressurized and thermalized cell. The transmitted light intensity is detected using a photodiode located right behind the cell.

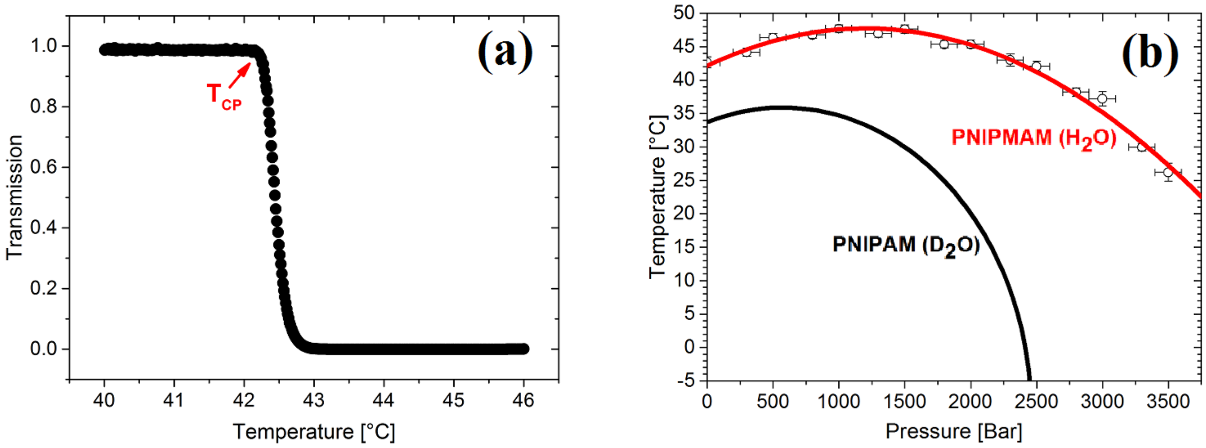

Figure 1.13:
Results from turbidity measurements on a 30 mg/ml PNIPMAM solution in H_2O: **(a)** light transmission during the heating process at a heating rate of 0.2 K/min at ambient pressure, **(b)** resulting p-T-phase diagram in comparison with the phase diagram of a 30 mg/ml PNIPAM solution in D_2O.

The investigated PNIPMAM having a molar mass of 20 kg/mol and a dispersity of 1.8 was synthesized using radical polymerization. The polymer was dissolved in H_2O at a concentration of 30 mg/ml to perform the turbidimetry measurements at ambient and high pressure, fig.

1.13. For subsequent turbidimetry and DSC measurements at ambient pressure, fig. 1.14, the PNIPMAM was dissolved in D_2O at concentrations between 5 mg/ml and 150 mg/ml.
The cloud point in H_2O from turbidity measurements at ambient pressure (fig. 1.13a, $T_{CP} = 42.6 \pm 0.8$°C) coincides well with values given in literature [2-4]. The turbidity measurements were carried out at pressures up to 3500 bar in order to map-out the phase diagram (fig. 1.13b). Compared to the phase diagram of PNIPAM measured earlier [5], a significant shift in the phase boundary is found, i. e. the additional methyl group in PNIPMAM stabilizes the one-phase region, even at elevated pressures.
Fig. 1.14a shows the heat flow from a DSC measurement during the heating process of a polymer solution. Two characteristic temperatures can be identified, namely the onset temperature, T_{Onset}, and the peak temperature, T_{Peak}. Fig. 1.14b shows their dependence on polymer concentration in comparison with T_{CP} from turbidimetry. In the range studied, both T_{Onset} and T_{Peak} decrease with increasing polymer concentration. Similar behavior was observed for T_{CP}, even though there is a difference in the absolute temperatures of about 5 K. Further investigations on the origin of this shift are still ongoing.

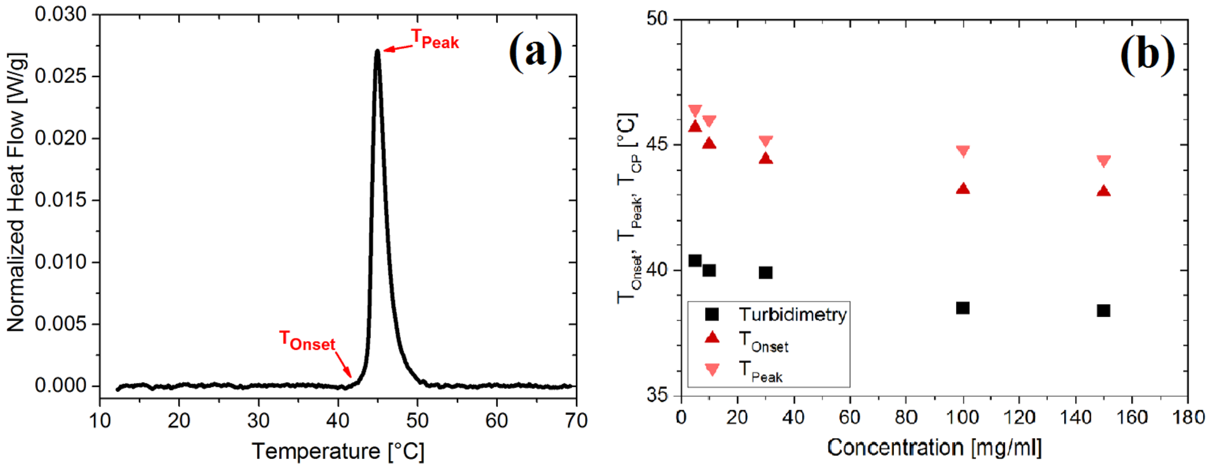

Figure 1.14:
Results from DSC measurements on a 100 mg/ml PNIPMAM solution in D_2O: **(a)** heat flow curve during the heating process at a rate of 1 K/min, **(b)** dependence of T_{Onset} (▲) and T_{Peak} (▼) on polymer concentration for heating rates of 1 K/min in comparison with T_{CP} (■) from turbidimetry for heating rates of 0.2 K/min.

In conclusion, PNIPMAM in aqueous solution exhibits behavior similar to the one of PNIPAM. The one-phase region is stabilized, also at high pressure, which may be mainly due to the presence of the additional methyl group in the vinyl backbone. The cloud points measured by turbidimetry differ substantially from the onset and peak temperatures from DSC.

[1] H.G. Schild. *Prog. Polym. Sci.* **17**, 163 (1992)

[2] Y. Tang, Y. Ding, G. Zhang *J. Phys. Chem. B* **112**, 8447 (2008)

[3] J. Dybal, M. Trchová , P. Schmidt *Vib. Spectrosc.* **51**, 44 (2009)

[4] M. Kano, E. Kokufuta, *Langmuir* **25**, 8649 (2009)

[5] S. Pinzek, B.Sc. Thesis, *TU München* (2015)

2 Thin polymer films

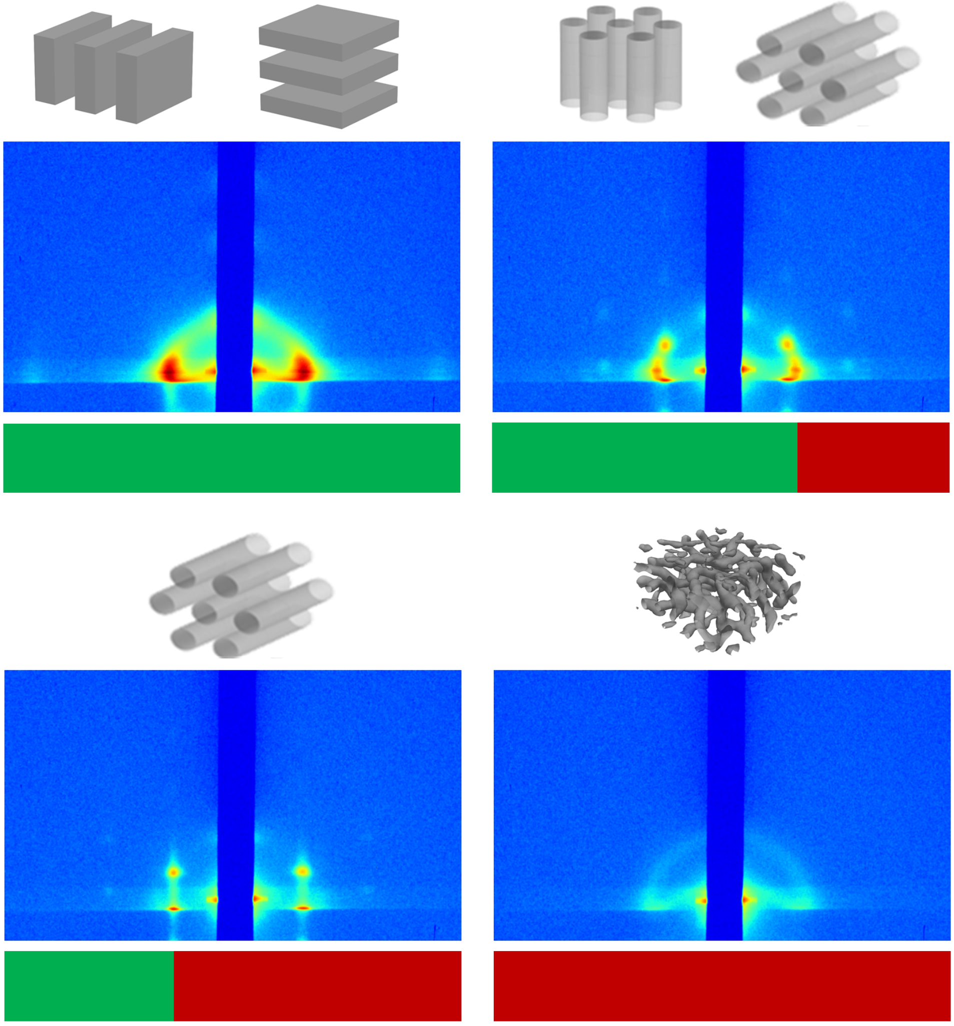

2.1 Structure formation in films of block copolymer mixtures: molecular simulations and GISAXS experiment

A. V. Berezkin, F. Jung, D. Posselt[1], D. M. Smilgies[2], C. M. Papadakis

[1] Roskilde University, IMFUFA, Denmark
[2] Cornell University, Ithaca, NY, USA

Block copolymer thin films feature an enormous morphological diversity, since their morphology and characteristic dimensions depend on the composition, block segregation strength, film thickness, and wetting properties of the blocks. Binary mixtures from diblock copolymers (DBCs) provide even broader structural diversity. By simple mixing of two DBCs, one can control the domain period, vary the morphologies, and even create new structures. However, DBC components of very different molar masses may demix into (macro)phases along with the microphase separation. The DBC mixtures have attracted growing interest in recent years for their potential applications in nanolithography, as functional templates for photovoltaics *etc.*, but many details of their micro- and macrophase separation in thin films are not clear yet.

To gain a deeper understanding of domain orientation and ordering in films from mixtures of two compositionally symmetric DBC, both in the one-phase and in the two-phase state, we combine coarse-grained molecular simulations (dissipative particle dynamics) and scattering experiments (Grazing Incidence Small-Angle X-ray Scattering, GISAXS) [1]. In the experiment, symmetric polystyrene-*b*-poly(2-vinyl pyridine) diblock copolymers having equal block molar masses of 57 kg/mol for the long copolymer and 8.2 kg/mol and 8.3 kg/mol respectively, for the short copolymer were used. The ratio of polymerization degrees was $\alpha = N_S/N_L = 1/6.9$, and the block segregation strength $\chi N_L = 194$. Simulation of the similar system were done at $\alpha = 1/7$, $\chi N_L = 200$ and the volume fraction of short chains in the mixture $\phi_S = 2/3$. We investigated the effects of the film thickness, mixture composition and selectivity of the substrate on the morphology and the character of macrophase separation.

In the film, vertical or lateral separation of the two-phase mixture may occur, as illustrated in Fig. 2.1. Within the macrophases, different lamellar orientations are possible. In lithographic applications, vertical macrophase separation and vertical lamellar oreintation are preferable. Molecular simulations and GISAXS experiments demonstrated that mixture separates laterally in thin films on non-selective substrates at $h \leq 116$ nm, whereas in thicker films, separation is vertical. The vertical separation is triggered by an elevated concentration of short copolymers near the film interfaces. This happens because smaller coils can come closer to the interfaces. This entropically-driven local increase of short DBC concentration (by about 5%), being amplified by the first-order type macrophase separation, results in one layer of a phase rich in long copolymers, "sandwiched" between two layers rich in short copolymers, adjacent to the film interfaces. GISAXS experiments, supported by simulations, show that a certain selectivity of the substrate or free film surface to one of the blocks facilitates the vertical macrophase separation that arises in thinner films (at $h \geq 78$ nm).

Orientation of lamellar nanodomains within the macrophases is of interest as well. We found that the orientation is mostly dictated by the selectivities of interfaces, confining the specific macrophase. In case of vertical macrophase separation, only phases rich in short copolymers contact with the interfaces. If these interfaces are non-selective, all the domains in the film are vertical. If the interfaces are selective, the lamellas within the phases rich in short chains are lying, but the orientation of thick lamellas in the film core stay vertical. Thus, due to two-phase structure of the film, the lamellar orientations in different phases get "decoupled" and can

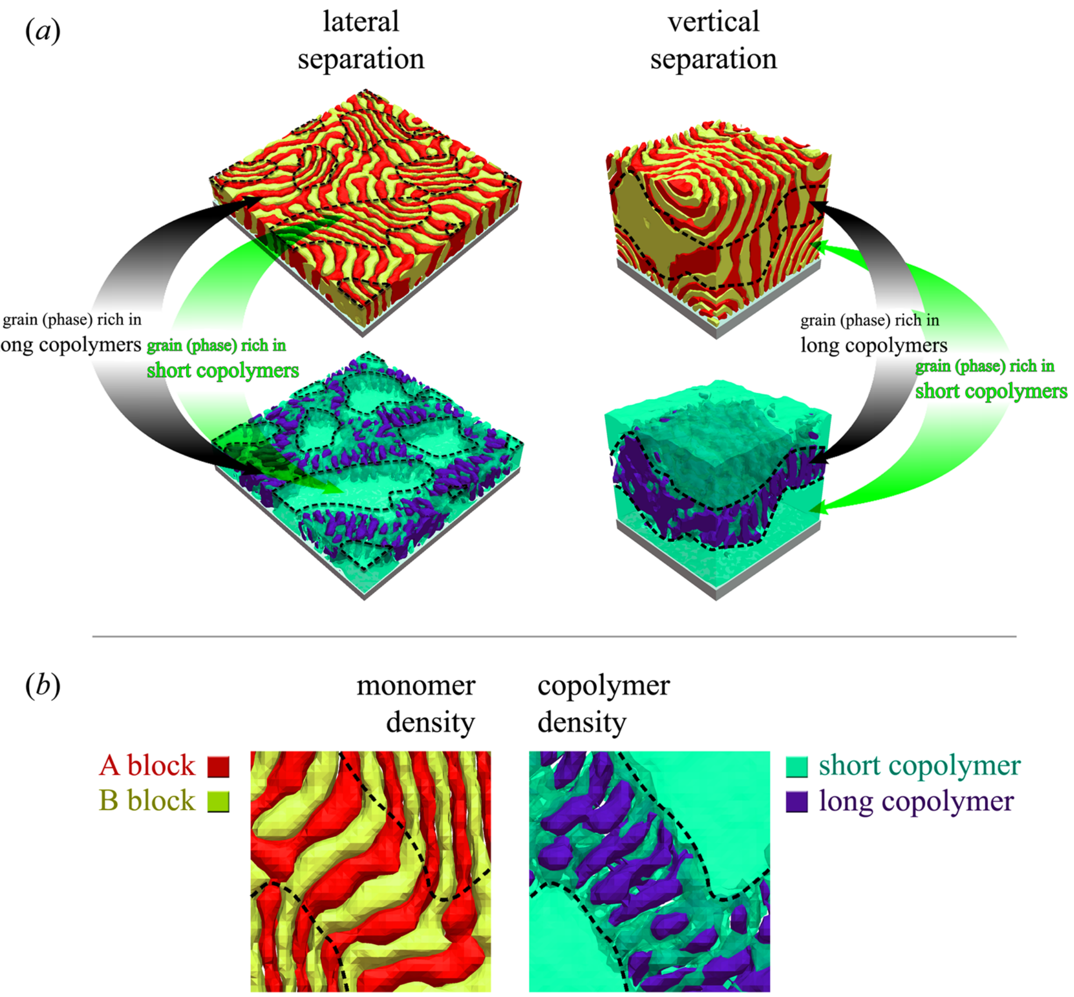

Figure 2.1:
Schematics of lateral and vertical macrophase separation of the BC mixture (*a*) and local distribution of monomers and BC of different lengths in the macrophases (*b*). Dashed lines show the boundaries between phases reach in short and long chains. Snapshots are taken from simulations.

be orthogonal. Decoupling is caused by a reconstruction and kink [2] of nanodomains at the interfaces between macrophases. In practice, this observation can be used to form vertically oriented domains in the film core by simple admixing of shorter DBC to the long one as an alternative to a more complex modification of the substrate.

The research was supported by Deutsche Forschungsgemeinschaft (project PA 771/10-2).

[1] A. V. Berezkin, F. Jung, D. Posselt, D.-M. smilgies, C. M. Papadakis, *ACS Appl. Mat. Interfaces* DOI: 10.1021/acsami.6b16563 (2017)

[2] R. K. W. Spencer, M. W. Matsen, *Macromolecules* **48**, 2840 (2015)

2.2 Printed diblock copolymer films embedded with magnetic nanoparticles

S. Xia, E. Metwalli, M. Opel[1], P. A. Staniec[2], E. M. Herzig[3], P. Müller-Buschbaum

[1] WMI, Garching, Germany
[2] DLS, Oxford, England
[3] MSE, Garching, Germany

Nanostructured materials have attracted increasing attention for a wide range of reasons, due to their superior properties at the nanoscale. Among the enhanced properties of nanostructured materials, magnetic nanoparticles (NPs) offer a good example with important technological implications. They have immense potential for applications in the areas of high-density storage and magnetic sensors [1-4]. Having been established and developed for years, printing techniques prove to be effective methods for film fabrication, especially in large-scale production. In the present work, magnetic thin films composed of poly(styrene-*b*-methyl methacrylate) PS-*b*-PMMA and PS-coated maghemite ($\gamma-Fe_2O_3$) nanoparticles (NPs) were printed. By applying an external magnetic field during printing, oriented nanostructures with high content of nanoscale arranged magnetic NPs were achieved. The achieved structures of the magnetic films and the arrangement of NPs within the polymer matrix were characterized in both real and reciprocal spaces.

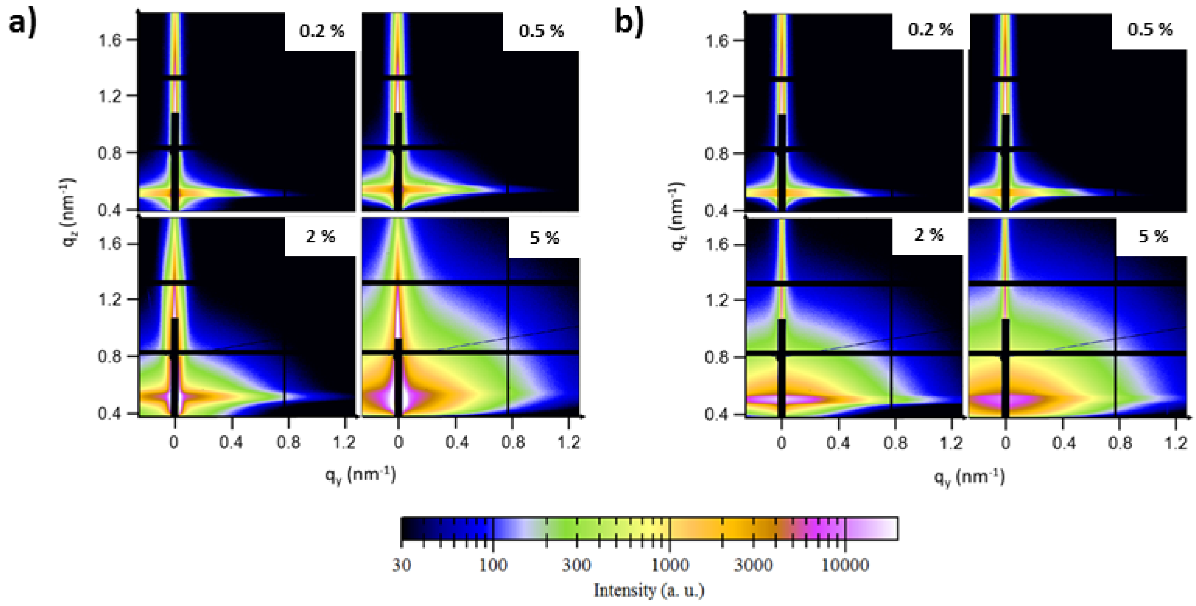

Figure 2.2:
Selected 2D GISAXS data of printed films with different NP concentrations, with the X-ray beam oriented (a) parallel and (b) perpendicular to the NP wires. Inserts on the top right corners show the corresponding NP concentrations.

Surface structures were probed via optical microscopy (OM), atomic force microscopy (AFM) and scanning electron microscopy (SEM). OM shows wires aligning along the magnetic field across the sample surface. With different NP loadings, wires with different lengths, widths and spacings are observed. AFM and SEM reveal that wires are composed of NPs densely packed together. In order to probe the buried nanostructure of printed nanocomposite films, grazing incidence small angle X-ray scattering (GISAXS) was employed for characterization. Results are shown in Fig. 2.2. Being coated with PS chains, NPs are selectively located inside the PS blocks at the nanoscale [2, 3]. Quantitative analysis of the GISASX data shows that the NPs initially disperse as single particles and then self-assemble into nano-sized clusters inside the PS domains as the NP concentration increases. Different growth behaviors of the PS domains are found in the two orientations measured in GISAXS (with the X-ray beam parallel and perpendicular to the NP wires), which reveals the shape anisotropy of films created by the external magnetic field during printing.

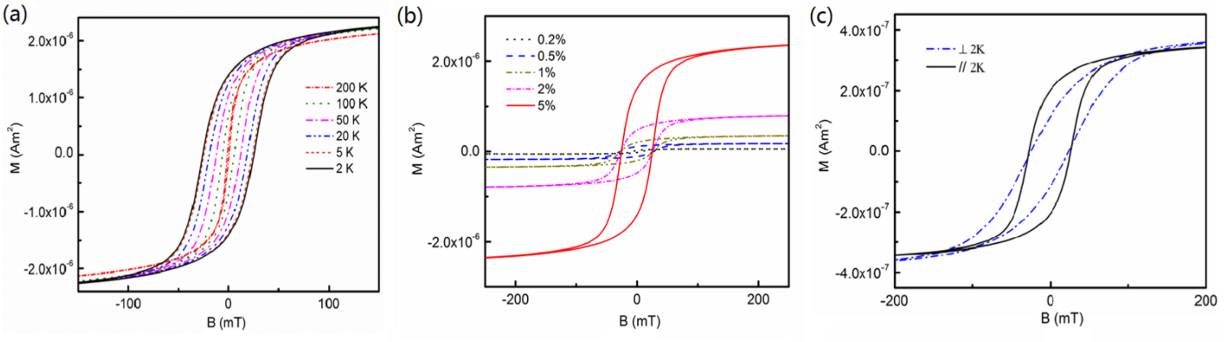

Figure 2.3:
(a) Magnetic moments measured as a function of the external magnetic field with a parallel orientation at different temperatures for a selected sample with 5 wt % NPs. (b) Magnetic moments measured as a function of the external magnetic field at 2 K with different NP concentrations. (c) Magnetization curves measured at 2 K with a parallel (black solid line) and perpendicular (blue dashed-dotted line) external magnetic field orientation for a selected sample with 1 wt % NPs.

Magnetic measurements were collected using a superconducting quantum interface device (SQUID). Fig. 2.3 (a) shows the influence of temperature, NP concentration and orientation on the magnetic properties. It is observed that the saturation magnetization is temperature-independent. With increasing temperature, the coercive fields become much smaller because of thermal agitation. Magnetic hysteresis is present for temperatures that are below a characteristic temperature, which is in agreement with a superparamagnetic behavior. Within the experimental error, the remanence stays constant with small fluctuations at low temperatures and reduces strongly at higher temperatures. The effect of NP concentration on the magnetic properties of the hybrid films is shown in Fig. 2.3 (b). Remanence and saturation magnetization increase linearly with increasing NP concentration, and also show the similar growing tendency at all measured temperatures. Additional hysteresis loops were measured at 2 K with the applied magnetic field parallel or perpendicular to the metal wires Fig. 2.3 (c). The results show that the sample is easier to magnetize along the metal wires direction than in the perpendicular direction. All magnetic data reveal that the printed thin hybrid films show superparamagnetic behavior and a pronounced shape anisotropy. Such magnetic properties render the nanocomposite films promising for applications related to magnetic sensors.

[1] Y. Yao, E. Metwalli, M. Opel, M. Haese, J.F. Moulin, K. Rodewald, B. Rieger, P. Müller-Buschbaum, *Adv. Mater. Interfaces.* **3**,1500712 (2016)

[2] Y. Yao, E. Metwalli, B. Su, V. Körstgens, A. Miasnikova, M. Opel, S V. Roth, P. Müller-Buschbaum, *ACS Appl. Mater. Interfaces.* **7**, 13080-13091 (2015)

[3] Y. Yao, E. Metwalli, J. F.Moulin, B. Su, M. Opel, P. Müller-Buschbaum, *ACS Appl. Mater. Interfaces.* **6**, 18152-18162 (2014)

[4] Y. Yao, E. Metwalli, M A. Niedermeier, M. Opel, C. Lin, J. Ning, J. Perlich, S V. Roth, P. Müller-Buschbaum, *ACS Appl. Mater. Interfaces.* **6**, 5244-5254 (2014)

2.3 Annealing of diblock copolymer thin films using solvent vapor mixtures at controlled temperatures

F. Jung, A. V. Berezkin, D.-M. Smilgies[1], D. Posselt[2], C. M. Papadakis

[1] Cornell University, Ithaca, NY, USA
[2] Roskilde University, IMFUFA, Denmark

Block copolymers have attracted a lot of interest due to their ability to self-assemble and form microdomains with length scales of 10-100 nm. This so-called bottom-up approach offers a wide range of interesting applications, e.g. for nanolithograhpy. For these applications, a defect-free, controllable structure is required.

Solvent vapor annealing (SVA) is a widely used method to enhance the order in nanostructured thin films, and has also been applied to modify their morphology [1]. In a selective solvent, chemically different nanodomains swell to a different extent, which implies a change in the effective volume fraction, f_{eff}, and potentially leads to an order-order transition.

In this work, the cylinder forming diblock copolymer polystyrene-$block$-poly(dimethyl siloxane) (PS-PDMS) in a thin film is investigated during SVA. For annealing, mixtures of the two solvents toluene and n-heptane are used, which are non-selective and selective for PDMS, respectively. The vapor is created by bubbling nitrogen through reservoirs of liquid solvent, and mixing the two streams of saturated vapor before guiding it to the sample chamber. Changing the composition of the vapor mixture allows one to navigate the diblock copolymer film through its phase diagram, namely by changing the composition from one pure solvent to the other. Experiments were performed both at room temperature and at elevated temperatures of the polymer film and of the solvents.

The films are investigated in-situ during SVA by means of time-resolved grazing-incidence small-angle X-ray scattering (GISAXS). Changes in the morphology are directly derived from the scattering patterns. Additionally, by using the scattering contrast, the distribution of the solvents inside the film can be extracted from the scattering experiments. The contrast is due to different refractive indices of the two microdomains, which change as a function of the solvent content. This allows for a calculation of the effective volume fraction f_{eff} and the effective interaction parameter χ_{eff}, which consequently defines a trajectory through phase space [2].

Experiments were performed at beamline D1 at the Cornell High Energy Synchrotron Source (CHESS). The wavelength was λ=0.1166 nm, the incident angle α_i=0.14 ° and the sample detector distance 1825 mm. Exposure times were 0.5 s and measurements were done every 30 s.

In Fig. 2.4 an example is shown. The film was first swollen in pure n-heptane, and then the fraction of toluene was increased stepwise. The temperature of the film was 45 °C. The as-prepared film featured randomly oriented cylinders, as is evident by the diffuse Debye-Scherrer ring (DDSR) (Fig. 2.4, (1)). When exposed to n-heptane vapor, the minority block (PDMS) was swollen selectively, which promoted a transition into the lamellar phase. The measured trajectory confirms this expectation, as f_{eff} increases. In the final stages of the initial swelling in n-heptane, a lamellar phase was indeed observed (Fig. 2.4, (2)), showing coexistence of standing and lying lamellae. During the vapor composition change, a transition from lamellae to cylinder is observed. The addition of the non-selective toluene decreases f_{eff}, and also χ_{eff} via the screening effect. The GISAXS data show well defined Bragg peaks, characteristic of a highly ordered hexagonally packed cylinder phase. At intermediate toluene content, lying and standing cylinders coexist in the film (Fig. 2.4, (3)), while at higher toluene content, only lying cylinders are observed (Fig. 2.4, (4)). Swelling in pure toluene induces a order-disorder transition, as the higher order Bragg peaks vanish and the scattering images instead show a DDSR with evenly distributed intensity (Fig. 2.4, (5)). Finally, during drying (removal of toluene), an ordered cylinder phase is reestablished (Fig. 2.4, (6)). The two sets of peaks indicate a coexistence of lying cylinders with two different orientations of their hexagonal lattice.

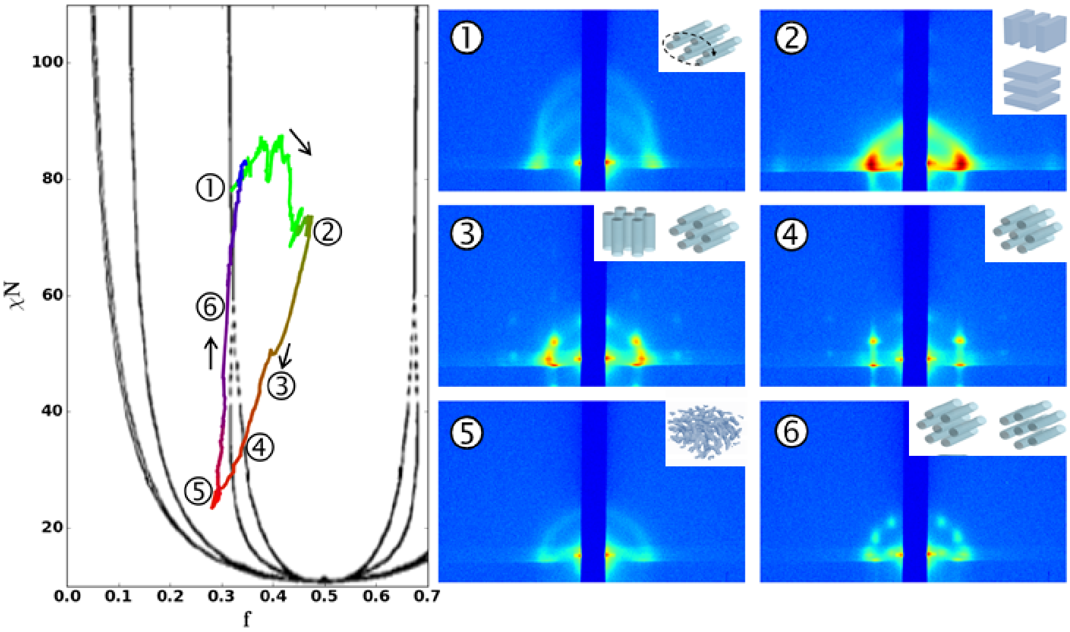

Figure 2.4:
Trajectory of a PS-PDMS thin film through the theoretical phase phase diagram during annealing in vapor mixtures from toluene and n-heptane at 45 °C. Representative points are indicated with numbers, and 2D GISAXS images as well as 3D illustrations of the observed structure are shown. Colors of the trajectory indicate high heptane content (green), high toluene content (red) and drying (blue).

To summarize, it was possible to navigate a diblock copolymer thin film through its phase diagram by varying the solvent vapor composition during SVA. A rich phase behaviour was observed, showing that SVA with solvent mixtures can be used to tune the morphology. Simultaneous heating of the film further improves the order.

The project is funded by DGF (Pa771/10-2) and the Russian Foundation for Basic Research.

[1] D. Posselt, J. Zhang, D.-M. Smilgies, A. V. Berezkin, I. I. Potemkin, C. M. Papadakis, *Prog. Polym. Sci.* **66**, 80–155 (2016)

[2] F. Jung, Master Thesis, TU München (2016)

2.4 In-situ polymerized PEDOT:Tos thin films for thermoelectric applications

M. Rafiq, N. Saxena, P. Müller-Buschbaum

Demand of energy is increasing day by day which raises the necessity for research on new and efficient energy resources. The environment is negatively affected because of the increasing greenhouse effect. Today, a significant part of the energy is wasted in the form of heat in energy conversion and many other processes. Thus, if it would become possible to use this waste heat energy, energy related problems could be solved on global scale. Typically, the heat energy wasted by a power plant is about 60 % and and that from an automobiles fed fuel is about 20 %. Moreover, the heat emitted by the humane body in the form of radiation is 60 W and also a lot of heat losses arise from household utilities because of poor insulation. These circumstances make scientists more and more interested in gaining back parts of the waste heat, which could be very environmental friendly. However, so far the energy share is dominated by oil, coal, and gas and waste heat recovery is underrepresented.

Thermoelectric materials are an efficient tool to convert waste heat into electrical energy in an environment-friendly manner. These materials make use of the Seebeck effect for the transformation of heat into electrical energy. Organic thermoelectric materials are cheap, easy accessible and very promising candidates for energy harvester devices. For example poly-3,4-ethylendioxythiophen: tosylate (PEDOT:Tos) thin films show higher Seebeck coefficients and conductivities as compared to PEDOT:PSS films.[1] Better thermoelectric behavior can be expected, since both quantities play a key role for the figure of merit ZT of a thermoelectric material

$$ZT = \frac{S^2\sigma}{\kappa}T \tag{2.1}$$

Here S, σ and κ denote the Seebeck coefficient, the electrical conductivity and the thermal conductivity. T is the temperature.

The thermoelectric relevant quantities can be improved in in-situ polymerized PEDOT:Tos by using additives and by performing pre- and- post-production treatments of thin films with different chemicals.

In the present study, the glass substrates were cleaned by an acid bath and subsequent oxygen plasma treatment. The solution for thin film deposition was prepared from iron tosylate powder mixed with 1-butanol and ethylene 3,4-dioxythiophene (EDOT) monomer, being added and stirred afterwards. A sticking layer was deposited by spin coating a thin layer of PEDOT:PSS on glass. Next, the mixture of iron tosylate and EDOT was deposited by spin-coating. Polymerization was initiated by heat treatement. In order to remove the remaining iron salt, the films were rinsed with ethanol. The PEDOT:Tos thin films were characterized regarding their electrical conductivity measured via a standard four-point probe method, their Seebeck coefficient measured using a custom-built setup and their thickness measured via profilometry. Many processing parameters were varied in order to detect how the Seebeck coefficient and electrical conductivity depend on these parameters and how they interconnect with each other.

Figure 2.5 illustrates the influence of different stirring times on the electrical conductivity and on the Seebeck coefficient, respectively. They seem to follow an opposite trend. With increasing stirring time the conductivity decreased for the first five hours while a pronounced increase in Seebeck coefficient was seen at the same time. After 5 hours both, conductivity and Seebeck coefficient remained constant within the experimental error bars.

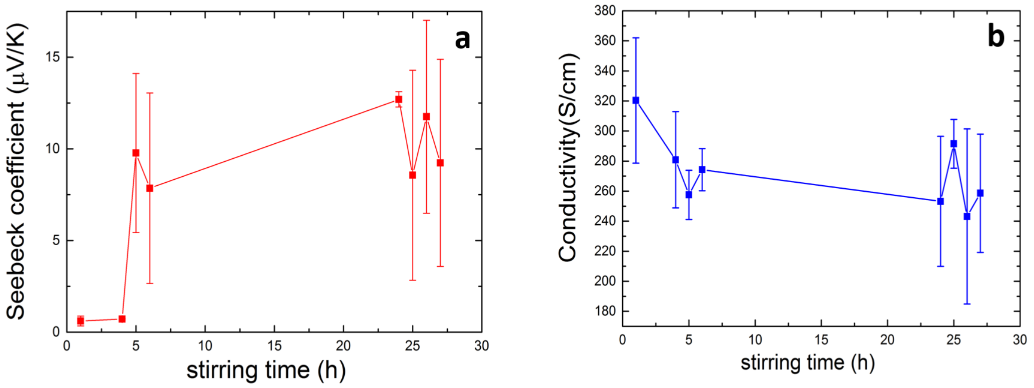

Figure 2.5:
a) Seebeck coefficient and b)electrical conductivity as function of stirring time of the EDOT:iron tosylate solution

One needs to note that the EDOT:iron tosylate solution became increasingly viscous with increasing stirring time, while also changing color from yellow to blue. These changes indicated a pre-polymerization of the PEDOT.

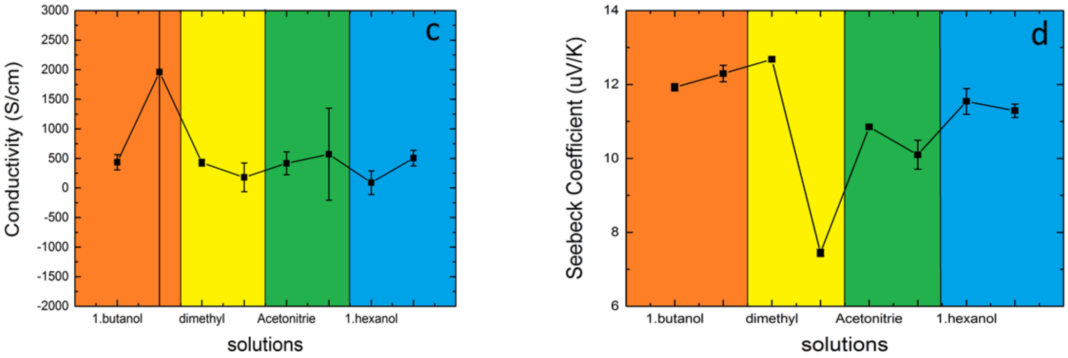

Figure 2.6: Influence of washing agent on a) electrical conductivity and b) Seebeck coefficient

In addition, the influence of the used washing agents on the thermoelectric properties of PEDOT:Tos thin films was investigated (see Figure 2.6). In Figure 2.6 the color orange, yellow, green and blue represent the washing agents 1-butanol, dimethyl, acetonitrile and 1-hexanol, respectively. Butanol appears to be a promising candidate for the washing purposes. Both, Seebeck coefficient and electrical conductivity of PEDOT:Tos thin films washed with 1-butanol showed optimum values for good thermoelectric properties among the tested washing agents. The results shown above represent a basis for further research on the thermoelectric properties of PEDOT:Tos thin films. It was reported that the film formation can be influenced by the introduction of high-boiling point solvents, leading to better ordered films. Also post-treatment with hydrochloric or sulfuric acid and sodium hydroxide seem to be promising approaches. [1] As an alternative to spin-coating, a method called vapor-phase polymerization was described in literature. [1]

[1] Z. U. Khan, O. Bubnovab, M. J. Jafari, *J. Mater. Chem. C* **3**, 10616–10623 (2015)

2.5 Investigations on hierarchically structured ZnO for enhanced light scattering in OLED applications

L. Bießmann, P. A. Staniac[1], P. Müller-Buschbaum

[1] DLS, Didcot, United Kingdom

During the last years organic light emitting diodes (OLEDs) gained an increasing importance for industrial applications like display technology and smartphones in particular. This is not only owed to the implementation of active matrix technology which allowed the realization of large high resolution displays, but also, even more importantly, was the cost effective production of efficient and long-life emitter materials. The development of colored displays raised since the fabrication of stable blue, green, yellow and red organic emitter materials was possible. The combination of these emitting materials enables the design of white OLEDs with tunable color temperature as well. Even if the enhanced efficiency and life expectancy made OLEDs suitable for commercial applications, the use of white OLEDs in room lighting is still behind its potential. In the recent years, research was mainly focused on the increase of the energy conversion of OLEDs and thus aimed to make them more efficient. Baldo et al. showed that one can triple the internal quantum efficiency and reach values close to 100 % by using phosphorescent emitting materials [1]. However, especially for white OLEDs the extraction of photons out of the device is still a limiting factor. For conventional device architecture, roughly 80 % of the photons are trapped in substrate and organic modes and eventually will be absorbed [2]. Therefore, there is still a high potential for enhancing the luminance of OLEDs by increasing the photon extraction.

Several approaches exists to raise the photon extraction which are mainly based on inserting additional scattering centers into different layers of the device stack. Besides the direct structuring of the substrate surface, e.g. with micro lenses [3], or different refractive index materials [4], the attachment of a transparent layer on the substrate is a very promising approach. Such layers were realized by simply attaching nanoparticles on the substrate surface or deposit a polymer film included some nanoparticles [5]. The combination of high chemical stability and a high refractive index makes nanostructures from metal oxides to another promising approach for creating such a scattering layer. In this work zinc oxide (ZnO) was chosen. Its optical band gap of 3.3 eV and its refractive index of 2.0 makes it to a suitable material for optical transparent scattering layers.

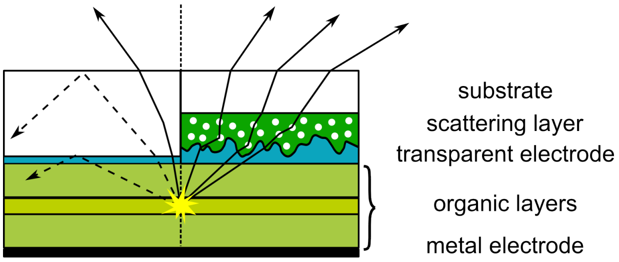

Figure 2.7:
Working principle of an additional scattering layer (right) in comparison to a standard device architecture (left). The illustrated light propagation shows the outcoupled modes as solid lines, whereas the dashed lines representing trapped modes, respectively.

The basic working principle of the investigated scattering layers is depicted in Figure 2.7. The photons generated in the emissive layer are directed to the forward hemisphere of the OLED. The standard device architecture suffers from low photon extraction caused by substrates and organic modes due to the high refractive index mismatch of the commonly used indium-tin oxide (ITO) to the glass substrate interface and the glass to air interface, respectively. An additional scattering layer in between the electrode and the substrate yield two advantages. First, the scattering centers of the layer cause a suppression of substrate modes by redirection of the generated photons and thus decrease the total internal reflection. Second, it is possible to tune

the total refractive index of the deposited scattering layer by creating a porous film which consists of an intermixed layer of different materials, e.g. ZnO and air. The combination of both effects holds the potential to increase the light-outcoupling of an OLED significantly.
The mentioned porous films in this work were produced by combining a structure giving diblock copolymer template with sol-gel chemistry and a solution processable metal oxide precursor. In this case polystyrene-block-polyethylene oxide (PS-b-PEO) was used as structure giving template, whereas zinc acetate dihydrate served as precursor for ZnO. To implement additional scattering centers for the visible light region 500 nm microspheres were added to the solution. Due to its high flexibility in case of substrate shape and substrate size and film thickness, spray deposition technique was applied on pre-cleaned glass substrates. Using the above preparation method the nano- and micro-structure of the ZnO films can be tuned to fit the desired needs.

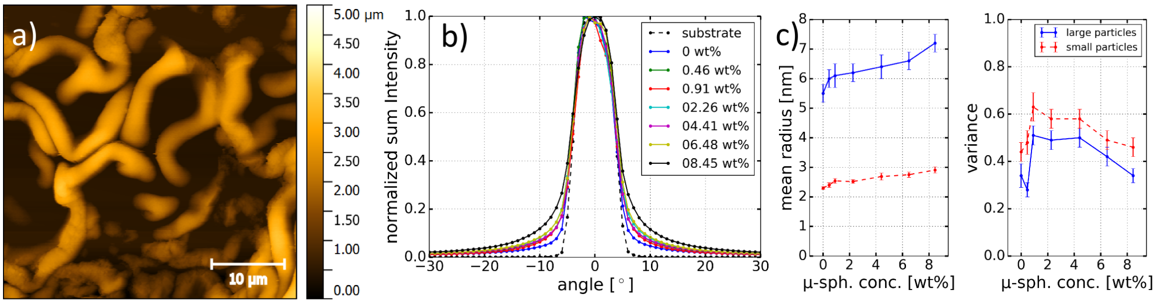

Figure 2.8:
a) Exemplary AFM image of ZnO scattering layer (40 um^2). b) Angular dependent scattered sum intensity of ZnO layers. c) Particle size and deviation of nano-structure, extracted from GISAXS measurements.

The obtained films were investigated regarding their surface structure by scanning electron microscopy (SEM) as well as their inner structure using grazing incidence small angle scattering (GISAXS) [6]. The GISAXS measurements were performed at the I22 Microfocus beamline at Diamond Light Source, UK. In addition, AFM measurement gives information about the height profile and film roughness. In Figure 2.8 a) an exemplary AFM image is depicted that shows a highly randomized micro structured film with high surface roughness. Angular dependent UV-Vis measurements show an increased scattering behavior for visible light, which is related to the amount of added microspheres. This influence is shown in Figure 2.8 b), where the angular dependent sum intensity of the overall scattered light is depicted. Finally, the conducted GISAXS measurements show only a slight change of the small structures (see Figure 2.8 c)) and also verified the high film porosity of roughly 90 %. In conclusion, the investigated porous ZnO films show a hierarchical structured surface with high scattering potential for the visible region of light. The randomized micro-structure provides a high interface area, whereas the nano-structure keeps mainly stable for different microsphere concentrations.

[1] M. A. Baldo, D. F. O'Brien, Y. You, A. Shoustikov, S. Sibley, M. E. Thompson, S. R. Forrest, *Nature* **395**, 151-154 (1998)

[2] S. Reineke, F. Lindner, G. Schwartz, N. Seidler, K. Walzer, B. Lüssem, K. Leo, *Nature* **459**, 234-238 (2009)

[3] J. Sun and S. R. Forrest, *J. Appl. Phys.* **100**, 073106 (2006)

[4] J. Sun and S. R. Forrest, *Nature Photonics* **2**, 483-487 (2008)

[5] H.-W. Chang, Y. H. Kim, J. Lee, S. Hofmann, B. Lüssem, L. Müller-Meskamp, M. C. Gather, K. Leo, C.-C. Wu, *Organic Electronics* **15**, 1028-1034 (2014)

[6] P. Müller-Buschbaum, *Anal. Bioanal. Chem.* **376**, 3-10 (2003)

2.6 Hybrid photovoltaics based on diblock copolymer structured, mesoporous Ge thin films

A. Hetzenecker, N. Hohn, M. Giebel[1], T. F. Fässler[1], P. Müller-Buschbaum

[1] Chemie-Department, LS Anorganische Chemie mit Schwerpunkt Neue Materialien, Garching, Germany

Hybrid photovoltaics opens new possibilities in solar cell design combining the mechanical stability and high charge carrier mobility of inorganic semiconductors with the potentially cost-efficient, large scale production and flexibility of organic materials. Similar to the synthesis of nanostructured titania films via sol-gel chemistry and diblock copolymer templating [1], a new method has been developed for nanostructuring germanium films. By using poly(styrene-b-ethylene oxide) (PS-b-PEO) as a template and K_4Ge_9 Zintl clusters as an inorganic precursor [2] for sol-gel synthesis, mesoporous germanium thin films can be achieved.

In Fig. 2.9 a) the synthesis routine is schematically presented. First, a transfer solution of PS-b-PEO and K_4Ge_9 in ethylenediamine has to be prepared. The solution is spin-coated on pre-cleaned substrates. In a second step a solution of toluene and 1-butanol is deposited on the resulting film. The good-poor solvent pair induces phase separation of the diblock copolymer, leading to a porous microstructure of the films. After three minutes of soaking, the films are spin-coated a second time to remove the residual solvent, followed by an annealing step of 15 min at 200 °C. All the described steps have to be performed in inert gas atmosphere, as K_4Ge_9 Zintl clusters are very sensitive to oxidation. Calcination of the prepared films above 500 °C removes residual polymers and enhances the crystallinity of the germanium structures.

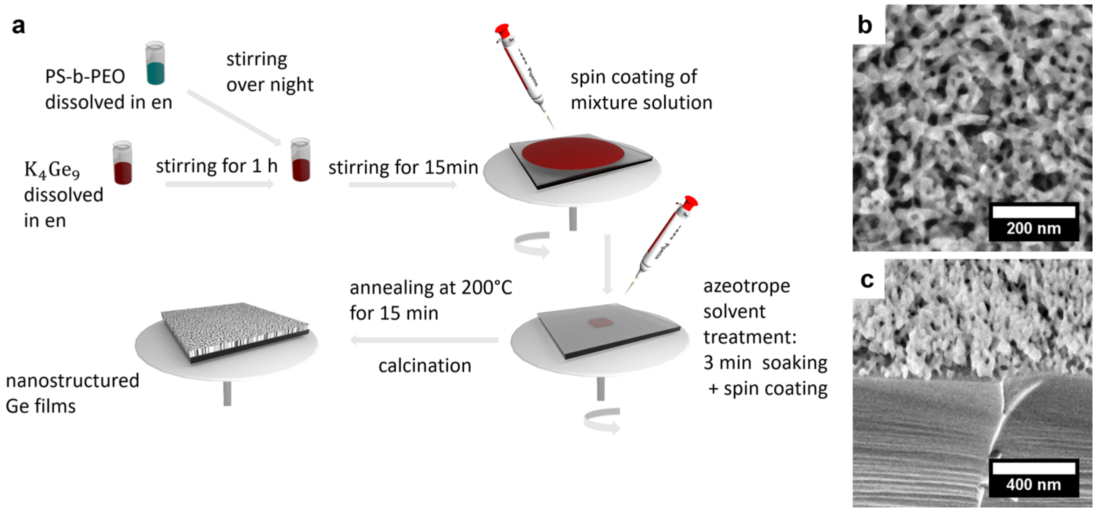

Figure 2.9:
a) Schematic representation of the synthesis routine for mesoporous germanium thin films.
b) SEM surface image of the resulting germanium film. c) Corresponding cross-sectional SEM image of the same sample.

Via scanning electron microscopy (SEM) the surface and cross-sectional structure can be analyzed, providing a good insight into the local morphology. In Fig. 2.9 b) and c) the resulting SEM images of a calcinated film on silicon substrate are depicted. In Fig. 2.9 b) a porous surface can be observed. It shows a random network of germanium structures. The pore sizes are mainly distributed between 20 nm and 100 nm, while the germanium filaments tend to be thinner than 50nm. In Fig. 2.9 c) a cross-sectional image of the same sample is shown. It reveals a high surface roughness and indicates that the porous structure visible on the surface can also be expected throughout the whole film. Furthermore, one can estimate a film thickness of about 200 nm from the cross-section.

UV/Vis spectroscopy was performed in order to determine the absorption behavior of the produced germanium films. In Fig. 2.10 the gained data of a mesoporous germanium film on glass substrate is shown in a Tauc plot in order to determine the optical bandgap. Measurements were performed over 21 days to study the stability in air. The absorption strongly decreases over time, which can also be noticed by a strong bleaching of the samples. This degradation can be attributed to continuous oxidation of the germanium film. Nevertheless, the fit of the linear region of the curves gives an optical bandgap of $E_g \sim 0.92$ eV for all measurements. For comparison the literature value of bulk germanium is 0.67 eV.

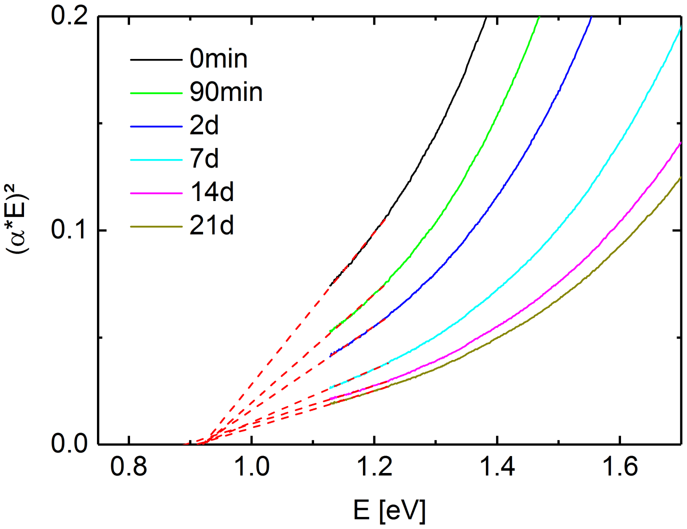

Figure 2.10:
Tauc plot from UV/Vis spectroscopy data of germanium thin films on glass substrate. Measurements were performed throughout 21 days while the sample was stored in air. The linear part of the curves was fitted in oder to determine the optical bandgap of the material.

For a future solar cell application, the pore sizes of the germanium films have to be in the range of around 100 nm. Smaller pores prevent efficient backfilling with an organic hole conductor. Different molar ratios between the diblock copolymer and the precursor have been tested to adjust the pore size. Although the films showed varying structure density, the average pore sizes did not change substantially. Further studies will have to be carried out to tune the morphology more precisely. However, the developed method provides a sophisticated way to produce mesoporous germanium thin films.

[1] Y.-J. Cheng, J. S. Gutmann, *J. Am. Chem. Soc.* **128**, 4658-4674 (2006)

[2] M. M. Bentlohner, M. Waibel, P. Zeller, K. Sarkar, P. Müller-Buschbaum, D. Fattakhova-Rohlfing, T. F. Fässler, *Angew. Chem. Int. Ed.* **55**, 2441-2445 (2015)

2.7 In-situ GISAXS investigation of the structure evolution of metal clusters on organic thin films during sputter deposition

F. C. Löhrer, V. Körstgens, M. Schwartzkopf[1], A. Hinz[2], O. Polonskyi[2], T. Strunskus[2], F. Faupel[2], S. V. Roth[1], P. Müller-Buschbaum

[1] DESY, Hamburg, Germany
[2] FAU Kiel, Kiel, Germany

Photoactive polymers have received high attention in recent years due to a large variety of different applications in organic photovoltaics (OPV) or light emitting diodes (OLED). Using polymer films as active material for energy conversion has a variety of potential advantages. The polymers can be synthesized from low-cost, abundant precursor materials and enable the formation of thin, light-weight and flexible films with tunable color. The devices can be produced via roll-to-roll processing, an easily up-scalable and thereby low-cost production technique. Due to these advantages, OPV or OLED devices could be integrated into a wide range of applications, combining functionality with design in fields as diverse as mobility, architecture or clothing. Although those devices mainly consist of organic materials, their electrodes are in many cases still made from metals. Thus, polymer-metal interfaces are inherently present in most organic electronic devices.

Understanding the growth mechanisms of metal contacts on polymer thin films plays a crucial role in identifying potential ways to enhance the performance of organic electronics. We investigated the morphological changes of a polymer-metal interface during the sputter deposition of metal contacts onto photoactive polymer films via in-situ grazing incidence small angle X-ray scattering (GISAXS). [1] This technique allows for highly time-resolved insights into the deposition behavior of the metal on the organic film, which strongly depends on the film structure.

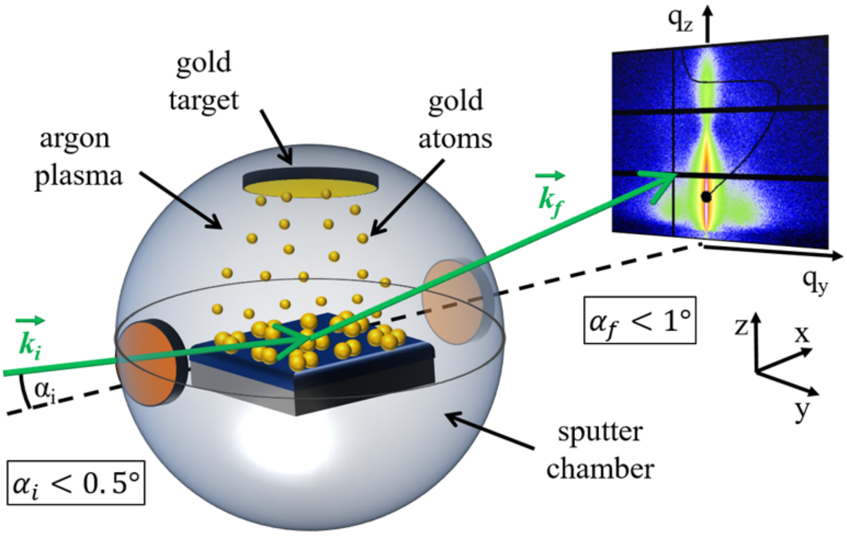

Figure 2.11:
Experimental set-up applied during the in-situ GISAXS investigation of gold clusters on a thin polymer film during the sputter deposition process.

Making use of the outstanding time resolution at the P03 instrument at DESY in Hamburg, we studied the deposition behavior of sputtered gold particles on thin films of typical photoactive polymers. With a mobile sputter chamber, which can be implemented directly into the GISAXS setup, we followed the creation and growth of gold clusters and the subsequent layer formation, as is illustrated in figure 2.11.

The acquired large data sequences were analyzed using the fast data reduction software DPDAK. Hereby, the 2D raw data were cut at specific regions of interest, such as the horizontal line cuts shown in figure 2.12 a, which give information about the lateral film morphology.

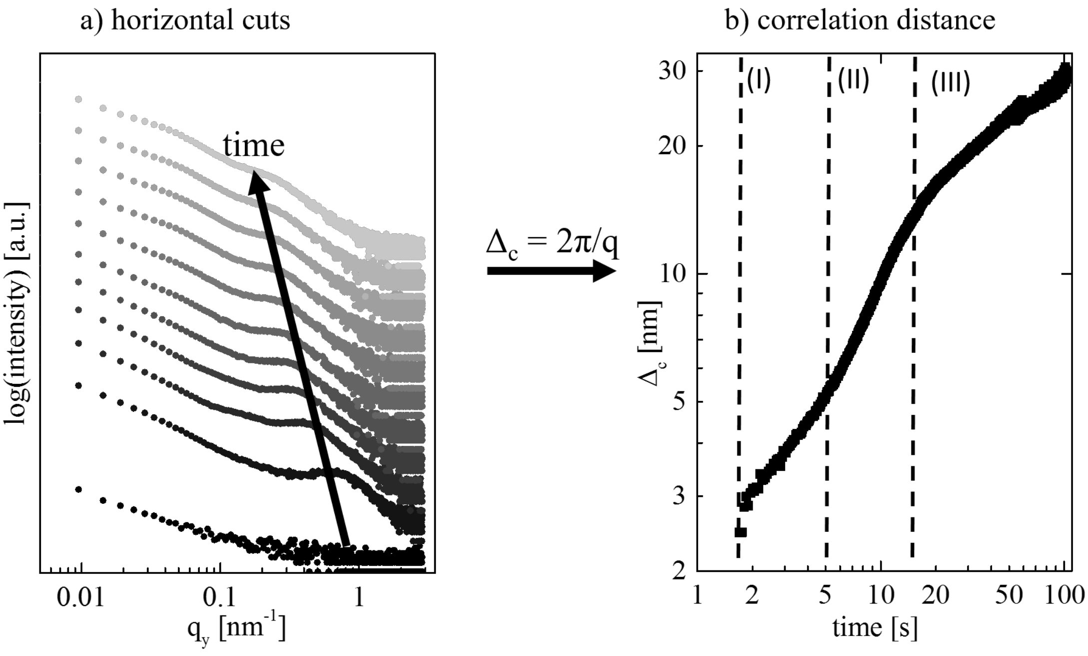

Figure 2.12:
Exemplary direct data analysis with a) horizontal cuts from the raw 2D GISAXS data taken after certain time intervals and b) the evolution of the corresponding correlation distance during the deposition process.

The evolution of the maximum over time can be translated into a real-space value, the so-called correlation distance Δ_c (see figure 2.12 b), which is a measure for the mean distance of gold clusters on the polymer surface. This direct data analysis gives an impression of the different growth rates during the deposition process. The results are in good accordance with a step-like growth model developed by Kaune et al. for a similar system. [3] In order to further validate the model, the calculated structure parameters were implemented into a simulation of the scattering data. Detailed analysis of these simulations is ongoing.

[1] P. Müller-Buschbaum, *Adv. Mater.* **26**, 7692—7709 (2014)

[2] M. Schwartzkopf, G. Santoro, C. J. Brett, A. Rothkirch, O. Polonskyi, A. Hinz, E. Metwalli, Y. Yao, T. Strunskus, F. Faupel, P. Müller-Buschbaum, S. V. Roth, *ACS Appl. Mater. Interfaces* **7**, 13547–13556 (2015)

[3] G. Kaune, M. A. Ruderer, E. Metwalli, W. Wang, S. Couet, K. Schlage, R. Röhlsberger, S. V. Roth, P. Müller-Buschbaum, *ACS Appl. Mater. Interfaces* **1**, 353–360 (2009)

2.8 Organic solar cells based on P3HT and PCBM with embedded inorganic nanoparticles

S. Grott, N. Hohn, P. Müller-Buschbaum

In the last decade organic photovoltaics gained increasingly interest to use the energy of the sun in order to generate electricity. Using polymers as photoactive material has several advantages for the solar cells, such as enabling flexible and lightweight devices. Furthermore, polymers offer the possibility to apply low-cost production methods, like roll-to-roll processing. However, solar cells based on polymers stay far behind conventional silicon based solar cells concerning long-term stability and efficiency. Thus, many research efforts target on improving the performance of polymer based solar cells. A schematic representation of the main steps during the organic solar cell production is shown in Fig. 2.13.

So far several research directions have developed, which enable improved organic solar cell performance. On the one hand the chemical structure of the applied polymers is improved to increase the photo-physical properties of the compounds used in the active layer. On the other hand processing techniques, like morphological nanostructuring of bulk heterojunction (BHJ) blends via annealing or solvent treatments, lead to an increased efficiency. Due to an optimized chemical composition of the used polymers, several reports power conversion efficiencies (PCE) were published which were close to or exceeded 10%. Examples are the low-bandgap semiconductiong polymer with thieno[3,4-b]thiophene/benzodithiophene units (PTB7) blended with [6,6]-phenyl C71-butyric acid methyl ester (PC71BM) [1] or poly[4,8-bis(5-(2-ethylhexyl)thiophen-2-yl)benzo[1,2-b;4,5-b']dithiophene-2,6-diyl-alt-(4-(2-ethylhexyl)-3-fluorothieno[3,4-b]thiophene-)-2-carboxylate-2-6-diyl)] (PTB7-Th or PBDTT-FTTE) with PCBM [2] and small molecule based blends containing the efficient fused-ring electron acceptor (ITIC-Th) based on an indacenodithieno[2,3-b]thiopehene core and thienyl side chains [3]. Regarding the morphological properties of BHJ blends many investigations were conducted over the past years to link the photovoltaic properties with the morphologic characteristics of the used blends. A further approach is the doping via inorganic nanoparticles altering the photochemical properties besides the morphological properties of a bulk hetero junction system [4].

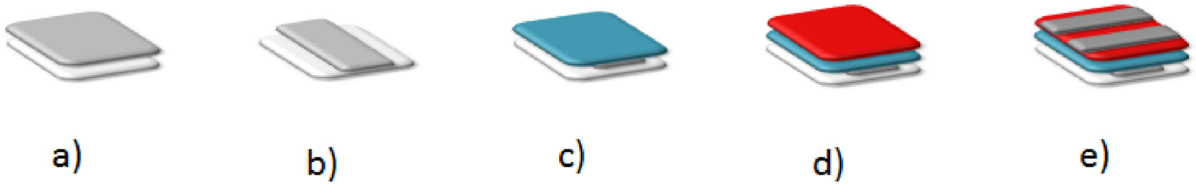

Figure 2.13:
Schematic representation of the main steps during organic solar cell preparation: a) ITO substrate as received b) patterned ITO substrate, c) addition of PEDOT:PSS as blocking layer, d) after depostition of the active layer and e) the entire organic solar cell with the top electrode.

In the present study we follow this track of doping via inorganic nanoparticles. As model system we use the well-studied BHJ pair of poly(3-hexylthiophen-2,5-diyl (P3HT) and phenyl-C61-butyric acid methyl ester (PCBM) to investigate the influence of inorganic nanoparticles on the photoactive properties. Recently, the influence of Fe_3O_4 nanoparticles within the active layer was investigated and led to an increase in efficiency of about 11 %. [4]

In the present study, instead of iron oxide nanoparticles we have selected germanium nanoparticles. The nanoparticles were surface functionalized to allow for a selective incorporation

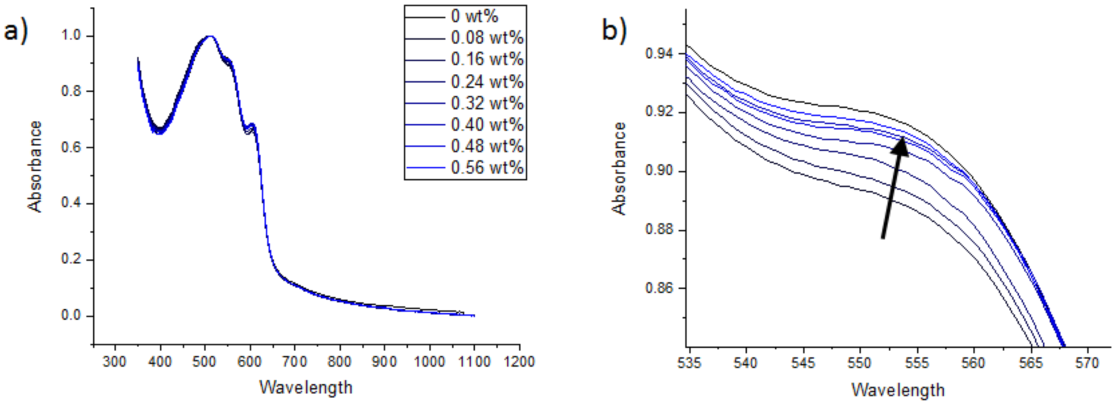

Figure 2.14:
a) UV-Vis spectra of P3HT:PCBM films with doped with different germanium nanoparticle concentrations as indicated and b) zoom-in to selected wavelength range.

in the active layer BHJ films. The influence of nanoparticle addition on the crystallinity of the active layer was investigated by UV-Vis spectroscopy. Selected UV-Vis spectra shown in Fig. 2.14a. The spectra show the typical absorption maxima of a P3HT:PCBM blend, with the main maximum at about 510 nm and to shoulder-like maxima at 550 nm and 630 nm. With a zoom-in a selected wavelength range around the shoulder-like maximum at 550 nm is shown (Fig. 2.14b). The changes in the absorbance in this wavelength range might indicate a decrease of the crystallinity of the active layer with addition of germanium nanoparticles. However increasing the nanoparticle concentration leads to an increase of crystallinity within the polymer blend as compared with the nanopartlice-free P3HT:PCBM reference, as seen in calculating the band-width from the fits to the absorbance spectra.

For a better understanding of the results gained by the UV-Vis spectra furter investigations via X-ray diffraction methods and complementary analysis methods like atomic force microscopy, X-ray reflectometry and grazing incidence mal/wide angel X-ray scattering (GIWAXS/GISAXS) are ongoing. Furthermore, first exploratory solar cells have been built and examined and will be evaluated in concern of power conversion efficiency and the corresponding morphology containing different concentration of germanium nanoparticles.

[1] Z. C. He, C. M. Zhong, S. J. Su, M. Xu, H. B. Wu, Y. Cao, *Nat. Photonics*, **6**, 591 (2012)

[2] S.-H. Liao, H.-J. Jhuo, P.-N. Yeh, Y.-S. Cheng, Y.-L. Li, Y.-H. Lee, S. Sharma, S.-A. Chen, *Sci. Rep.*, **4**, 6813 (2014)

[3] Y. Yankang, Z. Zhi-Guo, B. Haijun, C. Shanshan, G. Liang, X. Lingwei, X. Changduk, L. Yongfang, *J. Am. Chem. Soc.*, **138**, 15011 (2016)

[4] D. Mosegui Gonzalez, V. Körstgens, Y. Yao, L. Song, G. Santoro, S. V. Roth, P. Müller-Buschbaum, *Adv. Energy Mater*, **5**, 1401770 (2015)

2.9 In-situ neutron reflectometry on H_2O – D_2O exchange kinetics of crosslinked PNIPAM microgel thin films

T. Widmann, L. P. Kreuzer, N. Hohn, K. Wang, J-F. Moulin[1], Y. Hertle[2], T. Hellweg[2], P. Müller-Buschbaum

[1] MLZ, Garching, Germany
[2] University of Bielefeld, Bielefeld, Germany

Cross-linked homo- or co-polymers are commonly referred to as microgels and are interesting for both, scientific research and industrial applications due to their softness and fast response to various external stimuli [1-2]. Such responsive behavior translates to a shift of the polymer properties like conductivity or volume upon variation of environmental conditions like pH value, light or temperature. In this context the polymer which received most attention so far is poly(N-isopropylacrylamide), PNIPAM [3]. A volume change arises due to the collapse transition of the polymer PNIPAM at a lower critical solution temperature (LCST) which causes changes of the chain conformation and manifests in thin films as a swelling or deswelling of the film with water from its surroundings.

For control and tune-ability, it is essential to gain a deeper understanding of the sorption and diffusion processes of low-molecular penetrants in thin polymer films. Therefore, neutron reflectivity (NR) measurements are used to observe the exchange kinetics between H_2O and D_2O penetrants in a thin PNIPAM microgel film.
Three films are prepared from a solution of PNIPAM homopolymer with 5 %wt., 7.5 %wt. and 10 %wt. of N,N'-Methylenebisacrylamide cross-linkers respectively (see Fig. 2.15 a)). The solution is cast on acid-cleaned silicon wafers and sediments under a water atmosphere for 15 min. Thereafter, the atmosphere is removed and the film is established via spin-coating at 2500 rpm for 15 min.

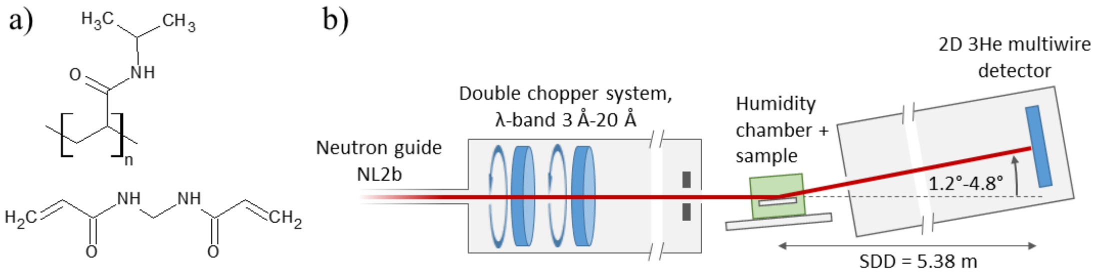

Figure 2.15:
a) Structure formulas of PNIPAM (top) and N,N'-Methylenebisacrylamide (bottom). b) REFSANS beamline set-up

The NR measurements were performed at the REFSANS instrument at MLZ (FRMII) in Garching (see Fig. 2.15 b)[4]). The measurements were run in time-of-flight (TOF) mode using a wavelength band of neutrons from 4 Å to 21 Å. This yields a range of equiangular incident wave-vectors with varying absolute values normal to the sample surface, thereby scanning a broad q-range band while keeping the incident angle of the neutron beam constant. The kinetics of the D_2O and H_2O penetration and diffusion are measured by adding 8 ml of liquid into a measurement chamber and measuring the corresponding NR spectra as function of time for six hours. A five step measurement protocol was followed, measuring the kinetics of the D_2O and H_2O exchange and a static measurement before between and after the kinetics, respectively.

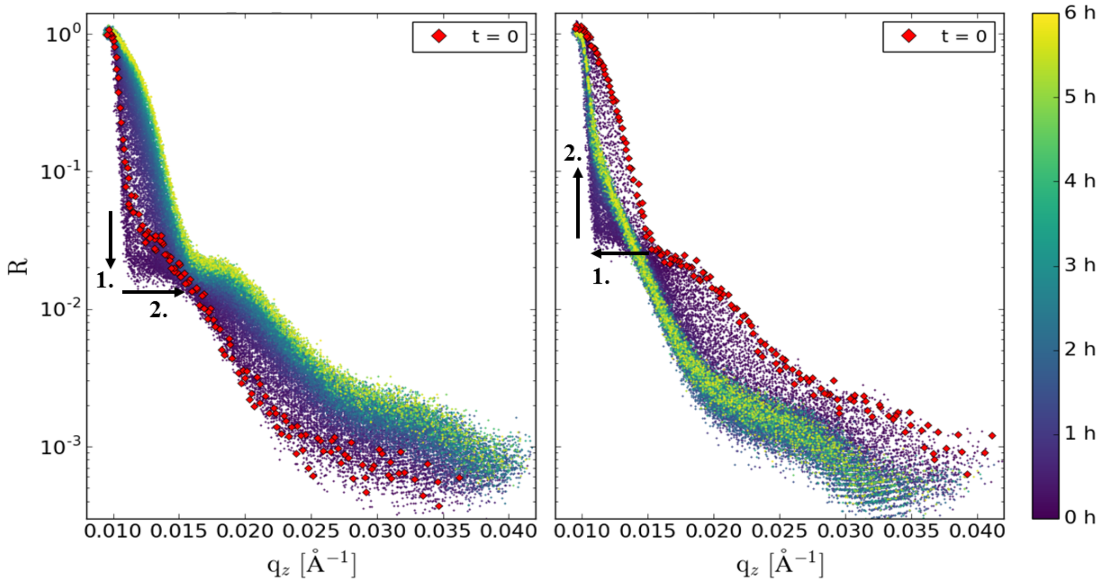

Figure 2.16:
a) NR on PNIPAM films with 10 %wt. cross-linker placed in a D_2O atmosphere for 6 h b) NR on the exchange of D_2O with H_2O by replacing the D_2O with a H_2O atmosphere

The static measurements were performed at an incident angle of $0.6\,^\circ\mathrm{C}$ and $2.4\,^\circ\mathrm{C}$, the kinetic measurements at $0.76\,^\circ\mathrm{C}$.
The measured swelling kinetics of the initial PINPAM microgel film is shown in Fig. 2.16 for a D_2O atmosphere. A film with with 10 %wt. cross-linker was measured. After a short time the initially prepared film (red diamonds) first appears to improve the large scale homogeneity of the film leading due to having more pronounced fringe after around 10 min (1). Thereafter, the D_2O continues to penetrate and diffuse into the film leading to an increase of the scattering-length-density of the film and subsequently to a shift of the critical edge and the whole NR spectrum to the right (2). The strongest shift happens during the first two hours, after which the measured signal already converges on the final state after six hours of measuring. Compared to that, the kinetics of the H_2O penetration into the film shown in Fig. 2.16 on the right hand side reveal much faster kinetics, with the final shape already being approached after the first hour. Reversely to the adsorption of D_2O the curve is first shifted to the left (1) and then increases in intensity at around $q = 0.012$ Å^{-1} exceeding the shape of the initial film (2). The final film shows narrower fringes compared to the D_2O saturated film, indicating a higher film thickness and possibly a higher affinity of the cross-linked PNIPAM towards H_2O. This is also reflected by the faster exchange kinetics of $D_2O \rightarrow H_2O$ compared to $H_2O \rightarrow D_2O$.

In order to get a deeper understanding and numerical representation of the observed exchange kinetics, a detailed analysis of the recorded NR data is necessary. Further experiments with Fourier transform infrared spectroscopy (FTIR) and white light interferometry (WLI) are planned to build upon the current measurements and improve our understanding of the diffusion and sorption of H_2O and D_2O in the polymer film.

[1] B. Wedel, Y. Hertle, O. Wrede, J. Bookhold, T. Hellweg, *Polymers* **8**, 162, (2016)

[2] S. V. Vinogradov, *Current Pharmaceutical Design*, **12**(36), 4703–4712 (2006)

[3] A. Campanella, Z. Di, A. Luchini, L. Paduano, A. Klapper, O. Petracic, M.S. Appavou, P. Müller-Buschbaum, H. Frielinghaus, D. Richter, *Polymer* **60**, 176-185 (2015)

3 Photovoltaics

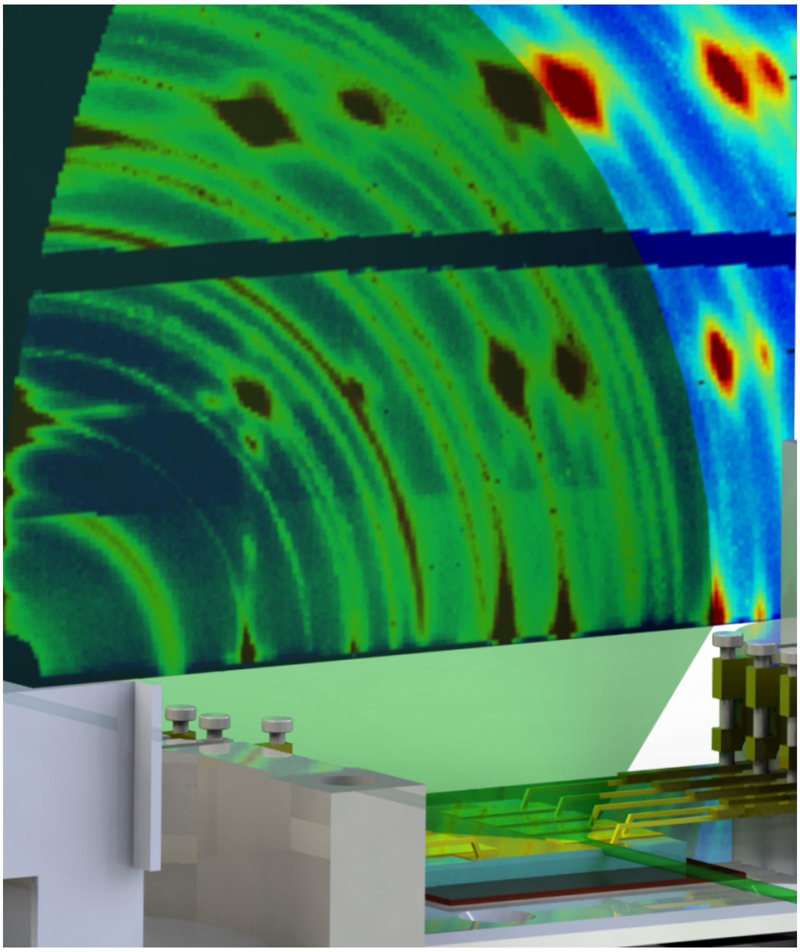

3.1 Employing water/alcohol soluble conjugated polymer as cathode interlayer in organic solar cells

D. Yang, B. Su, W. Wang, S. V. Roth[1], P. Müller-Buschbaum

[1] DESY, Hamburg, Germany

Organic solar cells (OSCs) are supposed to be a cost-effective way to solve the energy crisis in the near future due to their potential of large-scale manufacturing by solution fabrication methods. Over the last decade, poly(3,4-ethylenedioxythiophene):poly(styrenesulfonate) (PEDOT:PSS) / indium tin oxide (ITO) coated glass substrates have been most widely used as bottom contact in OSC device configuration. However, an acid solution of PEDOT:PSS can cause corrosion of the ITO layer, which results in a decrease of the stability of OSCs manufactured with such bottom contacts. In recent years, inverted device geometry has strongly attracted researchers' attention. In this configuration, PEDOT:PSS/ITO bottom contacts and other reactive metals such as Ba and Ca used at the electron collecting electrode can be avoided. As a consequence, the stability of OSCs is increased if an inverted device geometry is used.[1] In the inverted device geometry, commonly metal oxides such as TiOx and ZnO are applied on the top of ITO. Recently, He et al. reported a water/alcohol soluble conjugated polymer as interlayer between the cathode and the organic active layer in an OSC, which was shown to improve the device performance by changing the interactions at the respective interfaces.[2] Water/alcohol soluble conjugated polymers have reached great success as electrode interfacial layer materials for organic optoelectronic devices. In the present work, a water/alcohol soluble conjugated polymer is used as interfacial layer at the cathode in inverted OSCs. The conjugated polymer poly[(9,9-bis(3'-(N,N-dimethylamino)propyl)-2,7-fluorene)-alt-2,7-(9,9-dioctylfluorene)] (PFN, see Fig. 3.1 a) is containing amino groups and thus, could modify the work function of ITO to match well with the LUMO level of $PC_{71}BM$. Two kinds of OSCs have been fabricated using different donor materials (PTB7-Th, Fig. 3.1 b and PffBT4T-2OD, Fig. 3.1 c) as depicted in Fig. 3.1 d and e. Both of them showed high efficiency, and especially the open circuit voltage was significantly improved (see Fig. 3.1 f).

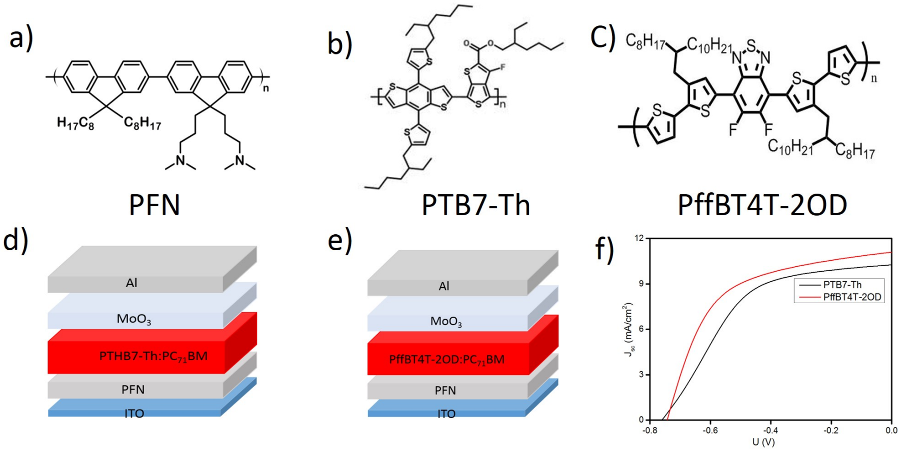

Figure 3.1:
Chemical structures of used polymers: a) PFN, b) PTB7-Th and c) PffBT4T-2OD; Sketch of the fabricated device structures with d) PTB7-Th and e) PffBT4T-2OD in the active layer; f) J-V curves of such solar cells.

PFN films show a phase separation as reported in literature from the analysis of X-ray reflectivity (XRR) data showing two scattering length densities. [1] Besides this knowledge about the vertical segregation in PFN layers, the influence of annealing conditions on the phase separation in PFN films is unknown. In particular, information about lateral structures is missing. Thus, PFN films were prepared with different annealing times and studied with GISAXS measurements to investigate the inner film morphology. To detect lateral structures, horizontal line cuts from the 2D GISAXS data (see Fig. 3.2 a) were done at the PFN Yoneda peak position. To extract the corresponding structure information, the horizontal line cuts were fitted with the model including three form factors and their corresponding structure factors (see Fig. 3.2 b). Compared with the data from the sample without annealing, the data of the annealed sample (10 min annealing) show a pronounced peak in the q_y region of 10^{-2}-10^{-1} nm^{-1}. While increasing annealing time to 30 min, the peak shifts to smaller q_y values. A shift to smaller q_y values corresponds to an increase in structure sizes. [3] After annealing for 40 min, the pronounced peak moves slightly back to larger q_y values. Moreover, a second weak peak appears at even lager q_y values of 10^{-1}-1 nm^{-1}. Thus, structures decreased in size as compared to the sample annealed for 30 min.

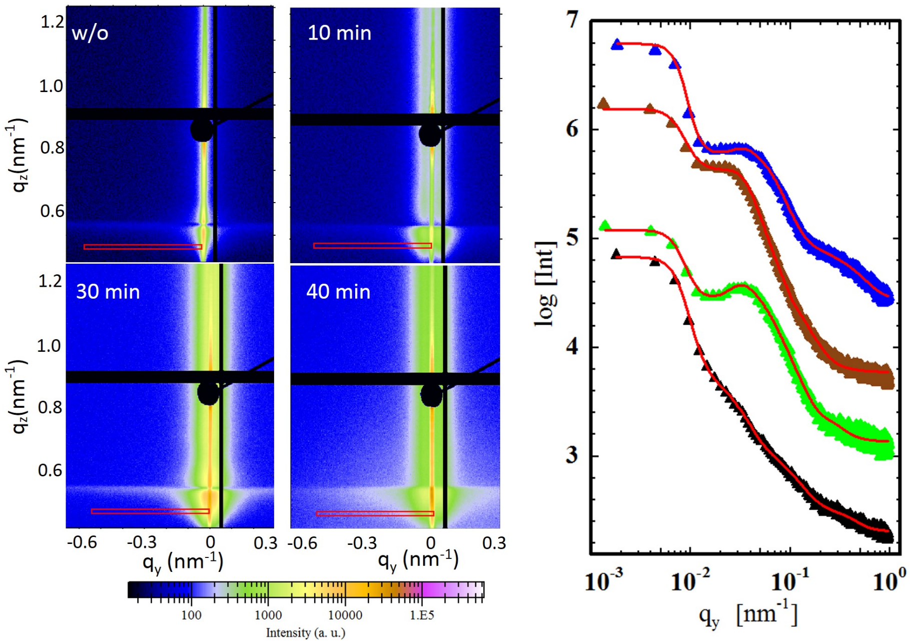

Figure 3.2:
a) 2D GISAXS data of PFN films with different annealing times as indicated in the figures; b) horizontal line cuts of the 2D GISAXS from the samples without annealing (black symbols), annealed for 10 min (green), annealed for 30 min (brown)and annealed for 40 min (blue). The fits to the data are shown with red lines.

In summary, in the PFN films a pronounced lateral structure is detected with GISAXS measurements besides the well-known vertical phase separation structure. The characteristic lateral structure sizes depend on the applied annealing conditions. Similar to the vertical phase separation, also the lateral structures are caused by a phase separation, which means that different parts of the layer show different composition. The resulting impact on the solar cell performance is presently studied.

[1] R. Xia, D. S. Leem, T. Kirchartz, S. Spencer, C. Murphy, Z. He, H. Wu, S. Su, Y. Cao, J. S. Kim, J. C. deMello, D. D. C. Bradley, J. Nelson,*Adv. Energy. Mater.* **3**, 718-723 (2013)

[2] Z. He, B Xiao, F. Liu, H. Wu, Y. Yang, S. Xiao, C. Wang, T. P. Russell, Y. Cao, *Nat. Photon.* **9**, 174-179 (2015)

[3] W. Wang, S. Guo, E. M. Herzig, K. Sarkar, M. Schindler, D. Magerl, M. Philipp, J. Perlich, Müller-Buschbaum,*J. Mater. Chem. A* **4**, 3743-3753 (2016)

3.2 Inserting silver decorated nanoparticles into the active layer of organic photovoltaics

V. Körstgens, M. Pfab, S. V. Roth[1], P. Müller-Buschbaum

[1] DESY, Hamburg, Germany

Among the manifold ideas to improve the power conversion efficiencies of organic photovoltaics quite a few can be summarized as the inclusion of nanoparticles in the set-up of the photovoltaic devices. Nanoparticles may be dispersed in the polymer matrix of the active layer or more densely as an additional interfacial layer. It is possible to enhance absorption rates considerably by light scattering caused by colloidal nanoparticles. An elongated path length of the incident light increases the possibility to build an exciton out of a photon. To have scattering effects, the refractive index must be different to the refractive index of the active layer. Metallic nanoparticles show aside from the scattering properties an additional effect on the absorption caused by surface plasmon resonace (SPR). At specific wavelengths when the conduction electrons at the metal surface are excited by light these electrons begin collectively to oscillate. The SPR leads to an absorption peak which for silver is located characteristically between 400 nm and 530 nm. Due to the oscillation the metal nanoparticles produce a localized electric field. This field and the interaction between the particles influences the exciton generation rate.

We transferred silver decorated silica nanospheres into the active layer of poly(3-hexylthiophene) (P3HT) and phenyl-C61-butyric acid methyl ester (PCBM) solar cells. For a successful transfer we chose Kapton foil which is temperature-stable up to 300 °C as the substrate for the decoration of nanoparticles. In the first step of the procedure we developed, silica nanospheres are attached to a Kapton film via a thin coating of polyethyleneimine (PEI). These films pictured in Fig. 3.3a) are the source material for the metal decoration process. The SEM image of silica nanospheres on Kapton foil (Fig. 3.3b)) shows the arrangement of nanoparticles in the film of approximately 750 nm thickness.

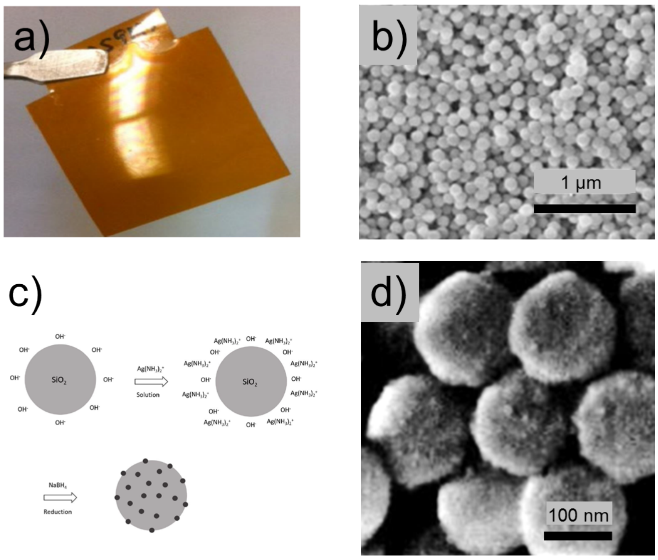

Figure 3.3:
Silver decoration of silica nanospheres attached to a Kapton foil substrate a) foil coated with silica spheres as source material for decoration process b) SEM image of silica nanospheres on Kapton foil c) General scheme for the decoration process of particles with silver nanoparticles with the two steps: 1) Attachment of silver ions, here complex ions $[Ag(NH_3)_2]^+$ and 2) application of a reducing agent for the generation of metallic silver d) SEM image of silica nanospheres after silver decoration.

The general scheme of metal decoration we followed is given in Fig. 3.3c). The process of metal growth on a particle consists in principal of two steps: First metal ions adhere to the surface of colloidal particles and in a second step metal ions are reduced to the metallic state. By choosing the suitable reducing agent and adjusting the concentration the finite size and distribution of the metal nanoparticles decorating the colloids can be controlled [1]. The scheme in Fig. 3.3c) shows the metal decoration with silver. In the first step particles are immersed in a solution of silver complex ions $[Ag(NH_3)_2]^+$. Due to the negative charge of the nanoparticles the attachment of complex ions is facilitated. In the second step shown in the bottom of Fig. 3.3c) the silver ions are reduced to metallic silver by immersion in a solution of a reducing agent, in our case sodium borohydride $NaBH_4$. For the silver decoration process aqueous solutions containing silver ions and a reduction agent are applied in a custom-built reaction vessel. In the reaction vessel several samples of Kapton foils coated with SiO_2 nanospheres as pictured in Fig. 3.3a) are exposed to the solution of $[Ag(NH_3)_2]^+$-ions under gentle stirring conditions. For the common approach with the growth process of particles in suspension [1] usually an elaborate washing and concentration procedure is necessary to remove residual silver ions from the solution before adding the reduction agent. The advantage of our procedure with coated substrate is that the washing step can be simplified to a single dipping process. Following that using the custom-built reaction vessel, coated substrates are immersed in a freshly prepared aqueous solution of the reduction agent. The successful decoration of the silica spheres with silver has been verified by UV/vis spectroscopy and can also be observed with SEM as shown in in Fig. 3.3d). Nanoparticles with a diameter of a few nanometer can be distinguished on the surface of the silica spheres. An example for the transfer of these particles to an active layer is given in Fig. 3.4. Silver decorated nanoparticles were transferred to P3HT film on a glass substrate in a process combining elevated temperature and pressure. The most efficient particle transfer was achieved at a temperature of 230 °C which is above the glass transition temperature of P3HT (214 °C), whereas the pressure was applied by putting a weight on the backside of the Kapton foil.

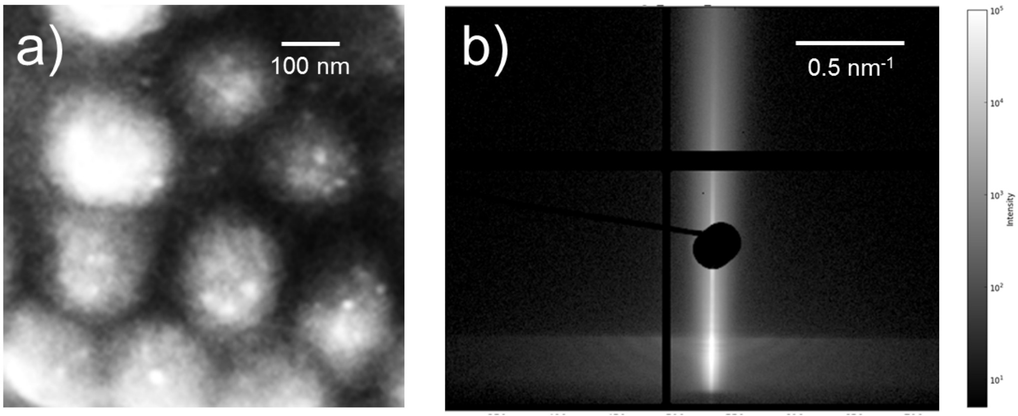

Figure 3.4:
Transfer of silver decorated nanoparticles into a film of P3HT a) SEM of embedded silver decorated nanoparticles in P3HT after transfer with Kapton foil at 230 ° b) corresponding 2D detector image of GISAXS measurement of the sample.

The successful transfer and embedding of nanoparticles in the P3HT film can be observed in the SEM image of Fig. 3.4a. The silica spheres with decoration of particles of silver appearing as bright spots in the SEM image are covered with a polymer layer of P3HT. We investigated the composite films of silver decorated silica nanoparticles with grazing incidence small angle x-ray scattering (GISAXS) at the P03 beamline at the synchrotron source PETRA III at DESY in Hamburg. Already in the 2D detector image Fig. 3.4b form factor oscillations from the spheres can be observed in the horizontal direction. Together with the GIWAXS investigation at the same positions of the sample, the distribution and also the crystalline structure of the nanoparticles can be elucidated. Furthermore in a proof of concept complete functional solar cells with integrated silver decorated silica nanoparticles in the active layer of P3HT/PCBM have been manufactured.

[1] J. Zhang, J. Liu, S. Wang, P. Zhan, Z. Wang, N. Ming, *Adv. Funct. Mater.* **14**, 1089-1096 (2004)

3.3 Optimization of thermoelectric properties of PEDOT:PSS thin films through a dedoping approach

A. K. Maurya, N. Saxena, P. Müller-Buschbaum

Due to the compelling need for renewable energies in the face of global threats in the form of climate change and the resulting socioeconomic implications, researchers have been heavily interested in ways to harvest energy from renewable sources. Thus far, energy generation from fossil fuels has driven industrial and societal advancement but is also responsible for rising global average temperatures through the greenhouse effect. While it is already possible to tap into energy in the form of solar radiation using solar cells or wind using wind turbines, one form of energy still cannot be harvested efficiently, namely heat. Waste heat is a byproduct of almost all processes which occur in daily life, be it in industrial fabrication, household appliances or even the human body. In principle, one could convert this low-quality form of energy into a high-quality or more useful form such as electricity by using thermoelectric materials. They transform a temperature gradient, which form along the materials, into electrical potentials which, in turn, can be used to power devices. A thermoelectric material is typically characterized using the figure of merit ZT, as given in equation 3.1.

$$ZT = \frac{\sigma \cdot S^2}{\kappa} T \tag{3.1}$$

In this equation, σ is the electrical conductivity, κ the thermal conductivity, T the temperature and S the so-called Seebeck coefficient or thermovoltage. The latter is a material-specific quantity which describes the magnitude of the voltage as function of a temperature difference. The higher the overall quantity ZT is, the higher also the thermodynamic conversion efficiency of heat to electricity becomes. It is typically assumed that a value of ZT of approximately 1 yields a reasonable thermoelectric material. In recent years, it has become possible to increase ZT to values of up to 2.6 through nanostructuring, i.e. introduction of grain boundaries, heteroatoms and introduction of superstructures.

For decades, inorganic thermoelectric materials have been synthesized and investigated by combining heavy elements such as bismuth, tellurium, sulfur, antimony, lead, etc. While they do possess high thermovoltages, there are also several drawbacks. These include fabrication procedures which are energy- and cost-intensive, rare, expensive, toxic materials and also the fact that these materials produce electricity more efficiently mostly at very high temperatures of more than 200° C. The aforementioned points have impeded the large-scale application of thermoelectrics for power generation in daily life.

This has driven a transition from inorganic to organic thin film thermoelectrics based on conducting polymers. Polymers offer a wide range of advantages, such as the possibility for large-scale fabrication and processing or flexibility of devices. Since carbon is abundant on earth, it also proves to be a suitable element to be used for thermoelectric applications.

While many conducting polymers have already been synthesized for different applications within the framework of organic electronics, PEDOT:PSS has attracted special interest in research. One reason for that is that the electrical conductivity of thin films has been shown to increase by up to three orders of magnitude upon treatment with different chemicals, such as high-boiling point solvents or acids. With these procedures, electrical conductivities of up to 3000 S/cm were achieved, which rival conventional materials such as indium tin oxide, among others.

Even though thin films of PEDOT:PSS exhibit considerably higher electrical conductivities than inorganic thermoelectrics, the former suffer from very low Seebeck coefficients of approximately 15 μV/K, while the latter possess Seebeck coefficients which are magnitudes larger. Thus, one

needs to find a compromise between higher Seebeck coefficients while maintaining decent electrical conductivities. [1]
In this work, PEDOT:PSS is treated with an inorganic salt, sodium sulfite, in a so-called dedoping approach. Since PEDOT:PSS only transports positive charge carriers, it is possible to 'neutralize' them using sodium sulfite, which itself has reducing properties. For this purpose, small amounts of sodium sulfite are mixed with the aqueous solution of PEDOT:PSS and left to shake for 30 min, before application on clean glass slides through spin-coating. Subsequent annealing at 140° C and treatment with ethylene glycol, a high-boiling point solvent, lead to morphological reorganization and enhancement of the electrical properties of the films.

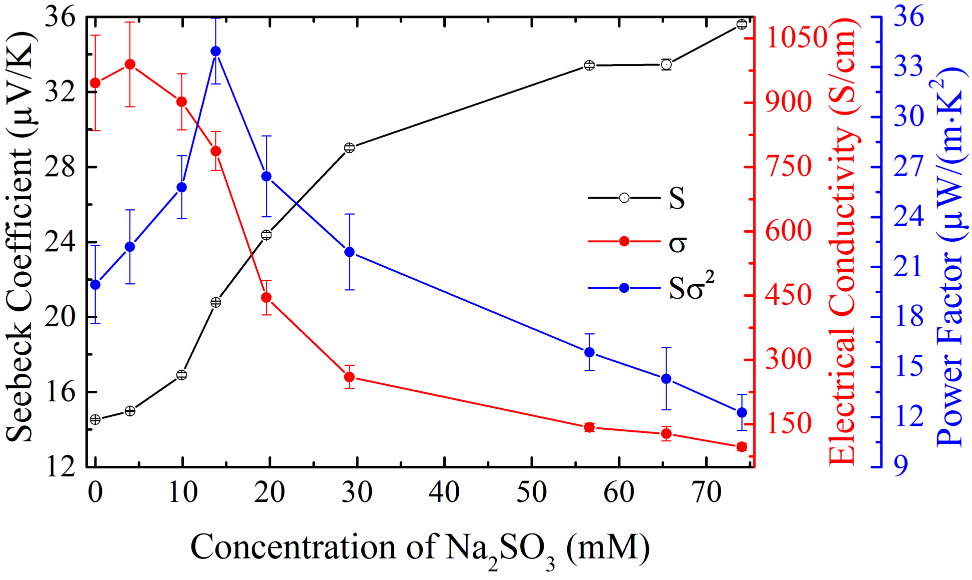

Figure 3.5:
Seebeck coefficient (S), electrical conductivity (σ) and power factor ($S^2\sigma$) as function of sodium sulfite concentration.

Figure 3.5 shows the evolution of thermoelectric properties as function of sodium sulfite concentration. The initially low Seebeck coefficient of 15μV/K steadily increases for higher sodium sulfite concentrations up to values of 36 μV/K. Since there is an inverse relation between Seebeck coefficient and electrical conductivity, a corresponding drop of electrical conductivity with sodium sulfite concentration from 950 S/cm to 100 S/cm is observed. The power factor is a quantity derived from the numerator of equation 3.1, and relates to the electrical power which can be extracted for a given temperature gradient. An optimal power factor of 33 μW/(K^{2}m) is found at a concentration of about 13 mM, representing an improvement by a factor of 1.5 compared to the samples without sodium sulfite. The measurement of the thermal conductivity gives a higher limit of 1.2 W/(Km) and lower limit of 0.77 W/(Km) for the reference sample and the highest concentration of 56.6 mM, respectively. Using these values, ZT can be calculated for an temperature of 110° C, according to equation 3.1. Compared to the reference samples, where a ZT value of 0.006 is achieved, the treatment of PEDOT:PSS thin films leads to an improved ZT in the range of 0.011 and 0.017. In addition, investigations using grazing incidence wide-angle x-ray scattering (GIWAXS) revealed morphological implications of the dedoping on the PEDOT:PSS thin films. The results of this work show that similarly to inorganic thermoelectrics, variation of the charge carrier concentration can be tuned using reducing agents, which in turn allows for optimization of the thermoelectric performance.

[1] H. Shi, C. Liu, Q. Jiang, J. Xu, *Adv. Electron. Mater.*, 1500017 (2015)

3.4 Impact of moisture on perovskite solar cells under operating conditions

M. Trunk, B. Su, R. Wang[1], L. Bießmann, H. Xu, S. Bernstorff[2] and P. Müller-Buschbaum

[1] MLZ, Garching, Germany
[2] ELETTRA, Basovizza, Italy

In order to overcome the commercially available silicon solar cells which are known to be heavy, immobile and expensive, the research in thin film photovoltaics attracts high interest since years. Amongst the different thin film solar cell concepts the organometal trihalide perovskite solar cells have gained a tremendous efficiency improvement over the last years, starting from power conversion efficiencies (PCEs) of 3.81 % [1] up to values exceeding 20 % [2]. The organometal trihalide perovskites consist in most cases of the organic cation methylammonium (MA) embedded in an inorganic matrix of lead and halogens (Cl, Br, I).

Even though the efficiency progress is highly promising, the lead–halide perovskite suffers from the instability of the material to atmospheric moisture conditions. This drawback has hindered any attempts towards real world applications of perovskite solar cells up to now. The moisture sensitivity of the lead perovskite has not yet been deeply addressed or even overcome.

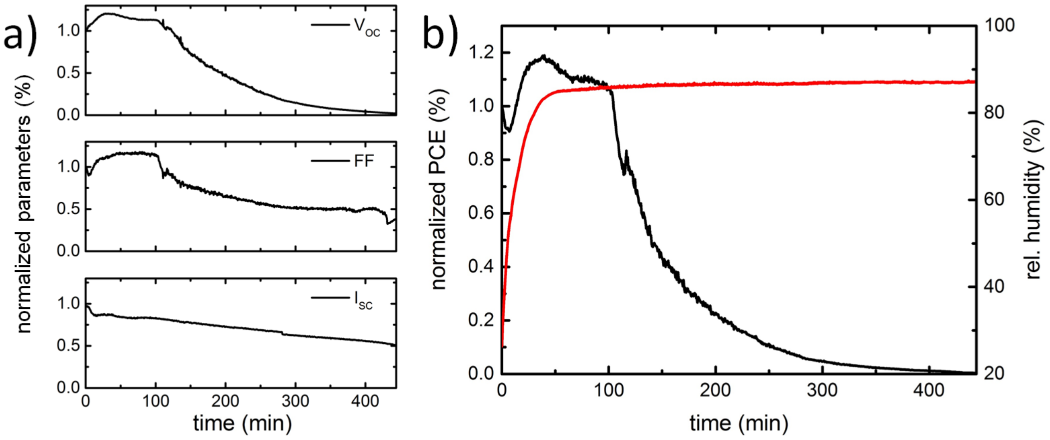

Figure 3.6:
Degradation of perovskite solar cell under humid environment. a) Temporal evolution of V_{oc}, FF and I_{sc} and b) overall PCE degradation (black) compared with the relative humidity (red) in the measurement chamber.

Due to the nature of the organic compound, the perovskite crystals show film degradation, which influences the performance of related solar cell devices. Besides very fundamental studies on the influence of humidty on the perovskite material [3,4], so far changes in the crystalline structure of perovskite solar cells caused by humidity are not probed during operation conditions. In order to study the degradation behavior of the solar cells under operation and controlled humidity conditions by grazing incidence X-ray scattering methods we operated an IV-measurement setup at the SAXS beamline at ELETTRA.

After functionalizing nanostructured TiO_2 as an appropriate transport material for negative charges, the heterojunction perovskite solar cell was prepared via solution processing. After full crystallization of the perovskite layer, spiro-OMeTAD was spin-casted on top, which is widely used as an organic hole transporting material in this class of solar cells. A thin gold layer serves as counter electrode.

The perovskite solar cells were measured in-operando in the measurement-setup, while a stable and controlled humid vapor was established. The humidity evolution and the temporal degradation of characteristic solar cell parameters are shown in Figure 3.6. First, we observe an increase of the PCE until the relative humidity establishes constant conditions in the measurement chamber, followed by a fast degradation of the device performance (cf. Figure 3.6 b). We identify the V_{oc} as the main driving parameter for degradation (cf. Figure 3.6 a).

In-operando we followed the perovskite crystals changes with GIWAXS during the full process. An example of the GIWAXS measurements of the solar cell is shown in Figure 3.7. Figure 3.7 a shows the 2D intensity measured for the perovskite solar cell at one time of the degradation study after transformation from detector pixels into q-space and applying the necessary data corrections. The inaccessible wedge-shaped area in the center of Figure 3.7 a is typical for GIWAXS measurements and due to the used scattering geometry. For the studied solar cells we observe Debye-Scherrer type rings with superimposed small Bragg spots instead of well-defined Bragg peaks. Thus, the studied perovskite film exhibits small crystallites with random orientations. For further data analysis the 2D scattering data were integrated to achieve line cuts. In these line cuts the typical perovskite Bragg peaks were observed. In Figure 3.7 b line cut data are shown for a limited q-range and for a short time interval from the degradation study to better visualize the observed changes. During degradation the intensity of the perovskite Bragg peaks decreases and also peak position changes slightly. However, Bragg peaks remain although the device performance decreases to zero efficiency.

In summary, we probed perovskite solar cells in-operando during solar cell degradation. To the best of our knowledge this is the first in-operando study of complete perovskite solar cells under working conditions in humid atmosphere. Thus, our study will help to better understand the degradation mechanisms of solar cells which turn out to be different from those being reported for the pure perovskite material. In turn, it will become possible to better stabilize perovskite solar cells against humid atmosphere and thereby solve of the two major drawback of this very promising class of thin film solar cells.

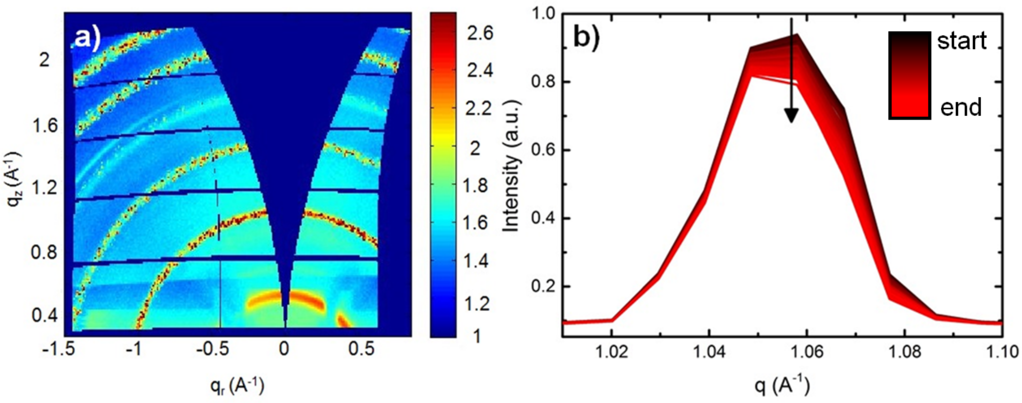

Figure 3.7:
a) Example of 2D GIWAXS data measured for the perovskite solar cell. b) Degradation of the crystal structure of the perovskite solar cell as followed with line cuts from the 2D GIWAXS data.

[1] A. Kojima, K. Teshima, Y. Shirai, T. Miyasaka, *J. Am. Chem. Soc.***131**, 6050–6051 (2009)

[2] G. Niu, X. Guo, L. Wang, *J. Mater. Chem. A* **3**, 8970-8980 (2015)

[3] J. H. Noh, S. H. Im, J. H. Heo, T. N. Mandal, S. I. Seok, *Nano Lett.***13**, 1764–1769 (2013)

[4] G. Niu, W. Li, F. Meng, L. Wang, H. Dong, Y. Qiu, *J. Mater. Chem. A* **2**, 705–710 (2014)

3.5 ZnO as a potential scattering layer for OLEDs

D. Schullerer, L. Bießmann, P. Müller-Buschbaum

Since the report of the first efficient thin-film organic light emitting diodes (OLEDs) by Tang and Van Slyke [1] development in this sector rapidly advanced. Today, OLEDs are used in many everyday applications such as mobile phones, car radios, digital cameras and television screens and lighting while future uses may encompass self-illuminating clothes and different signal lights in cars. Their main advantages are the absence of necessary backlighting in display technologies, leading to a possibly higher overall efficiency and lower weight, as well as the ability to construct bend or even flexible devices.

So far, the main disadvantages of OLEDs are the limited possibilities for upscaling of the fabrication processes and a low overall efficiency. Regarding the low device efficiencies, Baldo et al. showed that an internal quantum efficiency of nearly 100 % can be reached by using phosphorescent emitting materials, [2] while in conventional devices only about 20 % of the generated photons are able to be extracted. All other photons are trapped in the substrate and organic modes to eventually be absorbed [3].

This problem of a low external quantum efficiency could possibly be solved by the implementation of scattering centers into the device. Such scattering centers can be either constructed by a direct surface structuring [4], by use of different refractive index materials [5] or by the addition of a transparent scattering layer. Earlier, those layers were produced by directly adding nanoparticles on top of the substrate or using a polymer film with integrated nanospheres [6]. An alternative to those approaches are metal oxides, combining high stability with a suitable refractive index. In particular, ZnO is a suitable material for this taks, due to its transmittivity in the entire visible spectrum, caused by its direct optical bandgap of 3.3 eV.

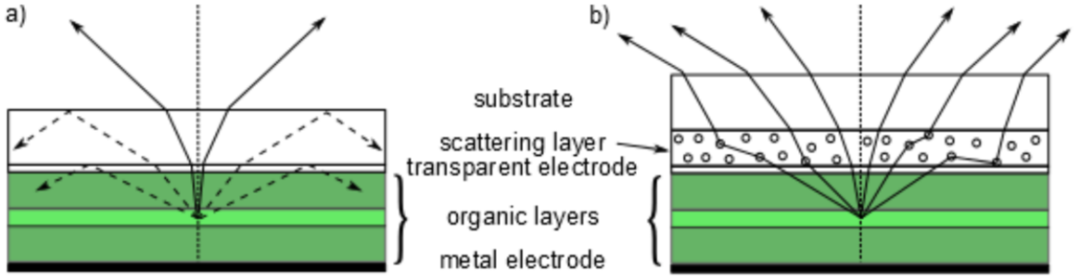

Figure 3.8:
Structure and photon extraction of an OLED a) without scattering layer and b) with a scattering layer. The solid lines show light paths leading to photon extraction, the dotted paths show thos leading to trapping. The scattering layer leads to a higher photon extraction, therefore increasing the device's efficiency [7].

Figure 3.8 shows the architecture of an OLED with (b) and without (a) a scattering layer as well as some corresponding light paths. The photons, after being generated in the emitter, have to pass several interfaces before extraction. The ITO-glass and glass-air interfaces in the conventional device lead to total reflection for many incident angles due to the high difference in the refractive indices between the two materials. Furthermore light is trapped in substrate modes. The scattering layer can reduce the amount of total reflection due to smaller steps in the refractive index. Additionally the scattering layer can also redirect the photons and suppress the substrate modes, all together vastly increasing the light out-coupling [7].

The ZnO scattering layer has to be porous to achieve the desired refractive index. To get mesoporous ZnO films a structure giving diblock copolymer template is combined with sol-gel chemistry, allowing tuning the structure and thereby the scattering index of the layer as a whole according to the needs. For this method the diblock copolymer polystyrene-block-polyethylene oxide (PS-b-PEO) is used to build the structural template since the PEO block can coordinate metal oxide precursors. A commercial precursor zinc acetate dihydrate (ZAD) is used to form ZnO. Additionally, polystyrene nanospheres, which get removed during the calcination treatment, are used to further structure the layer. Spray coating was chosen as the deposition technique due to the ability to predetermine the film thickness over a wide range. It will be studied further how one can influence the layer structure and how this can be used to increase the photon out-coupling of OLEDs. Therefore the scattering layer itself is investigated via scanning electron microscopy (SEM). Figure 3.9 shows SEM pictures of a ZnO layer mixed with varying concentration of nanospheres. As seen in the SEM pictures, the addition of nanospheres increases the overall proposity. The more nanospheres added, the higher the porosity, or the lower the refractive index.

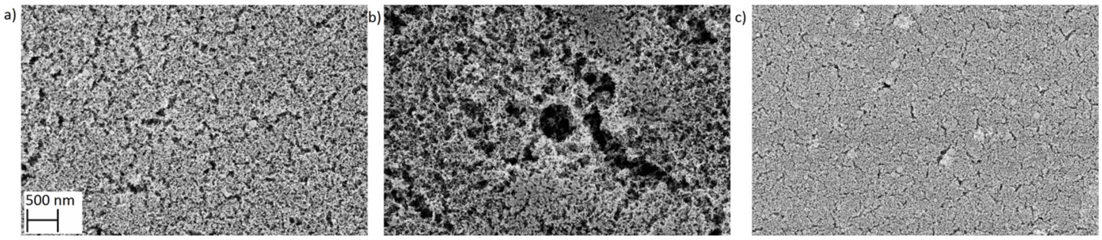

Figure 3.9:
SEM images of ZnO layer after calcination with a a) nanosphere concentration of 2.1 mg/ml, b) 3.9 mg/ml and c) without nanospheres. Higher concentration of nanospheres leads to an increased porosity.

Also UV-Vis measurements and goniophotometric measurements are done to further characterize the scattering behavior. For the uncalcined thin films of about 250 nm there is a strong scattering of white light over the whole spectrum, especially when compared to pure glass. This behavior is mostly lost during the calcination step, as only the ZnO, of which only a low concentration was used, remains, leading to a much thinner film.

Parallel to this study standard OLEDs and OLEDs with a scattering layer are prepared and compared in order to directly study the effect in a device. For the emissive layer the well-studied Super Yellow (PDY-132) system is used, although such OLEDS cannot be expected to reach top efficiencies as no triplet states are excited.

[1] C. W. Tang, S. A. VanSlyke, *Applied Physics Letters* **51**, 913-915 (1987)

[2] M. A. Baldo, D. F. O'Brien, Y. You, A. Shoustikov, S. Sibley, M. E. Thompson, S. R. Forrest, *Nature* **395**, 151-154 (1998)

[3] M. A. Baldo, D. F. O'Brien, Y. You, A. Shoustikov, S. Sibley, M. E. Thompson, S. R. Forrest, *Nature* **395**, 151-154 (1998)

[4] S. Reineke, F. Lindner, G. Schwartz, N. Seidler, K. Walzer, B. Lüssem, K. Leo, *Nature* **459**, 234-238 (2009)

[5] J. Sun, S. R. Forrest, *Journal of Applied Physics* **100**, 073106 (2006)

[6] J. Sun, S. R. Forrest, *Nature Photonics* **2**, 483-487 (2006)

[7] H.-W. Chang, Y. H. Kim, J. Lee, S. Hofmann, B. Lüssem, L. Müller-Meskamp, M. C. Gather, K. Leo,C.-C. Wu, *Organic Electronics* **15**, 1028-1034 (2014)

3.6 Tailoring nanogranular gold structures on polymer surfaces using sputter deposition

M. Schwartzkopf[1], M. Hinz[2], O. Polonskyi[2], T. Strunskus[2], F. C. Löhrer, V. Körstgens,
P. Müller-Buschbaum, F. Faupel[2], and S. V. Roth[1,3]

[1] DESY, Hamburg, Germany
[2] CAU, Kiel, Germany
[3] KTH, Stockholm, Sweden

The installation of nanogranular metal-polymer thin films plays an important role in many areas of technology and science [1]. Its range of applications stretches from organic photovoltaics [2] to sensors [3]. The most commonly used method in industry for a reproducible low-cost fabrication of such films is sputter deposition. However, for an efficient production of technological applications, high deposition rates are favored. Hence, it is very important to investigate the nanostructural evolution of such nanogranular metal-polymer thin films at different deposition rates at room temperature.

In first fundamental studies we have extensively investigated in-situ and in real-time the growth kinetics of gold nanocluster using microbeam grazing incidence small angle x-ray scattering (GISAXS) on amorphous silicon oxide substrates [4,5]. In a next step, a combined real-time monitoring of optical properties and Au growth morphologies on a polystyrene (PS) thin film during sputter deposition using GISAXS and UV-Vis Specular Reflectance Spectroscopy (SRS) was performed in situ [6]. Being very surface sensitive, these techniques facilitate in a unique way to correlate the morphological evolution of the nanostructured Au film on PS with the related optical properties, such as antireflective behavior and color changes in the UV-Vis regime during radio frequency (RF) sputter deposition. This fundamental approach using the model system Au on spin-cast PS thin films allows for tailoring the optoelectronic properties of polymer-metal interfaces.

In order to determine the role of sputter deposition rate on the growth kinetics, we combined time-resolved GISAXS with a dedicate direct current (DC)-magnetron sputter deposition chamber to explore the evolution of gold nanogranular structures on spin-casted PS thin films. The experiments were performed at the beamline P03 of the PETRA III storage ring at DESY (Hamburg, Germany) [7]. The wavelength was λ=0.095 nm at a sample-to-detector distance of 2640 mm and an incident angle of α_i=0.45°. The PILATUS 1M detector (1043x981 pixels, pixel size of $172\,\mu\mathrm{m}^2$) was used with a frame rate of 20 frames per second.

We monitored the temporal evolution of the metallic layer morphology from the submonolayer regime towards rough metal nanolayers at deposition rates ranging from 0.04 nm/s to 1.5 nm/s regarding changes in the key scattering features as a function of the effective gold layer thickness. Using an analytical geometric modeling, the average cluster radii and their center-to-center distances are quantified, which enabled the visualization of the impact of different deposition rates on the growth regimes: The increase in deposition rate affects primarily the nucleation process and the adsorption-mediated growth, whereas rather small effects on diffusion-mediated growth processes are observed. Only at higher rates, initial particle densities are higher due to an increasing influence of random nucleation, and an earlier onset of thin film percolation occurs.

Fig. 3.10a) shows the GISAXS pattern at an effective gold film thickness of around 6 nm obtained during sputter deposition at different sputter power P. The peak positions $\mathrm{q}_{\mathrm{y,max}}$ are shifted to larger values indicating a decrease in the most-prominent interparticle distance with increasing power P. At higher power, this key scattering feature is more smeared out due to earlier onset of branching and thin film percolation. Following the analysis via geometrical modeling, an increase of deposition rates leads to smaller particles in smaller distances at similar deposited Au thickness.

To summarize, we have combined time-resolved GISAXS and DC-Magnetron sputter deposition to observe the role of sputter deposition rate during the nanostructural growth of gold on PS thin films. The obtained results are discussed to identify optimized parameters for tailoring metal-polymer nanostructures for various applications, e.g. heterogeneous catalysis, organic photovoltaics and sensors, as a function of the effective layer thickness and deposition rate.

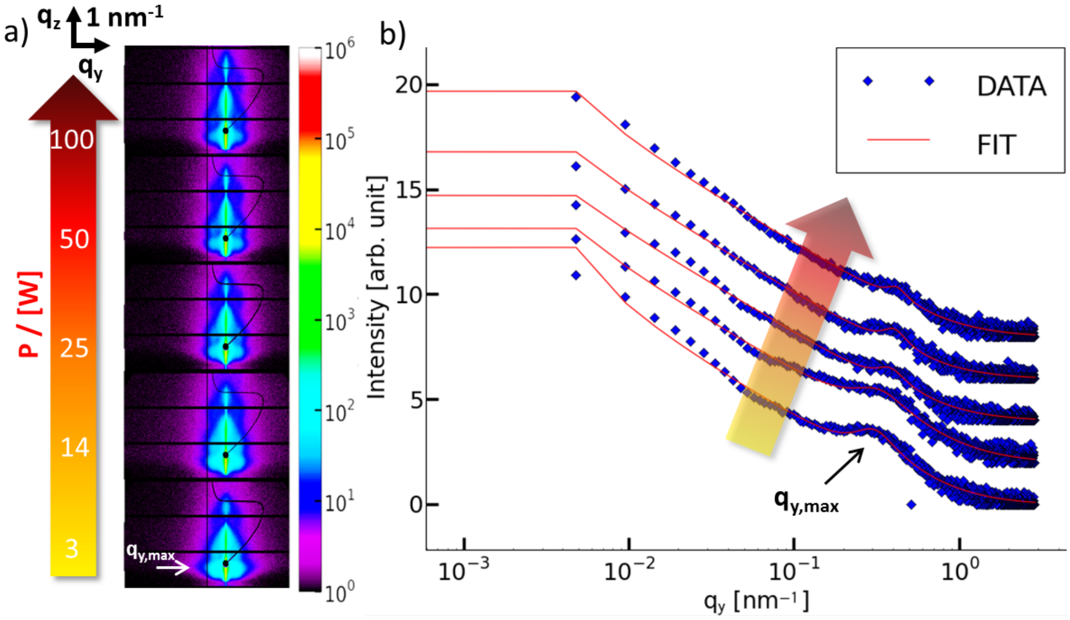

Figure 3.10:
a) GISAXS images at 6 nm effective gold layer thickness obtained during sputter deposition at different sputter power (from top to bottom: P = 100, 50, 25, 14, and 3 W respectively)
b) Corresponding averaged horizontal intensity distribution along the silicon Yoneda peak (DATA: blue diamonds) at 6 nm effective gold layer thickness obtained during sputter deposition at different sputter power (from top to bottom: P = 100, 50, 25, 14, and 3 W respectively). The corresponding fits using a superposition of Lorentzian functions (FIT: red line) are indicated.

[1] F. Faupel, V. Zaporojtschenko, T. Strunskus, M. Elbahri, *Adv. Eng. Mater.* **12**, 1177 (2010)

[2] E. Stratakis, E. Kymakis, Mater. Today 16, 133 (2013)

[3] G. Amarandei, C. O'Dwyer, A. Arshak, D. Corcoran, *ACS Appl. Mater. Interfaces* **5**, 8655 (2013)

[4] M. Schwartzkopf, S. V. Roth, Nanomaterials 6, 239 (2016)

[5] M. Schwartzkopf, A. Buffet, V. Körstgens, E. Metwalli, K. Schlage, G. Benecke, J. Perlich, M. Rawolle, A. Rothkirch, B. Heidmann, et al., *Nanoscale* **5**, 5053 (2013)

[6] M. Schwartzkopf, G. Santoro, C.J. Brett, A. Rothkirch, O. Polonskyi, A. Hinz, E. Metwalli, Y. Yao, T. Strunskus, F. Faupel, et al., *ACS Appl. Mater. Interfaces* **7**, 13547 (2015)

[7] A. Buffet, A. Rothkirch, R. Döhrmann, V. Körstgens, M. M. Abul Kashem, J. Perlich, G. Herzog, M. Schwartzkopf, R. Gehrke, P. Müller-Buschbaum, et al., *J. Synchrotron Radiat. 19*, 647 (2012)

3.7 Water-processable hybrid solar cells with a vertical compositional gradient

F. Buschek, V. Körstgens, M. Wörle[1], H. Iglev[1], R. Kienberger[1], S.V. Roth[2], P. Müller-Buschbaum

[1] LS Laser- und Röntgenphysik, TU München, Garching, Germany
[2] DESY, Hamburg, Germany

Hybrid solar cells are characterized by an active layer, which consists of an electron donating metal oxide such as titania and a light harvesting polymer as electron acceptor in a bulk heterojunction geometry. In order to create a sustainable system with low environmental impact and energy demand for production, laser ablated titanium dioxide nanoparticles and the polymer poly[3-(potassium-6-hexanoate)thiophene-2,5-diyl] (P3P6T) were successfully implemented in a completely water based treatment [1]. The usage of P3P6T, a water-soluble derivative of the well investigated polythiophene P3HT, comes with the drawback of a lower hole mobility but makes it possible to avoid organic and possibly toxic solvents. The low temperature processing begins with the laser treatment of titania nanoparticle dispersion to enhance functionalization with the polymer, which is afterwards added in form of a solution in the desired ratio. The resulting mixture is the basis for the active layer of the solar cell. To improve the photo conversion efficiency of the device the thickness of this film has to be optimized on the one hand. On the other hand a vertical concentration gradient is applied by using mixtures with varying ratios of titania and polymer. This can be done by spray coating, a technique that is especially suitable for nanoparticle dispersions. It ensures a homogeneous film and allows for a good control over the thickness by choosing the amount of solution being sprayed. For the solar cells the inverted cell geometry is used because it is possible to implement a second blocking layer to enhance charge carrier extraction and therefore improve performance.

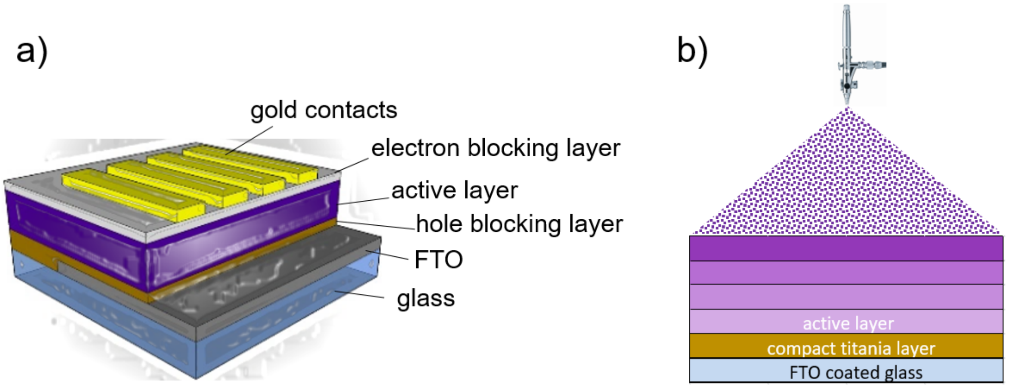

Figure 3.11:
a) Solar cell built up in inverted geometry and b) sequential spray process for the active layer consisting of four layers with different ratios between titanium dioxide and P3P6T.

The solar cell is composed of a fluorine doped tin oxide (FTO) glass substrate, a compact titania layer, the active layer, a PEDOT:PSS film and gold contacts. It is schematically depicted in Fig. 3.11a). The FTO substrate is a transparent conductive oxide and thus enables both incoming light passing through with minimal absorption and electrons being extracted. It is in a first step partially etched away with zinc and hydrochloric acid to reduce boundary effects and possible short circuits. After a 4-step cleaning process and treatment in an oxygen plasma, the compact titania layer is spin coated and calcinated. It acts as a hole blocking layer and thus prevents charge carrier recombination. A 45-minute titanium tetrachloride bath is applied to improve the contact between the dense titania layer and the nanoparticles in the active layer. The latter is deposited by spray coating and for the concentration ratio gradient the spraying process is realized through four different solutions, starting with a titania rich solution and ending with a mixture that has a higher concentration of P3P6T schematically depicted in Fig. 3.11b). The hole conducting polymer poly(3,4-ethylene dioxythiophene):poly(styrenesulfonate) (PEDOT:PSS) is selected as electron blocking layer and spray coated on top. Before and after the evaporation of gold contacts the solar cells are annealed at 120 °C to improve crystallinity of the polymers, extract solvent residues and improve the contact to the gold electrodes.

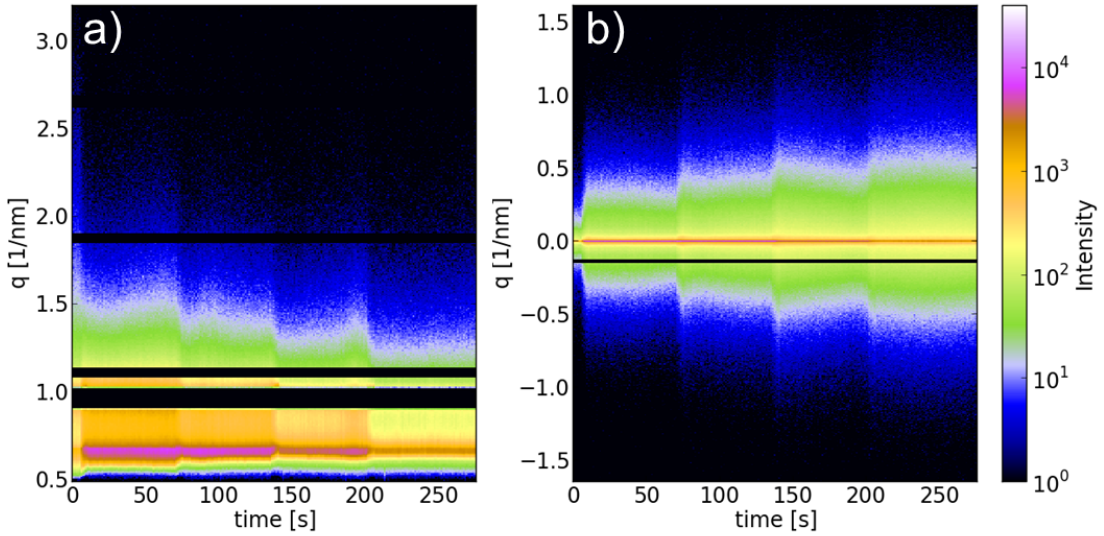

Figure 3.12:
In-situ GISAXS measurement during spray deposition of a homogeneous blend of titania and P3P6T: Evolution of a) vertical and b) horizontal cuts. The employed spray protocol is 4 sprays for 5 s with a 60 s pause in between making the spray events clearly visible in this mapping presentation.

The solar cells with the compositional gradient show a performance increase, but still suffer from low absolute photo conversion efficiencies. As the morphology and crystallinity of the active layer are crucial for the optimization of solar cells, in situ measurements were carried out at the P03 instrument at DESY, Hamburg. Grazing-incidence small angle X-ray scattering (GISAXS) at a synchrotron source is due to the high photon flux a tool with high spatial and temporal resolution and therefore allows to track changes very precisely. In order to gain insight into the formation process of domains in the bulk heterojunction, the mixture of titania and P3P6T is sprayed on a glass substrate with the hole blocking layer on top. The evolution over time of horizontal and vertical cuts during a GISAXS measurement is exemplarily shown in Fig. 3.12. The vertical cuts contain information about the structure normal to the surface like roughness and thickness whereas horizontal cuts are used to gain insight into the lateral properties such as domain sizes and spacing. Different spray protocols for a homogeneous mixture and a layer structure with four varying solutions are currently investigated and compared with regards to crystallinity and morphology.

[1] V. Körstgens, S. Pröller, T. Buchmann, D. Mosegui Gonzalez, L. Song, Y. Yao, W. Wang, J. Werhahn, G. Santoro, S. V. Roth, H. Iglev, R. Kienberger, P. Müller-Buschbaum, *Nanoscale* **7**, 2900-2904 (2015)

3.8 Investigation of the gold contact formation on water-processed hybrid solar cells by in-situ GISAXS sputter deposition

A. Haussmann, V. Körstgens, F. Löhrer, L. Bießmann, M. Wörle[1], H. Iglev[1], M. Schwartzkopf[2], A. Rothkirch[2], A. Hinz[3], O. Polonskyi[3], T. Strunskus[3], F. Faupel[3], S. V. Roth[2], R. Kienberger[1], P. Müller-Buschbaum

[1] LS Laser- und Röntgenphysik, TU München, Garching, Germany
[2] DESY, Hamburg, Germany
[3] Institut für Materialwissenschaften, CAU, Kiel, Germany

Nowadays energy is desired to be CO_2-neutral, environmental friendly and non-toxic and should be available for low-cost fabrication. To combine all these features is a great challenge and needs large effort to reach this goal. In the present work water-processed hybrid solar cells are investigated since the used polymer is non-toxic and so they combine all the above mentioned features.

While the fabrication and functionality has already been investigated by Körstgens et al. [1], especially the deposition of the gold contact on the electron blocking layer on top of the active layer is of great interest. For this purpose the gold sputter deposition is applied. The investigation is carried out by in-situ grazing incidence small angle x-ray scattering (GISAXS) gold sputter deposition and grazing incidence wide angle x-ray scattering. Afterwards different and complementary measurements as scanning electron microscopy (SEM) and x-ray reflectivity (XRR) are carried out. The used cell geometry is inverted compared to the standard cell geometry of organic solar cells. In this case two layers are of specific interest. First, the active layer consisting of laser-ablated titania nanoparticles and the water-soluble polymer poly[3-(potassium-6-hexanoate)thiophene-2,5-diyl] (P3P6T). The structure of the active layer is a bulk hetreojunction. The other layer is the electron blocking layer which is the copolymer PEDOT:PSS closest to the gold contact in actual devices. Both layers are deposited on the silicon substrate by spray coating.

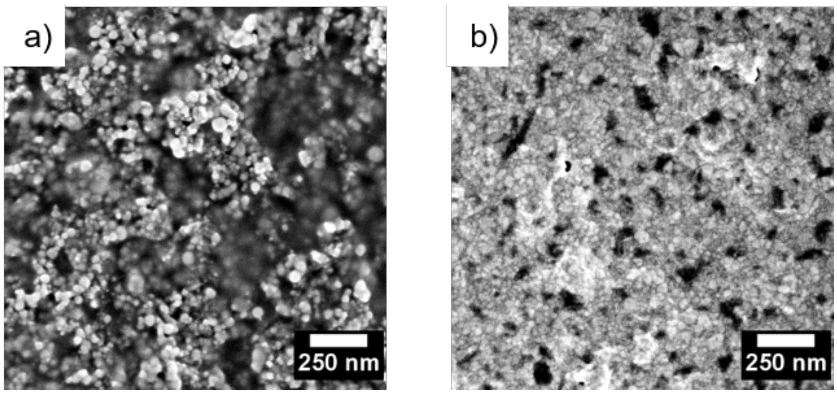

Figure 3.13:
SEM images of spray-coated active layer with PEDOT:PSS on top a) before gold sputter deposition: the spherical and clustered titania nanoparticles are clearly visible. b) After gold sputter deposition: the sample is smoother and a nanoscale structure is clearly visible.

The real-time monitoring of the gold sputter deposition is applied on the active layer, then on the electron blocking on top of the active layer, on the pure electron blocking layer and on a pure P3P6T layer. This way the influence of each individual layer of the cell geometry can be distinguished. Since especially the full cell geometry for later energy conversion is of high interest, the focus in this report will be kept on gold sputter deposition on the electron blocking layer on top of the active layer which are the relevant layers for the gold contact. The SEM images in Fig. 3.13 clearly show a difference before and after gold sputter deposition. Beforehand the mainly spherical TiO_2-nanoparticles are visible with their laser-ablated induced clustering. One gets also an idea of the high roughness of the spray-coated films. After the gold deposition the film is smoother even though it is not completely flattened out. Another recognizable feature is the nanoscale structure of the order of $5-10$ nm which can be described by the clustered growth of the gold.

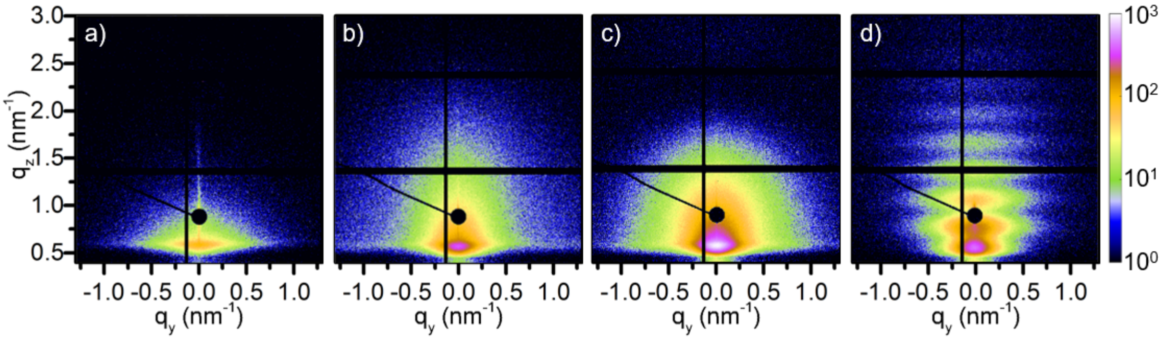

Figure 3.14:
2D GISAXS data at a) start of deposition. Here the scattering of the pure film can be seen, mainly arising from the TiO_2. b) After 6 s of deposition gold scattering is observable. c) After 12 s of deposition the scattering intensity rises isotropically. d) After 120 s of deposition the oscillations of the scattering intensity in q_z-direction due to the gold layer thickness can be seen.

In Fig. 3.14 the images obtained in the GISAXS measurement are depicted. The sputter deposition takes place in an evacuated chamber with an argon plasma. In the first detector image one can see the scattering result just from the sample without gold. Since there is titania embedded in the film the diffuse scattering is intense and makes it difficult to observe the gold side peaks at the raw detector image. The side peaks arise because of the resulting gold clusters on the sample surface and move from high q_y-values towards the center in reciprocal space meaning that the correlation distance D between the clusters increases. For an easier evaluation out-of-plane cuts at the Yoneda region are performed for every frame from which the position and the full width at half maximum (FWHM) of the side peak is determined. The FWHM gives information about the distribution of correlation distance D. The behavior of the curve is assumed to be exponential. The average layer thickness has been calculated by the XRR measurement.
To obtain the correlation distance D and size of the generated gold clusters one has to assume a model. The model Schwartzkopf et al. [2] developed could be applicable under slight modifications for the films used in this work. The original simple model assumes that the gold forms hemispherical clusters with radius R and distance D on a flat plane on which the gold cluster can diffuse and coalesce. Especially the high roughness and the presence of titania nanoparticles in the case of the investigated active layers make modifications of the geometrical model necessary. The fit of the data for gold sputtering on top of the active layer of water-processed hybrid solar cells is currently in progress.

[1] V. Körstgens, S. Pröller, T. Buchmann, D. Mosegui González, L. Song, Y. Yao, W. Wang, J. Werhahn, G. Santoro, S. V. Roth, H. Iglev, R. Kienberger, P. Müller-Buschbaum, *Nanoscale* **7**, 2900-2904 (2015)

[2] M. Schwartzkopf, A. Buffet, V. Körstgens, E. Metwalli, K. Schlage, G. Benecke, J. Perlich, M. Rawolle, A. Rothkirch, B. Heidmann, G. Herzog, P. Müller-Buschbaum, R. Röhlsberger, R. Gehrke, N. Stribeck, S. V. Roth, *Nanoscale* **5**, 5053-5062 (2013)

3.9 Nanoparticles enable polaron spin tuning in organic solar cells

D. Moseguí González, F. Dreher, P. Müller-Buschbaum

To make them competitive versus inorganic technologies, improvement of the performance of organic solar cells (OSCs) feature, amongst others, matching of the donor-acceptor (D-A) length scales in the device active layer with the mean exciton diffusion length. Excitons created in the OSCs have a limited diffusion length. They need to diffuse to a D-A interface in order to become separated charge carriers. So far, most of the strategies pursuing this aim consist of tuning the D-A morphology to make the demixing between the components intimate enough, so that most of the excitons can reach the interfaces. However, tuning the active layer morphology at nanometer length scales is technically challenging and costly. An alternative that progressively gains interest is the elongation of the exciton lifetime and, thereby, of the diffusion length.

One possibility to extend exciton diffusion lengths consists of the introduction of nanoparticles (NPs) in the OSC active layer. Orbital overlap of organic molecules with heavy metallic elements locally increase spin-orbit coupling, increasing the likelihood for excitons to transition from the singlet to the triplet spin states (Intersystem Crossing, ISC), from which the radiative recombination to the singlet ground state is less efficient. Thereby, the average exciton lifetime increases. Investigations in this sense have been performed recently, and promising results have been reported. For example, Moseguí González et.al. reported improvements of up to 11 % in efficiency upon inclusion of Fe_3O_4 NPs. [1,2]

There are further mechanisms that can lead to an enhanced ISC. The mix between exciton singlet and triplet states required for ISC can be as well achieved by Zeeman splitting, if the system is immersed in a magnetic field. Hereby, the modified active layer is locally subjected to inhomogeneous magnetic fields, due to the presence of round-shaped NPs. This induces a rotation with different Larmor frequencies for the different constituents of the exciton, ultimately forcing them to spin-rephase, i. e. to switch spin multiplicity.

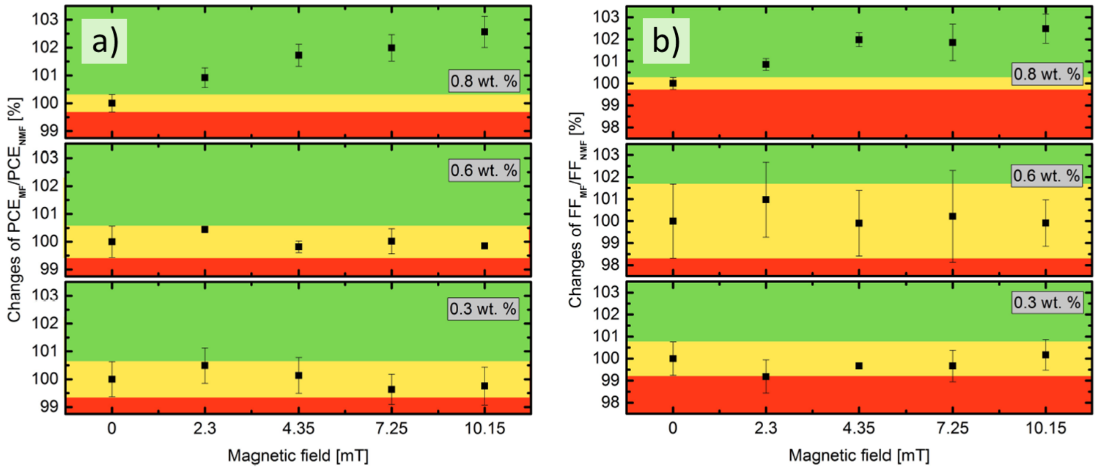

Figure 3.15:
Low magnetic field-dependence for low wt.% of Fe_3O_4 NPs of the normalized a) power conversion efficiency and b) fill factor.

Fig. 3.15 show the effect of a weak magnetic field on OSCs modified with NPs for the most beneficial concentration as determined in the absence of magnetic field. Magnitudes normalized to the performance of the cell without applied magnetic field (100%) are displayed. From the investigated samples, 0.8 wt.% of NPs showed a positive response to the magnetic stress, showing an almost linear increase in performance up to 10.15 mT, where the relative improvement topped at 2.6 %. As it happens in absence of magnetic field [2], the main driver of the improvement on PCE is the increase in fill factor (FF). Its increase, combined with the observed constant evolution of the device series and shunt resistances (not shown) lower device recombination, as it is expected from the increased ISC associated to the Zeeman splitting [3].

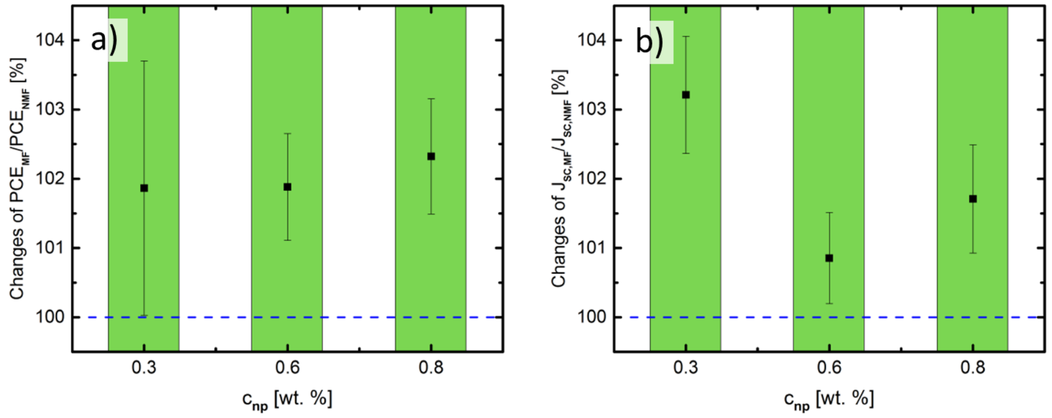

Figure 3.16:
High magnetic field-dependence for low wt.% of Fe_3O_4 NPs of the normalized a) power conversion efficiency and b) short-circuit current density.

Fig. 3.16 presents the results from preliminary experiments featuring more intense magnetic fields. In this second series of experiments, the samples were exposed to a magnetic field of around 440 mT, i.e. about 40 times stronger than in Fig 3.15. We observe as well an improvement of the PCE of around 2 %. However, in this high field regime, qualitative differences appear. Improvement in PCE appears for multiple wt.% between 0 and 0.8. In this case the device short-circuit current-density (J_{SC}) shows an improvement, whereas the correlation between PCE and FF appears less conclusive (not shown). An increase in J_{SC} is as well compatible with a decrease in device recombination. However, in light of the qualitative different behavior, further physical effects playing a role at this range of magnetic fields, like coupling with strong magnetic fields (Paschen-Back effect) or disruption of the diffusion/drift charge carrier transport processes, can so far not yet be discarded.

In conclusion, we see how the introduction of heavy metallic magnetic nanoparticles can push forward the quest for higher efficiencies in OSCs. Further research in greater detail regarding the effect of magnetic fields on OSC functioning is needed. All in all, introduction of nanoparticles feature a simple, practical and cheap approach to boost efficiencies, by-passing the expensive challenge of nanostructuring organic samples at length scales of the exciton diffusion length.

[1] W. Zhang, Y. Xu, H. Wang, C. Xu, S. Yang, *Sol. Energ. Mater. Sol. Cells* **95**, 2880-2885 (2011).

[2] D. Moseguí González, V. Körstgens, Y. Yao, L. Song, G. Santoro, S. V. Roth, P. Müller-Buschbaum, *Adv. Energ. Mater.* **5**, 1401770 (1-10) (2015).

[3] B. Qi , J. Wang , *Phys. Chem. Chem. Phys.* **15**, 8972 (2013).

3.10 Nanocrystals addition for forming polymer hybrid active layers in bulk heterojunction solar cells

W. Chen, D. Yang, P. Müller-Buschbaum

Bulk heterojunction (BHJ) organic solar cells (OSCs) are a promising technology in the photovoltaics field due to the low costs. OSCs can be fabricated by solution processing which enables rapid roll to roll printing making such production compatible with present industrial demands. As compared with heterojunction solar cells with two or more blocking layers, BHJ solar cells with a single blocking layer have many advantages, like a simplified fabrication process flow, better tunability and use of variable components for donor and acceptor parts.
During the past several years, the highest power conversion efficiencies (PCEs) of OSCs have increased only slightly from about 11 % to 12.1 % [1, 2]. Using an active layer with a ternary hybrid as components in the BHJ solar cell was realized to achieve the present champion devices. However, it appears to be increasingly difficult to further increase the PCE of OSCs following traditional approaches. The generally used fullerene acceptors have many intrinsic drawbacks, such as the difficulty to tune their energy levels, a poor visible light absorption, and an inherent tendency of easy aggregation and cluster formation. Therefore, the obvious optimization of charge transportation in the active layers appears inevitably limited from the presently used types of OSCs [3]. As a consequence, use of alternative approaches might enable a big step towards higher PCEs.

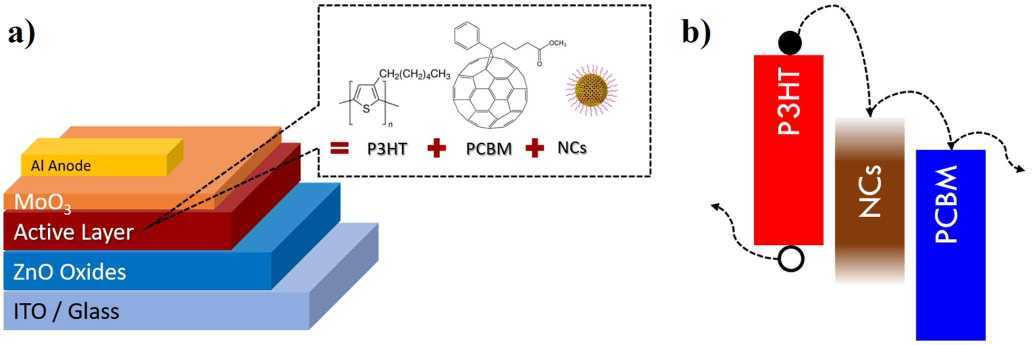

Figure 3.17:
a) Device schematic of NCs optimized OSC and b) proposed charge transportation diagram at short-circuit conditions.

Nanocrystal (NC) semiconductors, commonly with sizes of 2 to 10 nm have attracted many researches as well in the past years. The most attractive property for the NCs would be the continuously variable band gap due to the quantum size effect of binary NCs. In case of ternary NCs, besides the size effect, in most cases the band gap is also largely controlled by the metal ratio composites at the initial stage of synthesis. Due to the tunable recombination energy band gap for light emitting, the NCs have been widely used in advanced lightings and displays. Additionally, the band gap of NCs could be tuned to a specific small band gap, even less than 1.3 eV [4], which could absorb photos in all the visible range and part of near infrared area from the solar spectrum. Moreover, NCs also possess high electron mobility and very good photo- or chemical stability [5]. All these factors would be greatly beneficial for applications of NCs in solar cells.
In the present study we have introduced NC in OSCs. A small amount of oleic acid capped NCs with a band gap around 1.5 eV was mixed into a conjugated polymer: fullerene (poly(3-

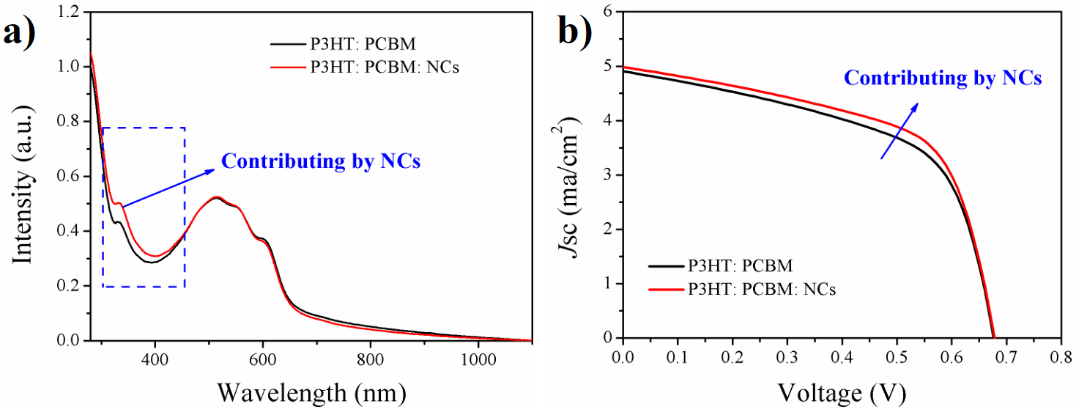

Figure 3.18:
a) Absorption spectra of active layers after annealing at 140 °C for 10 min. b) Best device performance under AM 1.5G for NCs' hybrid and regular solar cell respectively.

hexylthiophene-2,5-diyl) (P3HT): phenyl-C61-butyric acid methyl ester (PCBM)) mixture to form the active layer of OSCs. The devices were fabricated in a typical inverse architecture as depicted in Fig. 3.17a). Fig. 3.17b) provides the proposed charge transportation in the active layer with NCs'. The regular device with P3HT:PCBM as the active layer was also fabricated using same procedures to allow for comparison with the classical approach.

Samples	Jsc (cm/cm^2)	Voc (V)	FF (%)	PCE (%)
P3HT: PCBM (1)	4.91	0.66	58.00	1.87
P3HT: PCBM (2)	4.69	0.67	53.26	1.67
P3HT: PCBM (3)	4.08	0.66	54.25	1.64
P3HT: PCBM: NCs (1)	4.98	0.66	60.41	2.00
P3HT: PCBM: NCs (2)	5.18	0.66	57.56	1.96
P3HT: PCBM: NCs (3)	5.17	0.66	55.98	1.91

Figure 3.19: Device performance for all effective pixels of solar cells.

From the absorption spectra the NCs have been verified to improve the photo absorption (Fig. 3.18 a). After NCs' addition to the active layer, the short current density is improved. Moreover, the obvious improvement of the fill factor (FF) of NCs' hybrid solar cells, Fig. 3.18 b), is ascribed to the optimization of charge transportation inside the active layer. All the device performances are also given in Fig. 3.19.

[1] T. Kumari, S. M. Lee, S. -H. Kang, S. Chen, C. Yang, *Energy Environ. Sci.***10**, 258–265 (2017)

[2] D. Baran, R. S. Ashraf, D. A. Hanifi, M. Abdelsamie, N. Gasparini, J. A. Rohr, S. Holliday, A. Wadsworth, S. Lockett, M. Neophytou, C. J. Emmott, J. Nelson, C. J. Brabec, A. Amassian, A. Salleo, T. Kirchartz, J. R. Durrant, I. McCulloch, *Nat. Mater.***16**, 363—369 (2017)

[3] Y. Yang, Z. G. Zhang, H. Bin, S. Chen, L. Gao, L. Xue, C. Yang, Y. Li, *J. Am. Chem. Soc.* **138**, 15011-15018 (2016)

[4] X. Lan, O. Voznyy, F. P. Garcia de Arquer, M. Liu, J. Xu, A. H. Proppe, G. Walters, F. Fan, H. Tan, M. Liu, Z. Yang, S. Hoogland, E. H. Sargent, *Nano. Lett.* **16**, 4630–4634 (2016)

[5] S. Ren, L. Y. Chang, S. K. Lim, J. Zhao, M. Smith, N. Zhao, V. Bulovic, M. Bawendi, S. Gradecak, *Nano. Lett.* **11**, 3998–4002 (2011)

4 Polymer-hybrid systems

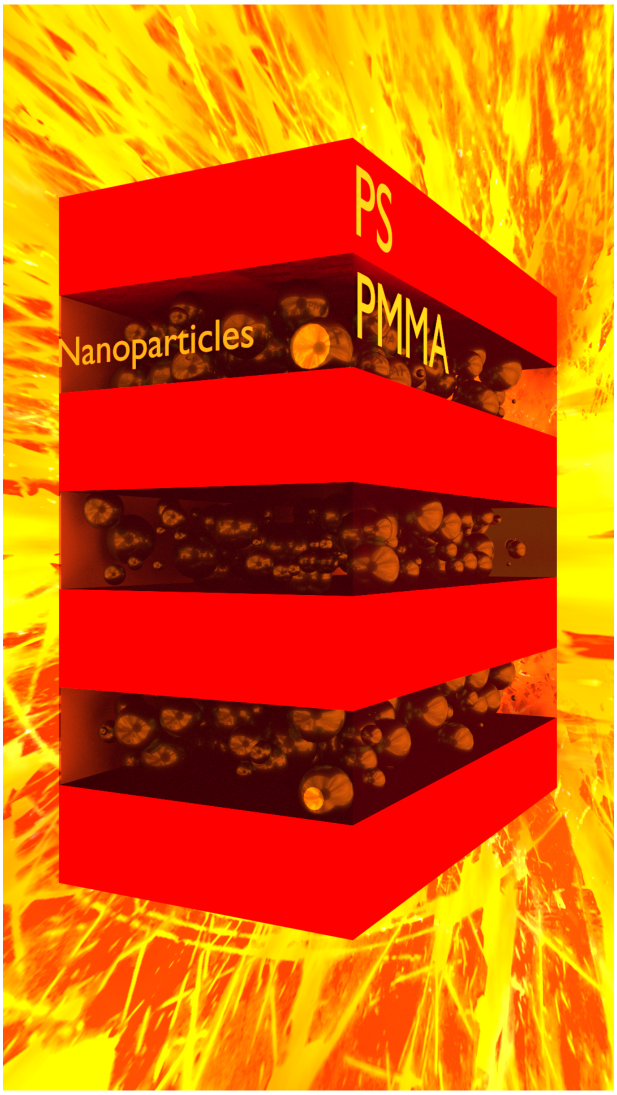

4.1 Investigation of novel materials for hybrid photovoltaic applications using sol-gel chemistry for mesoscale-structural control

N. Hohn, W. Ohm[1], M. Boone[2], E. Rivard[2], S. V. Roth[1], P. Müller-Buschbaum

[1] DESY, Hamburg, Germany
[2] Department of Chemistry, Edmonton, Canada

Within the frame of the present work novel materials for hybrid photovoltaic (HPV) applications are characterized with regard to their suitability for HPV. Whereas organic materials have been found to offer various, promising advantages for HPV like flexibility and the potential of low-cost and large scale production, inorganic materials are equally important. Through a hybrid approach the chemical and physical stability of the inorganic part is added to the material system and, thus, addressing the major issue of limited lifetimes in purely organic solar cells (OPV). Thereby, the inorganic material acts as a framework inhibiting structural degradation and enhancing HPV lifetime stability, which usually is a big issue in OPV research. Nevertheless, the inorganic component must fulfill several conditions to be suitable for a HPV device. Primarily, the possibility of infiltrating the layer with an organic counterpart must be assured.

Poly(styrene-block-ethylene oxide) templated sol-gel chemistry is used to synthesize high surface-to-volume ratio, mesoporous titania thin films based on the precursor titanium(IV) isopropoxide (TTIP). This approach allows for precise structure control and an increased amount of interface [1,2]. The n-type, electron conducting titania thin film serves as a basis for novel organic material studies [3]. Furthermore, the foam-like network structure is supposed to facilitate the backfilling process. As a consequence, the studies aim to introduce new material combinations to the field of HPV and to open up pathways for enhanced efficiency in terms of energy conversion and band alignment.

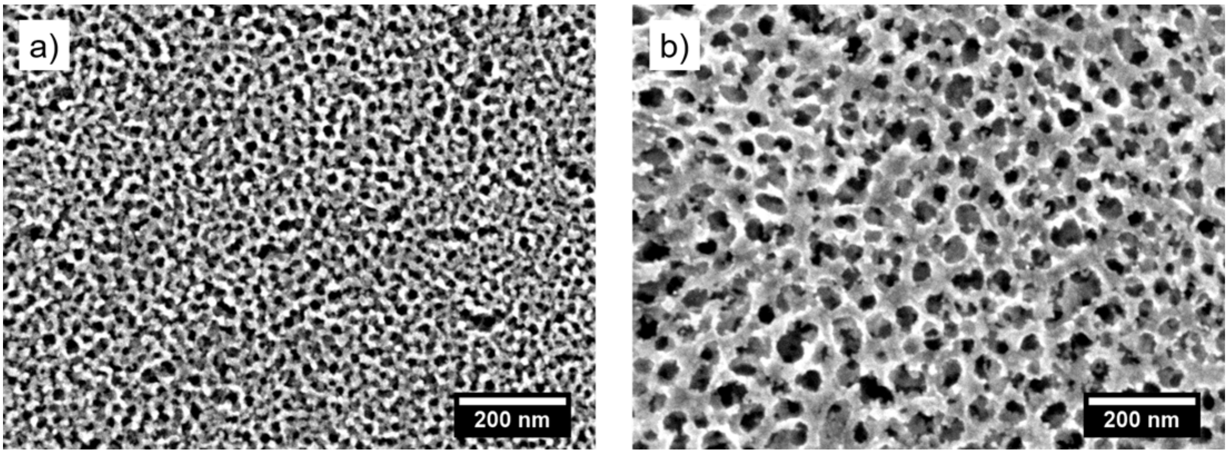

Figure 4.1:
Scanning electron microscopy images of mesoporous titania thin films synthesized via block copolymer templated sol-gel chemistry using different block lengths of the polymer template. Changes in pore sizes by a factor of 3 are clearly visible for the smaller pores in a) and the larger pores in b).

Following this approach mesoporous titania films of tuned pore sizes are synthesized via changing the block lengths of the respective block copolymer template. Surface investigation with scanning electron microscopy (SEM) shows a foam-like network of crystalline titania with different pore sizes (Fig. 4.1). Tuning the pore sizes is especially important when, later on aiming for high degrees of backfilling with an organic counterpart. The successfully fabricated thin titania films are supposed to result in different degrees of backfilling due to a difference of factor 3 in their pore size. Furthermore, the foam-like network character of the crafted films is very well visible, which enhances their suitability for HPV applications and successful backfilling.

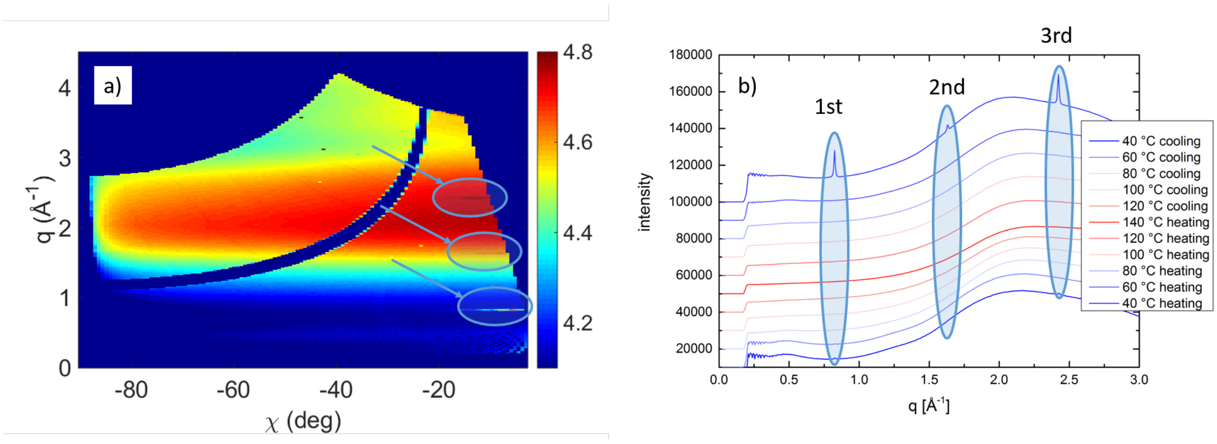

Figure 4.2:
a) Exemplary 2D GIWAXS data and b) temperature dependent q-cuts obtained at the beamline PO3, DESY, indicate recrystallization of a small molecule (TPA_4) thin film after heating to 140 °C and cooling back down to room temperature.

Addressing the organic side of HPV novel, custom-made small molecules are analyzed with regard to their photovoltaic potential. Thin films of these tellurium based triarylamines molecules (TPA_4) are spin-coated and the crystalline behavior is observed by grazing-incidence small angle X-ray scattering (GIWAXS) at the beamline PO3 at the DESY in Hamburg. The advantage of this technique is the almost non-destructive character combined with goods statistics due to the small incident angle and the high flux at the beamline. In figure 4.2 an exemplary corrected GIWAXS image on a Pilatus 300K is shown. In 20 °C steps images are taken starting from room temperature, heating to 140 °C and cooling down to room temperature again. Initial peaks in intensity disappear upon temperature increase and reappear after cooling down with increased intensity. Thereby, we could successfully observe disordering of small molecule domains as well as their rearrangement forming domains of enhanced ordering.

Thus, the influence of sample annealing on the novel molecule TPA_4 could be simulated and found beneficial for potential HPV application due to enhanced crystallinity after annealing at 140 °C. Furthermore, the small size of the molecule itself makes it an especially promising candidate for HPV, since backfilling is supposed to be much more efficient compared to the commonly employed P3HT.

[1] Y. Cheng, J. S. Gutmann., *JACS*, **128.14**, 4658-4674 (2006)

[2] K. V. Peinemann, V. Abetz, S. Peter, *Nat Mater*, **6.12**, 992-996 (2007)

[3] M. Rawolle, M. A. Niedermeier, G. Kaune, J. Perlich, P. Lellig, M. Memesa, P. Müller-Buschbaum, *Chem Soc Rev*, **41.15**, 5131-5142 (2012)

4.2 On the chemical origins of crystalline preferred orientations in hybrid organometallic lead halide perovskite thin films

S. Pratap, J. Schlipf, P. Müller-Buschbaum

Solar cells based on organometallic lead halide perovskites have established themselves as a promising alternative to commercial thin film solar cells. The crystallographic versatility of the material allows the possibility of extensive chemical tuning, which manifests in the material as a spectra of properties that may be obtained. This entices research on hybrid perovskite structures combining different organic and inorganic groups into a crystalline framework.

Remarkably, diverse routes of fabrication may be employed for the preparation of such perovskite thin films, with the processing techniques and parameters affecting final film morphology [1]. In order to achieve controlled composition of hybrid perovskites, a one-step method employing precisely engineered precursors with calculated stoichiometries of the required components were utilized for spin-coating thin films onto disordered mesoporous titania substrates. Systems based on mixed perovskite $(MAPbBr_3)_x(FAPbI_3)_{1-x}$ and mixed halide $(MAPbBr_3)_x(MAPbI_3)_{1-x}$ were methodically investigated, with x = 0, 0.15, 0.50, 0.85, 1.

Hybrid perovskite systems were demonstrated wherein the individual components reacted with each other at an atomistic scale in order to give rise to a new structure, much alike in a solid solution, as verified by x-ray diffraction. Prominently, all mixture ratios exhibited distinct reflexes in XRD as compared to their precursors or pure perovskite species, with some systems demonstrating poor crystallinity as compared to others (especially in mixed halide perovskites). There was a linear decrease in the lattice parameter of hybrid perovskites with increase in bromide content for both mixed halide and mixed perovskite systems.

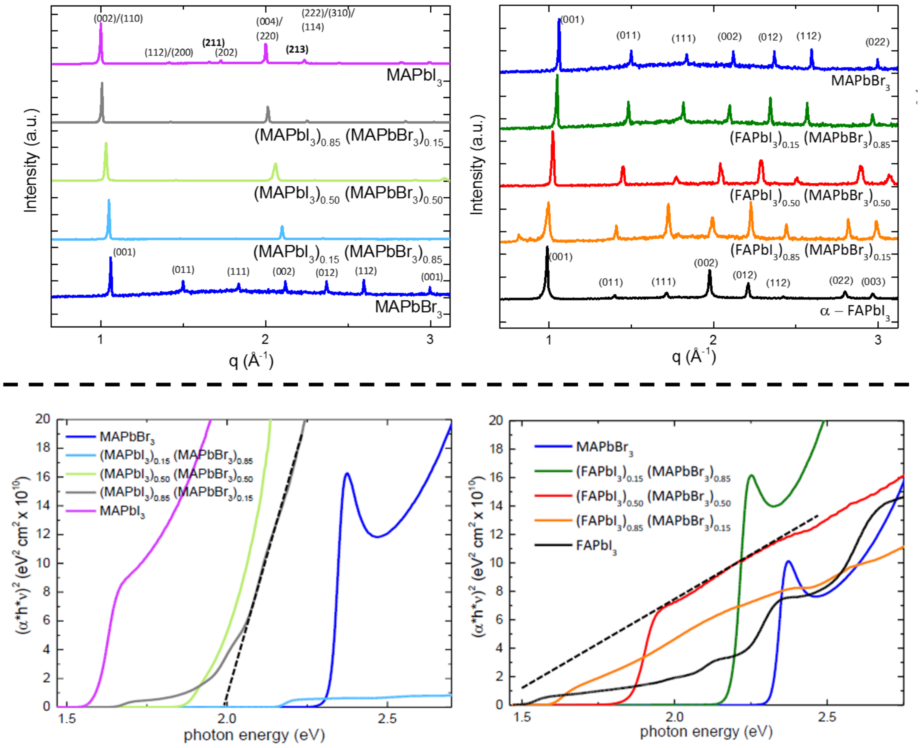

Figure 4.3:
X-ray diffraction patterns (top panel) and Tauc-plots (bottom panel) of mixed halide (left) and mixed perovskite systems (right) alongside plots displaying the linear relationships between composition and lattice parameters, band gaps extracted from XRD, UV-vis data.

In order to probe the photoactive nature of the materials, UV-vis spectroscopy was carried out on perovskite thin films. To gauge the nature of the band gap, Tauc-plots were analyzed, which suggested that optical transitions near the band edge had a predominantly direct nature. Additionally, the investigation exhibited signatures suggesting contributions from other, possibly non-direct optical transitions. A linear trend in the change of band gaps was observed with change in composition with pure iodide systems displaying smaller band gaps as compared to bromide counterparts.

Film morphology of perovskite systems fabricated through the one-step method of deposition of precursors, with rapid crystallization aided by means of an antisolvent was studied. No specific preferred orientations in films was expected owing to the presence of the disordered mesoporous titania matrix and the methodology of deposition, but curiously, films even though formed by fast-crystallization during spin-coating exhibited distinctly diverse morphologies, studied by SEM and grazing incidence wide angle x-ray scattering (GIWAXS). Preferential orientations of the crystalline hybrid perovskites were probed and correlated to the film's morphological and chemical characteristics by GIWAXS. Remarkably, perovskite thin films prepared by the same methodologies displayed varying behaviors of preferred orientations, as their chemical composition was varied.

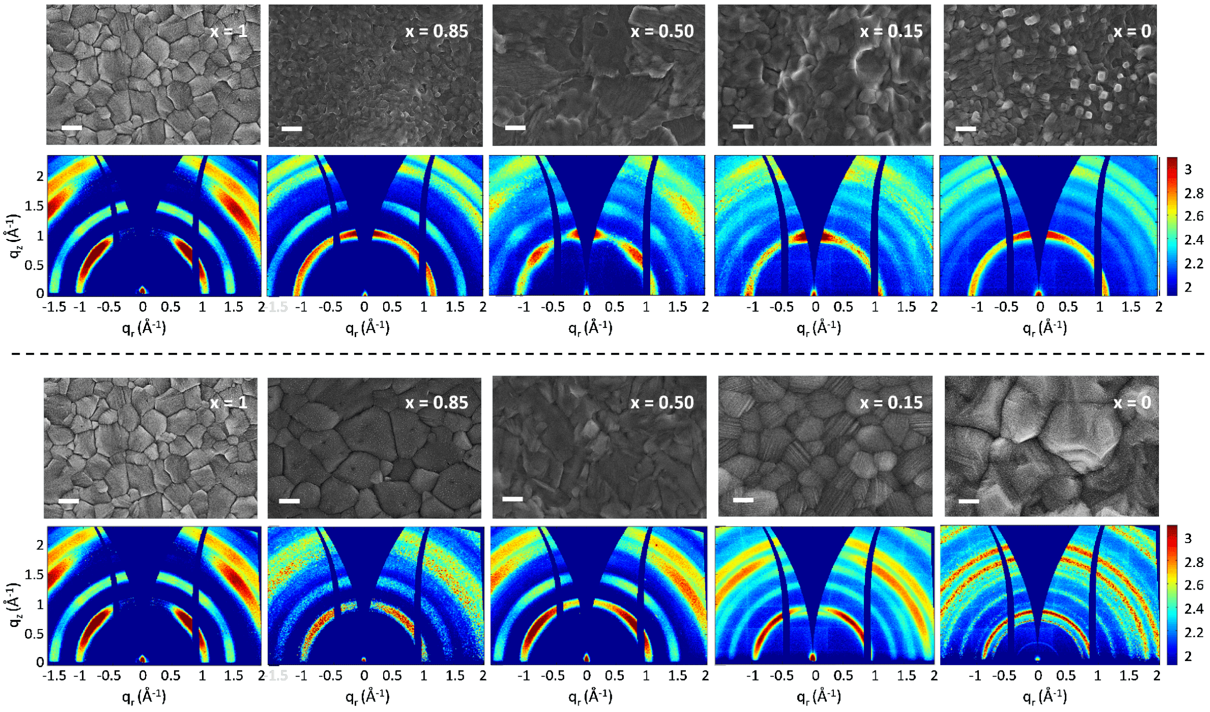

Figure 4.4:
SEM images and corresponding 2D GIWAXS patterns of mixed halide $(MAPbBr_3)_x(MAPbI_3)_{1-x}$ perovskites (top) and mixed perovskites $(MAPbBr_3)_x(FAPbI_3)_{1-x}$ (bottom). Scale-bar on SEM images corresponds to lengthscales of 200 nm.

Although it is well known that crystalline preferred orientations of materials may be varied by employing different routes of fabrication, these results strongly suggest that crystalline orientations also have a chemical origin. Thus, for the first time it is possible to propose controlling morphology and crystallinity of spin-coated thin films by tuning the ingredients of and the treatment of the chemical precursor solution used for spin coating.

[1] L. Oesinghaus, J. Schlipf, N. Giesbrecht, L. Song, Y. Hu, T. Bein, P. Docampo, P. Müller-Buschbaum, *Adv. Mater. Interfaces* **3**, 1600403 (2016)

4.3 Morphological evolution in mixed dimensional perovskite thin films - a grazing incidence scattering study

R. Wang[1], K. Wang, E. Kentzinger[2], H. Frielinghaus[1], P. Müller-Buschbaum

[1] MLZ, Garching, Germany
[2] JCNS, Jülich, Germany

Lead halide hybrid perovskite materials have undergone extraordinary evolution in the last five years. Benefit by its intrinsic advantageous of large absorption coefficienct and long charge carrier diffusion length, perovskite based solar cells have achieved a best record power conversion efficiency (PCE) over 22%.[1] Notablly, three-dimensional (3D) perovskite frameworks can be synthetically altered into two-dimensional (2D) structures by using long organic cation to replace small organic cation. At the opposite quadrant, the in-built quantum well structure in 2D perovskite generates large exciton binding energy, quantum confinement phenomenon and energy transfer in between quantum wells, all expanding the versatility of perovskite materials into light-emitting and laser applications.[2] However, the formation of these low dimensional structures are still not well understood. In this report, we combined surface imaging technique with advance scattering methods to achieve a deep understanding about the structure formation in mixed dimensional perovskite thin films.

In the present work, a long organic molecule octylammonium bromide (OABr) was used to retard the 3D $CH_3NH_3PbBr_3$ perovskite frameworks built-up. Due to OABr's inherent large size, it can not diffuse into the $PbBr_2$ matrix but dangle outside the crystal. Therefore, the crystal growth in three dimensionals is retarded with 2D cyrstallites generation. Samples were prepared by varying OABr content and named as PeOA10 (10 wt%), PeOA20 (20 wt%) and PeOA40 (40 wt%).

Figure 4.5 a-c show the surface morphology of the resulting samples. Remarkable differences are revealed. Sample PeOA10 contains large uniform domains on the fractions of tens micrometer scale. The film surface is well-covered without any distinct gap at this probing length. The averaged domain size decreases with the increasing of OABr content. At the largest OABr content of 40%, gaps emerge on the surface and stacking layer structures are likely formed, which suggesting the existence of 2D perovskite in the sample. In order to investigate the morphology evolution in a more statistical view, all samples were probed by grazing incidence wide/small angle X-ray scattering (GIWAXS/GISAXS).

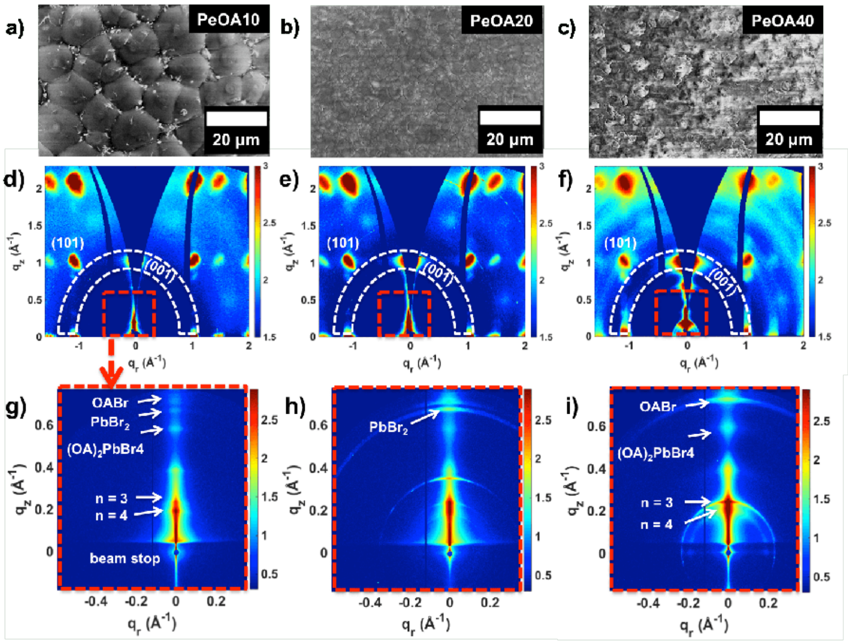

Figure 4.5: Scanning electron microscopy (SEM) images of mixed dimensional perovskite thin films with varying OABr content: a) 10 wt% (PeOA10), b) 20 wt% (PeOA20) and c) 40 wt% (PeOA40). GIWAXS data (d-f) and GISAXS data (g-i) for the resulting perovskite films with OABr content: d,g) 10 wt%, e,h) 20 wt% and f,i) 40 wt%, respectively.

GIWAXS/GISAXS data measured under a constant incidence angle of 0.4° are shown in Figure 4.5 d-i. The obtained results are analyzed from larger q value ($q > 1\mathring{A}^{-1}$) down to the smaller

q region ($q < 1Å^{-1}$), corresponding to the information of 3D bulk $CH_3NH_3PbBr_3$ crystal and 2D perovskite crystallites. In the 2D GIWAXS results, firstly, in the absence of a homogeneous Debye-Scherrer ring, distinct intensive Bragg peaks are revealed for all three samples. This feature suggests that the 3D perovskite crystals adopt a well-ordered face-on orientation on the deposited substrate. In the second place, the scattering intensities $q < 1Å^{-1}$ increases with loading higher content of OABr, which resulted from the larger population of 2D crystallites in the sample.
Further understanding of the origin of these sacttering patterns are done through GISAXS data analysis. In Figure 4.5 g-i), the GISAXS scattering patterns are dominated by five distinct peaks. Transforming the obtained reciprocal peak positions into real space d-spacings, the five peaks can be assigned to perovskite 2D platelets with unit cell thickness (n) of 4 ($q_z = 0.19Å^{-1}$) and 3 ($q_z = 0.23Å^{-1}$), the single lead bromide 2D layer $(OA)_2PbBr_4$ (q_z = 0.59 $Å^{-1}$) and the crystallized precursors $PbBr_2$ ($q_z = 0.67Å^{-1}$) and OABr ($q_z = 0.77Å^{-1}$). In sample PeOA10, both 2D crystallites and precursors are highly orientated parallel to the substrate surface, which is identical to 3D bulk MAPbBr3 crystals. In contrast, additional varied intensities emerged depending on the azimuthal angle at higher OABr content. For sample contains the highest OABr content (PeOA40), azimuthal intensity rings appear for both perovskite 2D platelets and OABr.

Further investigation are carried out by azimuthal integration around q = 0.77 $Å^{-1}$and q = 0.23 $Å^{-1}$, corresponding to the respective diffraction rings of OABr and 2d platelets (n = 4). An azimuthal integration is also performed for 3D perovskite (001) reflection peak for an overall comparison. The obtained results are shown in Figure 4.6. The integrated intensity profiles show all three kinds of crystals are highly oriented parallel to substrate in sample PeOA10. Upon further loading the OABr content, additional strong preferential orientation at $\chi <$ -10° start to appear. Considering the fact that the bigger organic molecule OABr can not diffuse into the $PbBr_4$ layer, the obtained results reflect that both 3D and 2D perovskite crystals reoriented alongside the OABr crystallites. This result in turn approves the SEM observation. In sample PeOA10, the out-of-plane oriented OABr suppresses the buildup of perovskite crystal framworks in surface normal direction and leading the formation of a full surface coverage with large grain size. On the other hand, the OABr random orientation offer more channels for precursors intercalation, that resulting an isotropic perovskite crystals orientation. A schematic illustration is listed in Figure 4.6 d.

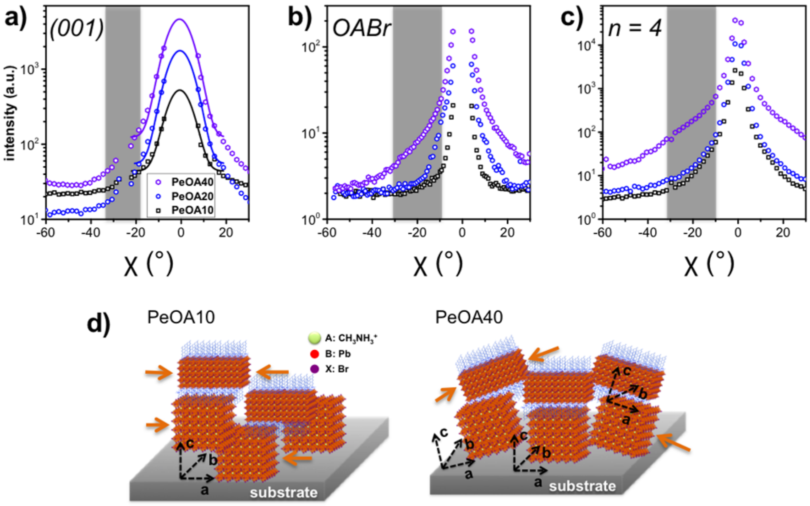

Figure 4.6:
Azimuthal integration results of a) 3D perovskite (001) reflection plane, b) OABr crystallites and c) 2D perovskite crystallites with four unit cells thickness. d) Schematic illustration for the morpholgy evolution in the mixed dimensional perovskite films.

[1] NREL, $http://www.nrel.gov/ncpv/images/efficiency_chart.jpg$ (2016)

[2] S. A. Veldhuis, P. A. Boix, N. Yantara, M. Li, T. C. Sum, N. Mathews, S. G. Mhaisalkar, *Adv. Mater.* **28**, 6804-6834 (2016)

4.4 The origin of crystal orientation in hybrid perovskite thin films for photovoltaic application

J. Schlipf, L. Oesinghaus, N. Giesbrecht[1], L. Song, Y. Hu[1], T. Bein[1], P. Docampo[2], P. Müller-Buschbaum

[1] Department of Chemistry and CeNS, LMU, Munich, Germany
[2] Newcastle University, Newcastle upon Tyne, UK

In recent years, perovskite solar cells based on methylammonium lead iodide (MAPI) have raised attention due to a rapid increase in power conversion efficiencies that crossed the 20 % mark in 2016. This high performance is possible due to the favorable material properties of MAPI, such as high crystallinity and a direct band gap that leads to a high absorption coefficient reminiscent of GaAs. The combination of potentially cheap production based on solution processing, the abundancy of precursor materials, and their potential environmental sustainability, makes perovskite solar cells a promising challenger to existing solar cell technologies. However, control over film morphology is crucial in order to achieve reproducible photovoltaic performance. Hybrid perovskite thin films are typically prepared by combining lead salts such as lead iodide (PbI_2) with organic cations like methylammonium iodide (MAI) or methylammonium chloride (MACl). Deposition techniques can be classified into two categories, namely 1-step methods, in which the precursors are mixed in the same solution with a common solvent, and 2-step methods, in which the precursors are applied sequentially. The choice of fabrication method is inherently linked to the morphology of the perovskite film and the performance of photovoltaic devices.

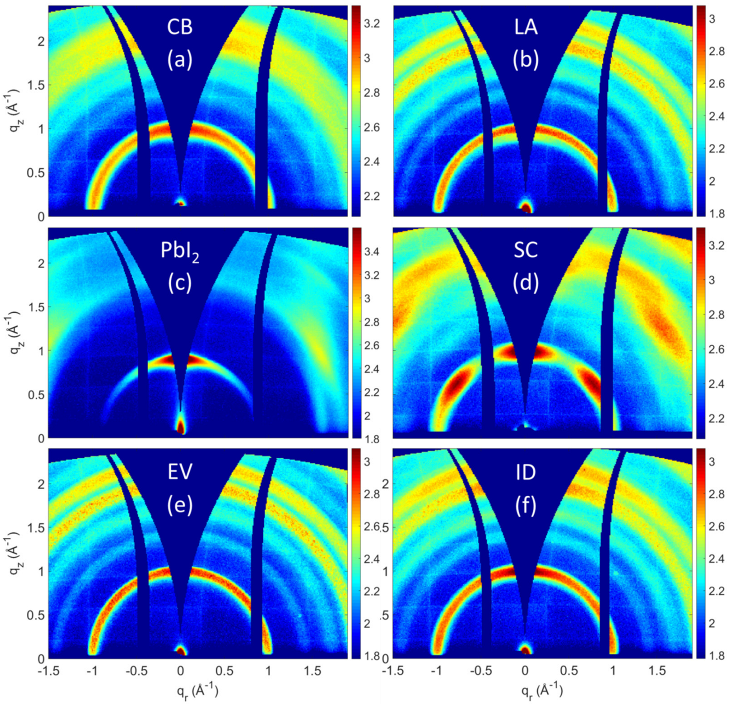

Figure 4.7:
GIWAXS data of five seminal perovskite thin film fabrication methods: 1-step methods with (a) anti-solvent drop (CB) and (b) lead acetate precursor (LA). 2-step methods starting from a PbI_2 film (c) being converted to perovskite by (d) conversion in solution (SC), (e) organic vapor (EV) or (f) interdiffusion (ID). The crystals in the films fabricated with 1-step methods showed slight preference for being oriented with (002) planes parallel to the substrate while the 2-step methods show qualitatively very different crystal orientations depending on the conversion method which suggests a link between conversion mechanism and crystal orientation.[1]

We compared five seminal fabrication methods (two 1-step and three 2-step methods) all of which have reached good device efficiencies.[1] The 1-step methods were using either lead acetate (LA) or PbI_2 as lead source, while in the latter case crystallization is induced by dripping the anti-solvent chlorobenzene onto the spinning sample (CB). The 2-step methods employed a PbI_2 film deposited at an elevated temperature, which resulted in a porous, crystalline film, that was subsequently transformed into perovskite by a dip in a mixed solution of MAI:MACl

(SC), MAI vapor (EV) or slow interdiffusion of a spin-cast solution of MAI (ID). Scanning electron microscopy (SEM) revealed very different surface morphologies. In order to gain insight into the inner structure of the films we performed grazing-incidence wide angle X-ray scattering (GIWAXS). In addition to the microstructural differences found by SEM, the films showed various degrees of preferential crystal orientations (see Fig. 4.7). The crystals in the films fabricated with 1-step methods showed slight preference for being oriented with (002) planes parallel to the substrate where crystallization starts due to oversaturation of the precursor solution and precipitation of the ionic precursors. On the other hand, the 2-step methods show qualitatively very different crystal orientations depending on the conversion method, in spite of being derived from the same PbI_2 precursor layer. This suggests that the conversion mechanisms have to be different and that certain orientations might be associated with them.

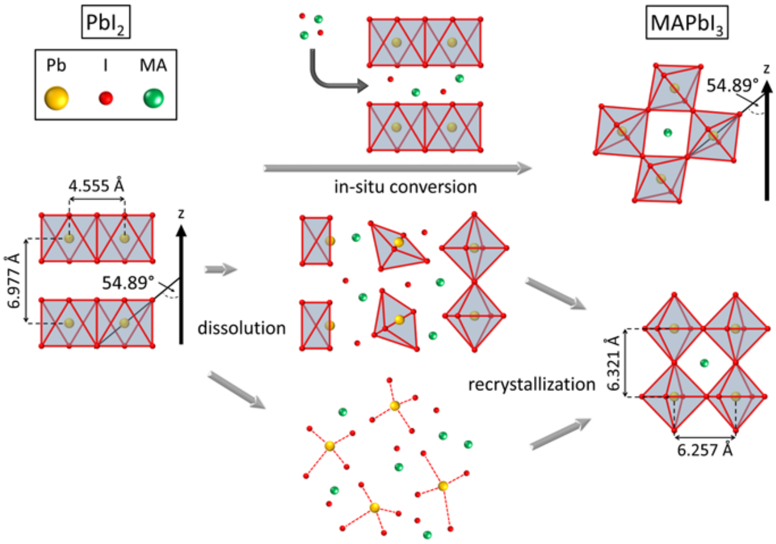

Figure 4.8:
Schematic representation of the two competing conversion mechanisms present in the SC method. In-situ conversion is dominant at low ion concentrations, e.g. in the bulk of the film, and the structure and orientation of the PbI_2 crystals are preserved. At higher ion concentrations, e.g. on the film surface, the reaction rates are higher which leads to a dissolution of PbI_2 crystals and recrystallization of MAPI in thermodynamically favorable morphologies.[1]

While the EV and ID methods likely are linked to a solid state transformation, the mechanisms in the SC method are happening in solution which leads to two preferential orientations. In an earlier study an analysis of GISAXS measurements of a PbI_2 and a MAPI film suggested a laterally confined crystal growth in the bulk of the film.[2] Due to the volume expansion associated with the different distances of neighboring Pb^{2+} ions in the perovskite, this leads to strain and breakage of crystals. Still, this in-situ conversion process mostly preserves the initial PbI_2 morphology, especially the crystal orientation. As PbI_2 is highly oriented (cf. Fig. 4.7c), this leads to perovskite crystals being tilted at an angle of roughly 55° as depicted in Fig. 4.8 which gives rise to the side peaks in Fig. 4.7d. On the surface, however, one observes cuboid-shaped, micron-sized crystals. Those are formed by dissolution of the PbI_2 crystals due to the higher ion concentration and associated higher reaction rates and subsequent recrystallization in thermodynamically favorable shapes and either random or (002) orientation similar to 1-step methods. Smaller crystals on the surface merge with larger ones by Ostwald ripening which is in agreement with our earlier GISAXS study.[2] As the dissolution of PbI_2 is stronger at the presence of Cl^- ions, this second process leads to the strong middle peak in Fig. 4.7d. The porosity of the PbI_2 film mitigates the effects of the volume expansion and leads to a higher contact area with the conversion solution.[1] Thus, the crystal morphology of MAPI films can be controlled by tuning PbI_2 film porosity and the composition of the conversion solution.

[1] L. Oesinghaus, J. Schlipf, N. Giesbrecht, L. Song, Y. Hu, T. Bein, P. Docampo, P. Müller-Buschbaum, *Adv. Mater. Interfaces* **3**, 1600403 (2016)

[2] J. Schlipf, P. Docampo, C. J. Schaffer, V. Körstgens, L. Bießmann, F. Hanusch, N. Giesbrecht, S. Bernstorff, T. Bein, P. Müller-Buschbaum, *J. Phys. Chem. Lett.* **6**, 1265 (2015)

4.5 Influence of processing parameters on the morphology of perovskite solar cells

A. Schreiber, J. Schlipf, P. Müller-Buschbaum

Over the last decade, especially lead halide perovskites as an organic-inorganic hybrid compound received attention due to the exceptional rise in the power conversion efficiency (PCE) of research solar cells to more than 20 % in early 2016. This vast increase efficiency creates the demand for easily producible perovskite solar cells for commercial purposes as this technology promises low production cost compared to e.g. silicon photovoltaics. The most common active layer material is methylammonium lead iodide ($MAPbI_3$). It can be fabricated using a solution conversion method consisting of firstly spin-coating lead iodide (PbI_2) and secondly immersing it in a solution of methylammonium iodide in 2-propanol. This leads to strong preferential crystal orientations as evidenced by grazing-incidence small angle X-ray scattering (GIWAXS) measurements. The crystal orientation is tunable via temperature variation of precursors of the perovskite and the use of additives into the precursor or conversion solution [1]. We expand this study by the use of mixed solvent approaches with processing additives in order to further tune the time scales of the crystallization processes and gain more control of the film morphologies of perovskite thin films as well as improving the reproducibility and long-term stability.
Since we chose a 2-step solution conversion method, we started to modify the fabrication of the lead iodide precursor. As a reference we chose a 0.85 M lead iodide solution in dimethyl formamide (DMF) for spin-coating. For the mixed solvent approach we prepared a blend of DMF and dimethyl sulfoxide (DMSO) in a volume ratio of four parts DMF to one part DMSO. As an additive we chose 0.13 M methylammonium iodide (MAI) for both solution variations. After spin-coating all four solutions on cleaned glass substrates at a temperature of 60 °C, we investigated the films with GIWAXS to observe influences on the morphology (figure 4.9).

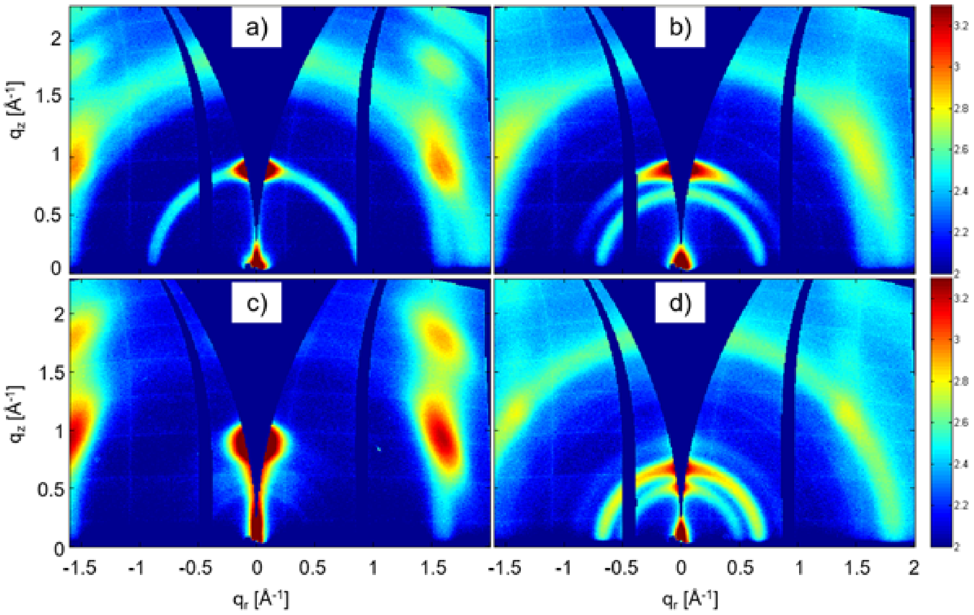

Figure 4.9:
GIWAXS images of lead iodide films: a) lead iodide in DMF b) in mixed solvent DMF + DMSO c) film a) with MAI additive d) film b) with MAI additive

As one can see in figure 4.9, the lead iodide film a) shows a strong preferential (001) orientation at $q = 0.895$ Å^{-1} while the mixed solvent film b) shows a broader peak at the same position being less oriented and additionally a ring at $q = 0.692$ Å^{-1} which is amorphous. The amorphous ring is likely caused by a complex of remnant DMSO and PbI_2 in the film with a bigger lattice constant of 9.11 Å.

The lead iodide film with MAI additive (cf. figure 4.9 c) is highly oriented with a peak at q = 0.874 $Å^{-1}$ while an amorphous ring is completely absent. The corresponding X-ray diffraction (XRD) data indicates rather a combination of two peaks at q values of 0.836 $Å^{-1}$ and 0.907 $Å^{-1}$ instead of one which is very broad in the q_z direction. The combination of mixed solvents and the additive can be seen in subfigure d) where the pure lead iodide ring (001) is only faintly visible and two additional rings at smaller q values (0.674 $Å^{-1}$ and 0.503 $Å^{-1}$) appear. Both show a preferential orientation in the same direction as the lead iodide ring combined with an amorphous ring. This is hypothesized to be caused by PbI_2-DMSO-MAI intermediate phase [2]. The GIWAXS measurement of the mixed solvent film (shown in figure 4.9 b) states the coexistence of a lead iodide and a DMSO-PbI_2 phase, which can either be caused by a low DMSO content preventing a pure PbI_2-DMSO complex film or DMSO evaporating out of the film. To investigate the timescale of this evaporation, we conducted transmission UV-VIS measurements (300 - 850 nm) to observe optical changes over time in all four films. This timescale can be crucial for the conversion to the perovskite film in the second step.

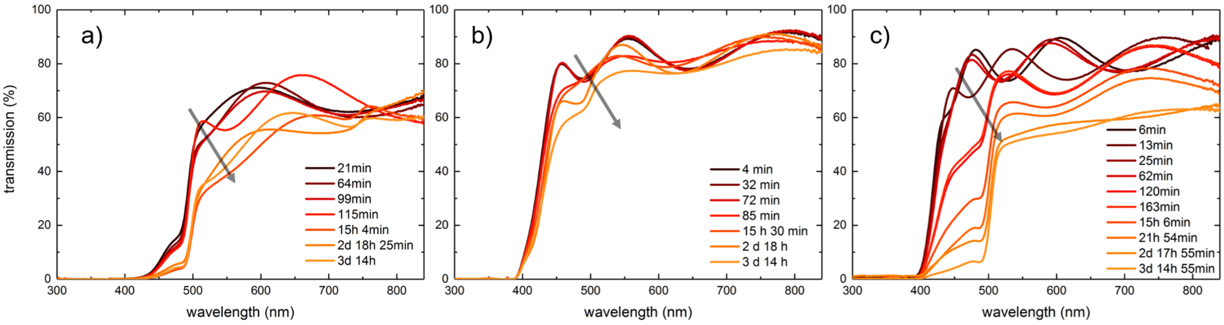

Figure 4.10:
Temporal evolution of UV-VIS spectra of lead iodide films where the semitransparent arrow indicates the time evolution trend for PbI_2 in a) DMF with MAI additive, b) mixed solvent DMF + DMSO, c) combination of mixed solvent DMF + DMSO and MAI additive

As seen in figure 4.10 a drastic change in the bandgap and optical transmission occurs after around 15 h in the film containing MAI additive and for the mixed solvent including MAI additive after approximately 2.5 h to 15 h. The spectra shown in figure 4.10 a and c (DMF with MAI additive a and combination of mixed solvent DMF + DMSO and MAI additive) approach towards a transmission curve typical for a pure reference PbI_2-film (not shown) while the film produced from a combination of mixed solvent DMF + DMSO and MAI additive even reaches this state after approximately 3.5 days. Thus, the methylammonium iodide additive and the DMSO slowly evaporate out leaving a film of crystalline lead iodide behind. In subfigure b) the mixed solvent film shows a good stability against ambient conditions even after 3 days compared to the films containing MAI.

In conclusion the DMSO and MAI containing lead iodide films should be converted to perovskite after 2 h latest to observe the interesting effects on the crystal lattice seen in the GIWAXS measurements which would also influence the conversion to a methylammonium lead iodide (MAPI) film for usage in a perovskite solar cell.

[1] L. Oesinghaus et al., *Adv. Mater. Interfaces* **3**, 1600403 (2016)

[2] N. Jeon et al., *Nature Materials* **13**, 897–903 (2014)

4.6 Tuning the pore size of mesoporous titania films for hybrid solar cells

S. Schlosser, N. Hohn, L. Biessmann, P. Müller-Buschbaum

Hybrid solar cells combine the mechanical stability of inorganic semiconductors and the versatility of organic semiconductors. Due to their potential for large-scale application, hybrid solar cells are especially interesting for low-cost industrial production. Titania films as an inorganic material combined with a conjugated polymer as an organic semiconductor are common for application in hybrid photovoltaics.

Since charge-separation can only take place at the interface of the two compounds, a nanoscale structure of the active layer is necessary in order to provide a high interfacial area. Mesoporous titania structures, which serve as a matrix for infiltration with the polymer are a promising concept for high-efficiency active layers. Challenges concerning this concept arise due to the difficulty of the infiltration with the polymer, since occlusion of the pores in the upper part of the layer can occur and prevent backfilling of pores in lower parts of the layers.

The titania films investigated combine the principles of the sol-gel technique [1], which is a well-established method to produce mesoporous titania films and the formation of integral-asymmetric polymer membranes [2]. The latter are pure polymer films, which are composed of an isoporous surface and a sponge-like sublayer with a gradient of the porosity. The original application of the integral-asymmetric polymer films is in membranes for filtration [2].

Combining both methods opens the possibility to achieve a vertical gradient of the porosity not only for a pure polymer film but also for mesoporous titania. The expectation is that larger pores in the lower layers can sufficiently be backfilled with the polymer.

We focus on the tuning of the pore size of mesoporous titania and the impact on the infiltration of the polymeric compound with respect to solar cell performance. In our experiments, a solution composed of an amphiphilic block copolymer and a precursor dissolved in an organic solvent is applied as a wet film. Immersion in an antisolvent after an evaporation step leads to a structure formation process in the composite film, so that the morphology depends both on the evaporation time and the immersion bath. After calcination, a mesoporous titania film is obtained.

The first films were prepared with casting a solution based on parameters from the sol-gel technique. Films transferred into the immersion bath after a well-defined evaporation time showed to have a network titania structure.

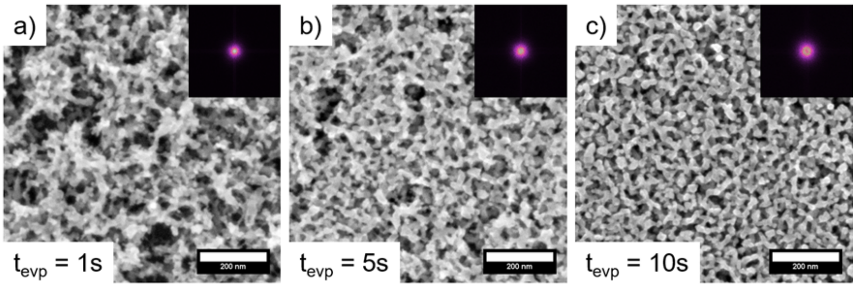

Figure 4.11:
Scanning electron microscopy images of titania films with increasing solvent evaporation times from a) to c) before antisolvent immersion. Increasing evaporation times lead to smaller and more regular structures.

For rather short evaporation times, a strong dependence of the morphology on the solvent evaporation time is observed. Upon increasing the evaporation time, the structures become smaller and more regular due to the decrease of the content of the good solvent. The corresponding

SEM images are shown in Fig. 4.11. For a broad range of longer evaporation times, there are only minor changes in the surface morphology, although the polymer concentrations in the films directly before immersion are expected to be significantly different. Without immersion, the films were compact with only small pores, which proofs the concept of structure formation in the immersion bath.

Another approach of tuning the surface morphology is to start with similar initial solution parameters and to increase both the polymer concentration and the precursor weight fraction by an extended evaporation time. Immersion solutions of different compositions and therefore different incompatibilities were applied. The corresponding SEM images are shown in Fig. 4.12. From image a) to image c), the structures look similar with only slight morphological changes. For image d) to image f), a stronger morphological change towards more compact structures can be observed. Image f) marks the transition from the network structures towards the compact structures with minor pores observed in image g) to image i).

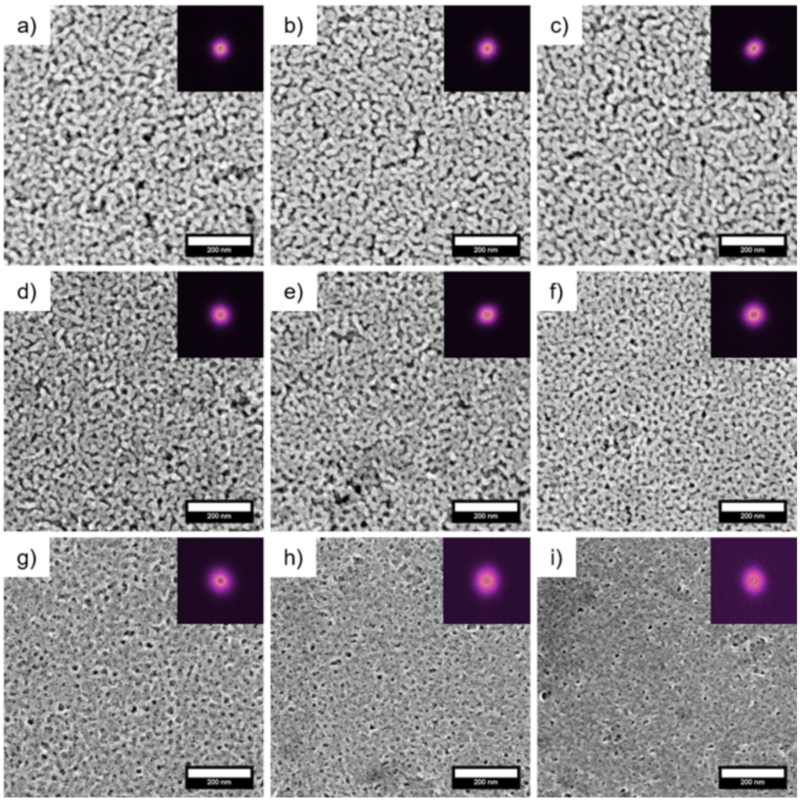

Figure 4.12:
Scanning electron microscopy images of titania films exposed to different immersion baths with decreasing incompatibility from a) to i). As the incompatibility is decreased, the structures become more compact.

[1] Ch. Ya-Jun, J. S. Gutmann. *JACS* **128.14**, 4658–4674 (2006).

[2] A. Volker. *Macromol. Rapid Commun.* **36.1**, 10–22 (2015).

4.7 Fabrication and characterization of mesoscopic perovskite solar cells

M. E. Thordardottir, O. Filonik[1], P. Müller-Buschbaum, E. M. Herzig [1]

[1] MSE, Garching, Germany

Photovoltaic solar cells have been regarded as a promising energy conversion method to keep up with the worlds increasing energy consumption. Organic solar cells yield promising prospects due to their low cost fabrication, light weight and mechanical flexibility. However, the efficiency of organic solar cells is still inferior to commercial silicon solar cells. Organometal halide perovskite solar cells are a new class of solar cells combining the advantages of organic and inorganic systems. The steep rise of the efficiency in the past decade makes them the fastest-advancing solar cell technology to date [1], due to properties like large carrier diffusion lengths, high charge-carrier mobilities and low exciton binding energy [2].

Perovskite is any material system which has the same crystal structure of calcium titanate, ABX_3, where A represents the organic cation and B the metal cation. These cations have been combined with halide anion, X. Perovskite materials have demonstrated superior charge transport properties with ambipolar characteristics [3]. As stated before, its excition binding energy is much lower than in organic materials [4]. The low binding energy, together with long diffusion lengths, account for the high power conversion efficiencies in the solar cells. The most widely studied perovskite material system and analyzed in this work is methylammonium lead triiodide ($CH_3NH_3PbI_3$). A perovskite solar cell is comprised of a substrate, electrodes, a perovskite active layer, together with additional functional layers for improved charge carrier transport [3].

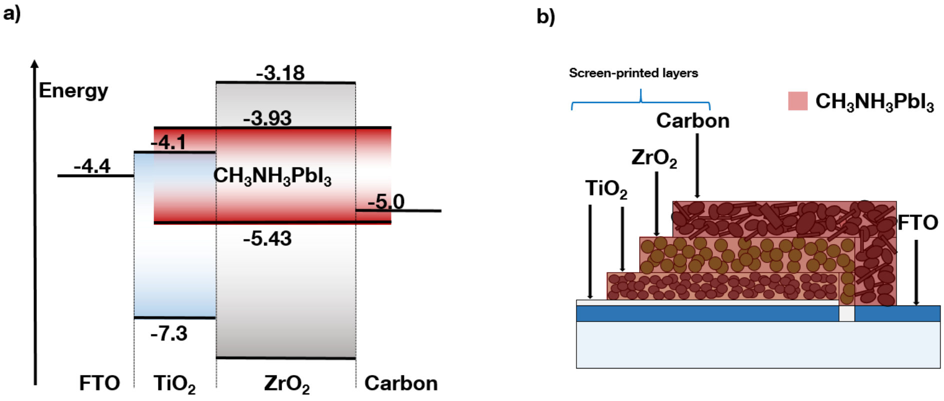

Figure 4.13:
a) Diagram of energy levels of each layer. b) A schematic of perovskite solar cell device structure.

The aim of the project is to realize mesoscopic perovskite solar cells by using a screen printer. Screen printing is an old printing technique where a mesh is used to transfer paste onto a substrate. A distribution blade is moved across the screen to fill the open mesh with paste. Then a squeegee is moved across in opposite direction with pressure so the screen touches the substrate momentarily. This causes the paste to print designed patterns on the substrate.

Our mesoscopic perovskite architecture is based on a triple-layer scaffold of m-TiO_2, m-ZrO_2 and m-Carbon. When using both m-TiO_2 and m-ZrO_2 scaffold infiltrated with perovskite, a hole conducting layer is not required [5]. In our set up, we use FTO coated glass where the FTO acts as a semi-transparent electrode. The compact TiO_2 is printed on the FTO. Subsequently, the mesoporous layers are then printed on top of the compact layer, first m-TiO_2 and then m-ZrO_2.

The TiO_2 layers acts as an electron collector and are used to decrease leakage current. The functionality of the insulating m-ZrO_2 is to hinder leakage current from the carbon layer to the TiO_2 layer. A m-Carbon is finally printed on top of the stack as a hole collector. The energy diagram of the stack can be seen in figure 4.13a. A perovskite solution is deposited on printed layers which infiltrates the mesoscopic layers. At a certain concentration, when annealed, crystal structure begins to form in the scaffold. In this architecture the perovskite works as an active material and hole conductor. For depositing the perovskite material onto the printed layers different casting methods will be compared to drop casting, for example slot die coating. The solar cell structure can be seen in figure 4.13b.

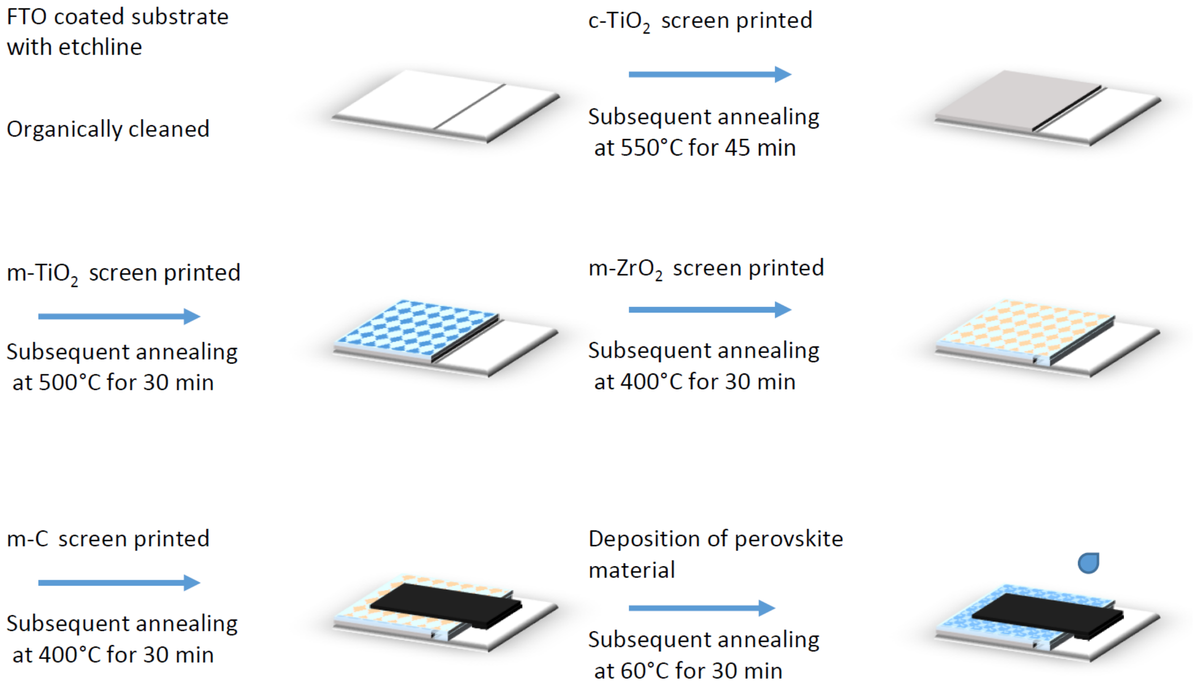

Figure 4.14: Fabrication process for screen printed solar cell step by step.

By adjusting the processing parameters, for example pressure on printing, the thickness of each layer can be optimized [6]. Before stacking the layers, each layer is printed individually to optimize the thickness and minimize the roughness. Then each layer is printed and annealed before the next layer is printed on top. The processing procedure can be seen in figure 4.14.
In addition, a humidity atmosphere setup will be implemented into the perovskite solution deposition and perovskite formation process, occurring in the mesoscopic triple-layer scaffold. The impact of humidity on the morphology and device performance will be investigated.

[1] Y. Rong, L. Liu, A. Mei, X. Li, H, Han, *Adv. Energy Mater.* **5.20**, 1501066 (2015)

[2] H. S. Jung, N. G. Park, *Small* **11**, 10 (2015)

[3] L. Yang, A. T. Barrows, D. G. Lidzey, T. Wang, *Rep. Prog. Phys.* **79**, 026501 (2016)

[4] Y. C. Hsiao, T. Wu, M. Li, Q. Liu, W. Qin, B. Hu,*J. Mater. Chem. A* **3**, 15372 (2015)

[5] A. Mei, X. Li, L. Liu, Z. Ku, T. Liu, Y. Rong, M. Xu, M. Hu, J. Chen, Y. Yang, M. Grätzel, H. Han, *Science* **345**, 294 (2014)

[6] T. Liu, L. Liu, M. Hu, Y. Yang, L. Zhang, A. Mei, H. Han, *J. Power Sources* **293**, 533 (2015)

4.8 A low temperature route towards hierarchically structured titania films for thin hybrid solar cells

L. Song, A. Abdelsamie, C. J. Schaffer, V. Körstgens, W. Wang, T. Wang, E. D. Indari,
T. Fröschl[1], N. Hüsing[1], T. Haeberle[2], P. Lugli[2], S. Bernstorff[3], P. Müller-Buschbaum

[1] Materialchemie, Chemie und Physik der Materialien, Universität Salzburg, Salzburg, Austria
[2] Department of Electrical Engineering and Information Technology, München, Germany
[3] Elettra, Trieste, Italy

Mesoscopic dye-sensitized solar cells (DSSCs) are promising alternatives to conventional inorganic devices due to low cost, ease of manufacturing processes and reasonable solar power conversion efficiency (PCE) values [1]. However, some serious problems such as liquid-electrolyte leakage and electrode corrosion are still to be tackled. Moreover, the DSSCs require high-temperature processing (typically above 400 ^{o}C) during fabrication, which prevents the possibility to produce flexible devices. Thus, producing solar device at low temperatures with solid-state electrolytes has a great significance with respect to energy savings and long device lifetimes. Conjugated polymers such as poly(3-hexylthiophene) (P3HT) have been extensively studied as solid-state electrolytes in DSSC as they have some unique properties. Besides the function of being a positive charge carrier transport material, it also can be used as the exciton generator. Therefore, hybrid solar cells can be simply fabricated by combining n-type titania and P3HT. The dye-free device could further lower production cost and pay-back times.

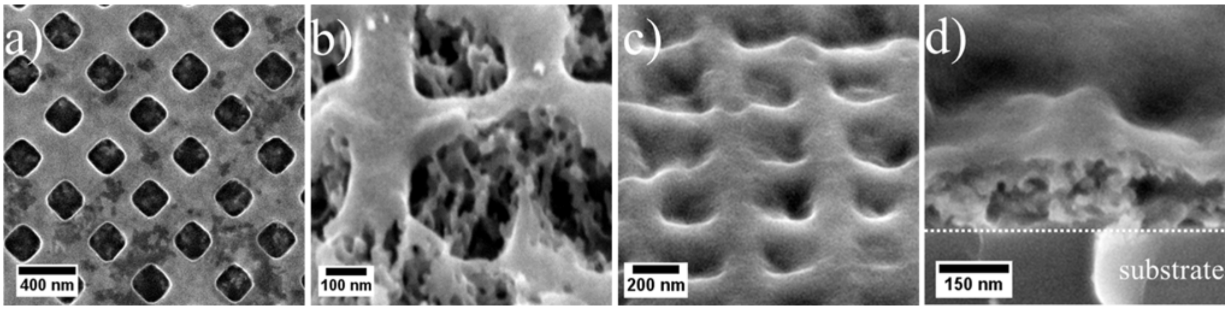

Figure 4.15:
a) SEM image of titania:PS-b-PEO composite film after NIL patterning process. b) Cross-section SEM images of nano-imprinted titania film after polymer-template extraction. c) SEM image of superstructured active layer measured at a tilt angle of 54^{o}. d) Cross-section SEM image of c).

Fabrication of dye-free hybrid solar cells at low temperatures is a cost-effective method to optimize current DSSC technology. Although many efforts have been made to develop hybrid solar cells, the device efficiencies are still very low. In order to improve photovoltaic performance of hybrid solar cells, the mesoporous titania photoanode is tailored with artificially ordered superstructures in the sub-micrometer length scale as a response to many research groups which have suggested that hierarchical titania structures could enhance light harvesting [2]. In the present work, the mesoporous titania nanostructures are achieved via a block copolymer template assisted sol-gel synthesis. In this approach, polystyrene-block-polyethylene oxide (PS-b-PEO) is used as structure directing agent, and a special titania precursor, ethylene glycol-modified titanate (EGMT), is applied to synthesize crystalline titania at low temperatures. After film deposition, the titania:PS-b-PEO composite samples are imprinted using nano-imprint lithography (NIL) to introduce artificial superstructures. After the NIL process, the titania:PS-b-PEO composite films undergo UV irradiation to remove the polymer template.

The removal of PS-b-PEO provides the formation of mesopores in the superstructured titania films. More detailed information can be found in literature [3].

Fig. 4.15a shows the superstructured titania:PS-b-PEO composite film. After the NIL patterning process, the film features highly ordered square pitch-like lattice superstructures without obvious defects, which indicates a sucessfull nano-imprinting. The pitch-like superstructures have a size of 200 × 200 nm^2 and a lattice period of 400 nm. After UV exposure, the polymer template is extracted and therewith mesopores appear as shown in Fig. 4.15b. The size of the mesopores, locating at the wall between pitches and the titania film underneath pitches, is in a range of 10 nm to 20 nm. The pitch-like superstructures are preserved but deformed from its original square shape, which is caused by the collapse of the titania nanostructures after the removal of polymer scaffold. Afterwards, the hierarchical titania films are backfilled with P3HT to achieve the active layer of hybrid solar cells. After backfilling, the pitch-like patterns are preserved instead of being completely filled or covered with P3HT as shown in Fig. 4.15c. The corresponding cross-section SEM image displays a thin active layer of about 170 nm (Fig. 4.15d).

The titania:P3HT active layer is subsequently sandwiched between two electrodes to form hybrid solar cells. The resulting devices are measured at various angles of light incidence. To make a comparison, the hybrid solar cells without artificial superstructures act as a reference under the same measuring conditions. At 0^o incident angle, the reference cell has a lower PCE as compared with the nano-imprinted device. To make an easy comparison between both types of solar cells, all angle-dependent PCE values are normalized to the values of the reference solar cell at 0^o (Fig. 4.16).

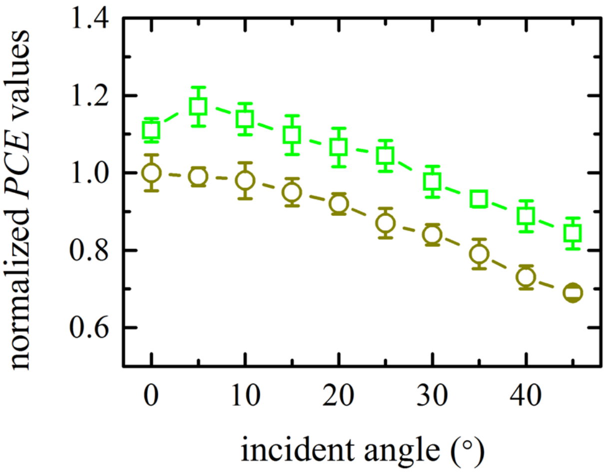

Figure 4.16:
Angular dependent PCE normalized to the reference solar cell measured at zero incident angle. The green squares and the dark yellow circles represent nano-imprinted and reference solar cells, respectively. The dashed lines are guides to the eyes.

The results show that the nano-imprinted hybrid solar cells perform better than the reference cells at every incident angle. The PCE enhancement is caused by the incorporated artificial superstructures which can significantly enhance light harvesting in the active layer [3]. The PCE of both devices shows a decreasing trend with increasing light incident angles, which is due to the fact that the increase of light reflection at the glass substrate leads to less light reaching the active layer of both hybrid solar cells. Moreover, it is noted that the nano-imprinted hybrid solar cell has a highest PCE at 5^o incident angle.

[1] M. Ye, X. Wen, M. Wang, J. Iocozzia, N. Zhang, C. Lin,Z. Lin, *Mater. Today* **18**, 155-162 (2015)

[2] S. Lou, X. Guo, T. Fan, D. Zhang, *Energy Environ. Sci.* **5**, 9195-9216 (2012)

[3] L. Song, A. Abdelsamie, C. J. Schaffer, V. Körstgens, W. Wang, T. Wang, E. D. Indari, T. Fröschl, N. Hüsing, T. Haeberle, P. Lugli, S. Bernstorff, P. Müller-Buschbaum, *Adv. Funct. Mater.* **26**, 7084-7093 (2016)

4.9 A low temperature route towards flexible nanostructured P3HT:TiO_2 films

W. Wang, T. Widmann, L. Song, P. Müller-Buschbaum

Hybrid solar cells, composing an organic semiconducting polymer as electron donor and an inorganic semiconductor as electron acceptor, have received great attentions over the past decades. Titania (TiO_2) is one of the most broadly used inorganic semiconductors. It has its distinct advantages like low cost, nontoxicity, high stability, and abundance. In addition, depending on the demand various of nanostructured TiO_2 film can be fabricated using the polymer template assisted sol-gel process. In general, following TiO_2 film deposition, calcination above 400 °C is necessary to obtain crystalline TiO_2 and to burn away the polymer template [1]. However, this process is not viable in the case of using flexible organic substrate such as poly(ethylene terephthalate) (PET), because this type of substrate normally cannot withstand such high temperatures. Therefore, low-temperature processing is significant for the application towards flexible devices. Furthermore, mechanical investigations on the TiO_2-based active layer are important since TiO_2 is intrinsically brittle.

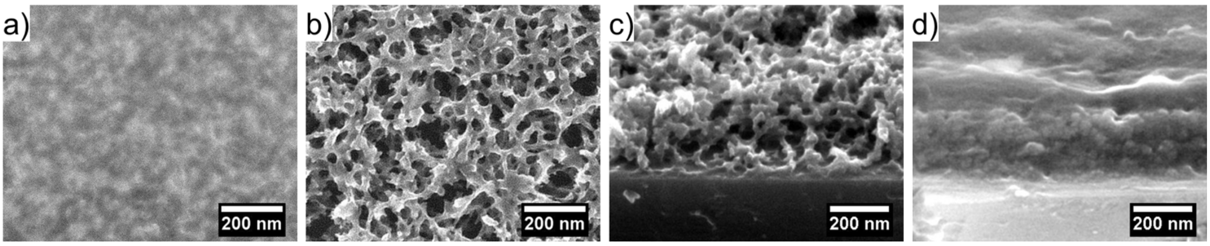

Figure 4.17:
SEM images of a) the as-prepared PS-b-PEO:TiO_2 hybrid film and b) porous TiO_2 film obtained from the solvent treatment., respectively. Cross sectional SEM images of c) porous TiO_2 film and d) the backfilled hybrid P3HT:TiO_2 film.

In the present work, we used an amphiphilic diblock copolymer poly(styrene-block-ethylene oxide) (PS-b-PEO) as the structure directing template and ethylene glycol modified titanate (EGMT) as the titania precursor to produce PS-b-PEO:TiO_2 films. Detailed description can be found in the reference [2]. The resulting samples were probed via SEM, as displayed in Fig. 4.17a. A wavy surface morphology was found, which is typical for polymer surfaces. Afterwards, in order to obtain porous TiO_2 films, solvent treatment was used to remove the template polymer PS-b-PEO. As illustrated by SEM images (Fig. 4.17b), the samples have a porous network-like structure, indicating that the polymer template is removed successfully from the top surface. Furthermore, cross-section SEM measurements were performed, confirming a complete extraction (Fig. 4.17c). The next step to finalize the active layer, which can be potentially used in hybrid solar cells, is to completely backfill into porous TiO_2 network with an electron donor material. In the present study, the conjugated polymer poly(3-hexylthiophene-2,5-diyl) (P3HT) was used. The cross sectional SEM measurements were carried out on the P3HT:TiO_2 hybrid films, as shown in Fig. 4.17d. A P3HT overlayer was found on top of the hybrid film. Moreover, a rather good infiltration of P3HT into mesoporous titania film is suggested since all pores are not visible anymore.

In order to test the flexibility, the TiO_2-based films on PET substrates are subjected to two-point bending measurements. They are bent for 5000 times. After bending test, all samples are examined by SEM measurements with three different magnifications as shown in Figure 4.18. For the mesoporous titania film, vast numbers of visible cracks are observed over the sample surface after bending for 5000 times, suggesting that the mesoporous titania film is not flexible (Figure 4.18a). The film failure is with detected the area fraction of cracks of about 11%. The width of cracks is determined to be about 100 nm. The P3HT:TiO_2 hybrid film is of great interest as it is the active layer of flexible hybrid solar cells. After bending measurements, the film is well preserved and no cracks are observed at the sample surface (Figure 4.18b). Thus, the hybrid film shows a great enhanced flexibility. In order to clear whether the cracks are hidden beneath the polymer, the bent hybrid film is immersed in a chlorobenzene bath to remove the P3HT completely. The porous nature of titania film is observed without any cracks, which rules out the existence of any hidden cracks.

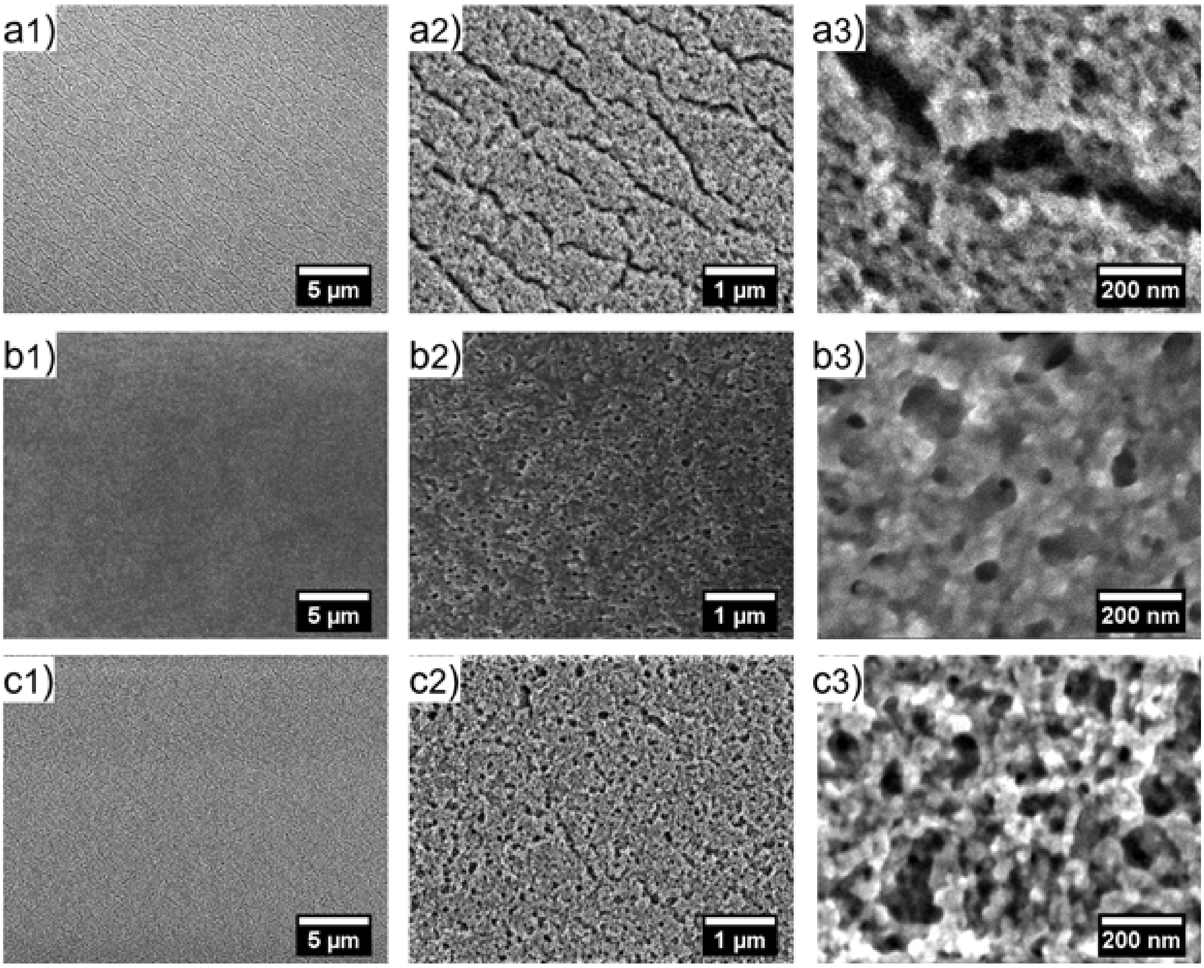

Figure 4.18:
SEM images of the TiO_2-based films after 5000 times bending cycles. a) The mesoporous titania film, b) the P3HT/TiO_2 hybrid film and c) the P3HT/TiO_2 hybrid film after P3HT extraction. 1, 2, 3 represent different magnifications.

In summary, the mesoporous titania film is brittle as many cracks appear st the sample surface after bending for 5000 times. After P3HT backfilling, the film flexibility is significantly improved. No cracks are observed either at the film surface or beneath the backfilled polymer after 5000 bending cycles. The strond flexibility of the P3HT:TiO_2 hybrid film shows a great potential application in flexible hybrid solar cells.

[1] V. Puddu, H. Choi, D. D. Dionysiou, G. L. Puma, *Appl. Catal., B* **94**, 211-218 (2010)

[2] W. Wang, *PhD thesis*, TU München (2016)

4.10 Nanostructured zinc oxide films for application in hybrid photovoltaics

K. Wang, V. Körstgens, L. Bießmann, D. Yang, N. Hohn, S. V. Roth[1], P. Müller-Buschbaum

[1] DESY, Hamburg, Germany

Nanostructured inorganic metal oxides with tunable morphologies are of great importance for hybrid solar cells. Among the inorganic metal oxides, zinc oxide (ZnO) has been widely explored due to its outstanding electrical and optical properties and rich variety of morphologies [1-2]. To date, many different routes towards ZnO nanostructures have been reported, of which the sol-gel process is one of the most widely used methods in solar cells. However, the structures obtained by the sol-gel process are limited, regarding both morphologies and structure sizes. A possible way to improve the film structure is to introduce amphiphilic block copolymers into the sol-gel process.

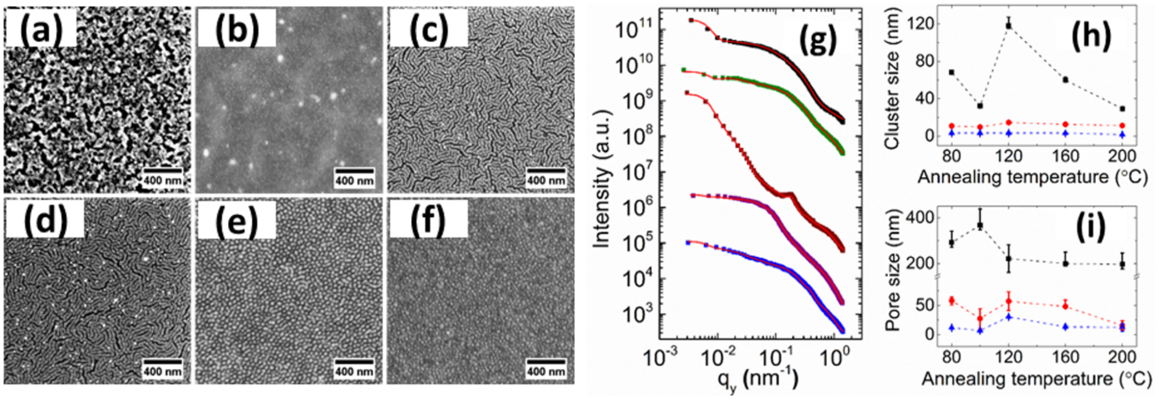

Figure 4.19:
SEM images of ZnO thin films produced at different annealing temperatures of (a) 80 °C, (b) 100 °C, (c) 120 °C, (d) 140 °C, (e) 160 °C and (f) 200 °C. (g) Horizontal line cuts obtained from the 2D GISAXS data for different annealing temperatures (80 °C, 100 °C, 120 °C, 160 °C and 200 °C from bottom to top). (h) Average Cluster and (i) pore sizes of ZnO films plotted as a function of the annealing temperature. The values are extracted from the fits.

Herein, polystyrene-block-polyethylene oxide (PS-b-PEO) template assisted sol–gel technique is used to prepare ZnO films. The phase behavior of PS-b-PEO is mainly depicted via a two-dimensional phase diagram showing the equilibrium microphase as a function of χN and f. According to the Flory-Huggins parameter χ, which describes the interaction between two polymers, temperature plays a very important role in the morphology tuning. Therefore temperature gives an easy way to control the morphology via adjusting the annealing temperature. SEM is a widely used method to measure the surface morphology, while for the structure buried in the film, grazing incidence small angle X-ray scattering (GISAXS) is investigated which can detect the domain size ranging from 1 nm to 1 um[3]. According to SEM and GISAXS data, the morphology changes strongly from foam-like through worm-like structures to spheres. In the horizontal line cuts of the 2D GISAXS, the sample synthesized at 80 °C shows only a plateau-like feature in the intensity which indicates the absence of lateral structures with a dominant length scale. In contrast, the curve for 100 °C shows one peak at around 0.6 nm^{-1} which indicates that there are much smaller structures appearing except the plateau-like feature at small q values. For ZnO films annealed at 120 °C, a dominant peak is present at about 0.2 nm^{-1}, which corresponds to the structure factor of the worm-like structure. The horizontal cuts for films annealed at 160 °C and 200 °C show a broad prominent peak, indicating a distribution over different length scales of the structures in the films. All horizontal cuts were analyzed with a model fit considering cylindrical objects of different sizes with a Lorentzian size distribution. The resulting fits reveal that the large ZnO cluster size first decreases, forming the non-uniform film when the temperature increases from 80°C to 100°C. Then it increases to form worm-like structure. When the annealing temperature goes to 160 °C and 200 °C, the large cluster size decreases again to gradually form spheres. The pore size and the distance between large clusters become larger while middle and small clusters become smaller compared with the pore sizes of film annealed at 80 °C. When increasing the temperature from 120 °C to 200 °C, the pore sizes decrease again as spheres are present. In the present study we use the diblock copolymer PS-b-PEO, in which ZnO can attach to the PEO block while the other block (PS block) has no further function than making micro-phase separation structures and consequently had to be removed to turn the ZnO:polymer nanocomposite film into ZnO nanostructues. The resulting ZnO template needed to be backfilled with a conducting polymer to establish the active layer of the hybrid solar cells. This backfilling turned out to be a very efficiency limiting step for solar cells. Therefore a new functional block copolymer PEO-b-P3HT is used, in which the P3HT block can be directly used as p-type semiconductor. No more polymer removal and backfilling steps will be necessary and the active layer of the hybrid solar cell can be prepared in a one-step approach. The surface morphologies of the ZnO nanostructures are studied with SEM and AFM. The inner structures of the samples are probed by GISAXS to get statistically relevant structure information. Fig. 2 shows the AFM and GISAXS data of hybrid ZnO:P3HT-b-PEO. From the images, we can see the film with the ratio of ω (P3HT-b-PEO): ω (P3HT): ω (ZnO)=0.2:1:2 shows much lower mean square roughness than the others. From the GISAXS data, the large and middle domain sizes show most prominent changes, which decrease first and then increase again. Therefore, the sample with the ratio of P3HT-b-PEO=0.2 indicates the most homogeneous film. Among the three domain sizes, the middle domain size of P3HT is expected to account for the variance of device performance as it coincides with the length scale of the exciton diffusion length [4]. For the film with a weight ratio of P3HT-b-PEO=0.2, it shows the smallest middle P3HT domain size (which is about 26 nm) compared with the other samples. This can be correlated with an improved efficiency of the corresponding solar cells. Smaller domain sizes lead to more interfaces between two components, and as a result, higher charge dissociation and concomitant higher efficiency can be achieved via this well intermixed morphology.

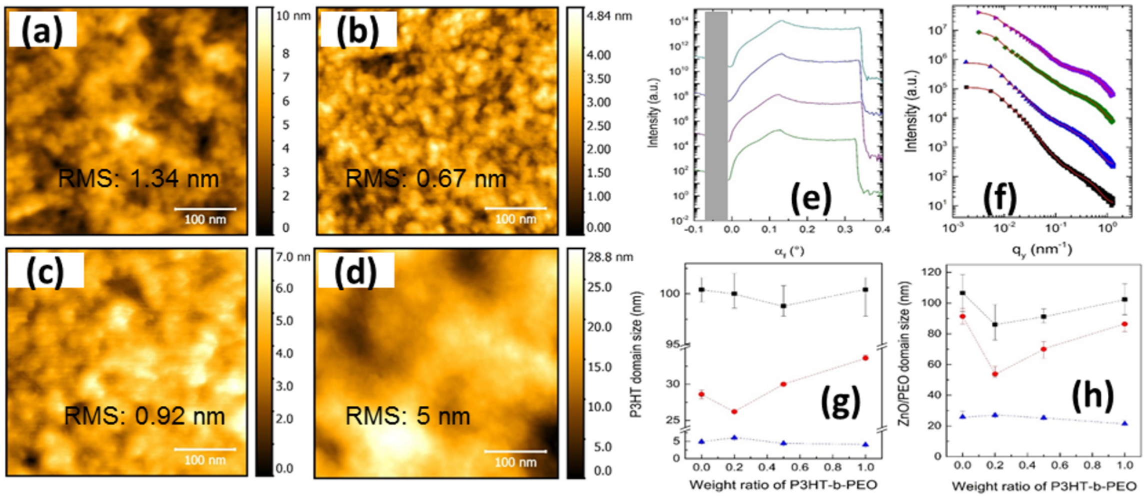

Figure 4.20:
AFM topography images of ZnO:P3HT-b-PEO thin films with various P3HT-b-PEO ratios as compared with P3HT (a) 0%, (b) 0.2%, (c) 0.5% and (d) 1%. (e) Vertical cuts at q_y = 0 nm^{-1} and (f) Horizontal line cuts for ZnO:P3HT-b-PEO thin films with increasing weight fraction of P3HT-b-PEO from bottom (0%) to top (1%). The grey shaded region is the direct beam region, which is covered by the beamstop. (g) Average P3HT and (h) ZnO:PEO domain sizes plotted as a function of the increasing weight fraction of P3HT-b-PEO. The values are extracted from the fits.

[1] S. Cho, J. Jang, A. Jung, A. S. Lee, J. Lee, J. S. Lee, K.Lee, *Langmuir* **27**, 371-378 (2011)

[2] H. Yu, Z. Zhang, M. Han, X. Hao, F. Zhu, *J. Am. Chem. Soc* **127**, 2378-2379 (2005)

[3] P. Müller-Buschbaum, *Adv. Mater.* **26**, 7692-7709 (2014)

[4] H.J. Son, B. Carsten, I.H. Jung, L. Yu, *Energy Environ. Sci.* **5**, 8158 (2012)

5 New materials

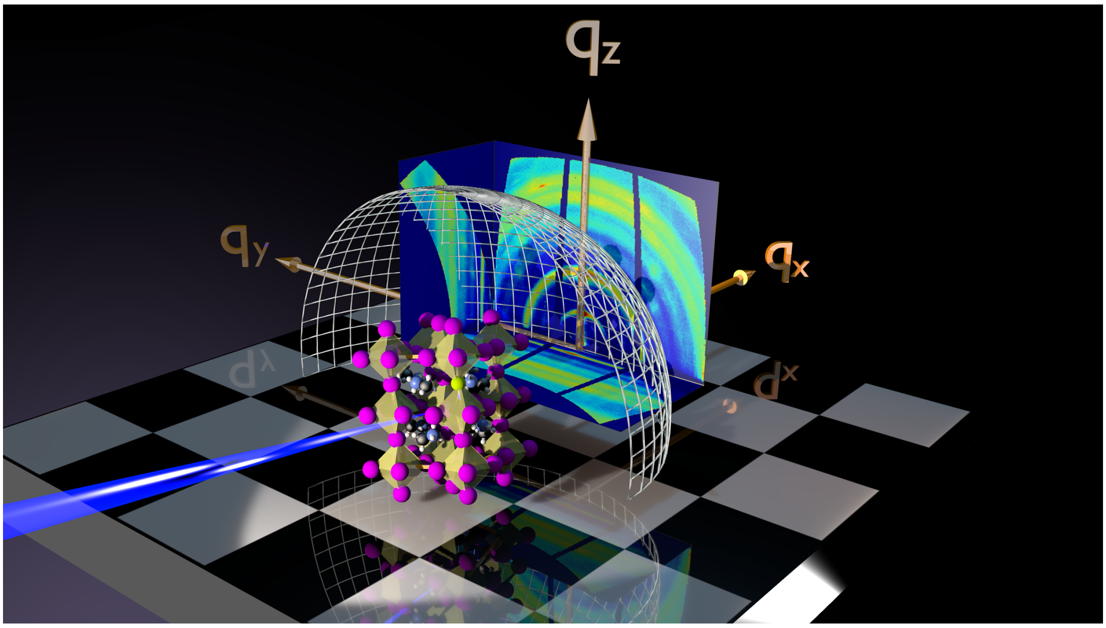

5.1 Macromolecular HPMA-based drug delivery system - behavior in protein environment

Xiaohan Zhang, Bart-Jan Niebuur, Petr Chytil[1], Tomas Etrych[1], Sergey K. Filippov[1], Alexey Kikhney[2], Florian Wieland[2], Dmitri I. Svergun[2], Christine M. Papadakis

[1] Institute of Macromolecular Chemistry, Prague, Czech Republic
[2] The European Molecular Biology Laboratory, Outstation Hamburg, Germany

In dilute aqueous solution, polymeric drug carriers based on *N*-(2-hydroxypropyl)methacrylamide (HPMA) copolymers (Fig. 5.1 a) with hydrophobic cholesterol side groups and the anti-cancer drug doxorubicin (Dox) have been found to form elongated core-shell nanoparticles (NPs) by self-assembly (Fig. 5.1 b) [1]. However, little is understood how these drug carriers behave in real human blood environment. Human blood contains hundreds of proteins, which are expected to interact with the NPs and make the investigation extremely complicated. Therefore, experiments where the effect of a single protein type is investigated are more appropriate. At this, we study the copolymers in an aqueous solution of human serum albumin (HSA), the most abundant protein in human blood.

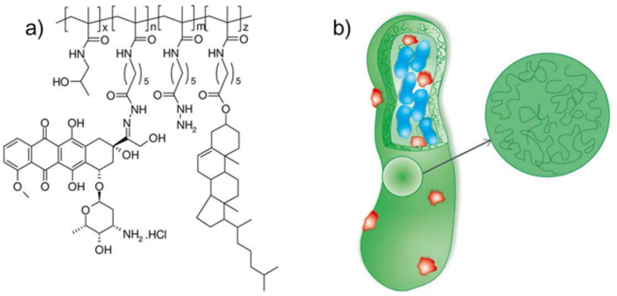

Figure 5.1:
a) Schematic drawing of the HPMA copolymer-drug conjugate bearing cholesterol moiety. b) Structure of the self-assembled NPs. green: HPMA, blue: cholesterol, red: Dox. Reprinted with permission from [1]. Copyright 2012 American Chemical Society.

In the present study, we focus on the interactions between NPs from the HPMA copolymer HPMA_{33k} ($\boldsymbol{M}_w$ = 33000 g/mol, 2 mol % cholesterol as side group, but without Dox) and HSA. We use synchrotron small-angle X-ray scattering (SAXS) to investigate the morphology of the NPs and the structural changes due to interactions with HSA in dependence on their respective concentrations in phosphate buffered saline (PBS) in a wide range.

All samples were dissolved in PBS, then mixed with an aqueous solution of HSA, resulting in HSA concentrations of 0.35 mg/ml, 3.5 mg/ml and 35 mg/ml. Polymer solutions without HSA were measured as control. All samples were measured at 37 °C at beamline P12, DESY, Hamburg. The scattering patterns were azimuthally integrated.

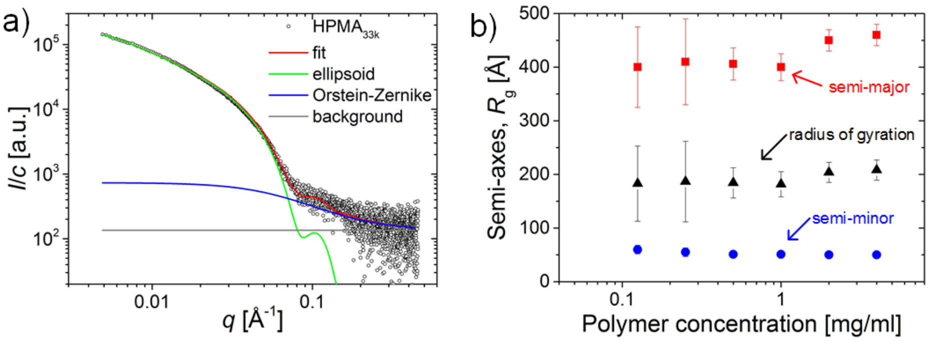

Figure 5.2:
(a) SAXS curve of HPMA_{33k} at 2.0 mg/ml in PBS together with the fit and its contributions.
(b) Resulting values of the semi-major axis, semi-minor axis and radius of gyration of the ellipsoidal NPs in dependence on its concentration.

The SAXS curves were modeled by a form factor of ellipsoids, together with an Ornstein-Zernike structure factor describing correlations between HPMA chains surrounding the NPs (Fig. 5.2 a). In the absence of HSA, the correlation length given by the Ornstein-Zernike term was fixed at 15 Å for all the cases. The semi-major axis of the ellipsoids increases with polymer concentration above 1 mg/ml, whereas the semi-minor axis does not change (Fig. 5.2 b). To observe the concentration dependence of the NPs' size, their radius of gyration was calculated and is found to increase at high concentrations (>1 mg/ml). Upon addition of HSA, the semi-major axis of the NPs decreases dramatically, together with a slight increase in the semi-minor axis (Fig. 5.3). The radius of gyration of the NPs decreases with increasing HSA concentration. We suspect that HSA binds to the cholesterol moieties and release them from the NPs (Fig. 5.4).

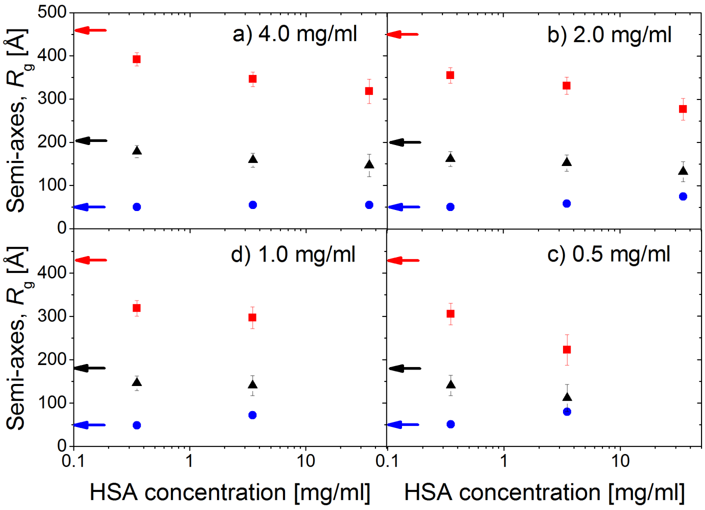

Figure 5.3:
SAXS results of mixed solutions of $HPMA_{33k}$ and HSA. Arrows indicate the radii of NPs without the presence of HSA. Red squares: semi-major axis, blue circles: semi-minor axis, black triangles: radius of gyration. The copolymer concentrations are given in the graphs.

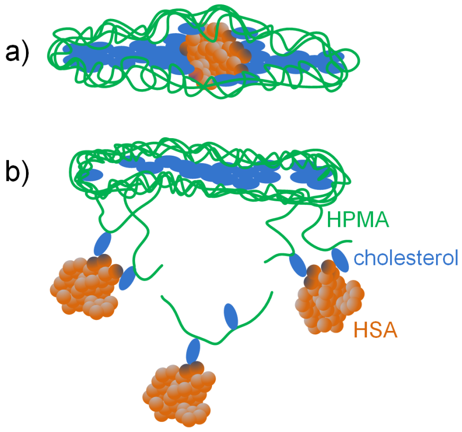

Figure 5.4:
Schematic drawing of the NP/HSA interaction: (a) HSA forms a complex with the NP and hinders the elongated packing of the cholesterol groups. (b) HSA releases cholesterol groups from the NP core. The colors indicate different components: green: HPMA, blue: cholesterol, yellow: HSA.

To summarize, we have investigated HPMA-based copolymers for drug delivery in the presense of the blood protein HSA by synchrotron SAXS. In the presence of HSA, a decrease in the NPs' size is observed. We speculate that HSA binds to cholesterol groups and releases them from the NPs.

The poject is funded by DFG (PA771/17-1) and the Grant Agency of the Czech Republic (grant no. 15-10527J) in the framework of the Memorandum of Understanding of Scientific Cooperation.

[1] S. K. Filippov, P. Chytil, P. V. Konarev, M. Dyakonova, C. M. Papadakis, A. Zhigunov, J. Plestil, P. Stepanek, T. Etrych, K. Ulbrich, and D. I. Svergun, *Biomacromolecules* **13**, 2594 (2012)

5.2 Self-assembled nanoparticles from weakly amphiphilic triblock copolymers as drug carriers

S. Jaksch, A. Schulz[1], Z. Di[2], R. Luxenhofer[3], R. Jordan[1], C.M. Papadakis

[1] Department Chemie, Technische Universität Dresden
[2] Jülich Centre for Neutron Science (JCNS), Forschungszentrum Jülich GmbH, Garching
[3] Functional Polymer Materials, University Würzburg

Self-assembled polymeric nanoparticles serve as pharmaceutical formulations to overcome the low water solubility of many commonly used drugs and to increase their residence time in the body. At this, a high loading capacity with the drug is desirable, and the carrier particles should not lead to side effects. Self-assembled micelles from amphiphilic block copolymers from poly(2-oxazoline)s (POx) feature these advantageous properties: They are hardly toxic, thus stimulate the immune system only weakly and provide good renal cleaning. Moreover, an exceptionally high loading capacity for hydrophobic drugs has been achieved for the cancer drug Paclitaxel (PTX) which is used to treat breast and ovarian cancer.

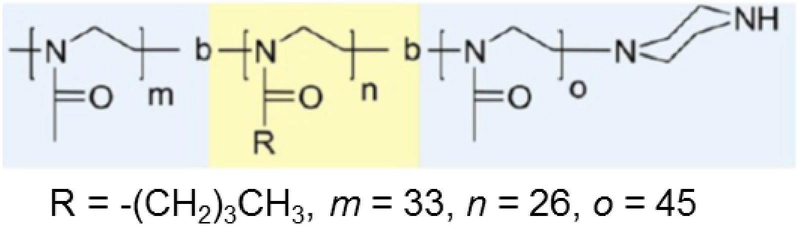

Figure 5.5: Chemical structure of PMeOx$_{33}$-*b*-PBuOx$_{26}$-*b*-PMeOx$_{45}$ [1].

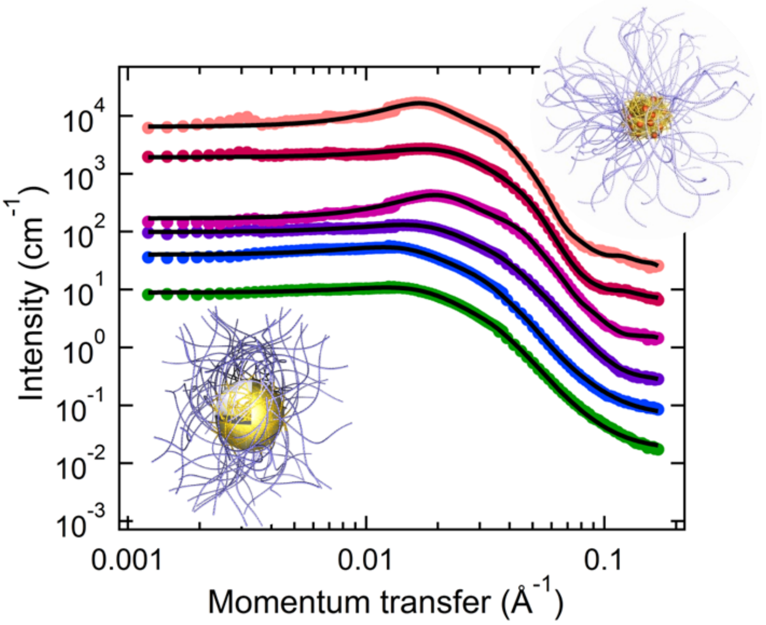

Figure 5.6: Small-angle neutron scattering data from solutions of PMeOx$_{33}$-*b*-PBuOx$_{26}$-*b*-PMeOx$_{45}$ in D_2O (10 g L^{-1}) loaded with (from below) 0, 0.2, 0.9, 1.9, 4.2 and 4.8 g L^{-1} PTX [2]. Insets: Structures of unloaded and PTX-loaded micelles. The PBuOx core is depicted in yellow, the PMeOx blocks in blue and PTX in red.

The POx system offers, among others, a fine-tuning of the water solubility of the blocks. We have investigated triblock copolymers having a weakly hydrophobic poly(*n*-butyl-2-oxazoline) (BuOx) middle block and hydrophilic poly(methyl-2-oxazoline) (MeOx) end blocks (Figure 5.5), PMeOx$_{33}$-*b*-PBuOx$_{26}$-*b*-PMeOx$_{45}$ (subscripts denote the degrees of polymerization). As a reference, similar triblock copolymers, but with a strongly hydrophobic poly(*n*-nonyl-2-oxazoline) middle block were studied as well. Surprisingly, the loading capacity for drugs is maximum for

the system containing PBuOx, e.g. for an only weakly (and not strongly) core-forming middle block [1].
To elucidate the origin of this behavior, structural methods elucidating the inner structure of the micelles and the distribution of the drug in the micelle are needed, such as small-angle neutron scattering (SANS) [2]. Solutions of micelles from PMeOx$_{33}$-*b*-PBuOx$_{26}$-*b*-PMeOx$_{45}$ were prepared in D_2O to maximize the scattering contrast. The polymer concentration was kept at 10 g L^{-1}, while the concentration of PTX was varied in fine steps up to 4.8 g L^{-1}. SANS experiments were carried out on the KWS-1 instrument at FRM II, Garching, sample-detector distances between 1.7 m and 19.7 m and a neutron wavelength of 0.69 nm. Measuring times were between 15 min and 30 min.
The SANS data are shown in Figure 5.6. For PTX loadings up to 0.2 g L^{-1}, they could be fitted by a model for homogeneous spherical particles having a radius of 4.6-5.0 nm (Figure 5.7), which corresponds to the radius of the micellar core (lower inset of Figure 5.6). For PTX loadings of 0.9 g L^{-1} and above, this model did not describe the data adequately. Instead, a model describing raspberry-like spherical particles could be used successfully. The radius of the micellar core was 5.3-6.1 nm in the entire concentration range studied, and it is surrounded by small spheres (radius 1.2-1.7 nm).

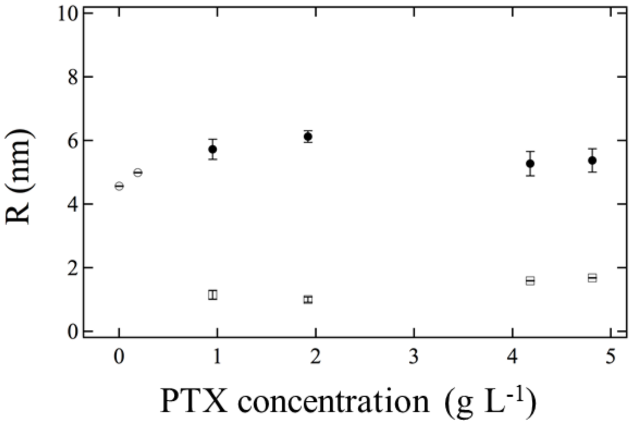

Figure 5.7:
Resulting radii. Open circles: core radii at low PTX loadings, closed circles: core radii of raspberry-like micelles, squares: radii of the embedded PTX particles.

Thus, the PTX molecules form small aggregates which are located near the interface between the PBuOx core and the PMeOx shell of the micelles (upper inset of Figure 5.6). This peculiar distribution of the drug within the micelle (which was not observed in the system with strongly hydrophobic cores) may explain the exceptionally high PTX loading capacity of this type of micelles.
Compared to other methods, such as transmission electron microscopy, SANS allows studying drug delivery systems in solution, and no preparation steps are needed, which may alter the structure of these delicate systems. Thus, SANS is of great use in designing drug delivery systems with high therapeutic effect and minimum side effects.
The authors gratefully acknowledge financial support by the DFG (Pa771/6-2, Jo287/4-3) and the National Cancer Institute Alliance for Nanotechnology in Cancer (U01 CA116591).

[1] A. Schulz, S. Jaksch, R. Schubel, E. Wegener, Z. Di, Y. Han, A. Meister, J. Kressler, A.V. Kabanov, R. Luxenhofer, C.M. Papadakis, R. Jordan, *ACS Nano* **8**, 2686-2696 (2014)

[2] S. Jaksch, A. Schulz, Z. Di, R. Luxenhofer, R. Jordan, C.M. Papadakis. *Macromol. Chem. Phys.* **217**, 1448-1456 (2016)

5.3 Star copolymers with a siliceous core affecting the mesoscale morphology of a model polyurethane

S. Koutsoumpis[1], K. N. Raftopoulos, M. Jancia[2], E. Hebda[2], C. M. Papadakis, K. Pielichowski[2], P. Pissis[1]

[1] Department of Physics, National Technical University of Athens, Greece
[2] Department of Chemistry and Technology of Polymers, Cracow University of Technology, Poland

Polyurethanes (PUs) tend to form hierarchical structures at various length scales [1]. In the scale 1-100 nm, their so-called hard segments (sequences of diisocyanates and short diols interconnected with urethane bonds) form domains inside a continuous soft phase consisting mainly of the so called soft segments (typically a polyether of M_w $1000-2000$ g/mol), which is called microphase separation. At a second level of organization, the hard domains tend to associate with each other and form structures, typically dendroidal, extending to several μm.
The morphology depends on the chemical nature of the components of the PU, the molar masses of the components, as well as on the thermal history. However, additives play a significant role as well. In this work, we studied the effects of a polyhedral oligomeric silsesquioxane with oligomeric PEG vertex groups. Traditionally regarded as nanoparticles, POSS consist of a polyhedral siliceous core with Si atoms on the vertices and O on the edges, with organic groups attached to the Si-vertices. These organic groups can be arbitrarily chosen to control compatibility with the host polymer or even allow covalent bonding with it. Thus, POSS combine the properties of nanoparticles with the versatility of organic chemistry, resulting in a complex interplay of the properties of the groups and the host polymer [2].

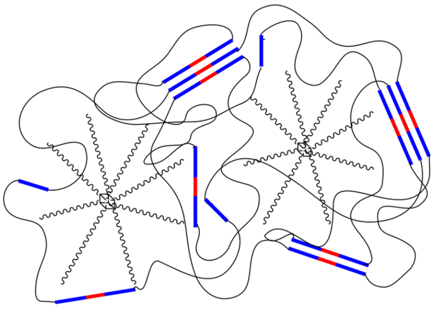

Figure 5.8:
Schematic representation of the system studied. Blue and red represent the diisocyanate and the short diol (chain extender), respectively. Together, they form the rigid hard segments, which associate with each other to form domains or remain diluted in the soft phase. Long lines represent the polyether serving as soft segments and the cubes with radiating curly lines the POSS moieties. Adapted with permission from [3]. Copyright 2016 American Chemical Society.

In the present work, the PU matrix comprises poly(tetramethylene ether glycol) with molar mass $\sim$ 1400 g/mol as soft component and methylene diphenyl isocyanate with butanediol as hard segments at a 1:1 mass ratio, resulting in M_w of the hard segments of 1400g/mol. The POSS comprise poly(ethylene glycol) with 600 g/mol as vertex groups. Hence, they may be described as a star oligomers with a siliceous core (Figure 5.8). Note here the similarity of the contour length of the main chain of PTMEG ($\sim$ 96 atoms) and the „expanded“ diameter of the POSS ($\sim$ 93 atoms). As opposed to conventional nanoparticles, the filler can interpenetrate the matrix. The POSS can hardly diffuse, both due to its chain architecture and to its relatively large size. The synthesis was carried out in two steps (prepolymer-chain extension) with the POSS present from the beginning.
In order to follow the effects of POSS on the morphology, we performed X-ray scattering experiments at three sample to detector distances (106.2, 406.2, and 1056.2 mm), covering both the small- and wide- angle q regions. A two-dimensional (2D) Pilatus 300K detector was used, while the samples were measured at room temperature in vacuum.
The scattering curves (Figure 5.9) confirmed that the POSS moieties do not form domains: neither the amorphous halo of the POSS ($\sim 1-2$ Å^{-1}) nor the features associated with long-range order ($\sim 0.2-0.9$ Å^{-1}) appear in the curves of the composites. This is due to the similarity and compatibility between the two oligoethers constituting the soft segments of the matrix and

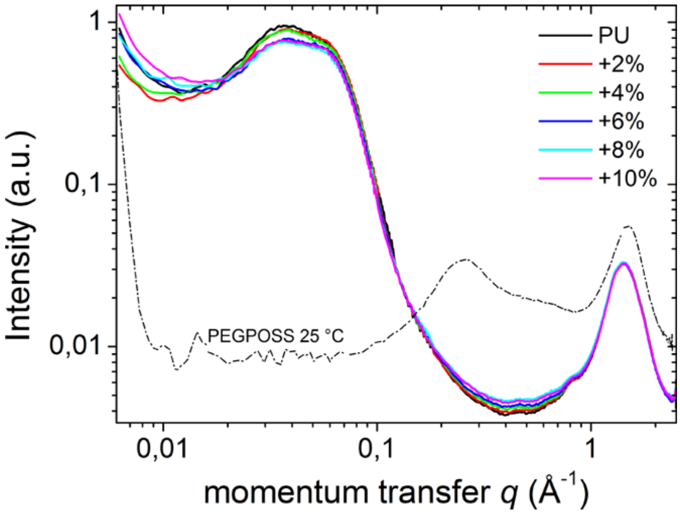

Figure 5.9:
Small- and wide-angle X-ray curves from the POSS filler, the PU matrix and the composites. Reprinted with permission from [3]. Copyright 2016 American Chemical Society.

the ligands of the filler. The effective blending is manifested also by a moderate decrease of the glass transition temperature of the soft domains with increasing filler content.
Meanwhile, the microphase separated structure of the host polymer manifests itself as a double peak between 0.02 and 0.1 Å^{-1}. The slight suppression of this peak with increasing filler content is rather indicative of the reduction of the hard domain fraction rather than a considerable effect on the size and shape of the hard domains.
In that light, it is striking that, on the μm scale, the POSS have a strong effect on the morphology (Figure 5.10): The hard domains form spherulitic structures barely exceeding a few μm in the pure PU. However, as the filler content increases, their size increases as well, and their growth stops only when boundaries of neighboring spherulites meet. The spherulites are considered to have a dendritic backbone of hard domains, on which soft chains are deployed, while the space between the spherulites consists of soft segments with unassociated hard domains. Within this model we interpret this effect as „swelling" of the dendritic structures by the star oligomers which blend very well into the soft phase [3].
Hence, in this project we showed that the star-like oligomeric filler with size comparable to the components of a common PU copolymer hardly affects the formation of hard domains, but has a significant effect on their arrangement.

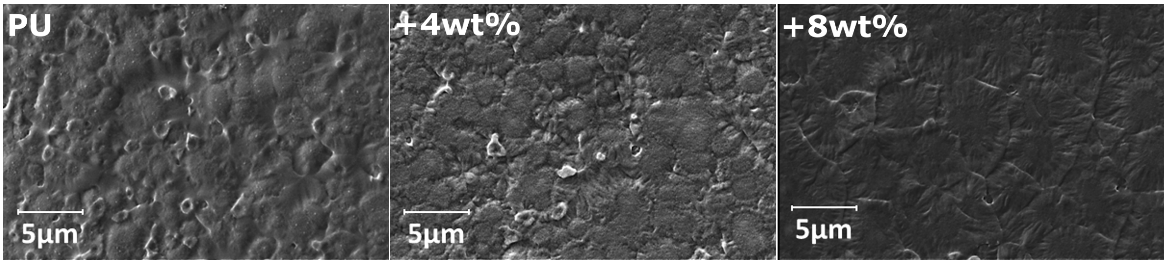

Figure 5.10:
Scanning Electron Microscopy images from PU and selected composites. Adapted with permission from [3]. Copyright 2016 American Chemical Society.

[1] Z. S. Petrovic, Y. J. Cho, I. Javni, S. Magonov, N. Yerina, D. W. Schaefer, J. Ilavsky, A. Waddon, *Polymer* **45**, 4285–4295 (2004)

[2] K. N. Raftopoulos, K. Pielichowski, *Prog. Polym. Sci.* **52** , 136–187 (2016)

[3] S. Koutsoumpis, K. N. Raftopoulos, M. Jancia, J. Pagacz, E. Hebda, C. M. Papadakis, K. Pielichowski, P. Pissis, *Macromolecules* **49**, 6507–6517 (2016)

5.4 Silver decoration of silica nanospheres coated on polymer films with a microfluidic process

K. M. John, V. Körstgens, P. Müller-Buschbaum

The sun gives an average power of $1300W/m^2$ (equivalent to 10^8 TW). The global average energy consumption was estimated to be roughly 13 TW in 2013 [1]. As such, solar energy is more than capable of meeting the global energy demand. Solar cells convert sunlight directly into electricity. Hybrid photovoltaics combine organic and inorganic components to get the best of both worlds – low-cost, flexible, scalable devices with efficiency comparable to conventional silicon solar cells. However, there are a few issues including the use of toxic materials and also the stability of these devices. One of the ideas to improve the conversion efficiency of hybrid photovoltaic devices is to include metal nanoparticles in the devices. For the case of silver nanoparticles, plasmonic absorption could be tuned by varying its size and shape [2] and hence could offer a better control of the solar cells. In this work, we focused on decorating silica nanoparticles [3] attached to a polymer-coated film with silver by the use of solution-processing and microfluidic techniques, intended for application in hybrid photovoltaics.

Polymer films consisting of a cyclic olefine were used as flexible substrates for the experiments. The substrates of a few mm^2 size were dipped in a polymer solution of polyallylamine hydrochloride (PAH) or polyethylenimine (PEI), respectively. These positively charged surfaces are intended for an improved attachment of silica nanospheres in the next dipping step into a commercially manufactured dispersion of silica spheres (diameter is 142 nm , standard deviation is 6 nm, and solid content is 50 mg/ml). The coated substrates are characterized with the optical microscope and then attached to modified microfluidic chips from Ibidi Company. The silver decoration of the silica spheres is achieved in a two-step aqueous microfluidic process. The initial step is the attachment of silver ions to the silica surface by a flow of solution for 30 minutes. After an intermediate washing step of 15 seconds with pure water in order to rinse the free silver ions out of the microfluidic chip, a solution of a reduction agent is flown through the device for 15 minutes. The reduction step leads to nanospheres of metallic silver decorating the silica spheres. Silver ion solutions are prepared by dissolving 127.4 mg of silver nitrate in 5 ml of water. Ammonia is added to this, to get an ammoniacal silver complex. Sodium borohydride solutions for the reduction step were prepared at 0.33 mg/ml concentration. The microfluidic experiments were performed at a flow rate of 0.1 ml/min for all of the above described steps. The samples were studied using optical microscopy and scanning electron microscopy (SEM) after the silver decoration.

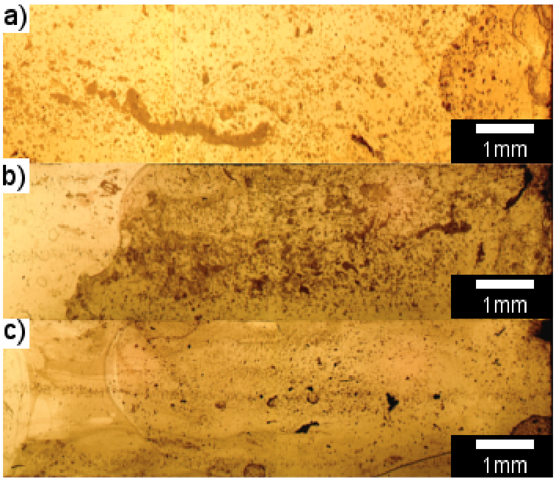

Figure 5.11:
Optical microscope images of flexible PEI-coated substrates after dipping process in a dispersion of silica nanospheres with exposure times of a) 1 min, b) 30 s and c) 15 s.

Different experiments were performed by varying some of the parameters in the process above, including the choice of the polymer coating (PAH and PEI, respectively) and the time of contact with the solutions. Other factors varied included the time the substrate was dipped in the polymer solution between 5 and 20 minutes, and the exposure to the silica nanospheres from 15 seconds to 5 minutes. Exemplary optical microscopy images of samples coated with silica nanospheres coated on flexible PEI-coated substrates (Fig 5.11 shows areas of heterogeneity on the samples due to the aggregation of nanoparticles. For the edges of the samples, these are caused by impurities due to the difficulties in handling the small-sized flexible substrates. The parameters of the microfluidic part of the experiment were not varied. Based on the results from the optical microscopy, the following conclusions could be drawn. The choice of polymer did not result in any significant difference between the samples produced. It was also seen that samples dipped in the polymer for around 10 minutes gave good results, and all microfluidic experiments were performed with samples produced with this standard time. The time of exposure to the silica nanospheres was seen to be very crucial in the film morphology. Samples with this time greater than a minute were seen to have multiple layers and aggregation of the nanoparticles into clusters. It was observed that 15 seconds was an ideal time in respect to the film morphology as well as reproducibility, as seen in Fig 5.11

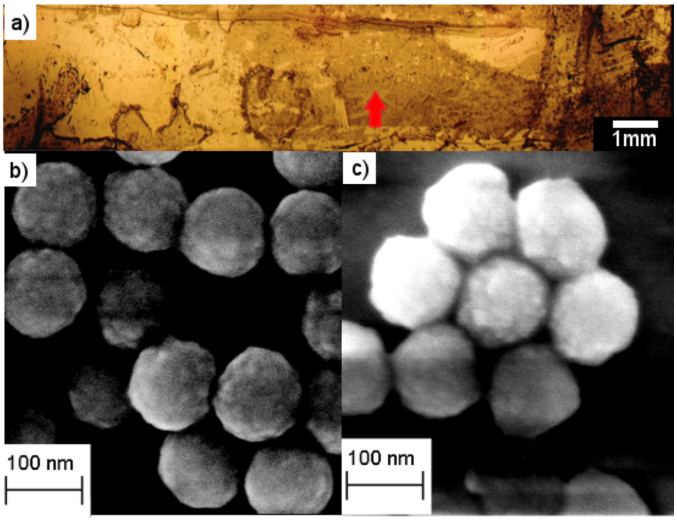

Figure 5.12:
Images of the sample with 15 seconds of silica exposure after silver depositon as seen with optical microscope (a) and SEM at 3kV and 80kX magnification in (b) and (c). The arrow in (a) is indicating the position on the samples where the SEM images were captured

The microfluidic silver decoration process was performed on the samples produced with an exposure of 15 seconds to the silica sphere dispersion. The achieved silver decorated films were studied with optical microscopy (Fig 5.12a)) and SEM, (Fig 5.12 b) and c)). The successful silver decoration can be observed from the SEM images, although the contrast is comparably low due to the challenging measurement conditions with the small flexible substrates.

[1] Key world energy statistics, *International Energy Agency*, (2016)

[2] L. Manai, B. D. Rezgui, R. B. Zaghouani, D. Barakel, P. Torchio, O. Palais, B. Bessais, *Plasmonics* **11**, 1273–1277 (2016)

[3] W. Wang, Y. Jiang, Y. Liao, M. Tian, H. Zou, L. Zhang, *J. Colloid Interf. Sci.* **358**, 567-574 (2011)

5.5 Magnetic structure in B2 $Ni_{2-x}Co_xMnAl$ compounds

P. Neibecker[1], X. Xu[2], A. Senyshyn[1], A. Okubo[2], R. Kainuma[2], W. Petry, M. Leitner

[1] MLZ, Garching, Germany
[2] Tohoku University, Sendai, Japan

Ni_2MnX Heusler alloys are versatile materials encompassing functionalities such as the ferromagnetic shape memory effect and the magnetocaloric effect. The cubic $L2_1$ full-Heusler structure can be described as 4 interpenetrating fcc sublattices from which two are occupied by Ni and the other two are occupied by Mn and the post-transition metal element X. At high temperatures, in most Ni_2MnX compounds a second-order phase transition to the B2 structure is observed, where Mn and X are randomly occupying their two sublattices.

The magnetic properties of these compounds mainly result from distance-dependent exchange interactions of Mn spins which are the dominant magnetic moments in the system. Specifically, neighbouring Mn spins tend to couple antiferromagnetically, while next nearest Mn-Mn neighbours couple ferromagnetically. Simultaneously, Ni is found to carry a small magnetic moment together with ferromagnetic exchange interactions to neighbouring Mn spins. This ferromagnetic interaction can be easily tuned via substituting the stronger ferromagnetic Co for Ni.

Introducing structural disorder, specifically between Mn and X, has thus a strong effect on the magnetic properties of Ni_2Mn-based Heusler materials. In fact, introducing structural disorder means introducing competing interactions with antiferromagnetic and ferromagnetic exchange interactions both present in the system. These competing interactions potentially result in interesting magnetic structures much more complicated than the one observed in the ferromagnetic $L2_1$ phase. At the same time, structural disorder is, due to the second-order nature of the B2-$L2_1$ phase transition and the large compositional stability of the $L2_1$ phase, inevitable in most Heusler systems. Hence, understanding the magnetic properties in these compounds is of crucial importance for mastering the functionality in these materials.

The Heusler system Ni_2MnAl was observed to adopt, while in B2 structural order, a helical magnetic structure [1]. This structure was reported to manifest itself in antiferromagnetic superstructure peaks together with satellite peaks at the (200) and (220) reflections. Quaternary NiCoMnAl however, despite displaying the same structural order as Ni_2MnAl, was found to possess totally different magnetic properties. First neutron diffraction results by Halder et al. [2] found no helical magnetic structure but instead prototypical ferromagnetic properties.

In this study, we intended to investigate the transition from the presumably helical magnetic order in Ni_2MnAl to the ferromagnetic order in NiCoMnAl via altering the Ni/Co ratio in the samples. Specifically, a series of samples from the $Ni_{2-x}Co_xMnAl$ system was prepared. Neutron powder diffraction measurements on these samples were performed at the SPODI high resolution neutron powder diffractometer [3] at FRM II in Garching, Germany. Data treatment was done as outlined in [4].

Fig. 5.13 shows diffractograms for the extreme compositions investigated in this study, Ni_2MnAl (at T = 10 K and T = 315 K) and $Ni_{1.2}Co_{0.8}MnAl$ (at T = 10 K). In the prototypical $L2_1$ Heusler structure in principle 3 peak families have to be distinguished: The A2 peak family, the B2 peak family and the $L2_1$ peak family. This means that if the sample shows A2 structural order, only the A2 peaks would be visible, upon B2 ordering, the A2 and B2 peaks would be present and, finally, once a $L2_1$ structure is adopted all 3 peak families would be observed in the diffractogram. Ferromagnetic ordering in the system would lead to a modification of the intensities of the existing structural peaks, while an antiferromagnetic superstructure would result in an enlargement of the unit cell and therefore the appearance of magnetic peaks in addition to the structural peaks. The position of the respective structural peaks are given in Fig. 1 below the diffractograms. It can be seen that both Ni_2MnAl (see curve at 315 K)

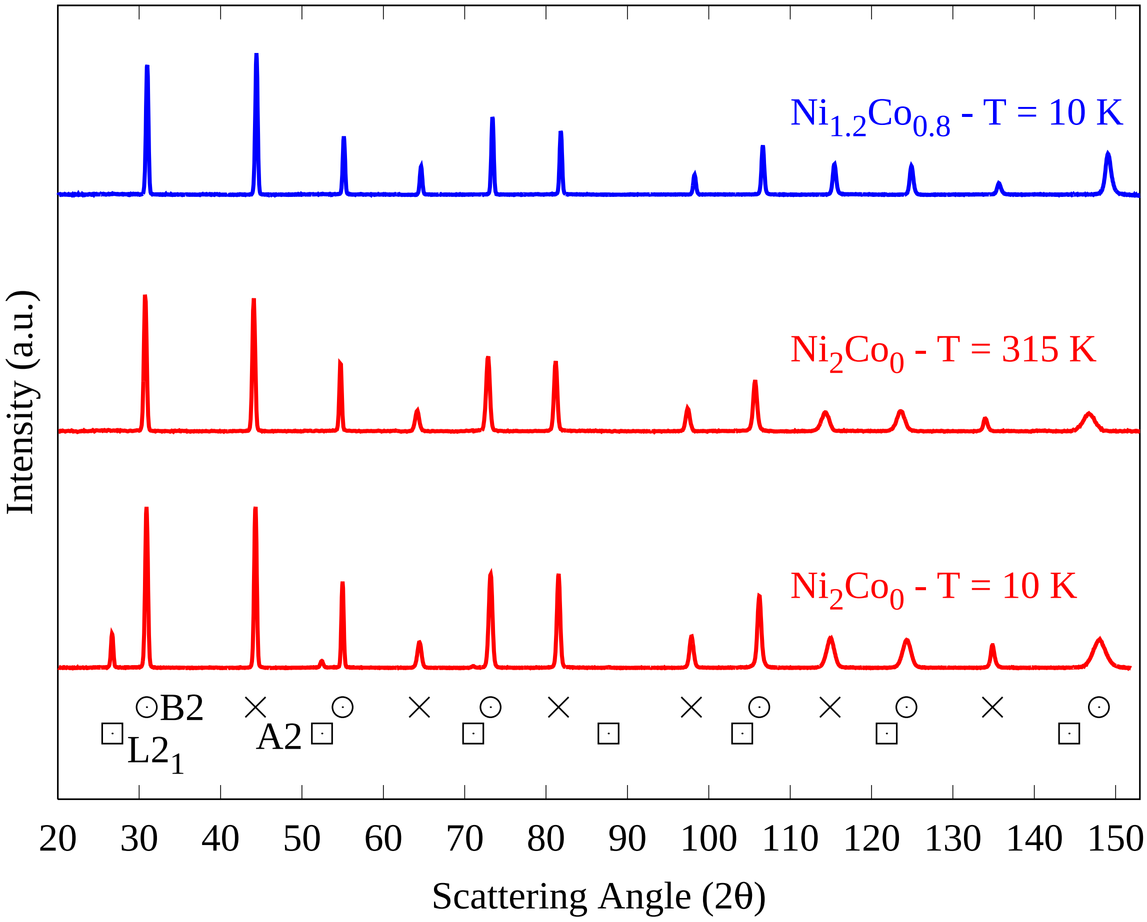

Figure 5.13:
Neutron powder diffraction data for Ni_2MnAl (at T = 10 K and T = 315 K) and $Ni_{1.2}Co_{0.8}MnAl$ (at T = 10 K).

and $Ni_{1.2}Co_{0.8}MnAl$ have a B2 structure with no $L2_1$ peaks visible. However, in Ni_2MnAl (see curve at 10 K) at low temperatures an antiferromagnetic superstructure at the $L2_1$ peak positions is observed. The magnetic nature of these peaks can clearly be deduced from their intensities decaying with scattering angle according to the characteristic magnetic form factor. Additionally, the peak intensities are temperature dependent and the superstructure peaks are not visible anymore in the paramagnetic state at 315 K. Satellite peaks as reported by Ziebeck et al. [1] are not visible in the presented diffractograms. Instead, the magnetic structure seems to be prototypically antiferromagnetic. In $Ni_{1.2}Co_{0.8}MnAl$, the absence of $L2_1$ peaks even at low temperatures indicates a ferromagnetic ordering of the spins. The transition between the antiferromagnetic and the ferromagnetic regime was found at compositions of approximately 10 at. % Co.

[1] K. R. A. Ziebeck, P. J. Webster, *J. Phys. F: Met. Phys.* **5**, 1756 (1975)

[2] M. Halder, M. D. Mukadam, K. G. Suresh, S. M. Yusuf, *J. Magn. Magn. Mat.* **377**, 220 (2015)

[3] M. Hoelzel, A. Senyshyn, O. Dolotko *Journal of Large-Scale Research Facilities* **1**, A5 (2015)

[4] M. Hoelzel, A. Senyshyn, N. Juenke, H. Boysen, W. Schmahl, H. Fuess *Journal of Nuclear Instruments and Methods A* **667**, 32-37 (2012)

5.6 Investigation of conductive polymers for thermoelectric applications

R. M. Kluge, N. Saxena, P. Müller-Buschbaum

Thermoelectric generators are a promising approach in renewable energies, as they are able to convert waste heat into electricity. Possible applications are large scale applications like recovering the waste heat of a car engine as electricity as well as niche applications like using the heat emitted by human skin to drive a watch. [1]
In order to build high efficiency thermoelectric devices, suitable thermoelectric materials are needed. Unfortunately, state-of-the-art thermoelectric materials have the drawback of using toxic or less abundant constituents, making it necessary to look for alternatives. One promising approach is to use conjugated polymers. They have the encouraging ability of easy and various types of scalable solvent processes like roll-to-roll printing. Although they are still less efficient than their inorganic counterparts, their easy synthesis, flexibility and eco-friendliness make them a valuable alternative. For building a thermoelectric generator, p- and n-type materials have to be combined as shown in Figure 5.14.

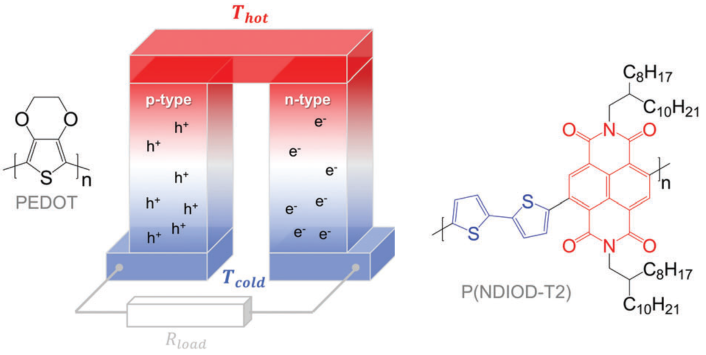

Figure 5.14: Sketch of a thermoelectric generator and the chemical structure of the used n- and p-type polymers next to the respective leg (modified from [2]).

A typical thermoelectric device consists of many thermocouples linked electrically in series and thermally in parallel. Traditionally, the thermocouple consists of an n- and a p-doped leg of semiconductors. Applying a temperature gradient across the thermocouple as shown in Fig. 5.14 forces the holes in the p-type leg and the electrons in the n-type leg to simultaneously flow to the cold side. This so-called Seebeck effect leads to an electrical potential that can be collected by connecting a load to the thermocouple.

A measure for the performance of a thermoelectric material is the figure of merit zT which is linked to the electrical conductivity σ, the thermovoltage S, the thermal conductivity κ and the temperature T according to formula 5.1.

$$zT = \frac{\sigma \cdot S^2}{\kappa} \cdot T \tag{5.1}$$

Among various, especially p-type, conducting polymers having been investigated as thermoelectric material, PEDOT is considered to be a very promising candidate. The reason why n-type polymers are rather neglected may be their little stability towards oxygen and moisture. Nonetheless, both types of materials are needed to build a thermoelectric generator. Therefore, we also focus on the thermoelectric properties of an n-type polymer P(NDI2OD-T2). Its successful application to transistors and solar cells encourages an auspicious try to build an

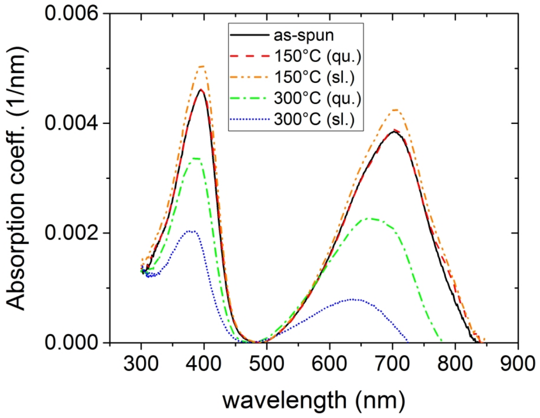

Figure 5.15: Influence of the annealing process of spin-coated P(NDI2OD-T2) thin films on the absorption spectrum. In the picture "sl." stands for slowly cooled and "qu." for quenched.

all-polymer thermoelectric generator. Both polymers which are investigated in this project are shown in Fig. 5.14 next to the leg where they are of potential use.

The main goal on the way to building an actual device is of course the improvement of the used materials. Hereby possible approaches may include chemical dopants to tune the amount of charge carriers in the material or to change the morphology of the material to enhance the mobility of the charge carriers. Both approaches lead to an increase in electrical conductivity and therefore to an improved thermoelectric behavior. Here, another approach will be introduced to enhance the properties of the n-type polymer P(NDI2OD-T2).

In order to increase the thermoelectric performance by a change in morphology and subsequently tuning the crystallinity and arrangement of the molecules in the thin film, the annealing temperature after spin-coating was investigated. Rivnay *et al.* showed that annealing the film at high temperatures above the melting point and subsequently slowly cooling the film down to room temperature can lead from an edge-on to a face-on arrangement of the molecules.[4] This may also have an impact on electrical transport as the overlap of adjacent π orbitals of the molecules may become larger or smaller, facilitating or hindering charge transport. In Fig. 5.15 the absorption properties of the thin films are shown giving a first insight in changes of the morphology. The absorption spectrum is characterized by a high-energy peak attributed to the π - π^* transition and a broad, low-energy band ascribed to the charge-transfer (CT) transition that evolves significant redistribution of electrons from the donor moiety to the acceptor unit along the main chain.[5] With lower annealing temperature both peaks are red-shifted, indicating that the transitions are easier. To make a clear statement, further investigations are necessary. However, this experiment opens the chance to tune morphology and electrical transport properties simply by adjusting one parameter, the annealing temperature.

[1] G. J. Snyder, *The Electrochem. Soc. Interface* **17**, 54–56 (2008)

[2] R. Kroon, D. A. Mengistie, D. Kiefer, J. Hynynen, J. D. Ryan, L. Yu, C. Müller, *Chem. Soc. Rev.* **45**, 6147-6164 (2016)

[3] J. Rivnay, R. Steyrleuthner, L. H. Jimison, A. Casadei, Z. Chen, M. F. Toney, A. Facchetti, D. Neher, A. Salleo, *Macromolecules* **44**, 5246-5255 (2011)

[4] R. Steyrleuthner, M. Schubert, I. Howard, B. Klaumünzer, K. Schilling, Z. Chen, P. Saalfrank, F. Laquai, A. Facchetti, D. Neher, *J. Am. Chem. Soc.* **134**, 18303-18317 (2012)

5.7 Mechanical characterization of pressure sensitive adhesives applied to fibers

V. Körstgens, J. Corella Puertas, P. Müller-Buschbaum

Pressure sensitive adhesives (PSAs) constitute a class of adhesives that form a bond to a surface when slight pressure is applied on them. The stickiness of PSAs is based on its visco-elastic properties and no solidification by a cross-linking process or solvent evaporation is involved. There are a multitude of applications that range from industrial applications as in the assembling of mobile phones to scotch tape and sticky notes. Another application used in daily life is in hair styling products like hair gels. In order to quantify the adhesive properties and investigate the debonding mechanisms of PSAs the probe-tack test is a well-established methodology [1]. The probe-tack test uses a cylindrical probe approaching a flat PSA surface. For the investigation of adhesive layers on curved surfaces the method has to be adapted. We developed a new methodology for characterizing the adhesion of PSAs on a monolayer of fibers. This methodology is studied in this work, and tested on a monolayer of either human hair or nylon fibers coated with a polymer blend representing a PSA with tack properties depending on humidity conditions.

The first prerequisite for meaningful tack measurements on fibers is the reproducible preparation of homogeneous samples. We developed a method to densely align fibers in parallel on a substrate without harming the surface properties of the individual fibers. In Fig. 5.16 the successful attachment of two types of fibers on a solid substrate is demonstrated. Fig. 5.16a) shows the top view of nylon fibers with 300 μm diameter attached to an adhesive-coated glass slide. The microscopy images for nylon fibers with 300 μm and 150 μm diameter, respectively (Fig. 5.16b) and c)) show the close contact of the individual fibers of the same diameter. In contrast for human hair as a natural fiber, the individual fibers have different diameters around 100 μm as can be observed in Fig. 5.16d). The microscopic images also reveal distinct surface features of the fibers: on one hand longitudinal corrugations for the nylon fibers caused by the spinning process and on the other hand the cuticle structure of hair.

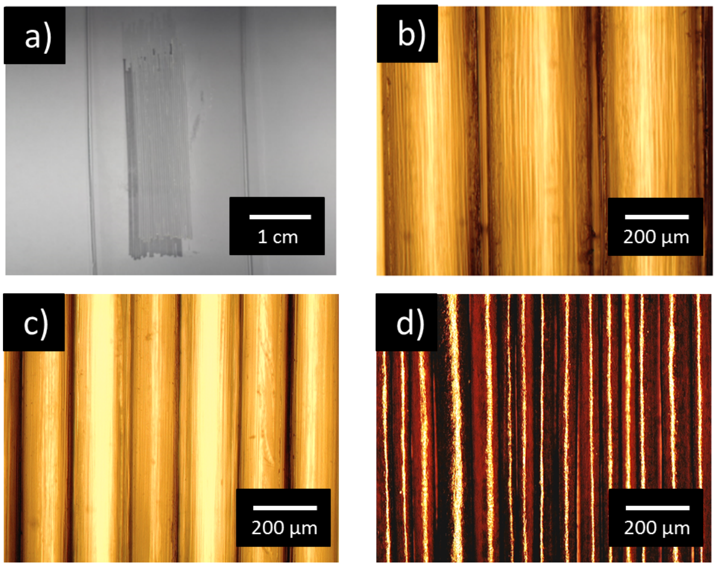

Figure 5.16:
Top view of monolayer of aligned fibers on glass substrates with adhesive layer a) b) picture and microscopy image of nylon fibers with 0.3 mm diameter, c) nylon fibers with 0.15 mm diameter and d) human hair.

As an example for the tack measurement on fibers we coated monolayers of human hair in a solution casting process with a blend of the copolymer polyvinylpyrrolidone-co-polyvinyl acetate (PVP-co-PVA, BASF VA64) and polyethlylene glycol (PEG). This polymer blend is investigated as a representative for a PSA with tack properties depending on humidity. The probe in a conventional probe tack test is a flat-ended incompressible cylinder of e.g. stainless steel. In our method we use a composite stamp which consists of natural leather at the top of the probe. Leather is chosen because of its similarity to skin. In this way the investigation of tack properties of polymer blends also used in commercial hair styling compositions mimics the experience of stickiness by touching hair with the fingers after hair styling product had been applied. The probe also contains a polyurethane foam core which allows the adaption of the leather to the probed curved adhesive surface.

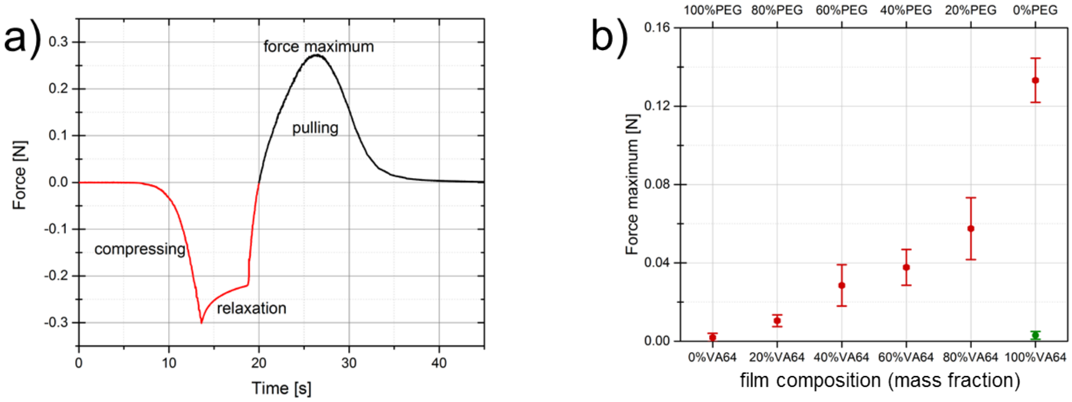

Figure 5.17:
Tack properties of a layer of a polymer blend of polyethylene glycol (PEG) and polyvinylpyrrolidone-co-polyvinyl acetate (PVP-co-PVA) on human hair. a) example measurement showing the uniaxial compression and relaxation (in red) and the retraction part of the experiment b) force maximum of the adhesion on the hair samples for different composition of the polymer blend. Measurements denoted by red circles are carried out at high humidity conditions. Only the pure PVP-co-PVA shows marginal tack at low humidity conditions (green circle).

The film coated sample of fibers is fixed to the apparatus below the stamp. The stamp moves with a constant velocity of 50 μm/s towards the sample until it touches it with a force of 0.3 N. The stamp remains for 5 s motionless and then is retracted from the sample at a constant velocity of 100 μm/s. During this protocol the force and the distance are recorded. Fig. 5.17a) shows a full measurement of polymer-coated fibers as measured force versus time. After the stamp stops moving as the maximum chosen force of 0.3 N is reached, relaxation of the measured force is observed. This is mainly due to the visco-elastic nature of the foam core and the leather of the stamp and has only a minor contribution by the thin adhesive layer. The stages of uniaxial compression and relaxation (marked in red in Fig. 5.17a)) is followed by the retraction part of the experiment. One quantity to be extracted from the force-distance curves is the force maximum during the debonding process. Tack properties of a layer of a polymer blend of PEG and PVP-co-PVA on human hair have been investigated. The force maxima for the polymer blend with varying composition are plotted in Fig. 5.17b). Measurements denoted by red circles are carried out at high humidity conditions above 70 % rel. humidity. The polymer blends do not show adhesive properties at dry conditions of below 30 % rel. humidity. Only the pure PVP-co-PVA shows marginal tack of (0.003±0.002) N at low humidity conditions (green circle). This example for the application of the probe tack methodology for fibers shows that PVP-co-PVA is the component of the polymer blend responsible for the tack properties and how increasing the mass fraction of PEG in the polymer blend allows for the adjustment of tack properties at high humidity conditions.

[1] P. Müller-Buschbaum, T. Ittner, E. Maurer, V. Körstgens, W. Petry, *Macromol. Mater. Engin.* **292**, 825-834 (2007)

5.8 Structural study of block copolymer electrolytes during lithium stripping/platting cycling

E. Metwalli, B. Springer, C. Herold, R. Cubitt[1], P. Müller-Buschbaum

[1] ILL, Grenoble (France)

Lithium ion batteries offer high energy densities as well as high discharge potential and low self-discharge, which makes them the most promising battery system currently available. However, in order to overcome safety concerns, solid polymer electrolytes are essential. Solid-state polymer electrolytes (SPE) such as polyethylene oxide (PEO) have been investigated extensively due to their high alkali metal conductive properties. To further improve the mechanical/thermal stability of PEO whilst maintaining good conductivity, the use of polystyrene-block-polyethylene oxide PS-b-PEO diblock copolymer (DBC) was investigated [1-3]. In these studies, the lithium-ion-doped DBC electrolyte proved advantageous over the polyethylene oxide (PEO) homopolymer, because the conductive PEO block has the ability to solvate lithium ions, the glassy polystyrene (PS) block offers a mechanically/thermally stable membrane, especially at elevated temperatures. In the present report, the structure of a Li-ion containing solid-state PS-*b*-PEO DBC electrolyte was investigated during lithium ion stripping/platting cycling. The aim of this study was to explore the evolved morphological modification of the Li-ion containing DBC electrolyte, as well as the electrode-electrolyte interface stability during galvanostatic cycling. The nanostructured Li-ion/DBC electrolyte (300 μm) film was sandwiched between two non-blocking lithium electrodes via a solution casting process. Time-resolved (10 s) in situ small angle neutron scattering (SANS) measurements were then performed at D22 beamline (ILL) during lithium stripping/platting cycling, with impedance spectroscopy measurements acquired at the end of each galvanostatic cycle, thereby obtaining the resistance of the cell. The duration of complete charge/discharge cycles was set at about 12 minutes. To act as a significant contrast to our electrolyte, deuterated PS (PSd) and protonated PEO blocks of the DBC were employed. As indicated by the scattering rings in the SANS 2D scattering patterns (Fig. 5.18), the prepared solid-state Li-ion/DBC ([Li]/[EO] = 0.1) successfully provided an adequate contrast to the nanostructured Li-ion/DBC electrolyte. The SANS 1D profiles plotted in Fig. 5.19 illustrate the cylindrical structure of the as-prepared Li-ion/DBC electrolyte. At both 20°C and 35°C, the SANS investigation revealed no significant morphological changes taking place during lithium stripping/platting cycles (Fig. 5.19); only the 35°C plots are shown), with a stable morphology observed that exhibited no structural modification up to 15 cycles. These results indicate that the nanostructured morphology is able to survive possible degradation during operation.

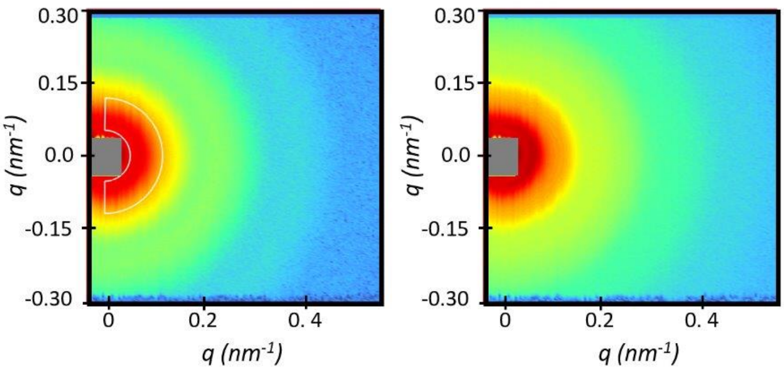

Figure 5.18:
2D SANS scattering patterns of Li-salt/DBC hybrid electrolyte sandwiched between two thin lithium metal electrodes at 20°C (left) and 85°C (right).

At higher temperatures of 65°C and 85°C (Fig. 5.19), extended inter-domain spacing was initially observed during the first cycle, indicating some structural changes. However, these structural modifications cannot ultimately explain the measured high conductivity enhancement

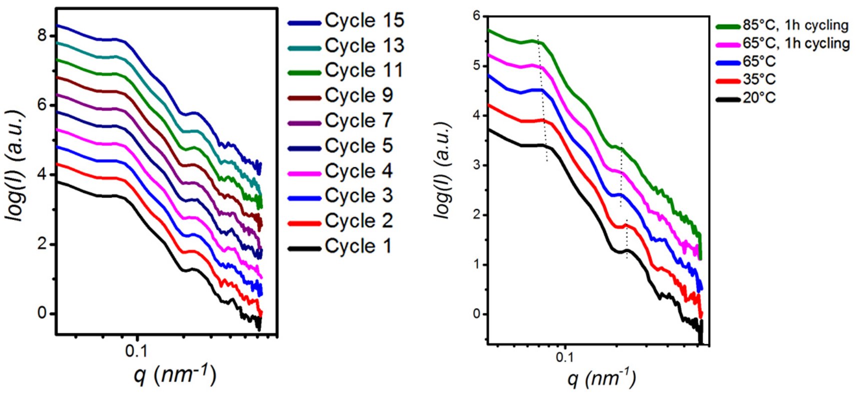

Figure 5.19:
1D SANS profiles of the Li-ion/DBC hybrid electrolyte during various lithium stripping/platting cycles at 20°C (left) and at different temperatures (right). The data are vertically offset for clarity.

(data not shown) of the electrolyte at the elevated temperatures. Nevertheless, following the first cycle at higher temperatures (>50°C), the morphology again showed no further changes, either in the form of phase-transformation or in inter-domain distance. The structure thus does not seem to be severely penalized by a high-temperature operation half-cell battery, even at an extended cycling time of one hour. Rather, the observed increase in domain spacing D and enhancement in the conductivity of the electrolyte may be attributed to an increase in Li-ion solubilization and concomitant PEO chain mobility enhancement at the elevated temperatures.

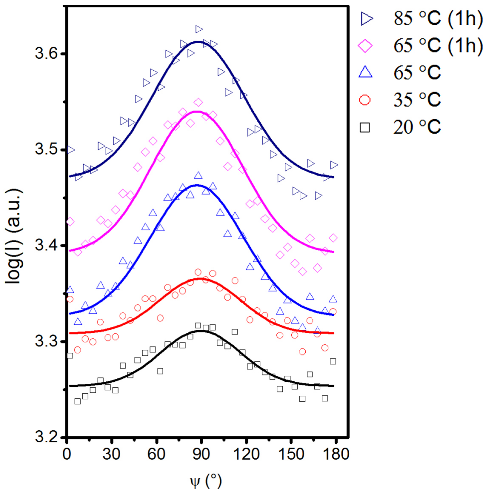

Figure 5.20:
Azimuthal SANS intensity profiles corresponding to the reciprocal space vector of the main interference maximum between 0.053-0.119 nm^{-1}. The solid lines represent fits of the data with Gaussian functions. The curves are vertically offset for clarity.

One exciting observation is the level of domain alignment following the increase in the temperature upon cycling (Fig. 5.20). The possible migration of the lithium ions during the galvanostatic process seems to open pathways between the two electrodes, so that at high enough temperatures domain re-orientation is favored. The absence of any new scattering features and stable nano-scale morphology strongly implies that any possible dendrite growth is highly suppressed by the solid-state electrolyte. Further analyses of these results are currently in progress.

[1] E. Metwalli, M. Rasool, S. Brunner, P. Müller-Buschbaum, *ChemPhysChem* **16**, 2882-2889 (2015)

[2] W. S. Young, W. F. Kuan, T. H. Epps, *J. Polym. Sci. Pol. Phys* **52**, 1-16 (2014)

[3] I. Gunkel, T. Thurn-Albrecht, *Macromolecules* **45**, 283-291 (2012)

5.9 In-situ small angle X-ray scattering investigation of solid-state polymer electrolyte for lithium-ion batteries

G. Möhl, E. Metwalli, B. Springer, R. E. Johnsen[1], P. Müller-Buschbaum

[1] TU Denmark, Roskilde, Denmark

The major concern regarding the safety of liquid electrolytes in lithium-ion batteries may potentially be overcome by the use of solid-state polymer electrolytes (SPE). Polystyrene-block-polyethylene oxide (PS-*b*-PEO) diblock copolymer (DBC) electrolytes have been recently investigated as a membrane for Li-ion batteries. The performance of these DBC electrolytes strongly depends on their morphology, where highly oriented PEO domains serve as pathways for lithium-ion migration. Thus, in-situ structural investigations of these Li-ion doped DBC systems is essential during cycling in an operating battery. A capillary-based micro-battery cell allowing simultaneous structural and electrical evaluation has previously been reported [1].
In the present study, a capillary-based lithium/SPE/lithium half-cell is prepared and the SPE is investigated using temperature dependent in-situ small angle X-ray scattering (SAXS) during lithium metal stripping/plating. The cell design is shown in figure 5.21, which depicts the glass capillary housing, the two electrodes and its polymer electrolyte fill.

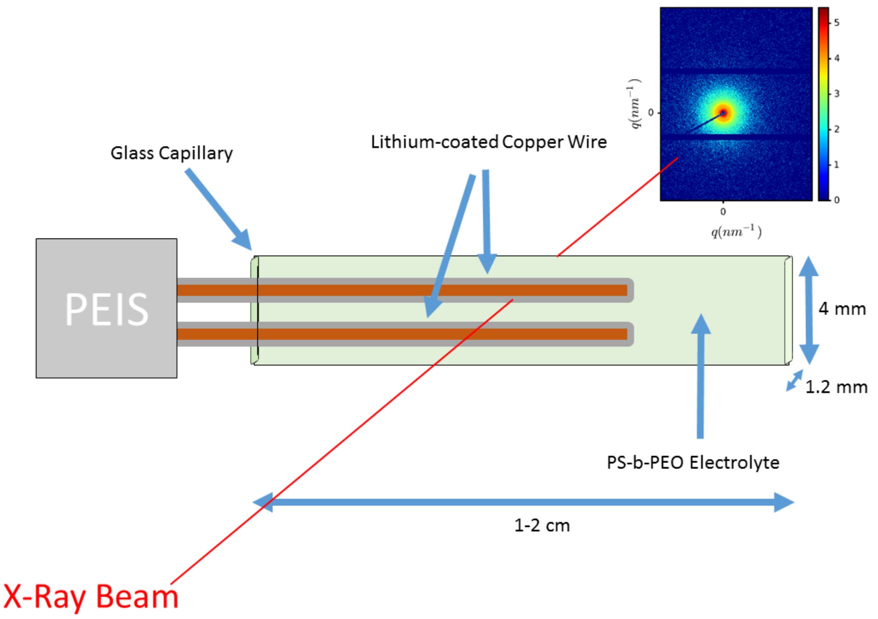

Figure 5.21: Schematic setup of the cell for in-situ SAXS measurements.

Thin lithium metal electrodes are prepared on copper metal sticks by electrochemical plating using a solution of bis(trifluoromethane)sulfonimide (LiTSFI) in tetrahydrofurane (THF). The electrolyte was composed of a solution 5 wt% PS-*b*-PEO (13500-33500 kg/mol) block copolymer in THF solvent, which was then solution cast on the two lithium electrodes. The lithium salt LiTSFI was added in an amount corresponding to a Li/EO ratio of 0.1, which has been found by Metwalli et al. [2] as being the optimum ratio regarding the ionic conductivity performance of the electrolyte. The capillary was filled with the electrolyte, left to dry and then sealed. Next, the half-cell was placed on a stage which was kept constantly at 25°C. The SAXS data were acquired in a static as well as in a dynamic setting during galvanostatic cycling, using a Ganesha 300 XL instrument by SAXSLAB, which includes a Genix 3D (XENIX) monochromatic X-ray source with a copper anode and wavelength of 0.15418 nm (K-alpha). The images were recorded on a Pilatus 300K detector having pixels of 172 x 172 μm in size at a distance of 1051 mm. Using impedance spectroscopy (IS), the resistance of the cell was evaluated at the end of each cycle. A result from such a measurement can be seen in figure 5.22, which depicts the impedance spectrum of the used cell after one selected cycle. As these curves did not change over cycling, only one is displayed as an example. The data has been fitted by using an equivalent circuit model as described by Schaper [3] from which a resistivity of approximately $3 * 10^6$ was extracted.

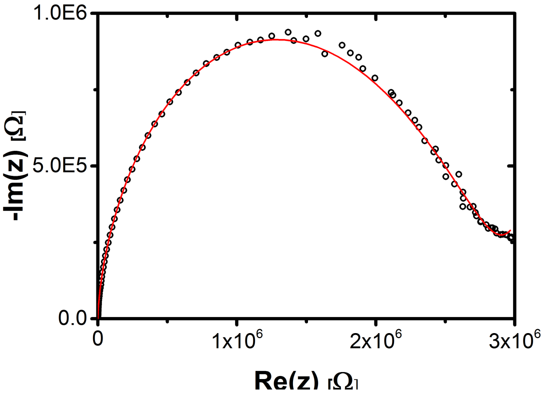

Figure 5.22: Nyquist impedance plot of the measured impedance data.

From the 2D SAXS images, one dimensional radial cuts where collected and plotted for several charge and discharge cycles, as can be seen in figure 5.23, the solid-state polymer electrolyte remains stable in its morphology over cycling at 25°C , without any noticeable changes neither a phase transformation nor a interdomain spacing. For future measurements, different temperatures should be measured in order to enhance the conductivity of the polymer and thus the performance of the half-cell.

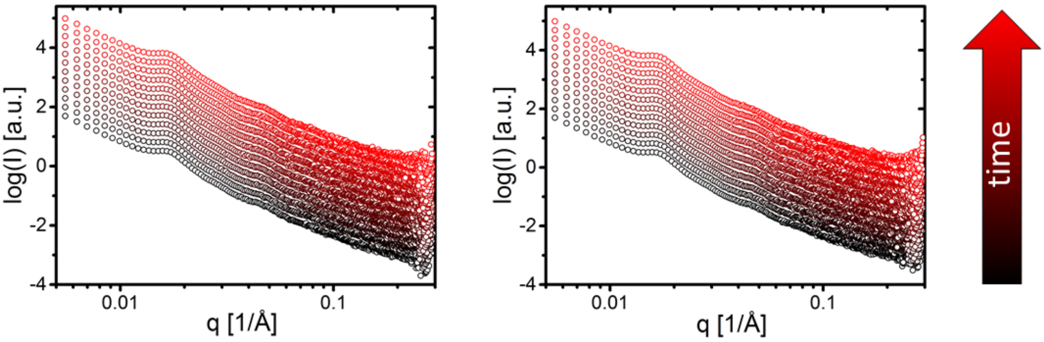

Figure 5.23:
Radial cuts of the 2D SAXS data for several charge (left) and discharge cycles measured in-situ during galvanostatic cycling.

[1] R. E. Johnsen, P. Norby, *Chem. Mater.*, **13**, 4682-4692 (2015)

[2] E. Metwalli, M. Rasool, S. Brunner, P. Müller-Buschbaum, *ChemPhysChem*, **13**, 2882-2889 (2015)

[3] S. Schaper, Self-assembled hybrid materials as a membrane for lithium-ion batteries, Master Thesis TU Munich (2016)

5.10 Structural study of lithium salt containing PLMA-*b*-PMAA block copolymer electrolytes

B. Springer, E. Metwalli, S. Pispas[1], P. Müller-Buschbaum

[1] Theoretical and Physical Chemistry Institute, NHRF, Athens, Greece

The increasing demand for renewable energies, in particular wind and solar energy, gives rise to an increased interest in energy storage. Lithium-ion batteries are very attractive energy storage media due to their remarkable characteristics, like high energy densities and low self-discharge rates [1]. Most commercially used Li-ion batteries operate a liquid electrolyte with a separator membrane to prevent short circuits. The liquid electrolyte poses a risk since they are instable and highly flammable. Block copolymers (BCPs) are a possible alternative due to their ability to self-assemble into nanostructures. This self-assembly can be tuned in different ways. For example, the fraction of one block is a very important factor to determine the evolved morphologies. Another way to modify the nanostructures is bringing charges into one of the blocks of the BCP [2]. This charged polymer give rise to an additional modification than that predicted by conventional BC phase diagrams, due to electrostatic interactions.

In the present study, we investigated the structure of poly(lauryl methacrylate-b-methacrylic acid) (PLMA-b-PMAA) diblock copolymer (DBC) upon lithium salt loading. The PLMA-b-PMAA DBC has a total molecular weight of 12600 kg/mol and a PLMA weight fraction of 0.50. The samples were prepared using the solution-casting method with THF as the solvent. A solution of 5 wt% was prepared and then pipetted on a mica window to prepare samples for small angle X-ray scattering (SAXS) measurements. Between each drop of solution we waited 20 minutes. After a complete drying, we assembled the sample holder for the SAXS measurements. All preparation steps were conducted under an argon atmosphere in a glove box. After assembly, the samples were annealed for 168 hours at 155° C in a vacuum oven. Each sample was measured at temperatures from 25° C to 295° C in 10° C steps during the SAXS measurements. For each temperature step the measurement lasted one hour.

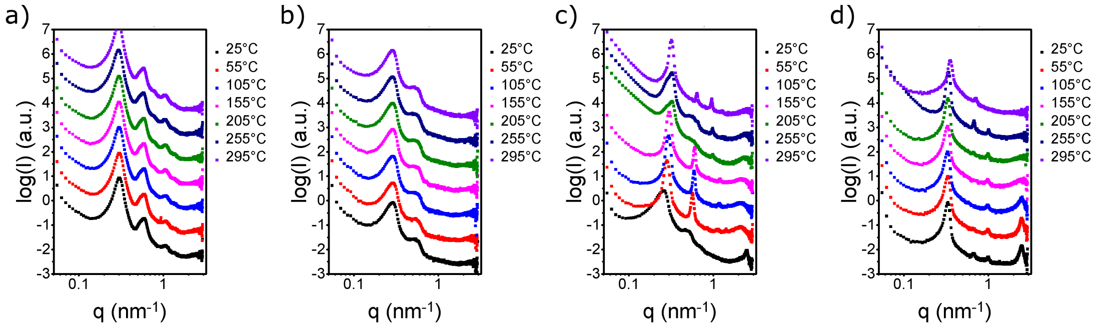

Figure 5.24:
Temperature dependent SAXS profiles of PLMA-b-PMAA DBC with four different [Li]/[LMA+MAA] ratios: a) 0 , b) 0.05, c) 0.1, and d) 0.2.

Figure 5.24 shows temperature dependent SAXS profiles of PLMA-b-PMAA DBC with four different [Li]/[LMA+MAA] ratios. A small structural change upon heating can be seen for 0, 0.05, and 0.2. However, a phase transformation upon heating is observed for r= 0.1. Figure 5.25 shows the room temperature SAXS profiles together with model fits. The data was fitted using

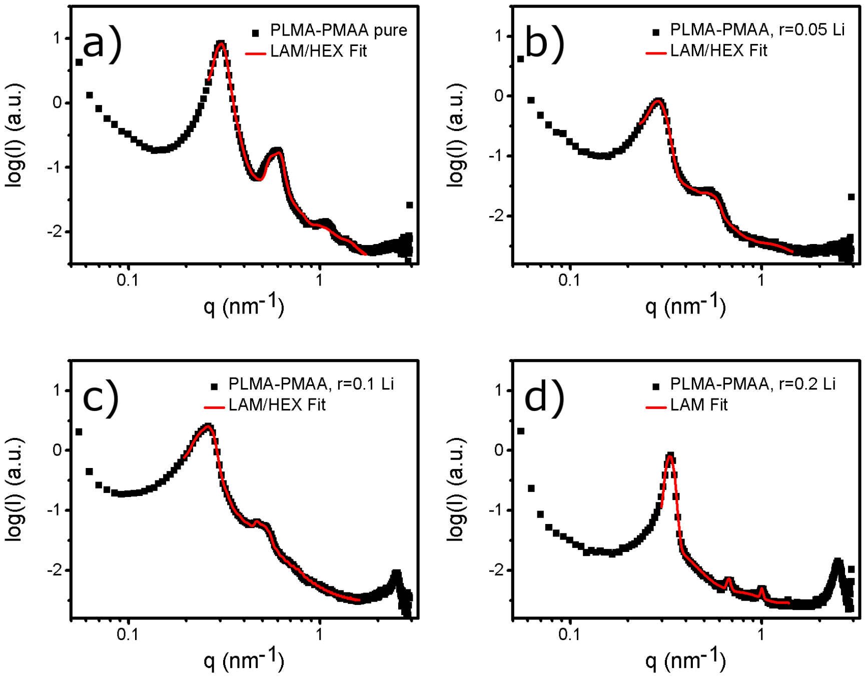

Figure 5.25:
Room temperature SAXS profiles (symbols) for [Li]/[LMA+MAA] ratios of a) 0 , b) 0.05, c) 0.1, and d) 0.2 shown together with model fits (lines) based on an model approach as indicated.

SASfit software. For 5.25 a) and 5.25 b) a mixed model of lamellae and hexagonal cylinders was used. In this model, the hexagonally packed cylinders are the majority phase. For 5.25 c) the same model was used, but further fittings are required due to morphological changes upon temperature increase. At high lithium salt upload (r = 0.2), the data were fitted using a lamellae model. This is very interesting, since we can see a change in the mesoscopic structure upon lithium ion incorporation. The structural modification upon salt incorporation can be attributed to the electrostatic cohesion effect predicted by theoretical studies [2]. Electrostatic cohesion effect means that the polar or even charged groups in our polymer will assemble around the lithium ions. According to Sing et al. [2] this cohesion will lead to a shift in the phase diagram, therefore leading to phase transformation. Sing et al. set a new parameter Γ, which expresses the strength of the electrostatic cohesion, similar to the Flory-Huggins parameter χ. Γ is given by

$$\Gamma = \frac{e^2}{8\pi\epsilon_0\epsilon_r k_b T} \tag{5.2}$$

Here, ϵ_0 is the relative dielectric constant of vacuum, ϵ_r is the relative permittivity of the polymer, a is the radius of the added ions and T is the temperature. In further analysis we will deal in detail with the change in morphology induced by the Li-ions. Also impedance measurements will be collected to monitor the effect of the morphology change on the ionic conductivity and its suitability for Li-ion battery applications.

[1] W. S. Young, W. F. Kuan, T. H. Epps III, *J. Polym. Sci. B: Polym. Phys.* **52**, 1-16 (2014)

[2] C. E. Sing, J. W. Zwanikken, M. Olvera de la Cruz, *Nat. Mater.* **13**, 694-698 (2014)

6 Instrumentation

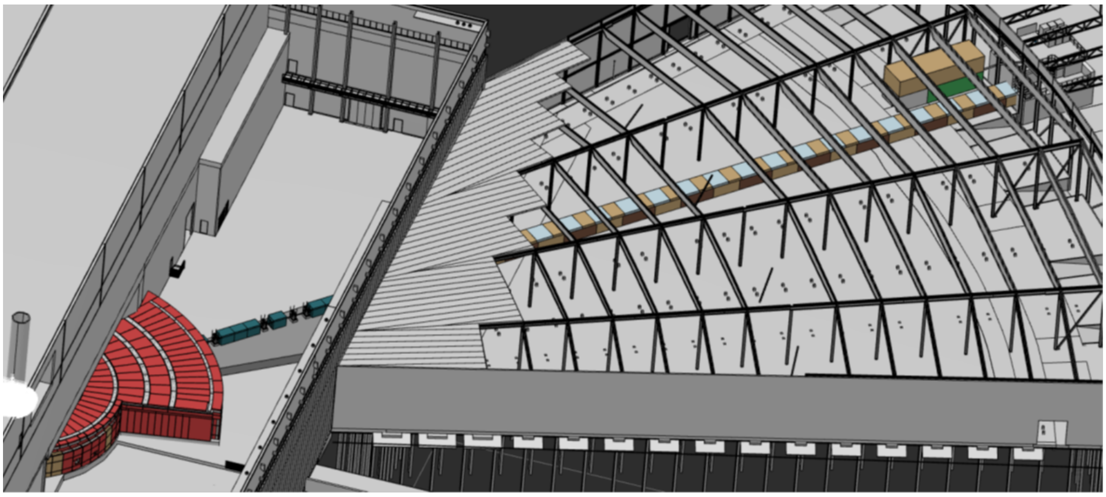

6.1 Vacuum chamber for in-operando grazing-incidence X-ray scattering experiments on novel thin-film solar cells

B. Kalis, J. Schlipf, P. Müller-Buschbaum

In-operando studies on solar cells have given fundamental insights into aging mechanisms of classical polymer:fullerene solar cells [1] and low band gap solar cells [2]. These experiments were performed with a special designed sample chamber which enabled x-ray scattering experiments in combination with illumination using simulated sun light conditions.
In the present project a new vacuum-chamber is designed and tested which enables grazing incidence wide angle x-ray scattering (GIWAXS) as well as the so far performed grazing incidence small angle x-ray scattering (GISAXS). A new design is created which consists of four main modules using the 3D-drawing program SOLIDWORKS. The modular construction enables an increased universality of the new chamber. It can be combined with several per-installed provider-setups and is easy to handle. The mentioned modules are namely the chamber itself, a chamber holder, a sample holder in the chamber and a construction to hold the pocket-solar-simulator in position, shown in Fig.6.1.

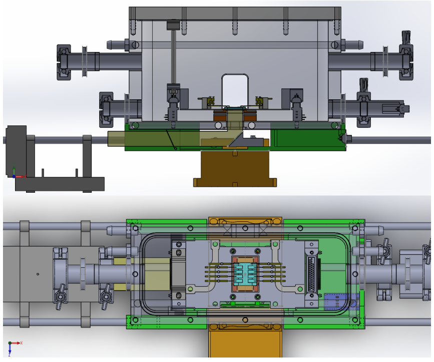

Figure 6.1:
Top) Sectional front-view of the setup with all modules and the light path. The chamber-holder is shown in green and the provider-setup in orange. The guidance for the pocket-solar-simulator is seen on the left side. Bottom) Top-view of the setup showing also the electrical contacts for measuring the solar cells (light blue).

Vacuum conditions in the new chamber will reduce background scattering of the x-ray beam when passing through it. Moreover, it will prevent aging of solar cell related to oxygen or humidity. The vacuum conditions are generated by a scroll-pump. In the new chamber a moderate vacuum of 0.078 mbar can be reached. This is an improvement as compared to the existing chamber in which commonly a vacuum of 0.2 mbar was reached [1]. Main reasons for the improved vacuum conditions are the use of a thicker chamber cap and the usage of a better sealing at the cap and flashes.

To be able to probe a large part of q space in GIWAXS, a big exit window for the scattered x-ray beam was implemented in combination with new electrical probes (Numb. 5 in Fig.6.2). Their body is slimmer and should reduce the shadowing effect by having a almost horizontal attachment. With the realized exit window it is possible to observe a 2Θ angle up to 60° in perpendicular direction to the sample-surface and a maximum angle of 42° parallel to the surface. With such angular range it if for example possible to observe the $\{210\}$ of a $MaPbI_3$ perovskite in the cubic structure [2].

This $\{210\}$ peak has its origin in a structural change of the perovskite happening at 54°C–57°C [2]. It can be observed in the new chamber as there is a PID-regulated temperature control of the sample which is powered with two Peltier elements of each 10.4 W. Since the Peltier elements can be controlled separately, it is possible to apply a temperature gradient in the sample. The temperature is measured by four PT100 which gives a failure security (1 out of 4 without gradient and 1 of 2 with gradient). As heat-sink the Peltier elements are connected to copper blocks which are again in contact with the cooled bottom of the chamber(Numb. 4 in Fig.6.2).

The cooling of the chamber (Numb. 3 in Fig.6.2)is necessary due to the partial illumination by the pocket solar and due to the heat transfer from the copper-blocks mentioned before. As water-cooling is the cheapest and easiest way a pipe system is implemented in the chamber walls which can be used in two directions for better incorporation into the existing sample environment. With combination of a temperature controlled water cycle the temperature of the chamber is well controlled.

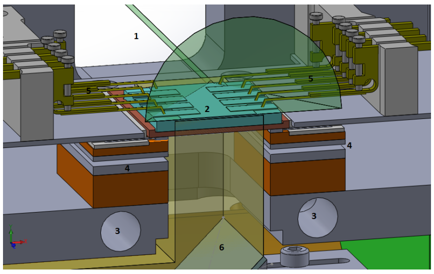

Figure 6.2:
Close-up of part of the new sample chamber: The X-ray beam (1) is scattered on the solar cell (2). The cooling pipes (3) are in the chamber bottom and the Peltiers elements are connected with copper blocks (4) on both sides. On top of the solar cell the electrical contacts (5) are placed and at the bottom the mirror (6) is visible.

The electrical contacts of all parts of the chamber are connected with a 44-Pin-D-Sub plug. This plug is used twice for a double side connection to the chamber and a symmetric fixation of the sample-holder. Presently, only 35 of the 44 Pins are used. As a consequence, the possibility to upgrade the functionality of the chamber with minimal effort is implemented.

The third part of the modularized setup is the chamber holder, which is directly attached to the provider-setup and allows a quick removing of the chamber. It also contains the mirror and guidance for the pocket-solar-simulator. A mirror is necessary as the illumination of the solar-cell should be from the bottom side (Numb. 6 in Fig.6.2), where also the fixation to the provider-setup takes place. With the guidance and fixed mirror, it is possible to calibrate the pocket-solar-simulator, days before a beam time and save valuable measurement time at the synchrotron. As all other parts, the chamber-holder has also a symmetry and can be rotated by 180° around its vertical axis.

Thus, symmetries of the chamber-cooling, the electrical connection and the 180° rotatability of the chamber-holder allow a flexible mounting at any provider-setup as one can choose the side of connection to cooling-water, electricity and the preferred space for the pocket-solar-simulator.

There is also space for some electronics in the design of the chamber-holder. By this it is possible to use a micro-controller to operate the measurement conditions. A graphical user interface is put in work for the control of the sample-temperature, the solar cell measurements and the illumination-shutter as well as for the monitoring of all temperatures and the measurements of the DHT11 sensor.

[1] C. J. Schaffer, C. M. Palumbiny, M. A. Niedermeier, C. G. Santoro, S. V. Roth, P. Müller-Buschbaum, *Adv. Mater.* **25**, 6760-6764 (2013)

[2] C. J. Schaffer, C. M. Palumbiny, M. A. Niedermeier, C. Burger, G. Santoro, S. V. Roth, P. Müller-Buschbaum, *Adv. Energy Mater.* **6**, 1600712 (2016)

[3] T. Baikie, Y. Fang, J. M. Kadro, M. Schreyer, F. Wei, S. G. Mhaisalkar, M. Grätzel, T. J. Whitec, *J. Mater. Chem. A* **1**, 5628-5641 (2013)

6.2 Optimization of a high-pressure cell and investigation of thermoresponsive polymers

P. Haslauer, B.J. Niebuur, K.L. Claude, A. Schulte[1], C. M. Papadakis

[1] University of Central Florida, Orlando, U.S.A.

Thermoresponsive polymers are an interesting class of materials, because they change their properties drastically upon a small change of temperature. One prominent example is poly(N-isopropylacrylamide) (PNIPAM). This polymer has a lower critical solution temperature (LCST) behavior, i.e. it is water-soluble above a certain temperature, T_{CP} (CP stands for cloud point), but water-insoluble above. The phase behavior of aqueous solutions of PNIPAM has been found to be pressure-dependent, and the phase diagram has been mapped out in dependence on temperature and pressure using turbidimetry (Figure 6.3, [1]).

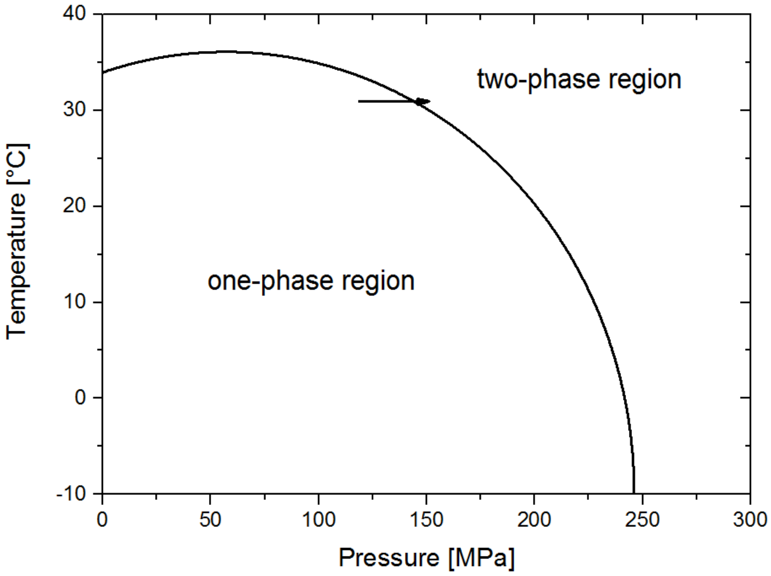

Figure 6.3:
Phase diagram of a 3 wt% solution of PNIPAM in D_2O, determined using turbidimetry [1]. The arrow indicates the pressure jump carried out in the present project.

The kinetics of aggregation of water-insoluble polymers upon crossing the phase transition gives information about the growth processes of the aggregates and thus the interactions between the polymers. Temperature jumps at ambient pressure have previously been carried out and have revealed complex behavior [2]. However, it is not straightforward to realize fast temperature jumps. Pressure jumps across the phase boundary are an interesting alternative to study the kinetics and aggregate growth mechanisms. We have modified the existing high-pressure setup to carry out time-resolved turbidity measurements during fast changes of pressure.

The modified setup is shown in Figure 6.4. It consists of a laser which impinges on the sample located in the pressurized and thermalized cell and a photodiode detecting the transmitted intensity. The temperature, pressure and the photocurrent are recorded digitally. To monitor the pressure, the pressure sensor was connected to a personal computer via a Keithley 2000 multimeter.

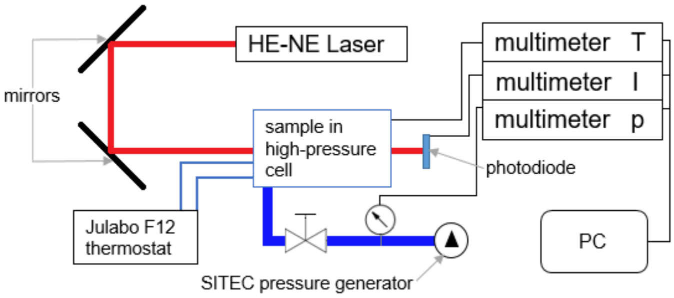

Figure 6.4:
Schematics of the high-pressure system.

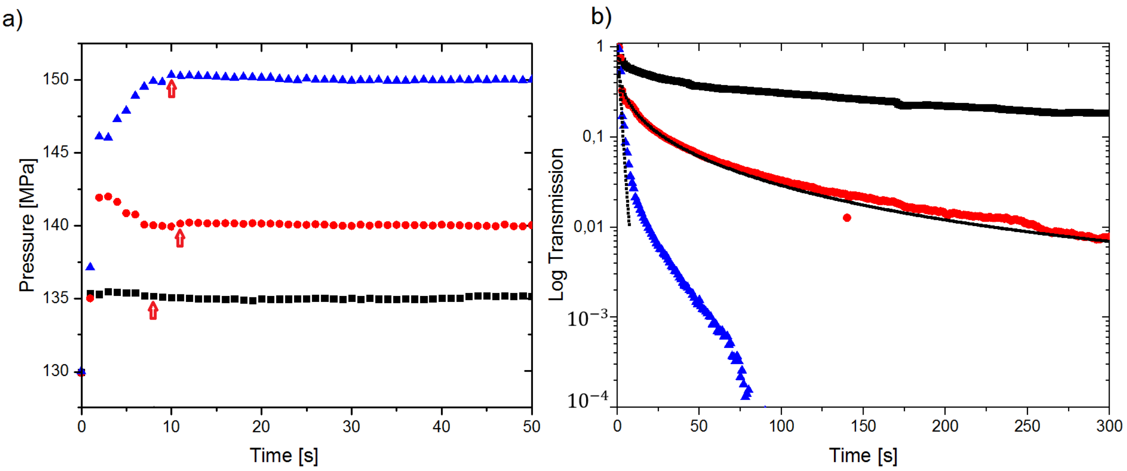

Figure 6.5:
(a) Pressure in dependence on time recorded during changes from 110 MPa to 135 MPa (squares), 140 MPa (circles) and 150 MPa (triangles) at 30°C. (b) Early stages of time-resolved light transmission during three pressure jumps in a semi-logarithmic representation. The same symbols are used.

Pressure jumps on a 3 wt% solution of PNIPAM in D_2O were carried out at 30°C to test the system, the pressure was changed manually from 110 MPa to 135 MPa, 140 MPa and 150 MPa, i.e. from the one-phase region to the two-phase region (Figure 6.3).

It can be seen in Figure 6.5 (a), that the time needed for a pressure change is in the range of 8-11 s and that, afterwards, the pressure can one qualify the magnitude of the pressure-fluctuations (< 0.2 MPa). Figure 6.5 (b) shows the time dependent transmission of the light for these jumps. A strong decay of the transmission is observed in all cases due to aggregation of PNIPAM. The initial parts of the decays could be fitted by stretched exponential functions with decay times in the range 4.2 - 188 s and stretching exponents in the range 0.35 - 1.10.

To summarize, the improvements of the high-pressure setup for turbidimetry now enable us to follow the changes of the light transmission after a fast change of pressure across the phase boundary of thermo-responsive polymer solutions.

[1] S. Pinzek, B.Sc. Thesis *Phase behavior of responsive polymers under high pressure*, TU München (2015)

[2] A. Meier-Koll, V. Pipich, P. Busch, C. M. Papadakis, P. Müller-Buschbaum, *Langmuir* **28**, 8791 (2012)

6.3 CSPEC: The cold time-of-flight spectrometer at the ESS

W. Lohstroh[1], P. P. Deen[1,2], J. Neuhaus[1], W. Petry[1], S. Longeville[3], J. Guyon Le Bouffy[3], C. Alba-Simionesco[3]

[1] E13 and MLZ, Garching, Germany
[2] European Spallation Source ESS, Sweden
[3] LLB, Saclay, France

In 2019, the European Spallation Source (ESS), a joint project of 17 European countries, will start operations. Among the endorsed instruments foreseen for day one instrumentation at the ESS, is the cold time-of-flight spectrometer CSPEC which is a joint project of the Technische Universiät München and the Laboratoire Léon Brillouin, Saclay, France.

In the CSPEC proposal, the long pulse structure and enhanced brilliance of the ESS have been exploited to develop a high performing cold chopper spectrometer that will gain an order of magnitude in neutron counting rate with respect to the existing cold chopper spectrometers. It will probe low-lying excitations and relaxation processes in materials ranging from hydrogenous materials, polymers to strong electronic correlations, to name a few. A main focus of CSPEC is to enable routine in-situ or time dependent experiments that will open new scientific frontiers.

Figure 6.6 shows the current floor plan of the future ESS. CSPEC will positioned in the west sector on beamport W3. The spectrometer will extend over three different buildings – experimental hall 2 with building designation D03, the guide hall with building designation E02 and finally the experimental hall 3 with building designation E01. CSPEC will utilize cold neutrons (2 < λ < 20 Å) that will be extracted from the 3 cm butterfly moderator. The 157 m, moderator to sample, distance enables measurements across a 1.75 Å wavelength bandwidth using Repetition Rate Multiplication within each ESS frame. By rephrasing the choppers to set the central wavelength, the energy transfers measured by CSPEC will cover 3 to 4 orders of magnitude, from few μeV (quasi-elastic scattering) up to 20 meV (inelastic scattering) with the corresponding change in the kinematic range. The chopper cascade consists of two bandwidth choppers, a counter rotating pulse shaping chopper pair (P-chopper), a counter rotating monochromating chopper pair (M-chopper) and a pulse removal chopper (PR-chopper). The later is used to adjust the number of pulses in Rate Repetition Multiplication. The cascade is optimised for energy resolutions down to $\Delta E/E = 1\%$, and it ensures that each incident wavelength arrives when

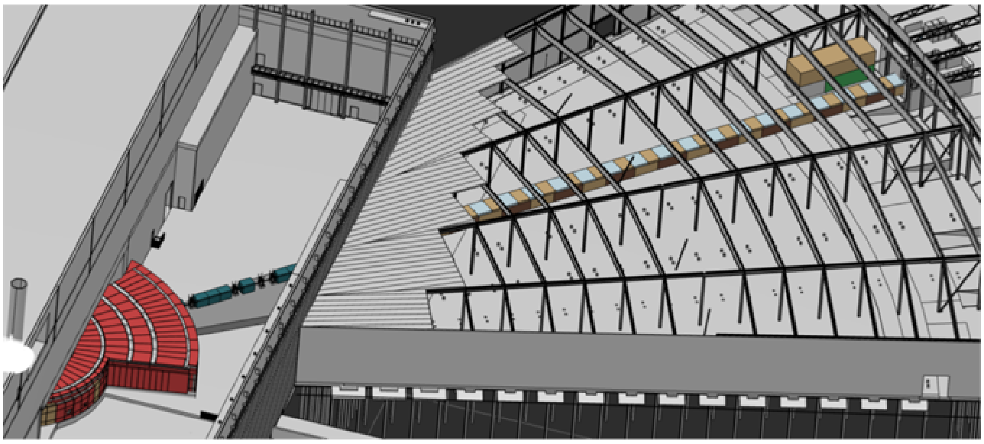

Figure 6.6:
Overview of CSPEC from the bunker up to the experimental cave, showing the extension over three experimental halls.

the scattering from the previous incident wavelength has reached background levels, whatever the scattering power of the sample. This is especially pertinent in a scientific age where the well-defined scattering features have been probed and the exciting science lies in scattering functions that are typically weak and broad in energy and reciprocal space thus the technique is highly background sensitive.
The neutron guide will feature both a curvature in vertical and horizontal direction. In the vertical direction an s - shape ensures the loss of direct line-of-sight to the moderator already in the common bunker, which extends up to 30 m from the target. In horizontal direction, the beam extraction is rotated by 1 deg in order to focus on the cold part of the moderator, an additional horizontal curvature is thus needed to bring the instrument axis back to its corridor. Following a ballistic transport section, the beam is compressed in an elliptic guide section towards the final M - chopper system. At the sample position, the beam will illuminate a sample area ranging from 4 x 2 cm^2 to 0.5 x 0.5 cm^2.

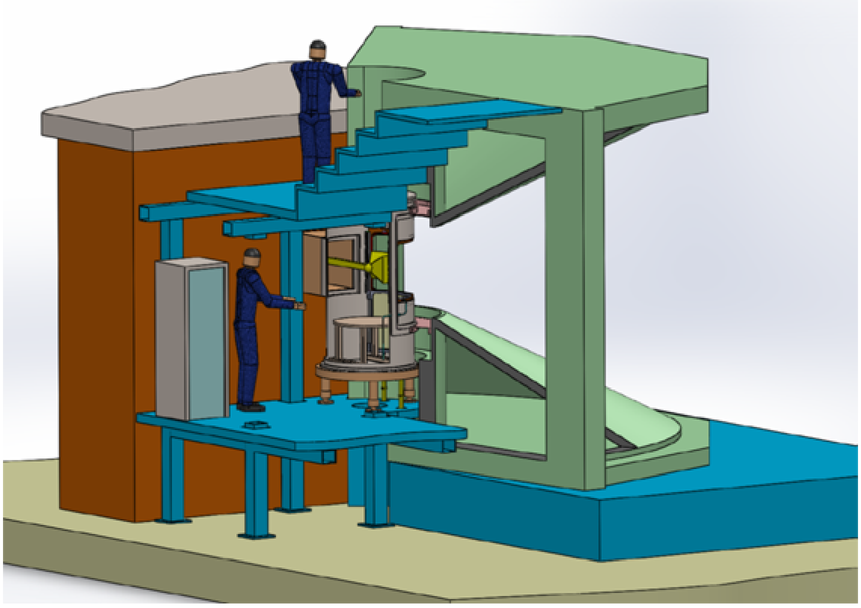

Figure 6.7:
Schematic representation of the sample area and its gate valve connection to the flight chamber.

The sample position will be easily accessible either from the top or from the side of the instrument, as illustrated in Figure 6.7, to facilitate the use of non-standard sample environment for in-situ or in-operando studies. By default, the detector vessel and the sample chamber are evacuated to cryogenic vacuum. An optional gate valve allows to isolate the sample area to have the sample area under ambient pressure conditions. Any sample environment needs to be compatible with the stringent background requirements. Additionally, a radial collimator positioned inside the detector vessel will minimize any spurious scattering.
The detector will be of ^{10}B multigrid type with 5 to 140 deg horizontal and ± 25 deg vertical angular coverage. First prototype test using this new technology show promising results and the development of the large area detector is ongoing.
During the preliminary design phase of CSPEC which started in 2016, the original instrument concept outlined in the proposal has been further developed and adapted to the engineering realities of the facility. In 2017, CSPEC is expected to enter the Detailed Design Phase (Phase 2) of the construction.

7 Teaching and outreach

7.1 Lectures, seminars and lab courses

Summer semester 2016
Prof. Dr. Peter Müller-Buschbaum, *Experimentalphysik 2 für MSE*
Prof. Dr. Christine M. Papadakis, *Angewandte Physik: Polymerphysik 2*
Prof. Dr. Peter Müller-Buschbaum, Dr. Martine Philipp,
Nanostructured Soft Materials 2
Prof. Dr. Christine M. Papadakis, *Höhere Physik 2*
Prof. Dr. Peter Müller-Buschbaum, Prof. Dr. Christine M. Papadakis,
Seminar über Struktur und Dynamik kondensierter Materie
Prof. Dr. Peter Müller-Buschbaum, Prof. Dr. Christine M. Papadakis,
Seminar: Polymere
Prof. Dr. Peter Müller-Buschbaum, Prof. Dr. Christine M. Papadakis,
Studentenseminar: Grundlegende Phänomene der Physik der weichen Materie
Prof. Dr. Peter Müller-Buschbaum, *Seminar: Aktuelle Probleme der organische Photovoltaik*
Prof. Dr. Peter Müller-Buschbaum, Prof. Dr. Christine M. Papadakis,
Bachelor-Seminar: Funktionelle weiche Materialien
Prof. Dr. Winfried Petry, Prof. Dr. Peter Böni, Dr. Tobias Schrader, Dr. Thorsten Schröder,
Seminar über Neutronen in Forschung und Industrie
Prof. Dr. Winfried Petry, *Blockseminar Erasmus Mundus MaMaSELF Summerschool*
Dr. Michael Leitner, *Materialphysik auf atomarer Skala 2*

Winter semester 2016/2017
Prof. Dr. Peter Müller-Buschbaum, *Experimentalphysik 1 für MSE*
Prof. Dr. Peter Müller-Buschbaum, Dr. Volker Körstgens, *Nanostructured Soft Materials 1*
Prof. Dr. Christine M. Papadakis, *Angewandte Physik, Polymerphysik 1*
Prof. Dr. Christine M. Papadakis, *Einführung in die Physik der kondensierten Materie*
Prof. Dr. Peter Müller-Buschbaum, Prof. Dr. Christine M. Papadakis,
Seminar über Struktur und Dynamik kondensierter Materie
Prof. Dr. Peter Müller-Buschbaum, Prof. Dr. Christine M. Papadakis, *Seminar: Polymere*
Prof. Dr. Peter Müller-Buschbaum, Prof. Dr. Christine M. Papadakis,
Studentenseminar: Grundlegende Phänomene der Physik der weichen Materie
Prof. Dr. Peter Müller-Buschbaum, *Seminar: Aktuelle Probleme der organische Photovoltaik*
Prof. Dr. Winfried Petry, Prof. Dr. Peter Böni, Dr. Tobias Schrader, Dr. Sebastian Mühlbauer,
Seminar über Neutronen in Forschung und Industrie
Prof. Dr. Winfried Petry, *MSC Radiation Biology*
Dr. Michael Leitner, *Materialphysik auf atomarer Skala 1*
Dr. Michael Leitner, *Physik mit Neutronen 1*

Lab courses 2016
JCNS Laboratory Course - Neutron Scattering (Forschungspraktikum)
Neutronenstreuung am FRM II (Fortgeschrittenenpraktikum)
Theoretische und praktische Einführung in AFM (Fortgeschrittenenpraktikum)
Thermische Analyse (Fortgeschrittenenpraktikum)

7.2 Conferences and public outreach

P. Müller-Buschbaum
TUM-DESY-CAU Workshop "The polymer-metal interface"
Garching, Mart 1 –2, 2016

Program

Tuesday 1.3.2016
Building Physik-Department (Physik I, Garching)
Lecture hall number 3
13.00 – 13.05 Opening and Welcome, Prof. Dr. Peter Müller-Buschbaum (TUM)
Session 1 (Chair: Dr. Ezzeldin Metwalli)
13.05 – 13.50 Metal/Polymer-Interfaces: Structure and Formation, Prof. Dr. Franz Faupel (CAU)
13.50 – 14.35 Real-time investigations of nanocomposite materials, Dr. Stephan V. Roth (DESY)
14.35 – 15.20 Polymer-metal interfaces in organic electronics, Prof. Dr. Peter Müller-Buschbaum (TUM)
15.20 – 16.00 Coffee break
Session 2 (Chair: Prof. Dr. Franz Faupel)
16.00 – 16.30 Metal/Polymer Interfaces: Chemical Aspects, Dr. Thomas Strunskus
16.30 – 17.00 In-situ investigation of gold film growth on polystyrene, Dr. Matthias Schwartzkopf (DESY)
17.00 – 17.30 Real-time investigation of metal nanoparticles growth on thin polymer films, Dr. Ezzeldin Metwalli (TUM)
17.30 – 18.00 Sputter deposition on PVDF-TrFE probed with in-situ GISAXS, Alexander Hinz (CAU)
18.00 – 18.30 Sputter deposition on P3HT probed with in-situ GISAXS, Dr. Volker Körstgens (TUM)
19.00 Dinner at Neuwirt (Garching)

Wednesday 2.3.2016
Session 3 (Chair: Dr. Stephan Roth)
9.00 – 9.30 Al growth on diblock-co-polymer thin films, Björn Beyersdorff (DESY)
9.30 – 10.00 Molecular dynamics simulation of gold cluster growth on a polymer surface, Jan Willem Abraham (CAU)
10.00 – 10.30 Sputter deposition on PTB7 probed with in-situ GISAXS, Franziska Löhrer (TUM)
10.30 – 11.00 Engineering aspects of practical experiments, Jan Rubeck (DESY)
11.00 – 11.30 Coffee Break
Session 4 (Chair: Dr. Volker Körstgens)
11.30 – 12.00 XPS and SEM Characterization of Metal/Polymer Interfaces, Oleksandr Polonsyki (CAU)
12.00 – 12.30 Metal-Biopolymer-Composites – First results, Wiebke Ohm (DESY)
12.30 – 12.50 Magnetic nanoparticles embedded in diblock copolymer films, Senlin Xia (TUM)
12.50 – 13.00 Closing Remarks, Prof. Dr. Franz Faupel (CAU)
13.00 – 14.00 Lunch break
14.00 – 18.00 Lab Tour with hands on experiments
19.00 Dinner at Paulaner (Nockherberg in München)

P. Müller-Buschbaum, K. Reuter
5th International SolTech Conference
Munich, April 5 – 8, 2016

SOLAR TECHNOLOGIES GO HYBRID

5th International SolTech Conference

April 5 – 8, 2016

Munich

Keynote Speakers:

Prof. Dr. Markus **Antonietti**
Max Planck Institute of Colloids and Interfaces, Potsdam, Germany

Prof. Dr. Udo **Bach**
Monash University,
Clayton Victoria, Australia

Prof. Dr. Jochen **Blumberger**
University College London, U.K

Prof. Dr. Daniel G. **Nocera**
Harvard University, USA

Prof. Dr. Licheng **Sun**
KTH Royal Institute of Technology, Stockholm, Sweden

Prof. Dr. Michael R. **Wasielewski**
Northwestern University, Evanston, USA

Agenda:

Tuesday, April 5th, 2016:

Start: 2:30 pm
- Reception
- Opening
- Welcome
- Introduction
- Keynote Lecture
- Buffet

Wednesday, April 6th, 2016:

- Registration
- Keynote Lectures
- Contributed Lectures
- Poster Session

Thursday, April 7th, 2016:

- Keynote Lectures
- Contributed Lectures
- Poster Session
- Conference Dinner

Friday, April 8th, 2016:

- Keynote Lecture
- Contributed Lectures
- Executive Committee Meeting

End: approx. 3 pm

P. Müller-Buschbaum, W. Petry

Lehrerfortbildung "Biophysik"

40. Edgar-Lüscher-Seminar

Zwiesel, 22 - 24 April 2016

Programm

Freitag, 22. April 2016

	am Gymnasium Zwiesel:
13.00 - 14.30	Studienberatung der TUM
	im großen Saal des Waldmuseums der Stadt Zwiesel:
15.30 - 16.30	**Festakt 40 Jahre Lehrerfortbildung in Zwiesel** *Staatssekretär StMBW Bernd Sibler* *Landrat Michael Adam* *Ministerialbeauftragter Ndb. Ltd. OStD Anselm Räde* *Prof. Dr. Winfried Petry, TU München* *Bürgermeister Franz Xaver Steiniger (Gastgeber)*
16.30 - 17.45	**Die unendliche Vielfalt des Lebens: Evolution als Zusammenspiel von Genetik und Physik** *Prof. Dr. Erich Sackmann, TU München*
17.45 - 18.00	**Diskussion**
18.00 - 19.00	**Empfang der Stadt Zwiesel**
19.00 - 19.45	**40 Jahre Lehrerfortbildung in Zwiesel – ein Rückblick** *Günther Haller und Prof. Dr. Walter Schirmacher*

Samstag, 23. April 2016

09.00 - 10.15	**Die treibenden Kräfte in der Biophysik - ein Zugang zur angewandten statistischen Physik im Unterricht** *Prof. Dr. Joachim Rädler, LMU München*
10.15 - 11.00	Diskussion und Kaffeepause
11.00 - 12.15	**NMR Spektroskopie zur Untersuchung von Biomolekülen** *Prof. Dr. Michael Sattler, TU München*
12.15 -12.30	Diskussion
14.30 - 15.45	**Selbstorganisierte biologische Maschinen** *PD Dr. Günther Woehlke, TU München*
15.45 - 16.30	Diskussion und Kaffeepause
16.30 - 17.45	**Mechanosensorik: Wie sie funktioniert und im Tierreich eingesetzt wird** *Prof. Dr. Leo van Hemmen, TU München*
17.45 - 18.00	Diskussion

Sonntag, 24. April 2016

09.00 - 10.15	**Streumethoden zur Untersuchung von Biomolekülen** *Prof. Dr. Frank Schreiber, Universität Tübingen*
10.15 - 11.00	Diskussion und Kaffeepause
11.00 - 12.15	**DNA als programmierbarer Konstruktionswerkstoff für die Nanowelt** *Prof. Dr. Hendrik Dietz, TU München*
12.15 - 13.00	Diskussion, Themenfindung für das 41. Edgar-Lüscher-Seminar

Organisation

Prof. Dr. Peter Müller-Buschbaum
TUM

Prof. Müller-Buschbaum ist Sprecher für das Netzwerk „Regenerative Energien (NRG)“ in der Munich School of Engineering (MSE) der TU München, Leiter des KeyLabs „TUM.solar“ im Forschungsnetzwerk „Solar Technologies Go Hybrid“, Deutscher Vertreter bei der European Polymer Federation (EPF) für den Bereich Polymerphysik und Associate Editor der Zeitschrift „ACS Applied Materials & Interfaces“ der „American Chemical Society“ (ACS). Er befasst sich in seiner Forschungsarbeit mit der Entwicklung polymerbasierter Materialien mit neuartigen Struktur-Eigenschaftsbeziehungen.

Prof. Dr. Winfried Petry
TUM

Prof. Petry ist Ordinarius am Lehrstuhl für Funktionelle Materialien (E13) des Physik Departments der TU München, Betreuungsprofessor für die Bayerische Eliteakademie und Wissenschaftlicher Direktor der Forschungsneutronenquelle Heinz Maier-Leibnitz (FRM II). Er forscht auf dem Gebiet der Materialwissenschaften mit Neutronen.

Organisatorische Hinweise

Organisation vor Ort:

OStD Heribert Strunz,	*Gymnasium Zwiesel*
OStR Christian Stoiber,	*Gymnasium Zwiesel*
StR Claus Starke,	*Gymnasium Zwiesel*
StR Josef Müller,	*Gymnasium Zwiesel*
StR Thomas Kufner,	*Gymnasium Zwiesel*

E-Mail: luescherseminar@gymnasium-zwiesel.de

Hinweise:

- Der Festakt, der Festvortrag und der Festabend finden im großen Saal des Waldmuseums der Stadt Zwiesel statt. Alle Vorträge am Samstag und am Sonntag finden in der Aula des Gymnasiums Zwiesel statt.
- Für 5,- € erhalten die Teilnehmer am Ende des Seminars eine CD mit sämtlichen freigegebenen Vorträgen und den bisherigen Festschriften.
- In den ausgewiesenen Kaffeepausen wird in der Mensa des Gymnasiums Kaffee und Kuchen gegen eine freiwillige Spende angeboten.
- Am Rande der Aula findet eine Ausstellung verschiedener Lehrmittelausstatter und Verlage statt.

Titelfoto: studycheck©

40. Edgar-Lüscher-Seminar

Biophysik

im großen Saal des Waldmuseums der Stadt Zwiesel

Freitag, 22. April 2016

und

am Gymnasium Zwiesel

Samstag, 23. April 2016 und Sonntag, 24. April 2016

Schirmherr:

Prof. Dr. Dr. h.c. mult. Wolfgang A. Herrmann,
Präsident der TUM

Veranstalter:

Ltd. OStD Anselm Räde,
Ministerialbeauftragter für die Gymnasien in Niederbayern

Wissenschaftliche Leitung:

Prof. Dr. Peter Müller-Buschbaum, *TUM*
Prof. Dr. Winfried Petry, *TUM*

M. Laus, P. Müller-Buschbaum
Europolymer Conference 2016 (EUPOC2016), Block Copolymers for Nanotechnology Applications
Gargnano, Italy, 22 – 26 May 2016

Invited Speakers

Uli B. Wiesner (Cornell University, USA), ”Block copolymer directed nanostructured hybrids”

Jean-Francois Gohy (Catholic University of Louvain, Belgium), ”Elaboration of novel organic electrode materials based on block copolymer architectures and hybrid technologies for advanced energy storage systems”

Igor I. Potemkin (Moscow State University, Russia), ”Effect of solvent in nanostructured block copolymer films”

Christopher K. Ober (Cornell University, USA), ”Processing of block copolymers for long range order using solvent vapour and laser spike annealing”

Michele Perego (CNR, MDM, Italy), ”Orientation and lateral ordering in asymmetric ps-b-pmma thin films”

Paul F. Nealey (University of Chicago, USA), ”Directed self-assembly (DSA) of performance materials”

Christine M. Papadakis (Technische Universität München, Germany), ”Structural changes in block copolymer thin films during solvent vapor treatment – in-situ, real-time gisaxs investigations”

Thomas Thurn-Albrecht (University of Halle, Germany), ”Structure formation in donor-acceptor block copolymers for photovoltaic applications”

Volker Abetz (Helmholtz Zentrum Geesthacht, Germany), ”Formation of isoporous membranes from block copolymers in flat sheet and hollow fibre geometries”

Raluca Tiron (CEA Let, Grenoble, France), ”Directed self assembly of block copolymers: from materials to integration”

Claudio De Rosa (University of Naples, Italy), ”Crystalline block copolymers: controlling morphology through controlled crystallization”

Teruaki Hayakawa (Tokyo Institute of Technology, Japan), ”Molecular technology for block copolymer lithographic materials forming perpendicularly oriented lamellar structures”

Peter Müller-Buschbaum (Technische Universität München, Germany), ”Probing nanostructures generated by block copolymer self-assembly using advanced scattering techniques”

P. Müller-Buschbaum, C.M. Papadakis

Summer School Polymer Physics

Obertauern, Austria, 21 – 24 June 2016

E13 Summer School
Bergheim, Obertauern
21.-24.06.2016

	Tuesday, 21.06.2016	**Wednesday, 22.06.2016**	**Thursday, 23.06.2016**	**Friday, 24.06.2016**
09:00 - 10:30	Journey from Garching	GISAXS / GISANS GIWAXS	Introduction to discussion groups	QENS Responsive polymers
10:30-11:00		Coffee break	Excursion	Coffee break
11:00 - 12:30		Conducting polymers Organic solar cells		Perovskite solar cells Presentation Discussion groups B1+B2
12:30-14:00	Lunch	Lunch		Lunch
14:00 - 15:30	Reciprocal space and FT SAXS /SANS	Discussion groups A1, A2, B1, B2, C1 and C2 seperately		Presentation Discussion groups A1 + A2
15:30-16:00	Coffee break	Coffee break		Coffee break
16:00 - 17:30	Polymer blends Block copolymers	Discussion groups A1+A2, B1+B2, C1+C2 together preparation of presentation		Journey to Garching
17:30-20:00	Dinner	Dinner	Dinner	
20:00 - 22:00	XRR / NR	Presentation Discussion groups C1 + C2	Poster	

W. Petry, T. Brückel
Netrons for Energy
Bad Reichenhall, 18 — 22 July 2016

W. A. Herrmann, T. Hamacher, N. Adams, H. Gasteiger, W. Lang, M. Lienkamp,
P. Müller-Buschbaum, H. Spliethoff, W. Wall
6th Colloquium of the Munich School of Engineering: "New Concepts in Energy Science and Engineering"
Garching, 7 July 2016

Munich School of Engineering
Technische Universität München

TUM

6th Energy Colloquium of the Munich School of Engineering

New Concepts in Energy Science and Engineering

07.07.2016 – 8.30 am to 9.00 pm
TUM – Institute for Advanced Study, Garching

8.30 - 9.00 am
Registration

9.00 - 9.15 am
Opening
Thomas Hamacher, Director Munich School of Engineering

9.15 - 9.45 am
Keynote: „How to Leverage Corporate Research to Lower the Cost of Wind Energy"
Dominic von Terzi, Manager Aerodynamics & Acoustics
GE Global Research

9.45 - 11 .00 am
Session Chair: Werner Lang, ZNB MSE

Demand Side Management Potential of Buildings in Germany's Future Energy System
Florian Sänger, Institute for Energy Economy and Application Technology

Optimizing the Refurbishment of a Single Family Home
Johannes Maderspacher, Centre for Urban Ecology and Climate Adaption

Energy Management and Electromobility in Plus Energy Homes and Districts
Claudia Hemmerle, Centre for Sustainable Building

11.00 - 11.45 am
Poster Presentation, Coffee Break

11.45 - 1.00 pm
Session Chair: Peter Müller-Buschbaum, NRG MSE

Metal Electrodes in Organic Photovoltaics - Why Contact Matters
Franziska Löhrer, Chair for Functional Materials

X-Rays, Neutrons, and Positrons: Strong Contributors in Revealing Fundamental Processes in Lithium-Ion Batteries
Irmgard Buchberger, Chair of Technical Electrochemistry

Elucidation of Adsorption Processes at the Surface of Pt(331) Model Electrocatalysts in Acidic Aqueous Media
Daniel Scieszka, Research Group Physics of Energy Conversion and Storage

1.00 - 2.30 pm
Poster Presentation, Lunch Break

2.30 - 2.50 pm
Teaching at MSE
Andreas Kremling, Specialty Division for Systems Biotechnology

2.50 - 4.05 pm
Session Chair: Markus Lienkamp, WZE MSE

Large-Scale Power System Design - Improving Decomposition Techniques
Paul Stursberg, Chair of Applied Geometry and Discrete Mathematics

Towards Fuel Production from Biomass via Electrocatalysis and Catalytic Hydrogenation at Ambient Conditions
Oliver Gutiérrez, Chair of Technical Electrochemistry II

Optimal Feedforward Control of Permanent-Magnet Synchronous Machines in Renewable Energy Systems
Lorenz Horlbeck, Chair of Automotive Technology

4.05 - 4.50 pm
Poster Presentation, Coffee Break

4.50 - 6.05 pm
Session Chair: Hartmut Spliethoff, CPG MSE

OpenGridMap: Automatic Power Grid Simulation Model Generation from Crowdsourced Data
Jose Rivera, Chair for Application and Middleware Systems

Flexible Power Generation with Thermal Power Plants: Process Analysis Using Dynamic Simulation
Steffen Kahlert, Institute for Energy Systems

Wind Farm Control for Power Maximization
Johannes Schreiber, Wind Energy Institute

6.05 - 6.35 pm
Keynote: „Beyond Oil and Gas – Mobility of the Future"
Ferdi Schüth, Director at the MPI für Kohlenforschung,
Vice President of the Max-Planck-Society

6.35 - 6.50 pm
Summary of the Day

6.50 - 9.00 pm
Poster and Presentation Award, Colloquium Dinner

Registration:
http://www.mse.tum.de

B. Frick (ILL, France), V. Garcia-Sakai (ISIS, UK), W. Petry and T. Brückel (Heinz Maier-Leibnitz-Zentrum)
50 years of neutron backscattering spectroscopy
Garching, 2 – 3 September 2016

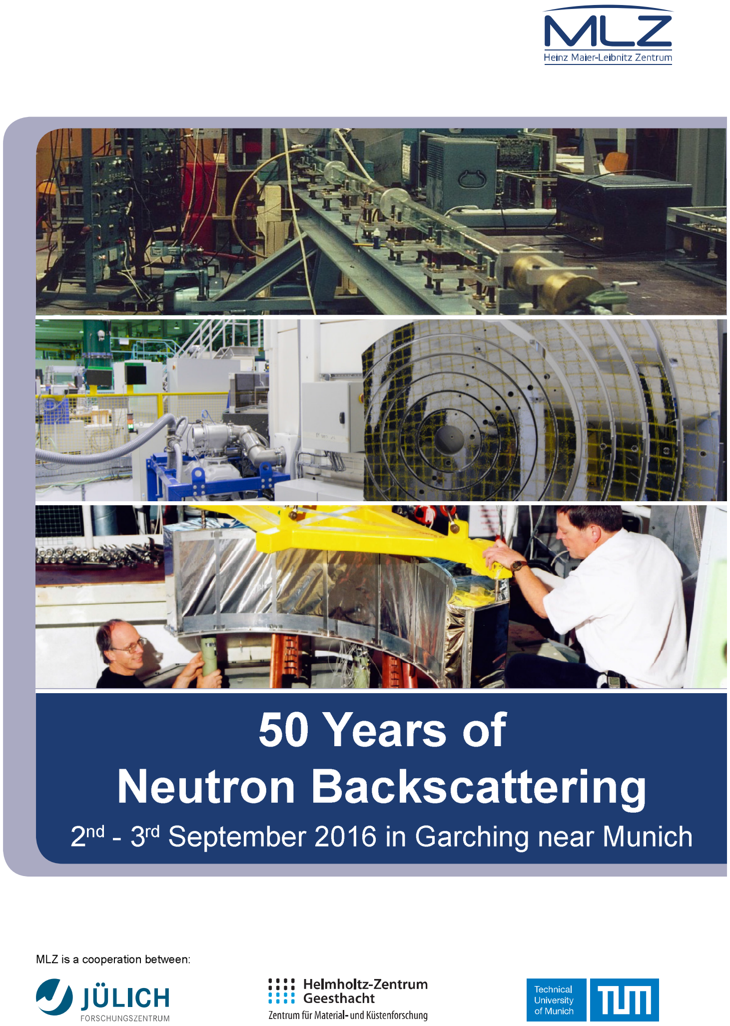

MLZ
Heinz Maier-Leibnitz Zentrum

50 Years of
Neutron Backscattering
2nd - 3rd September 2016 in Garching near Munich

MLZ is a cooperation between:
JÜLICH FORSCHUNGSZENTRUM
Helmholtz-Zentrum Geesthacht
Zentrum für Material- und Küstenforschung
Technical University of Munich TUM

W. Petry, R. Gilles, Verein deutscher Ingenieur (VDI)
VDI-TUM Expertenforum 2016
Garching, 15 September 2016

VDI-TUM Expertenforum 2016

Hochleistungswerkstoffe im Einsatz – Herausforderung für die zerstörungsfreie Prüfung

Modernste Hochleistungswerkstoffe und –technologien stehen im Fokus des 6. VDI-TUM Expertenforums. Diese bringen auch große Herausforderungen und höchste Ansprüche an die zerstörungsfreie Prüfung für die zahlreichen technischen Anwendungen und Einsatzszenarien mit sich. Dies zeigt sich bei vielen Anwendungen mit Strukturen und Bauweisen aus Leichtmetall- oder Superlegierungen, leistungsfähigen Kompositstrukturen oder auch in neusten Entwicklungen in der Batterietechnik. Dabei werden sowohl etablierte Prüftechniken, wie Ultraschallprüfung, Thermographie, Tomographie und Eigenspannungsanalytik als auch neuartige, noch in der Entwicklung befindliche Verfahren, wie beispielsweise die 3D Terahertzbildgebung oder Analysemethoden aus der Neutronenstreuung eingesetzt.

Experten aus Industrie (ALCOA, BMW, Dr. Mirtsch GmbH) und Forschung (Fraunhofer [IFAM, IKTS, IPM], MLZ, University Manchester, VDI) berichten aus vielfältigen Anwendungsbereichen wie Sie ihre Fragestellungen mithilfe von zerstörungsfreien Prüfmethoden gelöst haben. In Form von Einzelgesprächen und einer abschließenden Podiumsdiskussion mit allen Referenten erhalten auch die Teilnehmer die Möglichkeit, direkte Fragen an die Experten zu stellen und eigene Problemstellungen einzubringen.

Zum Abschluss der Veranstaltung wird eine Führung durch die Forschungs-Neutronenquelle Heinz Maier-Leibnitz (FRM II) angeboten.

Die Teilnahme ist **kostenlos**, aufgrund der begrenzten Teilnehmerzahl ist jedoch eine Anmeldung erforderlich.

(C) Siemens AG

A. Kyritsis, C. M. Papadakis,
Greek-German Workshop 2016 'From polymer assembly to stimuli-responsive materials'
Athens, 26 – 30 September 2016

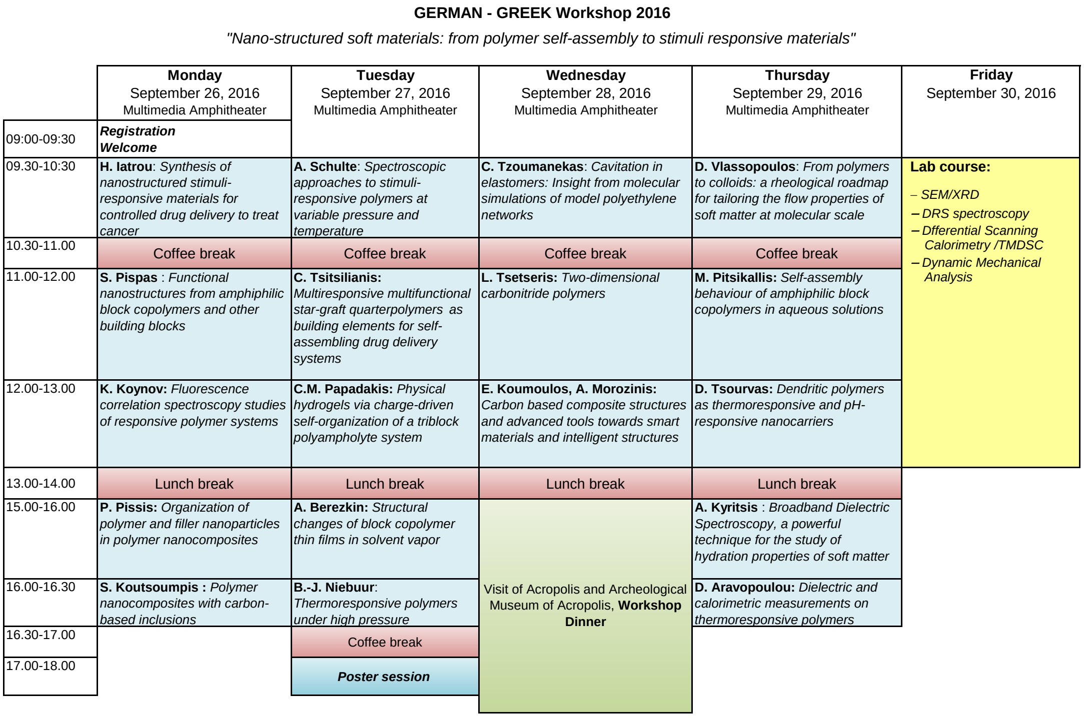

GERMAN - GREEK Workshop 2016

"Nano-structured soft materials: from polymer self-assembly to stimuli responsive materials"

	Monday September 26, 2016 Multimedia Amphitheater	**Tuesday** September 27, 2016 Multimedia Amphitheater	**Wednesday** September 28, 2016 Multimedia Amphitheater	**Thursday** September 29, 2016 Multimedia Amphitheater	**Friday** September 30, 2016
09:00-09:30	***Registration*** ***Welcome***				
09.30-10:30	**H. Iatrou**: *Synthesis of nanostructured stimuli-responsive materials for controlled drug delivery to treat cancer*	**A. Schulte**: *Spectroscopic approaches to stimuli-responsive polymers at variable pressure and temperature*	**C. Tzoumanekas**: *Cavitation in elastomers: Insight from molecular simulations of model polyethylene networks*	**D. Vlassopoulos**: *From polymers to colloids: a rheological roadmap for tailoring the flow properties of soft matter at molecular scale*	**Lab course:** – *SEM/XRD* – *DRS spectroscopy* – *Dfferential Scanning Calorimetry /TMDSC* – *Dynamic Mechanical Analysis*
10.30-11.00	Coffee break	Coffee break	Coffee break	Coffee break	
11.00-12.00	**S. Pispas** : *Functional nanostructures from amphiphilic block copolymers and other building blocks*	**C. Tsitsilianis:** *Multiresponsive multifunctional star-graft quarterpolymers as building elements for self-assembling drug delivery systems*	**L. Tsetseris:** *Two-dimensional carbonitride polymers*	**M. Pitsikallis:** *Self-assembly behaviour of amphiphilic block copolymers in aqueous solutions*	
12.00-13.00	**K. Koynov:** *Fluorescence correlation spectroscopy studies of responsive polymer systems*	**C.M. Papadakis:** *Physical hydrogels via charge-driven self-organization of a triblock polyampholyte system*	**E. Koumoulos, A. Morozinis:** *Carbon based composite structures and advanced tools towards smart materials and intelligent structures*	**D. Tsourvas:** *Dendritic polymers as thermoresponsive and pH-responsive nanocarriers*	
13.00-14.00	Lunch break	Lunch break	Lunch break	Lunch break	
15.00-16.00	**P. Pissis:** *Organization of polymer and filler nanoparticles in polymer nanocomposites*	**A. Berezkin:** *Structural changes of block copolymer thin films in solvent vapor*	Visit of Acropolis and Archeological Museum of Acropolis, **Workshop Dinner**	**A. Kyritsis** : *Broadband Dielectric Spectroscopy, a powerful technique for the study of hydration properties of soft matter*	
16.00-16.30	**S. Koutsoumpis :** *Polymer nanocomposites with carbon-based inclusions*	**B.-J. Niebuur**: *Thermoresponsive polymers under high pressure*		**D. Aravopoulou:** *Dielectric and calorimetric measurements on thermoresponsive polymers*	
16.30-17.00		Coffee break			
17.00-18.00		***Poster session***			

P. Müller-Buschbaum
Edgar-Lüscher Lectures, Lehrerfortbildung "Bionik"
Dillingen, 28 – 30 September 2016

EDGAR–LÜSCHER–LECTURES DILLINGEN/DONAU 2016
Thema: Bionik
Datum: Mittwoch, 28. September bis Freitag, 30. September 2016
Tagungsort: Akademie für Lehrerfortbildung Dillingen
Veranstalter: Akademie für Lehrerfortbildung Dillingen und TU München
wissenschaftliche Leitung: Prof. Dr. Peter Müller-Buschbaum,
Technische Universität München.

Programm

Mittwoch, 28. 09. 2016
15:00 – 15:30 Begrüßung
StD Werner Ettinger / Prof. Dr. Peter Müller-Buschbaum (Physik-Department TUM)

15:30 – 17:00 Prof. Dr. Harald Luksch (Lehrstuhl für Zoologie, TUM)
Lernen von der Natur - Bionik und Neurobionik

18:30 – 20:00 Dr. Michael Gebhardt (Lehrstuhl für Zoologie, TUM)
Haften, Reibung, Reflexion: einfache bionische Experimente für den Unterricht

Donnerstag, 29. 09. 2016
8:30 – 10:00 Dr. Nicolas Plumere (Molecular Nanostructures, Ruhr-Universität Bochum)
Biologische Solarzellen für künstliche Photosynthese

10:00 – 10.30 Kaffeepause

10:30 – 12:00 Dr. Michaela Eder (Max-Planck-Institut für Kolloid- und Grenzflächenforschung, Golm)
Wie Pflanzen Vorbilder für Bionik sein können

15:30 – 17:00 Prof. Dr. Oskar Paris (Institut für Physik, Montanuniversität Leoben)
Funktionalität durch hierarchisch strukturierte Materialien

18:30 – 20:00 Dr. Tobias Kraus (Leibniz-Institut für Neue Materialien, Saarbrücken)
Biologisch inspirierte Materialstrukturierung

Freitag, 30. 09. 2016
8:30 – 10:00 Prof. Dr. Antonia Kesel (Hochschule Bremen)
Marine Bionik

10:00 – 10.30 Kaffeepause

10:30 – 12:00 Prof. Dr. Cordt Zollfrank (Professur für Biogene Polymere, TUM)
Struktur und Funktionsmaterialien mit Biotemplaten

Ab 12:00 Lehrgangsabschluss
Prof. Dr. Peter Müller-Buschbaum / StD Werner Ettinger

R. Gehrke, P. Müller-Buschbaum, S. V. Roth
International Workshop 'GISAXS2016'
Hamburg, 16–18 November 2016

Keynote speakers
Tilo Baumbach, KIT Karlsruhe (GER): "Advanced X-ray Scattering Techniques of the in-situ characterization of Semiconductor Nanostructures"
Hiroshi Okuda, Kyoto University (JPN): "Use of tender X-rays for depth-dependent structure analysis for self-organized thin films and related materials"
Moonhor Ree, Pohang University of Science and Technology (POSTECH) (Korea): "GISAXS on functional materials"
Michael Toney, SLAC Stanford (US): "Morphology in Organic Photovoltaics as Probed by Grazing Incidence X-ray Scattering"

Invited speakers
Henrich Frielinghaus, FZJ Jülich (GER): "Structure and Dynamics of Membranes at the Solid-Liquid Interface"
Tiberio Ezquerra, CSIC Madrid (ESP): "On the application of Grazing Incidence X-ray Scattering to characterize functional gratings, from polymer systems to fullerene grooves"
Rainer Gehrke, DESY (GER): "Software for SAXS/WAXS/GISAXS@DESY"
Eva Herzig, TU München (GER): "Exploiting in-situ grazing incidence x-ray scattering to resolve morphology formation mechanisms in organic thin films"
Peter Müller-Buschbaum, TU München (GER): "GISANS"
Christine Revenant, CEA Grenoble (F) "GISAXS from solution-processed oxide thin films"
Stephan V. Roth, DESY (GER): "High-speed GISAXS"
Shun Yu, KTH Stockholm (SWE): "In situ GISAXS study on the metallic nanostructure at the interfaces in organic electronics"
Matthias Schwartzkopf, DESY (GER): "GISAXS and High-Throughput - Current status and future challenges"
Joachim Wuttke, FZJ Jülich (GER): "BornAgain: software to simulate and fit GISAS"

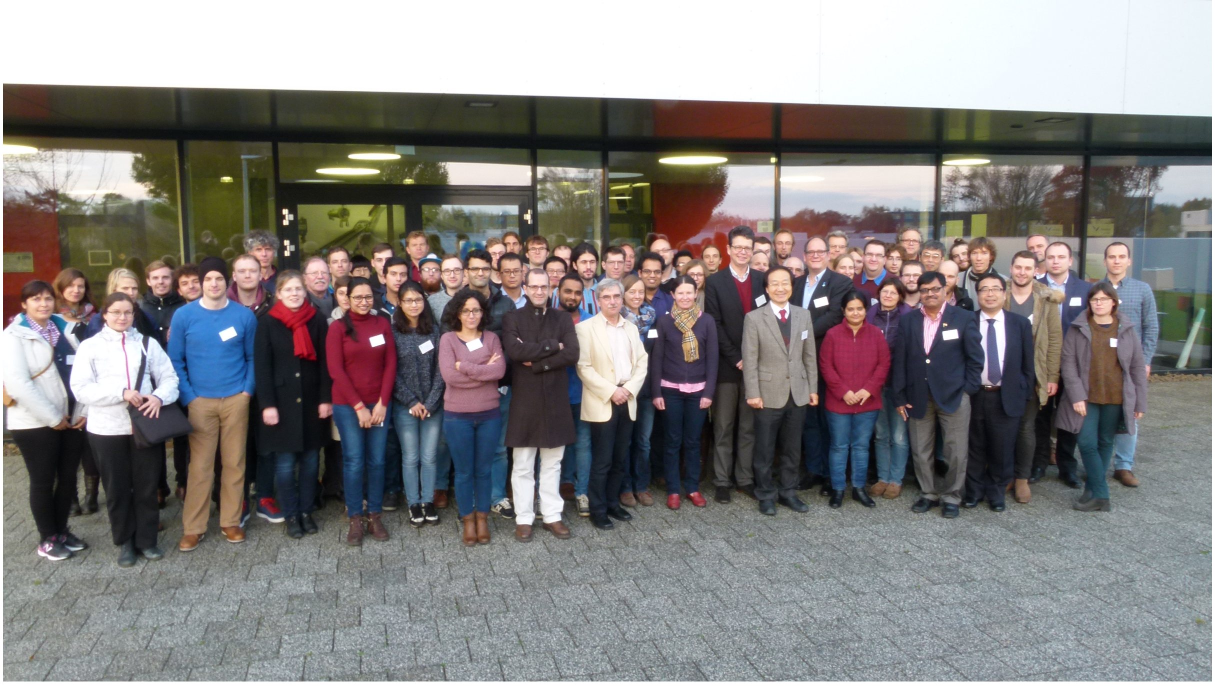

7.3 Service to the community

Prof. Dr. Peter Müller-Buschbaum:

- Since 9/2016 spokesman of “Munich School of Engineering” Graduate School
- Since 1/2016 head of research network “Solar Technologies go hybrid (SolTech)”
- Since 3/2015 member of “Advanced Light Source (ALS) Review Panel”
- Since 9/2014 member of “Heinz Maier-Leibnitz Zentrum (MLZ) Review Panel“
- Since 6/2014 member of Stanford Synchrotron Radiation Lightsource (SSRL) Review Panel
- Since 9/2012 Associate Editor of journal “ACS Applied Materials & Interfaces“ of the American Chemical Society
- Since 3/2012 head of KeyLab ”TUM.Solar” at TU Munich
- Since 1/2012 member of the Scientific Selection Panel of the Helmholtz-Zentrum Berlin für Materialien und Energie (HZB)
- Since 2011 member of European Spallation Source (ESS) Scientific Advisory Panel (Reflectivity)
- Since 2011 German representative at the European Polymer Federation (EPF) for polymer physics
- Since 2010 spokesman of the regenerative engergies section (NRG) at the Munich School of Engineering (MSE) of TU Munich
- Since 2010 member of TUM Energie at TU Munich
- Since 2010 German representative at the European Synchrotron User Organization (ESUO)
- Since 2008 chairman of “DESY Photon Science User Committee“ at the synchrotron radiation laboratory DESY in Hamburg

Prof. Dr. Christine M. Papadakis:

- Since 4/2015 Editor-in-Chief for Colloid & Polymer Science, Springer
- Member of the subcommittee "College 9: Structure and Dynamics of Soft-Condensed Matter" at Laue-Langevin Institute (ILL), Grenoble, France
- Vice women's representative of the Physics Department at TU München

Prof. Dr. Winfried Petry:

- Since 2015 member of the Neutron Scientific Advisory Committee of the National Research Center Kurchatov Institute "Petersburg Nuclear Physics Institute" (PNPI, Gatchina)
- Since 2012 member of the Scientific Advisory Board of NaWi Graz
- Since 2007 member of the Steering Comittee of the Laue Langevin Institute and chairman of the instrumentation review panel of the CEA Leon Brillouin Laboratory
- Since 1999 liaison professor of Bayerische Eliteakademie (Bavarian Leadership Academy) and since May 2011 member of the Board of Trustees
- Since 2016 member of the Evaluation Panel for Neutron Research of the Swedish Research Council

8 Publications, talks and funding

8.1 Publications

- M. Al-Hussein, E.M. Herzig, M. Schindler, F. Löhrer, C.M. Palumbiny, W. Wang, S.V. Roth, P. Müller-Buschbaum
  Comparative study of the nanomorphology of spray and spin coated PTB7 polymer: fullerene films
  Polymer Engineering and Science **56**, 889–894 (2016)

- M.A. Barrett, M. Trapp, W. Lohstroh, T. Seydel, J. Ollivier, M. Ballauff, N.A. Dencher, T. Hauß
  Alzheimer's peptide amyloid-β*, fragment 22–40, perturbs lipid dynamics*
  Soft Matter **12**, 1444–1451 (2016)

- M.M. Bentlohner, M. Waibel, P. Zeller, K. Sarkar, P. Müller-Buschbaum, D. Fattakhova-Rohlfing, T.F. Fässler
  Zintl clusters as wet chemical precursors for germanium nanomorphologies with tunable composition
  Angew. Chem. Int. Ed. **55**, 2441–2445 (2016)

- A.V. Berezkin, C.M. Papadakis, I.I. Potemkin
  Vertical domain orientation in cylinder-forming diblock copolymer films upon solvent vapor annealing
  Macromolecules **49**, 415–424 (2016)

- A. Campanella, A. Brás, K.N. Raftopoulos, C.M. Papadakis, O. Vassiliadou, A. Kyritsis, M.S. Appavou, P. Müller-Buschbaum, H. Frielinghaus
  Dielectric relaxations of nanocomposites composed of HEUR polymers and magnetite nanoparticles
  Polymer **96**, 70–80 (2016)

- A. Campanella, O. Holderer, K.N. Raftopoulos, M.P. Staropoli P. Müller-Buschbaum, H. Frielinghaus
  Multi-stage freezing of HEUR polymer network with magnetite nanoparticles
  Soft Matter **12**, 3214–3225 (2016)

- H. Ceeh, J. A. Weber, P. Böni, M. Leitner, D. Benea, L. Chioncel, H. Ebert, J. Minár, D. Vollhardt, Ch. Hugenschmidt
  Local electron-electron interaction strength in ferromagnetic nickel determined by spin-polarized positron annihilation
  Sci. Rep. **6**, 20898 (2016)

- T. Cheng, G. Zhang, Y. Xia, Z. Sun, Z. Yang, R. Liu, S. Xia, E. Metwalli, Y. Xiao, X. Wang, M. Wang, J. Ban, L. Yang, Q. Ji, B. Qiu, G. Chen, H. Chen, Y. Lin, X. Pei, Q. Wu, J.-Q. Meng, Z. Liu, L. Chen, T. Xiao, L.-D. Sun, C.-H. Yan, H.J. Butt, P. Müller-Buschbaum, Y.-J. Cheng
  Porous titania/carbon hybrid microspheres templated by in situ formed polystyrene colloids
  J. Colloid Interface Sci. **469**, 242–256 (2016) and erratum J. Colloid Interface Sci. **470**, 230 (2016)

- J. Cui, Á. Rodríguez-Rodríguez, M. Hernández, M. C. García-Gutiérrez, A. Nogales, M. Castillejo, D. Moseguí González, P. Müller-Buschbaum, T. A. Ezquerra, E. Rebollar
  Laser-induced periodic surface structures on P3HT and on its photovoltaic blend with $PC_{71}BM$
  ACS Appl. Mater. Interfaces. **8**, 31894–31901 (2016)

- W.H. de Jeu, U. Ziener, K. Rahimi, E.M. Herzig, P. Müller-Buschbaum, M. Möller, A. Mourran
  Substituted septithiophenes with end groups of different size: Packing and frustration in bulk and thin films
  Langmuir **32**, 1433–1541 (2016)
- R. Flaschmann, J. Ye, N. Paul, F. Bern, P. Esquinazi, P. Müller-Buschbaum, J. Stahn, P. Böni, J.-G. Zheng, T. Aoki, A. Paul
  Self-organized in-plane ordering of nanostructures at epitaxial ferroelectric-ferromagnetic interfaces
  J. Appl. Cryst. **49**, 1693–1703 (2016)
- N. Giesbrecht, J. Schlipf, L. Oesinghaus, A. Binek, T. Bein, P. Müller-Buschbaum, P. Docampo
  Synthesis of Perfectly Oriented and Micrometer-Sized $MAPbBr_3$ *Perovskite Crystals for Thin-Film Photovoltaic Applications*
  Energy Lett. **1**, 150–154 (2016)
- J. Gong, N. Paul, B. Nagy, M. Dolgos, L. Bottyan, P. Müller-Buschbaum P. Böni, J.-G. Zheng, A. Paul
  Morphology of Fe nanolayers with Pf overlayers on low temperature annealing
  J. Appl. Cryst. **49**, 1682–1692 (2016)
- M. Grübel, S. Meister, U. Schulze, K.N. Raftopoulos, F. Baumer, C.M. Papadakis, T. Nilges, B. Rieger
  Synthesis of diisocyanate-containing thiophenes and their use in PDMS-based segmented polymers
  Macromol. Chem. Phys. **217**, 59–71 (2016)
- T. Hollmer, W. Petry
  A novel monolithic LEU foil target based on a PVD manufacturing process for 99 Mo production via fission
  Applied Radiation and Isotopes **118**, 290–296 (2016)
- Y. Hu, J. Schlipf, M. Wussler, M. L. Petrus, W. Jaegermann, T. Bein, P. Müller-Buschbaum, P. Docampo
  Hybrid Perovskite/Perovskite Heterojunction Solar Cells
  ACS Nano **10**, 5999–6007 (2016)
- K. Hülber, J. Wessely, A. Gattringer, D. Moser, M. Kuttner, F. Essl, M. Leitner, M. Winkler, S. Ertl, W. Willner, I. Kleinbauer, N. Sauberer, Th. Mang, N. E. Zimmermann, S. Dullinger
  Uncertainty in predicting range dynamics of endemic alpine plants under climate warming
  Glob. Change Biol. **22**, 2608–2619 (2016)
- S. Jaksch, A. Schulz, Z. Di, R. Luxenhofer, R. Jordan, C.M. Papadakis
  Amphiphilic triblock copolymers from poly(2-oxazoline) with different hydrophobic blocks: Changes of the micellar structures upon addition of a strongly hydrophobic cancer drug
  Macromol. Chem. Phys **13**, 1448–1456 (2016)
- T. M. Koh, V. Shanmugam, J. Schlipf, L. Oesinghaus, P. Müller-Buschbaum, N. Ramakrishnan, V. Swamy, N. Mathews, P. P. Boix, S. G. Mhaisalkar
  Nanostructuring Mixed-Dimensional Perovskites: A Route Toward Tunable, Efficient Photovoltaics
  Adv. Mater. **28**, 3653–3661 (2016)

- M. Kofu, N. Hashimoto, H. Akiba, H. Kobayashi, H. Kitagawa, M. Tyagi, A. Farone, J.R.D. Copley, W. Lohstroh, O. Yamamuro
  Hydrogen diffusion in bulk and nanocrystalline palladium: A quasielastic neutron scattering study
  Physical Review B **94**, 064303 (2016)

- S. Koutsoumpis, K.N. Raftopoulos, M. Jancia, J. Pagacz, E. Hebda, C.M. Papadakis, K. Pielichowski, P. Pissis
  POSS moieties with PEG vertex groups as diluent in polyurethane elastomers: Morphology and phase separation
  Macromolecules **49**, 6507–6517 (2016)

- S. Kripotou, C. Psylla, K. Kyriakos, K.N. Raftopoulos, J. Zhao, S. Pispas, C.M. Papadakis, A. Kyritsis
  Structure and crystallization behvaior of poly(ethylene oxide) (PEO) chains in core-shell brush copolymers with poly(propylene oxide)-block-poly(ethylene oxide) side chains
  Macromolecules **49**, 5963–5977 (2016)

- K. Kyriakos, M. Philipp, C.-H. Lin, M. Dyakonova, N. Vishnevetskaya, I. Grillo, A. Zaccone, A. Miasnikova, A. Laschewsky, P. Müller-Buschbaum, C.M. Papadakis
  Quantifying the interactions in the aggregation of thermoresponsive polymers: The effect of cononsolvency
  Macromol. Rapid Commun. **37**, 420–425 (2016)

- K. Kyriakos, M. Philipp, L. Silvi, W. Lohstroh, W. Petry, P. Müller-Buschbaum, C.M. Papadakis
  Solvent dynamics in solutions of PNIPAM in water/methanol mixtures - a quasi-elastic neutron scattering study
  J. Phys. Chem. B **120**, 4679–4688 (2016)

- M. Leitner, J.A. Weber, H. Ceeh
  Fermi surface determination from momentum density projections
  New J. Phys. **18**, 063033 (2016)

- S.R. Maity, M. Ceretti, M. Meven, J. Schefer, L. Keller, W. Petry, W. Paulus
  MS19-P8 Temperature dependent structural studies of the oxygen ion conductor Pr1. 5Sr0. 5NiO4 investigated by single crystal neutron diffraction
  Foundations of Crystallography **72**, 287 (2016)

- E. Metwalli, H.E. Hermes, E. Calzada, U. Kulozik, S.U. Egelhaaf, P. Müller-Buschbaum
  Water ingress into a casein film quantified using time-resolved neutron imaging
  Phys. Chem. Chem. Phys. **18**, 6458–6464 (2016)

- S. Mühlbauer, A. Heinemann, A. Wilhelm, L. Karge, A. Ostermann, I. Defendi, A. Schreyer, W. Petry, R. Gilles
  The new small-angle neutron scattering instrument SANS-1 at MLZ—characterization and first results
  Nuclear Instruments and Methods in Physics Research A **832**, 297—305 (2016)

- P. Müller-Buschbaum
  GISAXS and GISANS as metrology technique for understanding the 3D morphology of block copolymer thin films
  Eur. Polym. J. **81**, 470–493 (2016)

- L. Oesinghaus, J. Schlipf, N. Giesbrecht, L. Song, Y. Hu, T. Bein, P. Docampo, P. Müller-Buschbaum
  Toward Tailored Film Morphologies: The Origin of Crystal Orientation in Hybrid Perovskite Thin Films
  Adv. Mater. Interfaces **3**, 1600403 (2016)

- A. Ostermann, T.E. Schrader, M. Monkenbusch, B. Laatsch, P. Jüttner, W. Petry
  MS9-P6 Neutron macromolecular crystallography at the FRM II-Or: what can neutrons do for you
  Foundations of Crystallography **72**, 229 (2016)

- C. M. Palumbiny, J. Schlipf, A. Hexemer, C. Wang, P. Müller-Buschbaum
  The Morphological Power of Soap: How Surfactants Lower the Sheet Resistance of PEDOT:PSS by Strong Impact on Inner Film Structure and Molecular Interface Orientation
  Adv. Electron. Mater. **2**, 1500377 (2016)

- S. Pröller, F. Liu, C. Zhu, C. Wang, T.P. Russell, A. Hexemer, P. Müller-Buschbaum, E.M. Herzig
  Following the morphology formation in situ in printed active layers for organic solar cells
  Adv. Energy Mater. **6**, 1501580 (2016)

- M. Reiner, A. Bauer, M. Leitner, Th. Gigl, W. Anwand, M. Butterling, A. Wagner, P. Kudejova, Ch. Pfleiderer, Ch. Hugenschmidt
  Positron spectroscopy of point defects in the skyrmion-lattice compound MnSi
  Sci. Rep. **6**, 29109 (2016)

- M. Rikkou-Kalourkoti, E.N. Kitiri, C.S. Patrickios, E. Leontidis, M. Constantinou, G. Constantinides, X. Zhang, C.M. Papadakis
  Double networks based on amphiphilic cross-linked star block copolymer first conetworks and randomly cross-linked hydrophilic second networks
  Macromolecules **49**, 1731–1742 (2016)

- L. Rodrigues, K. Kyriakos, F. Schneider, H. Dietz, G. Winter, C.M. Papadakis, M. Hubert
  Characterization of lipid-based hexosomes versatile vaccine carriers
  Mol. Pharmaceutics **13**, 3945–3954 (2016)

- S. Säubert, R. Jungwirth, T. Zweifel, M. Hofmann, M. Hoelzel W. Petry
  Neutron and hard X-ray diffraction studies of the isothermal transformation kinetics in the research reactor fuel candidate U–8 wt Mo
  J. Appl. Cryst. **49**, 923–933 (2016)

- C.J. Schaffer, C. Wang, A. Hexemer, P. Müller-Buschbaum
  Grazing incidence resonant soft x-ray scattering for analysis of multi-component polymer-fullerene blend thin films
  Polymer **105**, 357–367 (2016)

- C.J. Schaffer, C.M. Palumbiny, M.A. Niedermeier, C. Burger, G. Santoro, S.V. Roth, P. Müller-Buschbaum
  Morphological degradation in low bandgap polymer solar cells – an in operando study
  Adv. Energy Mater. **6**, 1600712 (2016)

- A. Sepe, J. Zhang, J. Perlich, D.-M. Smilgies, D. Posselt, C.M. Papadakis
  Towards an equilibrium structure in lamellar diblock copolymer thin films using solvent vapor

annealing - An in-situ time-resolved GISAXS study
Eur. Polym. J. **81**, 607–620 (2016)

- L. Silvi, E. Röhm, M. Fichtner, W. Petry, W. Lohstroh
  Hydrogen dynamics in β-Mg (BH 4) 2 on the picosecond timescale
  Phys. Chem. Chem. Phys. **18**, 14323–14332 (2016)

- L. Song, W. Wang, V. Körstgens, D. Moseguí González, Y. Yao, N. K. Minar, J. M. Feckl, T. Bein, D. Fattakhova-Rohlfing, S. V. Roth, P. Müller-Buschbaum
  Spray deposition of titania films with incorporated crystalline nanoparticles for solid-state dye-sensitized solar cells using P3HT
  Adv. Funct. Mater. **26**, 1498–1506 (2016)

- L. Song, A. Abdelsamie, C. J. Schaffer, V. Körstgens, W. Wang, T. Wang, E. D. Indari, T. Fröschl, N. Hüsing, T. Haeberle, P. Lugli, S. Bernstorff, P. Müller-Buschbaum
  A low temperature route towards hierarchically structured titania films for thin hybrid solar cells
  Rev. Sci. Instrum. **26**, 7084–7093 (2016)

- A.M. Stadler, E. Knieps-Grünhagen, M. Bocola, W. Lohstroh, M. Zamponi, U. Krauss
  Photoactivation Reduces Side-Chain Dynamics of a LOV Photoreceptor
  Biophys. J. **110**, 1064 – 1074 (2016)

- M. Stana, B. Sepiol, R. Kozubski, M. Leitner
  Chemical ordering beyond the superstructure in long-range ordered systems
  New J. Phys. **18**, 113051 (2016)

- N.S. Vishnevetskaya, V. Hildebrand, B.-J. Niebuur, I. Grillo, S.K. Filippov, A. Laschewsky, P. Müller-Buschbaum, C.M. Papadakis
  Aggregation behavior of doubly thermoresponsive polysulfobetaine-b-poly(N-isopropylacrylamide) diblock copolymers
  Macromolecules **49**, 6655–6668 (2016)

- W. Wang, S. Guo, E.M. Herzig, K. Sarkar, M. Schindler, D. Magerl, M. Philipp, J. Perlich, P. Müller-Buschbaum
  Investigation of morphological degradation of P3HT:PCBM bulk heterojunction films exposed to long-term host solvent vapor
  J. Mater. Chem. A **4**, 3743–3753 (2016)

- M. Wang, Y. Xia, X. Wang, Y. Xiao, R. Liu, W. Qiang, B. Qiu, E. Metwalli, S. Xia, Y. Yao, G. Chen, Y. Liu, Z. Liu, J.-Q. Meng, Z. Yang, L.-D. Sun, C.-H. Yan, P. Müller-Buschbaum, J. Pan, Y.-J. Cheng
  Silicon oxycarbide/carbon nanohybrids with tiny silicon oxycarbide particles embedded in free carbon matrix based on photoactive dental methacrylates
  ACS Appl. Mater. Interfaces **8**, 13982–13992 (2016)

- M. Winnacker, M. Neumeier, X. Zhang, C.M. Papadakis, B. Rieger
  Sustainable chiral polyamides with high melting temperature via enhanced anionic polymerization of a menthone-derived lactam
  Macromol. Rapid Commun. **37**, 851–857 (2016)

- Y. Yao, E. Metwalli, M. Opel, M. Haese, J.-F. Moulin, K. Rodewald, B. Rieger, P. Müller-Buschbaum

Lamellar diblock copolymer films with embedded maghemite nanoparticles
Adv. Mater. Interfaces **3**, 1500712 (2016)

- X. Zhang, K. Kyriakos, M. Rikkou-Kalourkoti, E.N. Kitiri, C.S. Patrickios, C.M. Papadakis
  Amphiphilic single and double networks: a small-angle X-ray scattering investigation
  Colloid Polym. Sci. **294**, 1027–1036 (2016)

- Q. Zhong, E. Metwalli, M. Rawolle, G. Kaune, A.M. Bivigou-Koumba, A. Laschewsky, C.M. Papadakis, R. Cubitt, J. Wang, P. Müller-Buschbaum
  Influence of hydrophobic polystyrene blocks on the rehydration of polystyrene-block-poly(methoxy diethylene glycol acrylate)-block-polystyrene films investigated by in-situ neutron reflectivity
  Macromolecules **49**, 317–326 (2016)

- T. Zweifel, N. Valle, C. Grygiel, I. Monnet, L. Beck, W. Petry
  Kr implantation into heavy ion irradiated monolithic U–Mo/Al systems: SIMS and SEM investigations
  Journal of Nuclear Materials **470**, 251–257 (2016)

8.2 Talks

- A.V. Berezkin, J. Oberhausen, F. Jung, D. Posselt, C.M. Papadakis
  Structure of films prepared from block copolymer mixtures: computer simulations and GISAXS experiments
  DPG Frühjahrstagung, Regensburg, 6 – 11 Mar 2016

- A.V. Berezkin, F. Jung, C.M. Papadakis
  Simulations of grazing incidence small angle scattering in BornAgain 1.5
  COST School on Surface Analytical Techniques, Regensburg, 4 – 7 Apr 2016

- A.V. Berezkin, C.M. Papadakis, I.I. Potemkin
  Effect of solvent vapour annealing onto the structure of block copolymer thin films
  EUPOC on Block Copolymers for Nanotechnology Applications, Gargnano, Italy, 22 – 26 May 2016

- A.V. Berezkin
  GISAS: grazing-incidence small-angle scattering
  Polymer Physics Summer School, Obertauern, Austria, 21 – 24 Jun 2016

- A.V. Berezkin, F. Jung, C.M. Papadakis
  Structural changes of block copolymer thin films in solvent vapor
  Greek-German Workshop 2016 'Nano-structured soft materials: From polymer self-assembly to stimuli-responsive materials', Athens, 26 – 30 Sep 2016

- L. Bießmann, N. Saxena, K. Wang
  Conducting polymers
  Polymer Physics Summer School, Obertauern, Austria, 21 – 24 Jun 2016

- H-Y.Chiang, W. Petry et al.
  Swift Heavy Ion Irradiation Induced Interactions in the UMo/X/Al Trilayer System
  TMS 2016, Nashville, Tennessee, USA, 14 -– 18 Feb 2016

- S. K. Filippov, B. Verbraeken, P. V. Konarev, D. I. Svergun, C. M. Papadakis, N. Vishnevetskaya, A. Radulescu, S. Rogers, P. Stepanek, M. Hruby, R. Hoogenboom
  Block and gradient copoly(2-oxazoline) micelles: Strikingly different on the inside
  252nd ACS National Meeting & Exposition, Philadelphia, USA, 21 – 25 Aug 2016

- E.M. Herzig
  Reciprocal Space & Fourier Transformation
  Polymer Physics Summer School, Obertauern, Austria, 21 – 24 Jun 2016

- N. Hohn, M.A. Giebel, M. Boone, E. Rivard, T.F. Fässler, P. Müller-Buschbaum
  Novel materials and structuring routines for hybrid solar cells
  ATUMS Semi-Annual Meeting, Chemistry Department, 14 Apr 2016

- N. Hohn
  Novel Materials for Hybrid Solar Cells
  Seminar talk, Physics-Department, 8 Jun 2016

- N. Hohn, F. Löhrer, M. Čorić
  General Polymer Topic Talk: Organic Solar Cells
  Polymer Physics Summer School, Obertauern, Austria, 21 – 24 Jun 2016

- N. Hohn, P. Müller-Buschbaum
  Novel Materials for Hybrid Solar Cells
  ATUMS Annual Meeting, Raitenhaslach, 7 – 11 Nov 2016

- F. Jung, A.V. Berezkin
  Software for analysis of GISAXS data
  COST School on Surface Analytical Techniques, Regensburg, 4 – 7 Apr 2016

- V. Körstgens, C. Mayr, S. Pröller, G. Santoro, S.V. Roth, H. Iglev, R. Kienberger, P. Müller-Buschbaum
  Spray deposition of the active layer of hybrid solar cells monitored with in-situ GISAXS and GIWAXS
  SAXS/WAXS workshop at DESY Photon Science Users' Meeting 2016, Hamburg, 27 – 29 Jan 2016

- V. Körstgens, F. Löhrer, L. Song, W. Wang, M. Schwartzkopf, T. Strunskus, O. Polonskyi, A. Hinz, M. Sommer, S.V. Roth, F. Faupel, P. Müller-Buschbaum
  Sputter deposition of gold on P3HT-films probed with in-situ GISAXS
  TUM-DESY-CAU workshop "The polymer-metal interface", Garching, 1 – 2 Mar 2016

- V. Körstgens, C. Mayr, S. Pröller, G. Santoro, S. V. Roth, H. Iglev, R. Kienberger, P. Müller-Buschbaum
  Water-based hybrid solar cells: spray deposition of the active layer monitored with x-ray scattering methods
  DPG-Frühjahrstagung, Regensburg, 6 – 11 Mar 2016

- V. Körstgens, C. Mayr, S. Pröller, G. Santoro, S. V. Roth, H. Iglev, R. Kienberger, P. Müller-Buschbaum
  Hybrid solar cells with laser-ablated titania
  EMRS spring meeting, Lille, France, 2 – 6 May 2016

- V. Körstgens
  GIWAXS grazing incidence wide angle x-ray scattering
  Polymer Physics Summer School, Obertauern, Austria, 21 – 24 Jun 2016

- V. Körstgens, S. Pröller, C. Mayr, C.-C. Huang, L. Song, S. V. Roth, H. Iglev, R. Kienberger, P. Müller-Buschbaum
  Hybrid solar cells based on laser-ablated titania – A review of aqueous processing and deposition methods for the active layer
  ICCE-24, International Conference on Composites/Nano Engineering, Hainan, China, 17 – 22 Jul 2016

- V. Körstgens
  X-ray scattering for soft matter – applications for solutions, films and fibers
  Zhejiang Sci-Tech University, Hangzhou, China, 10 Oct 2016

- K. Kyriakos, A.V. Berezkin, M. Philipp, A. Zaccone, I. Grillo, A. Miasnikova, A. Laschewsky, P. Müller-Buschbaum, C. M. Papadakis
  Cononsolvency in thermoresponsive micellar solutions: Pathway of aggregate formation DPG-Frühjahrstagung, Regensburg, 6 – 11 Mar 2016

- A. Laschewsky, V. Hildebrand, N. M. Nizardo, E. Schönemann, E. Wischerhoff, P. Müller-Buschbaum, C. M. Papadakis, N. Vishnevetskaya

New poly(sulfobetaine)s as versatile stimuli-responsive building blocks
Biennial Meeting of the GDCh Division of Macromolecular Chemistry and Satellite Meeting of the SFB Transregio 102, Halle, 11 – 14 Sep 2016

- J. Lebert, D. Mosèguí Gonzalez, S. Pröller
  Polymer Blends
  Polymer Physics Summer School, Obertauern, Austria, 21 – 24 Jun 2016
- F. C. Löhrer, V. Körstgens, M. Schwartzkopf, A. Hinz, O. Polonskyi, T. Strunskus, F. Faupel, S. V. Roth, P. Müller-Buschbaum
  In-situ x-ray investigation of the structure formation of metal films on photoactive polymers
  DPG-Frühjahrstagung, Regensburg, 6 – 11 Mar 2016
- F. C. Löhrer, V. Körstgens, M. Schwartzkopf, A. Hinz, O. Polonskyi, T. Strunskus, F. Faupel, S. V. Roth, P. Müller-Buschbaum
  Metal electrodes in organic photovoltaics - why contact matters
  6th Colloquium of the Munich School of Engineering, Garching, 7 Jul 2016
- E. Metwalli
  Real-time investigation of metal nanoparticles growth on thin polymer films
  TUM-DESY-CAU Workshop, Garching, 1 – 2 Mar 2016
- E. Metwalli, M. Rasool, S. Brunner, P. Müller-Buschbaum
  Challenges and opportunities of nanostructured block copolymer membranes for lithium-ion batteries
  DPG-Frühjahrstagung, Regensburg, 6 – 11 Mar 2016
- E. Metwalli, Y. Yao, J.-F. Moulin, M. Opel, P. Müller-Buschbaum
  Assembly of metal-oxide nanoparticles directed by nanodomain orientation in block copolymer thin films
  DPG-Frühjahrstagung, Regensburg, 6 – 11 Mar 2016
- E. Metwalli, S. Schaper, M. Kaeppel, M. Rasool, S. Brunner, P. Müller-Buschbaum
  Block copolymer electrolytes for lithium-ion microbatteries:Challenges and opportunities
  E-MRS, Lille, France, 2 – 6 May 2016
- E. Metwalli, Y. Yao, V. Körstgens, M. Schwartzkopf, S.V. Roth, P. Müller-Buschbaum
  Real time observation of metal nanoparticles growth on block copolymer thin films
  EUPOC, Lake Garada, Italy, 22 – 26 May 2016
- E. Metwalli
  Nanomaterials in motion: Real-time science
  The German Science Day, Cairo, 28 May 2016
- E. Metwalli
  X-Ray and Neutron Reflectivity
  Polymer Physics Summer School, Obertauern, Austria, 21 – 24 Jun 2016
- D. Moseguí González, C. J. Schaffer, S. Pröller, J. Schlipf, L. Song, S. Bernstorff, E. M. Herzig, P. Müller-Buschbaum
  Links between organic solar cell performance and morphological properties
  DPG-Frühjahrstagung, Regensburg, 6 – 11 Mar 2016

- P. Müller-Buschbaum
  Report of the Users Committee (DPS-UC) - report 2015
  DESY User Meeting 28 – 29 Jan 2016

- P. Müller-Buschbaum
  Improved power conversion efficiency of organic solar cells caused by nanoparticle addition
  15th SAXS/WAXS sattelite workshop of DESY Esers Meeting in Hamburg, 28 – 29 Jan 2016

- P. Müller-Buschbaum
  Polymer-metal interfaces in organic electronics
  TUM-DESY-CAU workshop ”The polymer-metal interface”, Garching, 1 – 2 Mar 2016

- P. Müller-Buschbaum, C.M. Palumbiny, F. Liu, T.P. Russell, A. Hexemer, C. Wang
  Following the crystallization in PEDOT:PSS films during printing
  DPG-Frühjahrstagung, Regensburg, 6 – 11 Mar 2016

- P. Müller-Buschbaum, B. Su, L. Song, S.V. Roth
  Towards low-temperature synthesis of polymer/titania hybrid films for application in photovoltaic
  251^{th} American Chemical Society National Meeting in San Diego, USA, 13 – 17 Mar 2016

- P. Müller-Buschbaum
  SolTech - an introduction of the network
  5th international SolTech conference, Munich, 5 – 8 Apr 2016

- P. Müller-Buschbaum
  Designer electronics out of the printer
  „Scientists Meet Scientists – Wednesday Coffee Talk“, IAS Garching, 13 Apr 2016

- P. Müller-Buschbaum
  Probing nanostructures in organic solar cells with GISANS, GISAXS and GIWAXS
  Polymerwissenschaftliches Seminar Bundesanstalt für Materialforschung und –prüfung (BAM) Berlin, 28 Apr 2016

- P. Müller-Buschbaum
  Tailoring Titania Nanostructures for Solar Cell Application
  E-MRS 2016 Spring Meeting, Lille, France, 2 – 6 May 2016

- P. Müller-Buschbaum
  Soft matter samples studied with neutron scattering
  8th MaMaSelf Status Meeting, Rigi Kulm, Switzerland, 10 – 13 May 2016

- P. Müller-Buschbaum
  Probing nanostructures generated by block copolymer self-assembly using advanced scattering techniques
  EUPOC2016, Gargnano, Italy, 22 – 24 May 2016

- P. Müller-Buschbaum
  Polymer and hybrid nanostructures for applications in organic solar cells investigated with advanced scattering techniques
  FOM Institute AMOLF, Amsterdam, Netherlands, 30 May 2016

- P. Müller-Buschbaum
  Polymer and hybrid nanostructures for applications in organic solar cells investigated with advanced scattering techniques
  Centre for Advanced Materials and Innovation Labs in Heidelberg, 2 Jun 2016

- P. Müller-Buschbaum
  TUM.solar - photovoltaic research at TUM
  Visit of GIZ Delegation from Mexico, Garching, 20 Jun 2016

- P. Müller-Buschbaum
  Printing of polymer electrodes for organic electronics: An in-situ study of PEDOT:PSS film formation
  International Conference on Composites/Nano Engineering (ICCE-24), Haikou, China, 17 – 23 Jul 2016

- P. Müller-Buschbaum
  Thermoresponsive properties of linear- and cyclic-poly(N-isopropylacrylamide) thin films
  Zhejiang Sci-Tech University, Hangzhou, China, 7 – 13 Oct 2016

- P. Müller-Buschbaum
  Polymer and hybrid nanostructures for applications in organic solar cells investigated with advanced scattering techniques
  Condensed Matter Seminar, University Oxford in Oxford, UK, 20 Oct 2016

- P. Müller-Buschbaum
  Studying soft matter surfaces and interfaces with in-situ and in-operando x-ray and neutron scattering
  International Workshop Synchrotron and Neutron Scattering in Biomaterials and Soft Matter, Malmö, Sweden, 26 – 28 Oct 2016

- P. Müller-Buschbaum
  GISANS – basics, challenges and possibilities
  International GISAXS 2016 Workshop, Hamburg, 16 – 18 Nov 2016

- P. Müller-Buschbaum
  FlexiProb – the GISANS module
  BMBF Kick-off Meeting, Garching, 8 Dec 2016

- P. Neibecker, M.E. Gruner, O. Dolotko, X. Xu, R. Y. Umetsu, R. Kainuma
  Ordering Tendencies and Eletronic Properties aim Full-Heusler NiCoMnAl and NiCoMnGa Alloys
  5th International Conference of Ferromagnetic Shape Memory Alloys 2016, Sendai, Japan 5 – 9 Sep 2016

- B.-J. Niebuur, X. Zhang, N. Vishnevetskaya, P. Chytil, S.K. Filippov, C.M. Papadakis
  Self-assembled micelles as drug carriers: Influence of molar mass and chain architecture
  DPG-Frühjahrstagung, Regensburg, 6 – 11 Mar 2016

- B.-J. Niebuur, C.M. Papadakis
  PNIPAM Solutions at High Pressure
  Greek-German Workshop 2016 'Nano-structured soft materials: From polymer self-assembly to stimuli-responsive materials', Athens, 26 – 30 Sep 2016

- C.M. Papadakis
  Thermoresponsive polymeric micelles - what can we learn from time-resolved small-angle neutron scattering? Bundesanstalt für Materialforschung und -prüfung, Berlin, 25 Feb 2016
- C.M. Papadakis
  Grazing-incidence small-angle X-ray scattering: A technique to investigate nanostructured polymer films and their structural changes
  COST School on Surface Analytical Techniques, Regensburg, 4 – 7 Apr 2016
- C.M. Papadakis, J. Zhang, A. Sepe, D.-M. Smilgies, D. Posselt
  Structural changes in block copolymer thin films during solvent vapor treatment - in-situ, real-time GISAXS investigations
  EUPOC on Block Copolymers for Nanotechnology Applications, Gargnano, Italy, 22 – 26 May 2016
- C.M. Papadakis
  Thermoresponsive block copolymers
  Istituto Superior Tecnico, Lisbon, Portugal, 17 Jun 2016
- C.M. Papadakis
  Physical hydrogels via charge driven self-organization of a triblock polyampholyte in dependence on charge asymmetry and ionic strength
  Self-Assembly in the World of Polymers, Prague, Czech Republic, 10 – 14 Jul 2016
- C.M. Papadakis
  Physical hydrogels via charge-driven self-organization of a triblock polyampholyte system
  German-Greek Workshop 2016, Athens, Greece, 26 – 30 Sep 2016
- W. Petry, M. Leitner, P. Neibecker, J. Neuhaus
  Temperature dependent phonon anharmonicity in elementary and martensite systems
  TMS 2016, Nashville, Tennessee, USA, 14 -— 18 Feb 2016
- W. Petry, T. Huber et al.
  The Thermal Properties of Fresh and Spent U-Mo Fuels: An Overview
  TMS 2016, Nashville, Tennessee, USA, 14 -— 18 Feb 2016
- W. Petry
  Neutrons for research, industry and medicine – Review of the conversion project
  FRM II – TUM, Garching, 25 – 26 Apr 2016
- W. Petry
  Experimental Possibilities at MLZ
  GIF funded project on “The influence of biopolymers and organic substances on mineralization in water treatment processes”, Sede Boqer Campus, Ben-Gurion-University, Israel 6 – 7 Nov 2016
- W. Petry
  Neutronen für Wissenschaft, Industrie und Medizin,
  Visit of „Kerntechnische Gesellschaft Süd“, FRM II – TUM, Garching, 13 Oct 2016
- W. Petry
  Industrial and medical applications using a modern und intense neutron source,
  European NuclearConference 2016, Warsaw, Poland 9 – 13 Oct 2016

- W. Petry
  Engineering science at a state-of-the art neutron source,
  CREMLIN workshop “Demands of European neutron users in materials science for the instrumentation of the upcoming PIK neutron science centre”, Kiel, 22 – 23 Sep 2016
- W. Petry
  Neutronen – wozu?
  6. VDI-TUM-Expertenforum, TUM Forschungscampus Garching, 15 Sep 2016
- W. Petry
  Nuclear fission and spallation neutron
  Raciri Summerschool, Repino, Russia, 21 – 28 Aug 2016
- W. Petry
  Neutronen für Wissenschaft, Industrie und Medizin
  Ringvorlesung Physik-Department, TUM, 15 Jun 2016
- W. Petry
  Medicine at MLZ
  Master Course “Radiation Biology”, FRM II – TUM, Garching, 12 Dec 2016
- M. Philipp
  Quasi-elastic neutron scattering (QENS)
  Polymer Physics Summer School, Obertauern, Austria, 21 – 24 Jun 2016
- M. Philipp, W. Petry, P. Müller-Buschbaum
  The role of nonlinearities at phase transitions in stimuli-responsive polymer solutions and hydrogels
  DPG Frühjahrstagung, Regensburg, 6 – 11 Mar 2016
- M. Philipp, W. Petry, J.K. Krüger, P. Müller-Buschbaum
  The role of nonlinearities and kinetics at phase transitions in stimuli-responsive polymer solutions
  University of Chemistry and Technology, Prague, Czechia, 16 Mar 2016
- S. Pratap, J. Schlipf, P. Müller-Buschbaum
  An investigation on the relationship of perovskite films with solvent media
  DPG-Frühjahrstagung, Regensburg, 6 – 11 Mar 2016
- S. Pratap, J. Schlipf, P. Müller-Buschbaum
  Following the morphological changes occurring in hybrid organometallic lead halide perovskites
  Tag der Physikerinnen/Day of Female Physicists, Garching, 14 Jun 2016
- S. Pratap, J. Schlipf, P. Müller-Buschbaum
  Following the morphological changes occurring in hybrid organometallic lead halide perovskites
  6th Colloquium of the Munich School of Engineering, Garching, 7 Jul 2016
- K.N. Raftopoulos, K. Kyriakos, O. Holderer, O. Ivanova, M. Ohl, P. Müller-Buschbaum, C.M. Papadakis
  PNIPAM dynamics in water-methanol mixtures
  DPG Frühjahrstagung, Regensburg, 6 – 11 Mar 2016
- K.N. Raftopoulos
  Small Angle Scattering
  Polymer Physics Summer School, Obertauern, Austria, 21 – 24 Jun 2016

- J. Schlipf, L. Oesinghaus, N. Giesbrecht, Y. Hu, S. Bernstorff, T. Bein, P. Docampo, P. Müller-Buschbaum
  Morphology and crystal orientation of hybrid perovskite thin films for application in high efficiency solar cells
  DPG-Frühjahrstagung, Regensburg, 6 – 11 Mar 2016
- J. Schlipf, L. Song, B. Su
  Hybrid Perovskite Photovoltaics
  Polymer Physics Summer School, Obertauern, Austria, 21 – 24 Jun 2016
- L. Song, A. Abdelsamie, C. J. Schaffer, V. Körstgens, W. Wang, T. Wang, E.D. Indari, T. Fröschl, N. Hüsing, T. Haeberle, P. Lugli, S. Bernstorff, P. Müller-Buschbaum
  A low temperature route towards hierarchically structured titania films for thin hybrid solar cells
  DPG-Frühjahrstagung, Regensburg, 6 – 11 Mar 2016
- L. Song, W. Wang, V. Körstgens, D. Moseguí González, Y. Yao, N.K. Minar, J.M. Feckl, T. Bein, D. Fattakhova-Rohlfing, S.V. Roth, P. Müller-Buschbaum
  Spray deposition of titania films with incorporated crystalline nanoparticles for solid-state dye-sensitized solar cells using P3HT
  25th Annual International Conference on Composites or Nano Engineering, Haikou, China, 17 – 23 Jul 2016
- N.S. Vishnevetskaya
  Thermo-responsive polymers
  Polymer Physics Summer School, Obertauern, Austria, 21 – 24 Jun 2016
- S. Xia
  Magnetic nanoparticles embedded in diblock copolymer films
  The polymer-metal interface, Garching, 1 – 2 Mar 2016
- S. Xia, D. Yang
  Block copolymers
  Polymer Physics Summer School, Obertauern, Austria, 21 – 24 Jun 2016
- X. Zhang
  pH-Responsive Polymers – Fundamentals of Polyelectrolytes
  Polymer Physics Summer School, Obertauern, Austria, 21 – 24 Jun 2016

8.3 Posters

- L. Bießmann, C. J. Schaffer, J. Schlipf, V. Körstgens, S. Bernstorff, P. Müller-Buschbaum
  Mesostructured ZnO scattering layers for OLED applications
  DPG-Frühjahrstagung, Regensburg, 6 – 11 Mar 2016

- L. Bießmann, P. Müller-Buschbaum
  Designing nanostructured scattering layers for OLED applications
  6th Colloquium of the Munich School of Engineering, Garching, 7 Jul 2016

- L. Bießmann, P.A. Staniac, P. Müller-Buschbaum
  Investigations on hierarchically structured ZnO for enhanced light scattering in OLED applications
  GISAXS 2016, Hamburg, 16 – 18 Nov 2016

- L. Bießmann, P.A. Staniac, P. Müller-Buschbaum
  Enhanced light scattering in OLED applications by hierarchically structured ZnO
  1st BornAgain School and User Meeting, Garching, 21 – 22 Nov 2016

- F. Buschek, C. Mayr, M. Wörle, H. Iglev, V. Körstgens, R. Kienberger, P. Müller-Buschbaum
  Hybrid solar cells with laser-ablated titania nanoparticles
  Polymer Physics Summer School 2016, Obertauern, Austria, 21 – 24 Jun 2016

- F. Buschek, C. Mayr, M. Wörle, H. Iglev, V. Körstgens, R. Kienberger, P. Müller-Buschbaum
  Hybrid solar cells with laser-ablated titania nanoparticles
  6th Colloquium of the Munich School of Engineering, Garching, 7 Jul 2016

- K.-L. Claude, S. Pinzek, K. Kyriakos, A. Schulte, A. Miasnikova, A. Laschewsky, P. Müller-Buschbaum, C.M. Papadakis
  Phase transition of thermoresponsive polymers in dependence on temperature and pressure.
  DPG-Frühjahrstagung, Regensburg, 6 – 11 Mar 2016

- K.-L. Claude, S. Pinzek, K. Kyriakos, A. Schulte, A. Miasnikova, A. Laschewsky, P. Müller-Buschbaum, C.M. Papadakis
  Phase transition of thermoresponsive polymers in dependence on temperature and pressure.
  Polymer Physics Summer School 2016, Obertauern, Austria, 21 – 24 Jun 2016

- K.-L. Claude, D. Aravopoulou, B.-J. Niebuur, A. Schulte, V. Hildebrand, A. Laschewsky, A. Kyritsis, C.M. Papadakis
  Phase behaviour of the thermoresponsive polymer PNIPMAM in dependence on temperature and pressure.
  Greek-German Workshop 2016 'Nano-structured soft materials: From polymer self-assembly to stimuli-responsive materials', Athens, 26 – 30 Sep 2016

- F. Dreher, D. Moseguí González, P. Müller-Buschbaum
  Effect of magnetic field on the performance of P3HT:PCBM organic solar cells modified with Fe_3O_4 *nanoparticles*
  Polymer Physics Summer School 2016, Obertauern, Austria, 21 – 24 Jun 2016

- A. Haussmann, V. Körstgens, P. Müller-Buschbaum
  Morphology interfaces of water-processed hybrid solar cells
  6th Colloquium of the Munich School of Engineering, Garching, 7 Jul 2016

- A. Haussmann, V. Körstgens, P. Müller-Buschbaum
  Morphology interfaces of water-processed hybrid solar cells
  Polymer Physics Summer School 2016, Obertauern, Austria, 21 – 24 Jun 2016
- C. Herold, M. Philipp, V. Hildebrand, A. Laschewsky, P. Müller-Buschbaum
  Phase-separating multi-stimuli-responsive polymer thin films
  Polymer Physics Summer School 2016, Obertauern, Austria, 21 – 24 Jun 2016
- A. Hetzenecker, N. Hohn, M. Giebel, T.F. Fässler, P. Müller-Buschbaum
  Hybrid photovoltaics based on diblock copolymer structured, mesoporous Ge thin films
  Polymer Physics Summer School 2016, Obertauern, Austria, 21 – 24 Jun 2016
- A. Hetzenecker, N. Hohn, M. Giebel, T.F. Fässler, P. Müller-Buschbaum
  Hybrid photovoltaics based on diblock copolymer structured, mesoporous Ge thin films
  6th Colloquium of the Munich School of Engineering, Garching, 7 Jul 2016
- N. Hohn, L. Song, M. Boone, E. Rivard, P. Müller-Buschbaum
  Tuning the interface of hybrid thin films for photovoltaic applications
  DPG-Frühjahrstagung, Regensburg, 6 – 11 Mar 2016
- N. Hohn, L. Bießmann, M. A. Giebel, M. Boone, E. Rivard, T.F. Fässler, P. Müller-Buschbaum
  Novel materials and structuring routines for HPV applications
  5th International SolTech Conference in Munich, Munich, 5 – 8 Apr 2016
- N. Hohn, M.A. Giebel, M. Boone, E. Rivard, T.F. Fässler, P. Müller-Buschbaum
  Developing alternative material systems for energy conversion through hybrid photovoltaics
  6th Colloquium of the Munich School of Engineering, Garching, 7 Jul 2016
- N. Hohn, M.A. Giebel, M. M. Bentlohner, D. Fattakhova-Rohlfing, T.F. Fässler, P. Müller-Buschbaum
  Ge9-Zintl Clusters as Wet Chemical Precursors for macro- and mesoporous Ge-Films in Hybrid Solar Cells
  10th IGSSE Forum, Raitenhaslach, 1 – 3 Jun 2016
- F. Jung, A.V. Berezkin, D.-M. Smilgies, D. Posselt, C.M. Papadakis
  Morphological changes in diblock copolymer thin films in solvent vapor mixtures
  DPG-Frühjahrstagung, Regensburg, 6 – 11 Mar 2016
- F. Jung, A.V. Berezkin, D.-M. Smilgies, D. Posselt, C.M. Papadakis
  Morphological changes in diblock copolymer thin films in solvent vapor mixtures
  Polymer Physics Summer School 2016, Obertauern, Austria, 21 – 24 Jun 2016
- F. Jung, A.V. Berezkin, D.-M. Smilgies, D. Posselt, C.M. Papadakis
  Annealing of diblock copolymer thin films using solvent vapor mixtures – an in situ GISAXS study
  GISAXS Workshop 2016, DESY Hamburg, 16 – 18 Nov 2016
- B. Kalis, J. Schlipf, P. Müller-Buschbaum
  In-Situ measurements of organic and hybrid solar cells
  Polymer Physics Summer School 2016, Obertauern, Austria, 21 – 24 Jun 2016
- T. Kaps, E. Metwalli, M. Schwartzkopf, S.V. Roth, P. Müller-Buschbaum
  Porous Titania-based Hybrid Films as Electrodes for Lithium-Ion Batteries
  Polymer Physics Summer School 2016, Obertauern, Austria, 21 – 24 Jun 2016

- C.-H. Ko, M.A. Dyakonova, K.N. Raftopoulos, S. Gkermpoura, M.M.S. Lencina, C. Tsitsilianis, C.M. Papadakis
  Multiresponsive hydrogels from telechelic polyelectrolytes
  DPG-Frühjahrstagung, Regensburg, 6 –11 Mar 2016
- C.-H. Ko, M.A. Dyakonova, K.N. Raftopoulos, S. Gkermpoura, M.M.S. Lencina, C. Tsitsilianis, C.M. Papadakis
  Multiresponsive hydrogels from telechelic polyelectrolytes
  Polymer Physics Summer School 2016, Obertauern, Austria, 21 – 24 Jun 2016
- V. Körstgens, M. Philipp, G. Santoro, S.V. Roth, P. Müller-Buschbaum
  Microfluidics and microGISAXS – in situ investigations at the solid-liquid interface
  DESY Photon Science Users' Meeting 2016, Hamburg, 27 – 29 Jan 2016
- V. Körstgens, C. Mayr, S. Pröller, G. Santoro, S.V. Roth, H. Iglev, R. Kienberger, P. Müller-Buschbaum
  Hybrid solar cells with laser-ablated titania: in situ spray deposition of the active layer
  5th International SolTech Conference in Munich, Munich, 5 – 8 Apr 2016
- F. C. Löhrer, V. Körstgens, P. Zhang, S. V. Roth, P. Müller-Buschbaum
  Optical and morphological investigation of photoactive low bandgap polymer films
  DESY Photon Science Users' Meeting 2016, Hamburg, 27 – 29 Jan 2016
- F. C. Löhrer, V. Körstgens, M. Schwartzkopf, A. Hinz, O. Polonskyi, T. Strunskus, F. Faupel, S. V. Roth, P. Müller-Buschbaum
  In-situ investigation of the structure evolution of metal electrodes for organic photovoltaics
  4th International SolTech Conference in Munich, Munich, 5 – 8 Apr 2016
- F. C. Löhrer, N. Hohn, D. Yang, K. Wang, J. Schlipf, D. Moseguí González, L. Song, B. Su, W. Wang, C.J. Schaffer, C. M. Palumbiny, V. Körstgens, P. Müller-Buschbaum
  Structural investigation of thin active layers for photovoltaic applications
  Inauguration of the Center for Nanosystems Chemistry, Würzburg, 7 Oct 2016
- F. C. Löhrer, V. Körstgens, M. Schwartzkopf, A. Hinz, O. Polonskyi, T. Strunskus, F. Faupel, S. V. Roth, P. Müller-Buschbaum
  In-situ GISAXS investigation of the structure evolution of metal contacts on polymer thin films
  DESY GISAXS Workshop 2016, Hamburg, 16 – 18 Nov 2016
- F. C. Löhrer, V. Körstgens, M. Schwartzkopf, A. Hinz, O. Polonskyi, T. Strunskus, F. Faupel, S. V. Roth, P. Müller-Buschbaum
  In-situ GISAXS investigation of the structure evolution of metal contacts on polymer thin films
  BornAgain School and User Meeting, Munich, 21 – 22 Nov 2016
- D. Moseguí González, C.J. Schaffer, S. Pröller, J. Schlipf, L. Song, S. Bernstorff, E.M. Herzig, P. Müller-Buschbaum
  Morphology and performance of organic solar cells studied with in-operando scattering techniques
  6th Colloquium of the Munich School of Engineering, Garching, 7 Jul 2016
- P. Neibecker, M. Leitner, M. Gruner, O. Dolotko, W. Petry
  Atomic order effects on the electronic properties of NiCoMnGa and NiCoMnAl Heusler alloys
  Retreat Meeting, TRR 80 program of the Deutsche Forschungsgemeinschaft (DFG), Freising, Germany 16 – 17 Feb 2016

- S. Pratap, J. Schlipf, P. Müller-Buschbaum
  Following the structural changes in mixed organometallic lead halide perovskite systems
  8th MaMaSELF status meeting, Rigi Kulm, Switzerland, 10 – 13 May 2016
- S. Pratap, J. Schlipf, P. Müller-Buschbaum
  Following the structural changes in mixed organometallic lead halide perovskite systems
  Polymer Physics Summer School 2016, Obertauern, Austria, 21 – 24 Jun 2016
- S. Pratap, J. Schlipf, P. Müller-Buschbaum
  Following the structural changes in mixed organometallic lead halide perovskite systems
  LMU Sektion Kristallographie thesis presentations, Munich, 15 July 2016
- M. Rafiq, N. Saxena, P. Müller-Buschbaum
  In-situ polymerization of PEDOT:Tos thermoelectric thin films
  Polymer Physics Summer School 2016, Obertauern, Austria, 21 – 24 Jun 2016
- J. Schlipf, L. Oesinghaus, N. Giesbrecht, Y. Hu, S. Bernstorff, T. Bein, P. Docampo, P. Müller-Buschbaum
  Morphology and crystal orientation of hybrid perovskite thin films for application in high efficiency solar cells
  5th International SolTech Conference in Munich, Munich, 5 – 8 Apr 2016
- J. Schlipf, L. Oesinghaus, N. Giesbrecht, Y. Hu, T. Bein, S. Bernstorff, P. Docampo, P. Müller-Buschbaum
  Morphology and crystal orientation of hybrid perovskite thin films for application in high efficiency solar cells
  6th Colloquium of the Munich School of Engineering, Garching, 7 Jul 2016
- J. Schlipf, L. Oesinghaus, L. Bießmann, E. Metwalli, L. Porcar, P. Müller-Buschbaum
  Ingression of moisture into hybrid perovskite thin films probed with in-situ GISANS
  Deutsche Neutronenstreutagung, Kiel, 20 – 22 Sep 2016
- J. Schlipf, L. Oesinghaus, L. Bießmann, E. Metwalli, L. Porcar, P. Müller-Buschbaum
  Ingression of moisture into hybrid perovskite thin films probed with in-situ GISANS
  1st BornAgain School and User Meeting, Garching, 21 – 22 Nov 2016
- S. Schlosser, N. Hohn, L. Bießmann, S. Xia, P. Müller-Buschbaum
  Graded porous titania films for photovoltaic application
  Polymer Physics Summer School 2016, Obertauern, Austria, 21 – 24 Jun 2016
- S. Schlosser, N. Hohn, L. Bießmann, S. Xia, P. Müller-Buschbaum
  Graded porous titania films for photovoltaic application
  6th Colloquium of the Munich School of Engineering, Garching, 7 Jul 2016
- A. Schulte, K.-L. Claude, S. Pinzek, P. Müller-Buschbaum, C. M. Papadakis
  Phase behavior of the thermoresponsive poly(N-isopropyl acrylamide) at variable pressure
  APS Annual Meeting, Baltimore, Maryland, USA, 14 – 18 Mar 2016
- A. Schreiber, J. Schlipf, P. Müller-Buschbaum
  Influence of processing parameters on the morphology of perovskite solar cells
  Polymer Physics Summer School 2016, Obertauern, Austria, 21 – 24 Jun 2016

- A. Schreiber, J. Schlipf, P. Müller-Buschbaum
  Influence of processing parameters on the morphology of perovskite solar cells
  6th Colloquium of the Munich School of Engineering, Garching, 7 Jul 2016
- C. Senfter, F.C. Löhrer, C. Schaffer, P. Müller-Buschbaum
  Degradation processes in high-efficiency polymer solar cells
  Polymer Physics Summer School 2016, Obertauern, Austria, 21 – 24 Jun 2016
- L. Song, W. Wang, V. Körstgens, D. Moseguí González, Y. Yao, N.K. Minar, J.M. Feckl, T. Bein, D. Fattakhova-Rohlfing, S.V. Roth, P. Müller-Buschbaum
  Spray deposition of titania films with incorporated crystalline nanoparticles for solid-state dye-sensitized solar cells
  5th International SolTech Conference in Munich, Munich, 5 – 8 Apr 2016
- L. Song, A. Abdelsamie, C.J. Schaffer, V. Körstgens, W. Wang, T. Wang, E.D. Indari, T. Fröschl, N. Hüsing, T. Haeberle, P. Lugli, S. Bernstorff, P. Müller-Buschbaum
  A low temperature route towards hierarchically structured titania films for thin hybrid solar cells
  6th Colloquium of the Munich School of Engineering, Garching, 7 Jul 2016
- B. Springer, E. Metwalli, P. Müller-Buschbaum
  Morphology of block copolymer electrolytes for rechargable lithium batteries
  DPG-Frühjahrstagung, Regensburg, 6 – 11 Mar 2016
- B. Springer, E. Metwalli, P. Müller-Buschbaum
  Morphology of block copolymer electrolytes for rechargable lithium-ion batteries
  6th Colloquium of the Munich School of Engineering, Garching, 7 Jul 2016
- B. Springer, E. Metwalli, P. Müller-Buschbaum
  Morphology of block copolymer electrolytes for rechargable lithium-ion batteries
  Polymer Physics Summer School 2016, Obertauern, Austria, 21 – 24 Jun 2016
- B. Su, H.A. Caller-Guzman, V. Körstgens, C. J. Schaffer, Y. Yao, S.V. Roth, P. Müller-Buschbaum
  Titania network structures prepared via spray coating for photovoltaic applications
  DPG-Frühjahrstagung, Regensburg, 6 – 11 Mar 2016
- B. Su, H.A. Caller-Guzman, V. Körstgens, C.J. Schaffer, Y. Yao, S.V. Roth, P. Müller-Buschbaum
  Titania network structures prepared via spray coating for photovoltaic applications
  5th International SolTech Conference in Munich, Munich, 5 – 8 Apr 2016
- B. Su, H. A. Caller-Guzman, V. Körstgens, C.J. Schaffer, Y. Yao, Y.C. Rui, S.V. Roth, P. Müller-Buschbaum
  Foam-like structure of spray coated titania films for perovskite solar cells
  6th Colloquium of the Munich School of Engineering, Garching, 7 Jul 2016
- M. Trapp, T. Gutberlet, C.M. Papadakis, T. Seydel, W. Lohstroh, M. Zamponi, D. Posselt
  Dynamics of biological membranes – quasi elastic neutron scattering studies of phospholipid model membranes
  Biomembrane Days 2016, Berlin, 5 – 7 Sep 2016
- M. Trunk, B. Su, R. Wang, P. Müller-Buschbaum
  Crystallization behavior of hybrid perovskite films on mesoporous titania templates

DPG-Frühjahrstagung, Regensburg, 6 – 11 Mar 2016

- M. Trunk, B. Su, R. Wang, P. Müller-Buschbaum
  Crystallization behavior of hybrid perovskite films on mesoporous titania templates
  6th Colloquium of the Munich School of Engineering, Garching, 7 Jul 2016

- M. Trunk, B. Su, R. Wang, P. Müller-Buschbaum
  Crystallization behavior of hybrid perovskite films on mesoporous titania templates
  Polymer Physics Summer School 2016, Obertauern, Austria, 21 – 24 Jun 2016

- F. Vazquez-Luna, N.S. Vishnevetskaya, C. Kessler, B. Ferse, C.M. Papadakis
  Thermoresponsive Nanocomposite Hydrogels with Magnetic Nanoparticles for Sensing Applications
  Polymer Physics Summer School 2016, Obertauern, Austria, 21 – 24 Jun 2016

- N.S. Vishnevetskaya, V. Hildebrand, A. Laschewsky, P. Müller-Buschbaum, C. M. Papadakis
  Aggregation Behavior of Doubly Thermoresponsive Polysulfobetaine-b-poly(N-isopropylmethacrylamide) Diblock Copolymers
  DPG-Frühjahrstagung, Regensburg, 6 – 11 Mar 2016

- K. Wang, Y. Tong, L. Song, L. Bießmann, S. Xia, J. Schlipf, C.J. Schaffer, P. Müller-Buschbaum
  Nanostructured zinc oxide films for application in hybrid photovoltaics
  DPG-Frühjahrstagung, Regensburg, 6 – 11 Mar 2016

- K. Wang, Y. Tong, L. Song, L. Bießmann, S. Xia, J. Schlipf, C.J. Schaffer, P. Müller-Buschbaum
  Nanostructured zinc oxide films for application in hybrid photovoltaics
  5th International SolTech Conference in Munich, Munich, 5 – 8 Apr 2016

- K. Wang, Y. Tong, L. Song, L. Bießmann, S. Xia, J. Schlipf, C.J. Schaffer, P. Müller-Buschbaum
  Nanostructured zinc oxide films for application in hybrid photovoltaics
  6th Colloquium of the Munich School of Engineering, Garching, 7 Jul 2016

- K. Wang, Y. Tong, L. Song, L. Bießmann, S. Xia, J. Schlipf, C.J. Schaffer, P. Müller-Buschbaum
  Nanostructured zinc oxide films for application in hybrid photovoltaics
  GISAS summer school: experiments and analysis, Garching, 17 – 22 July 2016

- R. Wang, Z. Di, P. Müller-Buschbaum, H. Frielinghaus
  Morphology and Optoelectronic Properties of P3HT-b-PS/PCBM bulk heterojunction system in organic photovoltaic application
  6th Colloquium of the Munich School of Engineering, Garching, 7 Jul 2016

- R. Wang, Y. Tong, A. Manzi, K. Wang, E. Kentzinger, A. Urban, J.J. Feldmann, P. Müller-Buschbaum, H. Frielinghaus
  Perfectly Orientated Mixed Dimensional Lead Bromide Perovskite Thin Film with Low ASE Threshold
  MML workshop 2016 DESY, Hamburg, 14 Dez 2016

- D. Yang, W. Wang, P. Müller-Buschbaum
  Printing High Efficiency Solar Cells
  DPG-Frühjahrstagung, Regensburg, 6 – 11 Mar 2016
- D. Yang, W. Wang, P. Müller-Buschbaum
  Printing High Efficiency Solar Cells
  5th International SolTech Conference in Munich, Munich, 5 – 8 Apr 2016
- D. Yang, W. Wang, P. Müller-Buschbaum
  Employing water/alcohol soluble conjugated polymer as cathode interlayer in organic solar cells
  6th Colloquium of the Munich School of Engineering, Garching, 7 Jul 2016
- D. Yang, W. Wang, P. Müller-Buschbaum
  Printing High Efficiency Solar Cells
  Tag der Physikerinnen/Day of Female Physicists, Garching, 14 Jun 2016
- D. Yang, W. Wang, P. Müller-Buschbaum
  Employing water/alcohol soluble conjugated polymer as cathode interlayer in organic solar cells
  GISAS summer school: experiments and analysis", Garching, 17–22 Jul 2016
- S. Xia, E. Metwalli, Y. Yao, M. Schwartzkopf, D. Chekrygina, B. Beyersdorff, S.V. Roth, P. Müller-Buschbaum
  Printed nanostructured block-copolymer/metal-oxide hybrid films
  DPG-Frühjahrstagung, Regensburg, 6 – 11 Mar 2016
- S. Xia, E. Metwalli, P. Müller-Buschbaum
  Neutron Reflectivity Investigation on Thermo-responsive Copolymers Embedded with Magnetic Nanoparticles
  German conference on neutron scattering, Kiel, 20 – 22 Sep 2016
- X. Zhang, B.-J. Niebuur, P. Chytil, T. Etrych, S.K. Filippov, A.Kikhney, F. Wieland, D.I. Svergun. C.M. Papadakis
  Macromolecular HPMA-Based drug delivery system - behavior in protein environment
  DPG-Frühjahrstagung, Regensburg, 6 – 11 Mar 2016
- X. Zhang, B.-J. Niebuur, P. Chytil, T. Etrych, S.K. Filippov, A. Kikhney, F. Wieland, D.I. Svergun, C.M. Papadakis
  Macromolecular HPMA-based drug delivery system - behavior in protein environment
  30th Conference of the European Colloid and Interface Society, Rome, 4 – 9 Sep 2016

8.4 Invited Talks at the Institute of Functional Materials

- Prof. Jiping Wang, Zhejiang Sci-Tech University, Hangzhou, Zhejiang, P.R China
  Global Textile Trends and Innovations
  27 Jan 2016

- Dr. Lucie Nová, Charles University in Prague, Czechia
  Molecular Simulations of flower-like micelles and micellar gels
  19 Apr 2016

- Prof. Apostolos Kyritsis, Dept. of Physics, National Technical University of Athens, Greece
  Thermal and dielectric studies on thermoresponsive polymers
  5 Jul 2016

- Prof. Dr. Richard J. Spontak, Depts. of Chemical and Biomolecular Engineering and Materials Science and Engineering, North Carolina State University, Raleigh, USA
  Controlling Morphological and Property Development in Network-Forming Multiblock Ionomers
  12 Jul 2016

- Linda Reuter, Imperial College, London, UK
  Novel approaches towards one dimensional photonic structures with a titanium oxide hydrate - PVAl – hybrid
  26 Jul 2016

- Lucas Kreuzer, Universität Bayreuth
  Enzyme-coated Metal Nanoparticles as Bio-Nanocatalyst
  Sep 6 2016

- Dr. Rune E. Johnson, Dept, of Energy Conversion and Storage, Technical University of Denmark
  In situ X-ray diffraction studies of electrode materials in working metal-ion batteries and other layered materials
  Sep 20, 2016

- Sebastian Grott, LMU München
  Scientific basic points – A journey through solid state chemistry and total synthesis
  27 Sep 2016

- Adj. Prof. Dr. Stephan V. Roth, DESY, Hamburg
  Advances In Thin Film Coating – the crucial role of X-rays
  30 Nov 2016

- Prof. Dr. Yajun Cheng, Department of Materials, University of Oxford, UK
  Polymer/Inorganic Nanohybrids: from Synthesis to Applications
  14 Dec 2016

8.5 Funding

Deutsche Forschungsgesellschaft:

- *Zweifach und orthogonal schaltbare Blockcopolymere aus zwitterionischen und thermoresponsiven Blöcken: Synthese und Strukturen in Lösung und im dünnen Film*
  Grant Number: MU 1487/17-1
  Project Leader: Prof. Dr. Peter Müller-Buschbaum

- *In-situ Untersuchungen zu Kondensation, Nukleation und Wachstum von Metallfilmen und Nanostrukturen auf organischen Oberflächen während Sputterbeschichtung*
  Grant Number: MU 1487/18-1
  Project Leader: Prof. Dr. Peter Müller-Buschbaum

- *Transport und Morphologie, Einfluss auf nichtgeminale Rekombination in Organischen Solarzellen*
  Grant Number: MU 1487/22-1
  Project Leader: Prof. Dr. Peter Müller-Buschbaum

- *Aufbau internationaler Kooperationen zum Thema 'Intelligente Textilien basierend auf thermoresponsiven Copolymerbeschichtungen'*
  Grant Number: MU 1487/23-1
  Project Leader: Prof. Dr. Peter Müller-Buschbaum

- Teilprojekt *Inorganic-organic hybrid photovoltaic solar cells using novel hybrid materials* im GRK 2022: University of Alberta / Technische Universität München Internationale Graduiertenschule für Funktionelle Hybridmaterialien (ATUMS) der DFG
  IRTG-2022
  Project Leader: Prof. Dr. Peter Müller-Buschbaum

- Within DFG Collaborative Research Centre SFB TRR 80/2:
  Elektronische Struktur und martensitische Phasenumwandlungen
  Teilprojekt: G4
  Project Leader: Prof. Dr. Winfried Petry

- Im Rahmen des Memorandums of Understanding on Cooperation between DFG and RFBR:
  Mischungen aus Lösungsmitteln und Mischungen aus Blockcopolymeren für die kontrollierte Präparation strukturierter dünner Blockcopolymerfilme
  Grant Number: PA 771/10-2
  Project Leader: Prof. Dr. Christine M. Papadakis

- *Zweifach und orthogonal schaltbare Blockcopolymere aus zwitterionischen und thermoresponsiven Blöcken: Synthese und Strukturen in Lösung und im dünnen Film*
  Grant Number: PA 771/14-1
  Project Leader: Prof. Dr. Christine M. Papadakis

- Im Rahmen des Memorandums of Understanding on Scientific Cooperation between DFG and GACR:
  Kugelförmiges Pferd im Vakuum oder anwendbare Mizellen? Verhalten und Form von Nanopoartikeln als Wirkstoffträger für Krebsmedikamente in reeller Blutumgebung
  Grant Number: PA 771/17-1
  Project Leader: Prof. Dr. Christine M. Papadakis

Bundesministerium für Bildung und Forschung:

- *FlexiProb: Flexible Probenumgebungen für die Untersuchung weicher Materie zur Implementierung an der ESS*
  Teilprojekt: 3
  Project Leader: Prof. Dr. Peter Müller-Buschbaum
- *Optische In-situ Methoden für das Flugzeitspektrometer TOFTOF*
  Project Leader: Prof. Dr. Peter Müller-Buschbaum

Bayerisches Staatsministerium für Bildung und Kultus, Wissenschaft und Kunst:

- Im Rahmen der Munich School of Engineering (MSE):
  Solar Technologies Go Hybrid (SolTech) - Forschungsnetzwerk TUM.solar
  Project Leader: Prof. Dr. Peter Müller-Buschbaum
- Im Rahmen der Munich School of Engineering (MSE): Netzwerk Regenerative Energien
  Aufbau eines interdisziplinären Netzwerks aus Lehrstühlen der Technischen Universität München und anderen Forschungseinrichtungen zur Förderung der Forschungsaktivitäten im Bereich der regenerativen Energien
  Project Leader: Prof. Dr. Peter Müller-Buschbaum
- Seedfunding im Rahmen der Energy Valley Bavaria (Munich School of Engineering, MSE)
  Novel Nanostructured Thermoelectric Hybrid Materials (NovelNTHM)
  Project Leader: Prof. Dr. Peter Müller-Buschbaum
- Nachwuchsgruppe im Rahmen der Energy Valley Bavaria (Munich School of Engineering, MSE)
  Organische Photovoltaik
  Project Leader: Dr. Eva M. Herzig

Technische Universität München:

- Im Rahmen der International Graduate School of Science and Engineering (IGSSE)
  Interface Science for Photovoltaics - a EuroTech GreenTech Initiative
  Project Leader: Prof. Dr. Peter Müller-Buschbaum

Others:

- Im Rahmen des Exzellenzclusters Nanosystems Initiative Munich (NIM)
  Nanosystems for Energy Conversion
  Pricipal Investigator: Prof. Dr. Peter Müller-Buschbaum
- Im Rahmen der Leonhard-Lorenz-Stiftung
  Untersuchung der magnetischen Domänenstruktur in ferromagnetischen Formgedächtnislegierungen
  Project Leader: Prof. Dr. Winfried Petry

- Im Rahmen der Leonhard-Lorenz-Stiftung
  Selbstdiffusion in Aluminium-Germanium Legierungsschmelzen untersucht mit quasi-elastischer Neutronenstreuung
  Project Leader: Prof. Dr. Winfried Petry

- Im Rahmen des Programms Hochschulpartnerschaften mit Griechenland (Deutscher Akademischer Austausch Dienst, DAAD)
  Thermoresponsive polymers of complex architecture (ResComp)
  Project Leader: Prof. Dr. Christine M. Papadakis; Co-Project Leader: Prof. Dr. Apostolos Kyritsis (National Technical University of Athens, NTUA).

9 The chair

9.1 Staff

Chair: Prof. Dr. Winfried Petry

Head: Prof. Dr. Peter Müller-Buschbaum

Professor:

Prof. Dr. Christine M. Papadakis

Fellows:

Dr. Anatoly V. Berezkin
Dr. Eva Maria Herzig
Dr. Volker Körstgens
Dr. Michael Leitner
Dr. Wiebke Lohstroh
Dr. Ezzeldin Metwalli Ali
Dr. Jürgen Neuhaus
Dr. Neelima Paul
Dr. Martine Philipp
Dr. Konstantinos N. Raftopoulos

PhD students:

Bruno Baumeister
Lorenz Bießmann
Antonella Campanella
Tobias Chemnitz
Wei Chen
Mihael Coriç
Stefan Döge
Margarita Dyakonova
Oliver Filonik
Sebastian Grott
Alexander Erwin Heldmann
Nuri Hohn
Tanja Huber
Lukas Karge
Lucas Kreuzer
Jenny Lebert
Xiaohu Li
Franziska Löhrer
David Magerl
Daniel Moseguí González
Pascal Neibecker
Bart-Jan Niebuur
Shambhavi Pratap
Stephan Pröller
Christian Reiter
Nitin Saxena
Christoph Johannes Schaffer
Rupert Schauer
Robert Schenk
Johannes Schlipf
Jingyi Shi
Luca Silvi
Lin Song
Christian Steyer
Bo Su
Sandro Szabó
Natalya S. Vishnevetskaya
Kun Wang
Rui Wang
Weijia Wang
Tobias Widmann
Stephan Wlokka
Senlin Xia
Dan Yang
Yuan Yao
Xiaohan Zhang

Master students:

Edoardo Barabino
Julian Becker
Florian Buschek
Pin-Yi Chiu
Kora-Lee Claude
Florian Dreher
Oliver Filonik
Moritz Futscher
Peter Haslauer
Adrian Haussmann
Christian Herold
Andreas Hetzenecker
Kiran M. John
Florian Jung
Maximilian Kaeppel
Bernhard Kalis
Thomas Kaps
Regina Kluge
Chia-Hsin Ko
Eva Kratzer
Anjani Kumar Maurya
Gilles Möhl
Lukas Oesinghaus
Ali Özkü
Shambhavi Pratap
Mubashar Rafiq
Anna Sanina
Simon Schaper
Steffen Schlosser
Armin Schreiber
Dominik Schullerer
Christian Schwarz
Christoph Senfter
Bernhard Springer
Richard Stockhausen
Margret Thordardottir
Markus Trunk
Fernando Vazquez Luna
Kejie Zhang

Bachelor students:

Jorge Corella Puertas
Martin Finkel
Arnulf Grimm
Erwin Heldmann
Ludwig Holleis
Mike J. Jost
Xaver Lamprecht
Philipp Moser
Matthias Nuber
Florian Pantle
Zoltan A. Perera
Dominik Petz
Margerita Pfab
Thomas Retzer
Josef Helmut Schmidbauer
Patrick Schnierle
Tobias Schreitmüller
Gabriele Semino

Students assistants:

Kiran Mathew John
Regina Kluge
Borja-Vicente Pano
Akhil Parameswaran Marar
Thomas Retzer
Hong Xu

Technical/administrative staff:

Susanna Fink
Reinhold Funer
Josef Huber
Josef Kaplonski
Carola Kappauf
Matthias Maier
Herbert Meier
Dieter Müller
Marion Waletzki

9.2 Graduations

- **Accomplished PhD Theses**

  Antonella Campanella
  Structure and dynamics of nanocomposites composed of hydrophobically modified ethoxylated urethanes and magnetite nanoparticles in the hydrogel and dried state

  Margarita Dyakonova
  Stimuli-responsive reversible hydrogels from polyampholytes

  Bettina Kracke
  Protein-based nanoparticles with thermoswitchable particle size

  Christoph Johannes Schaffer
  Morphological degradation in polymer-fullerene solar cells

  Weijia Wang
  Nanostructure-performance relationship in polymer-based solar cells

  Yuan Yao
  Ordered maghemite nanoparticles in diblock copolymer films

- **Accomplished Master Theses**

  Edoardo Barabino
  Characterization of PTB7-Th:PC71BM Bull Heterojunction Solar Cells: the Influence of Blend Ratio

  Florian Dreher
  Enhancing triplet exciton population in organic solar cells

  Maximilian Valentin Kaeppel
  Morphology and conductivity of ionic liquid/block copolymer hybrid electrolytes for lithium-ion batteries

  Thomas Kaps
  Porous Titania-based Hybrid Films as Electrodes for Lithium-Ion Batteries

  Chia-Hsin Ko
  Multi-responsive hydrogels from telechelic polyelectrolytes

  Florian Jung
  Annealing of Diblock Copolymer Thin Films Using Solvent Vaper Mixtures at Controlled Temperatures

  Anjani Kumar Maurya
  Optimization of the thermoelectric properties of conducting polymer thin films by dedoping and hybrid approaches

  Lukas Oesinghaus
  The morphology of perovskite solar cells studied by GIWAXS

  Ali Özkü
  Structuring routines for high efficiency solar cells

  Shambhavi Pratap
  Chemical origins of crystalline preferred orientationin hybrid organometallic lead halide perovskite thin films

Simon Jakob Schaper
Self-assembled hybrid materials as a membrane for lithium-ion batteries

Christoph Senfter
Degradation Analysis of Low-Bandgap Organic Solar Cells

Richard Stockhausen
Degradation in printed polymer: fullerene thin films for organic photovoltaics

Hong Xu
Structure and properties of thermoresponsive diblock copolymers embedded with metal oxide nanoparticles

- **Accomplished Bachelor Theses**

Jorge Corella Puertas
Pressure sensitive adhesives applied to fibers

Martin Finkel
Experiments to determine the monocrystalline elastic constants in polycrystalline materials from diffraction

Arnulf Grimm
Study of Improvement Methods for a Sputtering Process in Nuclear Fuel Development and Development of a Suitable Measuring Sample Holder

Erwin Heldmann
Evaluation of Prompt Gamma Spectra Using Different Models

Ludwig Friedrich Wilhelm Holleis
Conductivity Study of PEO-based block copolymer electrolyte

Xaver Lamprecht
Influence of ionic liquids on thermoelectric properties of polymer thin films and design of a new Seebeck coefficient measurement setup

Philipp Moser
Role of molecular interactions for stimuli-responsive polymers of potential use in soft robotics

Florian Pantle
Single crystal perovskite solar cells

Zoltan Abel Perera
Smart nano-sensors made of stimuli-responsive hydrogels

Margerita Pfab
Metal decorated colloidal films for application in organic photovoltaics

Thomas Retzer
Drug carrier based on HPMA copolymers investigated in a protein environment

Josef Helmut Schmidbauer
Compton Scattering across the semiconductor-to-metal transition in FeSi

Patrick Schnierle
Metal-polymer hybrid composites for sensor applications

Tobias Schreitmüller
Nanoparticles via laser ablation for hybrid solar cells

Gabriele Semino
Analysis of GISAXS data of gold nanostructures on a polymer film

9.3 Guests

- Prof. Dr. Jiping Wang, Zhejiang Sci-Tech University, PR China
  26 – 27 Jan 2016
- Prof. André Laschewsky, Universität Potsdam
  1 Feb 2016
- Dr. Lucie Nová, Dr. Peter Košovan, Charles University, Prague, Czechia
  19 Apr 2016
- Prof. Dr. Alfons Schulte, University of Central Florida, USA
  17 May – 22 Jul 2016; 7 – 13 Sep 2016
- Prof. Dr. Richard Spontak, North Carolina State University
  1 – 31 Jul 2016
- Prof. Apostolos Kyritsis, National Technical University of Athens, Greece
  4 – 9 Jul 2016
- Prof. Dr. Qi Zhong, Zhejiang Sci-Tech University, PR China
  5 – 19 Sep 2016
- Dr. Rune E. Johnson, Technical University of Denmark
  20 Sep 2016
- Katerina Giannakopoulou, National Technical University of Athens, Greece
  1 Oct – 15 Dec 2016
- Prof. Dr. Stephan V. Roth, DESY Hamburg
  30 Nov 2016
- Prof. Dr. Yajun Cheng, Dept. of Materials, University of Oxford, UK
  14 Dec 2016